3D MODELING OF THE HUMAN UPPER LIMB INCLUDING THE BIOMECHANICS OF JOINTS, MUSCLES AND SOFT TISSUES

THÈSE N^{O} 1906 (1998)

PRÉSENTÉE AU DÉPARTEMENT D'INFORMATIQUE

ÉCOLE POLYTECHNIQUE FÉDÉRALE DE LAUSANNE

POUR L'OBTENTION DU GRADE DE DOCTEUR ÈS SCIENCES

PAR

Walter MAUREL

DEA Informatique Image,ENSM, Saint Etienne
Ingénieur ENSAM, Paris, France
de nationalité française

acceptée sur proposition du jury:

Prof. D. Thalmann, directeur de thèse
Prof. B. Arnaldi, rapporteur
Prof. E.B. Pires, rapporteur
Prof. M. Kunt, rapporteur

Lausanne, EPFL
1999

Résumé

L'enjeu des recherches envers la modélisation d'humains virtuels est de parvenir à représenter les caractéristiques essentielles de l'être humain avec le plus de réalisme possible. Le succès d'une telle entreprise permettrait la simulation et l'analyse de nombreuses situations faisant intervenir l'homme. L'intérêt de la simulation réside dans la possibilité d'extraire du modèle des informations permettant de prédire, voire de reproduire, les phénomènes qui se produiraient en situation réelle. Les techniques de visualisation et de simulation informatiques offrent des avancées majeures dans ce sens.

Les processus physiologiques de génération de force et de coordination du mouvement comptent parmi les phénomènes dont il reste encore beaucoup à comprendre. L'épaule est aussi probablement l'articulation du corps humain qui mérite, plus qu'aucune autre, d'être qualifiée "terra incognita". Une étude envers la modélisation et la simulation du membre supérieur est ainsi présentée dans ce document. Cela comprend l'analyse approfondie de l'anatomie et la biomécanique squelettique et musculaire du membre supérieur, des lois constitutives biomécaniques pour la modélisation des muscles et des tissus organiques, de la mécanique nonlinéaire des milieux continus ainsi que des méthodes numériques, en particulier les méthodes d'éléments finis incrémentales, employées pour leur simulation.

Sur la base de ces analyses, un modèle tridimensionnel du système musculosquelettique du membre supérieur a ensuite été développé, employant les données du Visible Human produites par la U.S. National Library of Medicine, et a été appliqué à la simulation dynamique du membre supérieur. Ces travaux de recherche ont été menés dans le cadre du projet ESPRIT Européen CHARM, dont l'objectif a été le développement d’une base de données humaines extensive pour l'animation, et d'un ensemble d'outils logiciels permettant la modélisation et la simulation dynamique du système musculosquelettique humain, y compris la simulation en éléments finis des contractions musculaires et des déformations des tissus organiques.

Dans un second temps, une application de ces connaissances pour la modélisation et l'animation réaliste du membre supérieur en animation par ordinateur est présentée. La modélisation anatomique et biomécanique de la contrainte scapulothoracique et des cones articulaires de l'épaule est proposée et appliquée à l'animation réaliste d'un squelette et d'une musculature virtuels.

Abstract

The challenge in virtual human modeling is to achieve the representation of the main human characteristics with as much realism as possible. Such achievements would allow the simulation and/or analysis of many virtual situations involving humans. Simulation is especially useful to derive information from the models so as to predict and/or reproduce the behaviors that would be observed in real situations. Computer methods in visualization and simulation have thus great potential for advances in medicine.

The processes of strength generation and motion coordination are some of these phenomena for which there is still much remaining to be understood. The human shoulder is also probably the articulation of the human body which deserves more than any other to be named "terra incognita". Investigations towards the biomechanical modeling and simulation of the human upper limb are therefore presented in this study. It includes thorough investigation into the musculoskeletal anatomy and biomechanics of the human upper limb, into the biomechanical constitutive modeling of muscles and soft tissues, and into the nonlinear continuum mechanics and numerical methods, especially the incremental finite element methods, necessary for their simulation.

On this basis, a 3-D biomechanical musculoskeletal human upper limb model has been designed using the Visible Human Data provided by the U.S. National Library of Medicine, and applied to the dynamic musculoskeletal simulation of the human upper limb. This research has been achieved in the context of the EU ESPRIT Project CHARM, whose objective has been to develop a comprehensive human animation resource database and a set of software tools allowing the modeling of the human complex musculoskeletal system and the simulation of its dynamics, including the finite element simulation of soft tissue deformation and muscular contraction.

An investigation towards the application of this knowledge for the realistic modeling and animation of the upper limb in computer animation is then presented. The anatomical and biomechanical modeling of the scapulo-thoracic constraint and the shoulder joint sinus cones are proposed and applied to the realistic animation, using inverse kinematics, of a virtual skeleton and an anatomic musculoskeletal body model.

Acknowledgements

I would like to thank my director **Daniel Thalmann** for welcoming me to *LIG*, the Computer Graphics Lab of EPFL, and for supervising my work during these years, as well as our secretary **Josiane Bottarelli** for handling the general administrative needs and providing casual support. I would also like to thank all the other assistants in *LIG-EPFL* and *MIRALab-University of Geneva* for our friendly relationship and collaboration. Thanks to all, your friendship has been very much appreciated every day!

In relation to this work, I would like to thank in particular:

- for useful advice on understanding LIG's libraries:
  Paolo Baerlocher, Tom Molet, Luc Emering, Ronan Boulic

- for useful advice on the use of Inventor/Rapidapp:
  Pierre Beylot, Olivier Paillet, Luciana Porcher-Nedel

- for useful design contributions:
  Mireille Clavien, Thierry Michellod, Olivier Paillet

- for reading my compositions and providing useful comments and corrections:
  Srikanth Bandi, Prem Kalra, Paolo Baerlocher

- for system management and occasional emergencies:
  Tom Molet, Christian Babski, Tolga Capin (SGI)
  Luc Emering, Pascal Becheiraz, Philippe Lang (PC/Mac)
  Jianhua Shen, Selim Balcisoy (Video Stuff)

I am also grateful to the *European Commission* and the *Swiss Federal Office of Education and Science* which funded the CHARM project at the origin of this thesis. I thank **Dr. Jakub Wejchert**, project officer, and **Prof. Rae Earnshaw**, project reviewer, as well as the other CHARM partners and subcontractors for the instructive collaboration I have benefited from:

Instituto Superior Técnico, **Prof. Eduardo Pires** and **João Martins** (IST)
Ecole des Mines de Nantes, **Prof. Gérard Hégron** (EMN)
Institut de Recherche en Informatique et Systèmes Aléatoires, **Prof. Bruno Arnaldi** (IRISA)
Universitat de Les Illes Balears, **Prof. Josep Blat** (UIB)
University of Geneva, **Prof. Nadia Magnenat Thalmann** (UG)
Universität Karlsruhe, **Prof. Alfred Schmitt** (UKA)

Many thanks in particular for allowing me to document this thesis with images and data from your contributions in CHARM.

In the context of CHARM, I would like to thank especially the assistants for our friendly relationship and for valuable discussions on the model development and implementation:

- **Prem Kalra, Philippe Gingins, Pierre Beylot, Yin Wu** (UG)
- **Rita Salvado, José Carvalho, Miguel Matéus, Sebastiao Barata** (IST)
- **Jean-Luc Nougaret, Franck Multon, Ali Razavi, Dominique Villard** (EMN)
- **Sven Dörr, Achim Stößer**, **Kurt Saar** (UKA)
- **Ramon Mas Sanso** (UIB)

Finally, I wish to express my full gratitude to **Dr. Pierre Hoffmeyer** and **Dr. Jean Fasel** (CMU – Cantonal Medical University – Geneva) for their advice in orthopaedy and anatomy, as well as to **Prof. Philippe Zysset**, **Prof. Alain Curnier** (DME – Département de Mécanique – EPFL), **Prof. Eduardo Borges Pires** and **Prof. João Martins** (IST) for their advice in nonlinear mechanics and numerical methods.

Special thanks to Mrs. Denise Ross, UK, for the English correction of this manuscript.

Preface

The challenge in virtual human modeling is to achieve the representation of the main human characteristics with as much realism as possible. The major investigations in this area concern the modeling of human motion, body deformations, photo-realistic rendering of skin, hair and clothes, as well as the modeling of the human senses and behavior.

Such achievements would allow the simulation and/or analysis of many situations involving humans. Simulation is especially useful to derive information from the models so as to predict and/or reproduce the behaviors that would be observed in real situations. Application of this research ranges from computer games to medicine, throughout cinema, sociology, communication, sport, trade, industry, army, aeronautics and astronautics.

Computers may currently not be powerful enough to allow the development of virtual humans including models for all the physiological processes involved in a real human being. We may think, however, of a forthcoming time, when it will not make much difference to use a highly realistic complex human model or to use a basic one with respect to performance and ease of use. Virtual humans are bound to this evolution. At the time when such models are achieved, considerable knowledge on the real phenomenon of our lives will have been gained.

The processes of strength generation and motion coordination are some of these phenomena for which there is still much remaining to be understood. The human shoulder is probably the articulation of the human body which deserves more than any other to be named "terra incognita". This may be one of the reasons for which, up to now, no specific model for the human shoulder has been developed in computer animation, although the current models hardly lend themselves to realistic deformations of this area of the body.

Another reason for this may be advanced that, except for closed views on naked shoulders, there is no need for a realistic model of the human shoulder. This may be true for the time being given that the interest for photo-realistic virtual humans is only emerging and that, currently, the whole body model is over-simplified. This may no longer be true, however, in the near future when virtual humans are used on every day advertisements and when the body models are anatomically correct and biomechanically controlled. Anatomically correct modeling is already being developed and an improved representation of the human shoulder will soon be necessary for consistency with this approach as well as for an improved control of the deformations.

Meanwhile, the realistic biomechanical modeling of the human shoulder is already the objective of numerous investigations for medical purposes. Computer methods in visualization and simulation have a great potential for advances in medicine. Research in

computer animation has also conversely a lot to gain from the investigations and simulation methods being applied to biomedical disciplines. An analysis towards the realistic modeling of an anatomical area of the human body can not seriously pretend to ignore one or the other of these approaches. Both must be jointly investigated in order to justify the choices before presenting a model. This is the intention of this study.

The essential part of this research has been achieved in the context of the EU ESPRIT Project CHARM. The objective of this project has been to develop a comprehensive human animation resource database and a set of software tools allowing the modeling of the human complex musculoskeletal system and the simulation of its dynamics, including the finite element simulation of soft tissue deformation and muscular contraction. The upper limb was chosen to start with, as one of the most complex articulations of the human body.

The responsibility of the Computer Graphics Lab of EPFL (LIG), and mine in particular, has been to develop the biomechanical human upper limb model underlying the other developments in the project and to provide a review of the available constitutive relationships for soft tissue modeling. For this reason, my own contribution, partially reported here, has essentially been theoretical. It has mainly consisted of thorough investigation into the musculoskeletal anatomy and biomechanics of the human upper limb, into the biomechanical constitutive modeling of muscles and soft tissues, and into the nonlinear continuum mechanics and numerical methods, especially the incremental finite element methods, necessary for their simulation.

These investigations have provided strong grounds for coordinating the development and the implementation of the whole model and of the associated simulation methods in the project. The originality of my contribution may thus not especially rely on the development of a better model than may have already been proposed by peers, but rather in the making of choices and suggestions in view of fully achieving the ambitious objectives of the project. Besides, its effectiveness has officially been demonstrated with three major publications, two papers and one book, as well as with the development and the results achieved by our partners, which are mainly presented in Chapter 5.

In the remaining time after the project, I have chosen to lead an investigation towards the implementation, on this theoretical basis, of a realistic shoulder model for computer animation, using the animation libraries developed at LIG. This choice has been agreed as part of an internal project aiming at developing an anatomically correct model of the human body. Timing constraints mean that I have limited my analysis to the development and implementation aspects of a shoulder model.

Consequently, I have proposed and achieved an extension of LIG's standard BODY *skeleton_* structure for allowing the realistic animation of the underlying skeleton layer, as required for the generation of realistic deformations around the shoulder. Another specific long term investigation will be necessary for designing, on the basis of this model, specific motion control procedures based on the animation techniques applied in LIG. This is left as potential future work.

As a conclusion to this preface, the content of each chapter of the present thesis report is briefly outlined as follows:

Introduction. This chapter raises the importance of the computer graphic realistic modeling of the human figure in general, and of the human body for biomedical applications in particular, and invokes the gap that remains to be filled concerning the understanding of the human upper limb biomechanics. In this context, it establishes the objectives of the CHARM project at the origin of this thesis, and presents the general justifying that I have provided towards their achievement, as detailed in the following chapters.

Skeleton Modeling. This chapter presents the analysis I have lead for developing the theoretical kinematic and rigid-body models of the human upper limb, on the basis of former investigations on the upper limb anatomy and biomechanics. It outlines, in particular, the choices that I have made in comparison with other existing models in order to fulfill the project constraints presented in the introduction on the model implementation and simulation.

Muscle Action Modeling. Complementing the previous analysis, the modeling of the muscles' action on the upper limb skeleton is presented, on the basis of similar anatomical and biomechanical studies of the upper limb musculature. Former models, methods and approaches are also presented as suggestions towards the simulation and the prediction of the muscles' contraction forces.

Soft Tissue Modeling. In this chapter, the biomechanical constitutive modeling of soft tissues and the incremental finite element simulation methods are investigated as bases towards the finite element simulation of soft tissue deformations. Models and methods for tendon, passive muscle and skin in particular are then suggested for application in CHARM. The development of a personal theoretical model of muscle contraction is also presented.

CHARM Implementations. In this chapter, the developments and implementations actually achieved in CHARM by my partners and myself are presented as an effective application of my investigations. In particular, this includes the development of the 3D topological biomechanical model of human upper limb, the development of high-level motion control procedures based on its dynamic simulation, the application of optimization methods for the prediction of muscles' forces, and the finite element implementation of constitutive relations for soft tissue deformation and muscle contraction simulation.

BODY Upper Limb Modeling. As an application of the extensive investigations on the human upper limb presented in the previous chapters, the attempt I have lead towards the improvement of the BODY model currently used in LIG for computer animation is presented in this chapter. It essentially consists of the adjustment and/or extension of the BODY *skeleton_* structure around the shoulder and elbow joints. An animation interface I have developed for animating the upper limb and shoulder models is used for their demonstration.

Joints Boundary Modeling. In this chapter, the analysis I have lead towards the adjunction of joint sinus cones onto the improved BODY upper limb model is detailed. The extension of the *Skeledit* skeleton editor for allowing the interactive design of joint sinus cones is also presented and illustrated by the design of biomechanical joint sinus cones on the model. Finally, the animation of the full model is evaluated using the animation interface presented in the previous chapter and its efficiency is discussed.

Conclusion. This final chapter summarizes the investigations, choices and suggestions I have made towards the modeling and simulation of the human upper limb for CHARM and for LIG, with an opening to the forthcoming developments expected to complement this thesis.

Table of Contents

1 Introduction

In theory, modeling consists of developing a representation of the properties of an object/phenomenon with respect to the goals of its analysis. In connection with that, the challenge in virtual human modeling is to achieve the representation of the main human characteristics with as much realism as possible. In practice, virtual characters are composed of several layers – i.e. the skeleton, the muscle and the skin layers – each handling one component of the body global deformation. The skeleton models generally used take the form of wireframe hierarchies of one-degree-of-freedom (DOF) rotational joints. Though this approach may be sufficient for modeling most parts of the human body, it does not easily lend itself to realistic animation, regarding the shoulder. This is because the shoulder is one of the most complex articulation of the human body. Its realistic biomechanical modeling is currently the objective of numerous investigations for medical purposes. In the scope of human upper limb modeling, a preliminary analysis of the general modeling approaches in computer graphics and biomechanics is necessary. This is the purpose of this introductory chapter.

1.1 Virtual Human Modeling

1.1.1 Virtual Humans Evolution

The First Humans. The first computer generated human model was introduced in 1959 under the direction of Hudson at the Boeing Airplane company as a *Landing Signal Officer* indicating the scale in a cockpit visibility simulation during landing for the CVA-19 class aircraft carrier. Viewed from the flight path, the figure was a 12-point silhouette with the lines representing two-dimensional edges only. The figure was then gradually improved to satisfy the degree of realism required by the simulations. The *First Man*, developed in 1968 for the Boeing 747 instrument panel conception studies, was composed of seven movable segments that could be articulated at the pelvis, neck, shoulders and elbows to approximate various pilot motions (Fig. 1.1). "He" was also the first virtual human to appear on TV during a 30-second commercial for Norelco (Fetter 82).

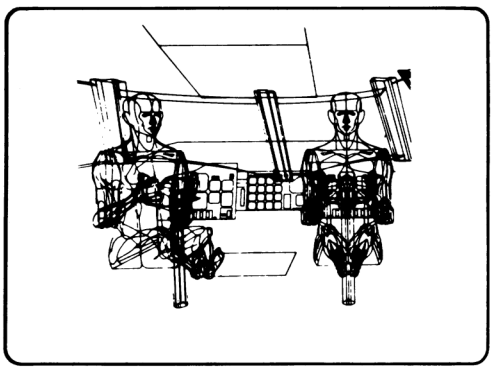

Fig. 1.1. The *First Man* (Fetter 82)

The model was soon improved into a more anthropometrically accurate 19-joint "Second Man". Test animations of the model included operating an aircraft control column, running and high jumping. The following development of the *Third Man* and *Woman* enriched the model with an order-of-magnitude in complexity, allowing the visualization of the human figures at different scales. A progression of databases was developed using one-point figures for demographic distribution, 10-point figures for queuing studies, and 100-point figures for anthropometrics. The 100-point figures were used with databases of other designed objects in display exercises where figures seated themselves in automobiles, walked in architectural environments, or rode the escalator to a monorail station. The *Fourth Man* and *Woman* were finally developed for geometry testing and for exploring the visual effects of hemispheric projection. They were the first virtual humans to appear on raster displays as highlighted, shaded, colored human models (Fig 1.2) (Fetter 82).

(Fetter 82)
Fig.1.2. The *4-th Man*

The Anthropometric Models. By the time the *Fourth Human* models were adjusted, a number of anthropometric modeling programs developed, aiming at aiding anthropometrists in the design of human-machine interfaces. *Cyberman* (Blackeley 80) was developed by Chrysler Corporation for the automobile industry. Its purpose was to analyze and define acceptable limb and body locations for a human model within a defined environment. It was used to analyze model drivers, passengers, and their activities in and around a car, such as driving or opening the trunk. *Combiman* (Bapu 80) was specifically designed at the Aerospace Medical Research Laboratory to determine the human reach capacity for aircraft cockpit configuration design and evaluation. *Sammie* (Fig 1.3) was designed at the University of Nottingham for general anthropometric analysis and design applications (Kingsley 81). Other anthropometric modeling programs were also developed for similar purposes by the Boeing Corporation (*Boeman*, *Car* – Fig. 1.4 – Harris 80), at Rockwell International (*Buford* – Fetter 82), or at the University of Pennsylvania (*Bubbleman* – Badler 79). Though the esthetics of all these models was not especially developed, their underlying skeletal structures were already profiling the skeleton models currently used in computer animation (Dooley 82).

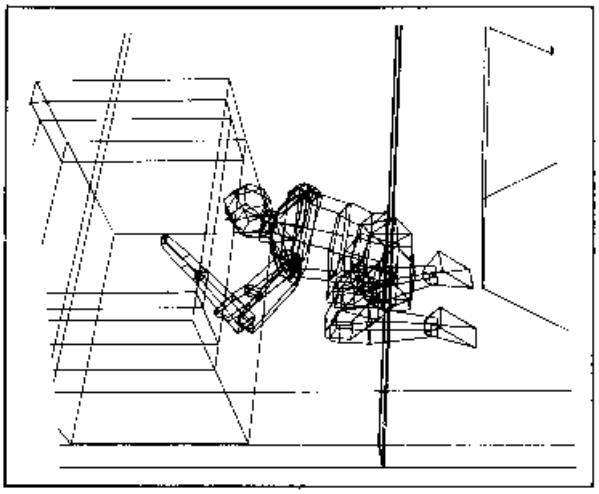

Fig. 1.3. Sammie (Kingsley 81)

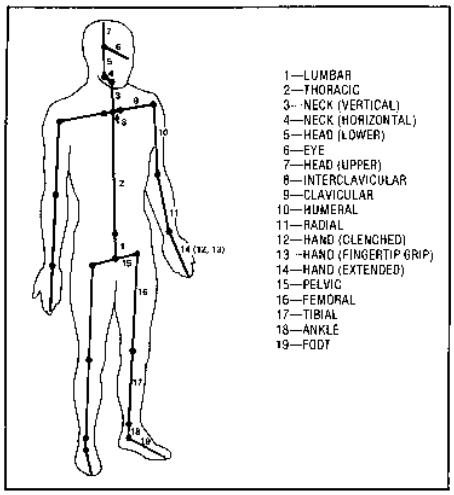

Fig. 1.4. Car (Harris 80)

(Willmert 82)
Fig. 1.5. Virtual crash test dummy

(Thalmanns 93)
Fig. 1.6. The virtual *Marilyn*

The Crash-Test Dummies. A large number of simulation programs were also developed to predict the uncontrolled motion of the human body under external influences. In these programs, the human body appeared as a collection of rigid members assigned with dynamic properties and connected by ball or pin joints similar to those crash-test dummies used in the real crash experiments. Many models were two dimensional, like in the Simula (Glancy 72) and Prometheus (Twigg 74) crash simulation programs, this being sufficient for simulating such events as head-on automobile collisions or the rapid forces inherent in aircraft takeoffs and landing (Fig. 1.5). For other situations, Three-Dimensional body models were developed using cylinders or ellipsoids to model the rigid limb segments. The realism of the output and the graphic capabilities of these programs were however generally poor (Willmert 82).

The Realistic Humans. The diversification of the applications requiring human simulation led the development of the virtual human modeling and animation techniques to become a research area in itself. The aim of this brand new research field naturally imposed itself as the realistic modeling of the human figure extensively. Investigations rapidly multiplied towards the realistic modeling of the human body, hands, face, hair, clothes as well as towards the development of specific techniques for their realistic animation. Methods borrowed from physics, mechanics, robotics, etc. (Thalmann 90), developed, allowing the generation of various human motions, such as walking, falling, grasping, etc. (Badler 93, Thalmanns 90, 93, 96). With realism, virtual humans democratized and gained major expansion within commercial or leisure applications, such as advertisement, computer games and the cinema. Some virtual characters even gained celebrity for the esthetics of their design and/or the realism of their animation, the most famous one being the Thalmanns' Marilyn (Fig. 1.6).

The Autonomous Agents. The development of visually realistic virtual humans motivated the development of their autonomous perception, intelligence and behavior. Virtual humans have thus been provided with synthetic senses, as well as with the capacity of analyzing and reacting to specific situations (Fig .1.7, 1.8). Such advances opened new areas of research and experiment for disciplines such as artificial intelligence, cognitive sciences, communication or sociology. Various devices and techniques also necessarily developed, allowing immersion in virtual environments and interaction with their inhabitants. Current research in this area includes vision/speech synthesis, gesture/speech recognition as well as individual/group behavior simulation (Thalmann 95, Emering 97, Noser 94-97, Becheiraz 98). Once the complete autonomy of virtual humans is achieved, the modeling of their individual emotions would probably be the last objective towards complete realism.

(Emering 97)

Fig. 1.7. Fight between real and virtual men

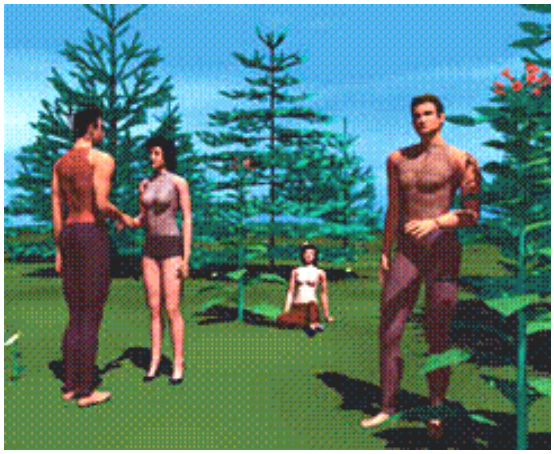

(Noser 94-97)

Fig. 1.8. Autonomous virtual humans

1.1.2 Virtual Body Modeling

Layered Models. In practice, virtual characters are composed of several layers, each one handling one component of the global deformation. The basic layer is a wire articulated skeleton composed of joints providing the rigid body motion of the character. Key posture sequences composed of joint rotation sequences may thus be played back on the skeleton in order to generate its rigid body animation. A basic approach to designing the character consists then of dressing it with a skin layer composed of rigid surface patches directly tied to the skeleton segments and deformable surface patches connecting them around the joints. This basic Joint-dependent Local Deformation (JLD) approach was applied by the Thalmanns in the making of virtual actors for the film "Rendez-Vous in Montreal". The JLD operators, specifically designed for each joint, were applied to deform the surface patches around the joints as functions of the joint rotation angles. For extreme flexion angles, however, as well as for complex joints like the shoulder, the method was not satisfying (Thalmanns 87, 88).

Another approach was followed by Chadwick et al. for the design of cartoon-like characters. Making use of the Free Form Deformation (FFD) method developed by Sederberg and Parry (Sederberg 86), skin deformation around the body was obtained by local deformation of embedding prisms, and mapping of the resulting deformation onto the embedded skin patches. Dynamic deformation was achieved by simulating the dynamics of mass-spring-dashpot lattices mirroring the embedding prisms. The motion of the mass particles was then mapped back onto the prisms' control points, which themselves determined the embedded skin deformation. This way, the joint-dependent local deformations were not directly applied to the skin patches (Fig. 1.9). Despite its efficiency for designing simple characters, this approach would however hardly lend itself to the realistic modeling of the complex anatomical deformations of the human body (Chadwick 89).

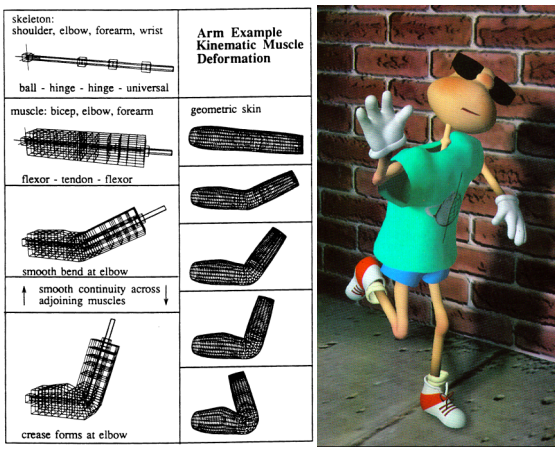

Fig 1.9. *Bragger Bones* animation (Chadwick 89)

The Metaball Models. In 1992, a graceful virtual ballerina was designed by Yoshimoto with 500 *Metaballs* and a personal computer. The figure was static, but the result was promising.

Metaballs consists of special spheres defined by additive density distributions (Nishimura 85). A threshold parameter determines the radius of the iso-density surface to be visualized. Thus, an isolated Metaball appears as a common sphere, whereas in the neighbourhood of other Metaballs, the density functions add so as to generate a smooth transition between them. The approach easily extends to ellipsoids. Yoshimoto's ballerina was thus designed by careful arrangement of ellipsoid and spheric Metaballs (Fig. 1.10) (Yoshimoto 92). The approach, however, was limited by the absence of a skeleton layer which would have allowed the design of different postures. This was actually the direction to follow to achieve better representations of the human anatomy.

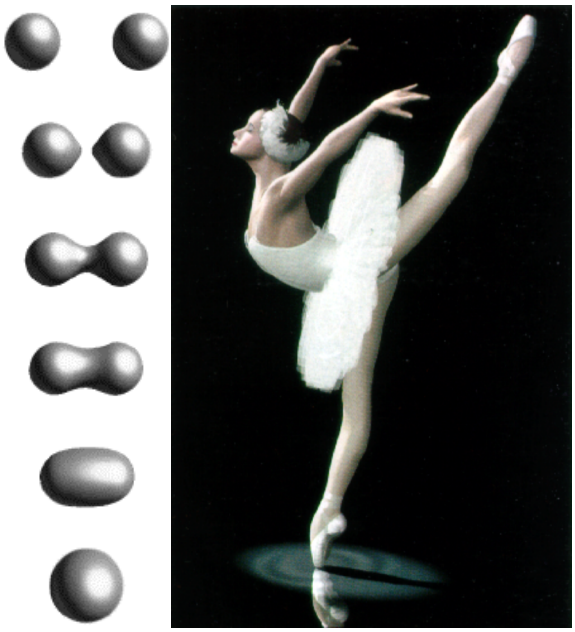

(Yoshimoto 92)

Fig. 1.10. A ballerina made of Metaballs

The idea was developed by Shen Jianhua at the Computer Graphics Lab of EPFL (LIG). The layered approach was improved by inserting between the skin and the skeleton layers, an intermediate layer composed of soft objects, similar to the muscles and soft tissues underneath the skin. Joint-dependent deformable Metaballs were then distributed around the skeleton so as to reproduce the anatomical body deformations during motion. Unblending Metaballs were used for some body parts like the members, in order to prevent them from fusing with the other body parts. A smooth skin layer could then be generated as the envelope of the underlying soft objects (Fig. 1.11, 1.12) (Shen 93, 95, Thalmann 96). On this basis, two approaches could be followed whether the Metaballs distribution refers to the real anatomical muscular composition or not. At this experimental stage, the real anatomy was ignored in order to focus on the development of a flexible interface, *BodyBuilder*, for use by designers.

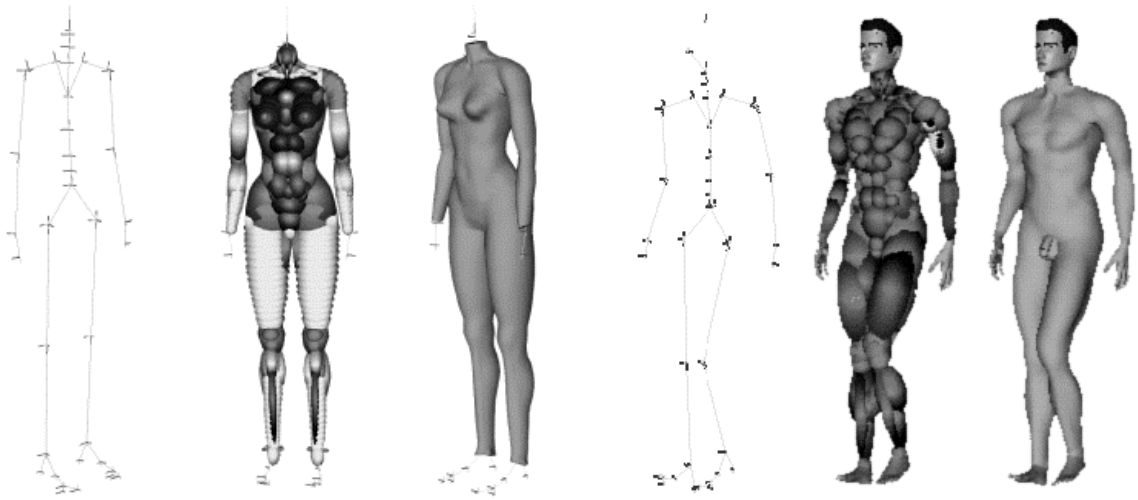

Fig. 1.11. Layered woman model (Shen 93, 95) **Fig. 1.12.** Layered man model (Shen 93, 95)

Anatomic Models. Anatomic modeling is currently the challenge in human body modeling. Applications range from realistic design to anatomic teaching and medical developments. In 1997, an approach for anatomic modeling of the human upper limb was presented by Sheepers et al. (Fig. 1.13). The model was based on elementary deformable ellipsoidal muscle components. Broad muscles like the *trapezius* or the *pectoralis major* were composed as arrangements of several primitives. Skin was finally obtained in adjusting the control points of bicubic patches on the implicit primitives (Scheepers 97). The same year, another approach was proposed by Wilhelms and van Gelder for vertebrate modeling. The muscle components were based on cylinder deformable lattices with elliptic cross-sections. Deformation was obtained by ellipse scaling and inter-slice spacing in function of the muscle length. A physically-based skin layer was added enveloping the muscles and smoothing the deformations. The approach was however not applied to human modeling, but to the modeling of a monkey instead (Wilhelms 97).

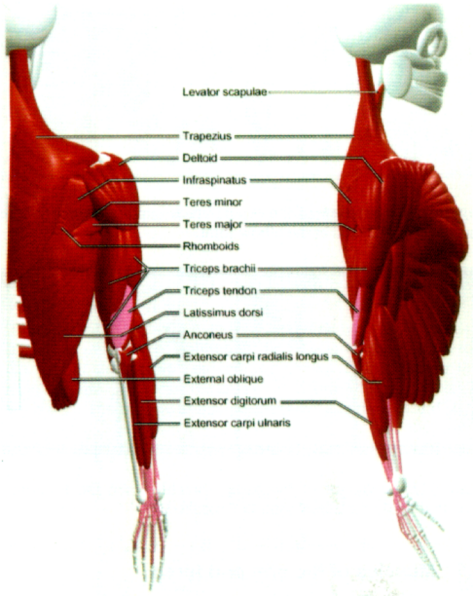

(Scheepers 97)

Fig. 1.13. Anatomic body modeling

At LIG, an internal project towards the anatomic modeling of the human body has been launched on the basis of Shen's development. The interface of *BodyBuilder* has been extended to allow the disposition of several ellipsoids along contour lines as well as the association of several ellipsoids into independent muscle entities. A complementary development has been initiated by Luciana Porcher-Nedel who proposed the anatomic modeling of the human body using physically-based deformable muscle components (Nedel 98b). The muscle components are developed in the form of elongated mass-spring prisms. The elastic deformation is then obtained as a function of the muscle length. The speciality of the model is the use of curvature springs to simulate the muscle volume conservation (Nedel 98a). Both approaches are currently being followed for developing fully anatomic body models (Fig. 1.14). In both case, the generation of the skin layer is still under development.

(Thierry Michellod) (Nedel 98a,b)

Fig. 1.14. Anatomic body models

Geometrical and physical anatomic human models are therefore about to come in the near future. The realism of the result highly depends on the model refinement. The more the model is close to the real anatomical constitution of the human body the more the model is bound to be realistic. This may however be to the detriment of the interactivity and the computing efficiency. If fast or real-time processing is necessary, a reduced model may therefore be preferential.

1.1.3 The Shoulder Case

Anatomically correct models are particularly needed for some areas of the human body which are not satisfyingly rendered by the current models. The human shoulder is probably the body area mostly concerned. This may be easily explained by the fact that the shoulder is one of the most complex articulations of the human body. If realistic images or animation sequences including shoulders have been successfully designed with the former non-anatomic models, this was often achieved by correction of the animation sequences or motion restrictions aiming at avoiding unrealistic postures. Two reasons may be given for this:

- the design of the underlying skeleton and muscle layers around the shoulder are inadequate to properly represent the motion and deformation of a real shoulder
- the animation techniques used are inadequate to properly control the shoulder model and generate realistic shoulder motions and deformations

The design of anatomically correct shoulders is thus likely to improve the realism of the virtual body model. This is however insufficient without an appropriate design of the skeleton layer and appropriate animation methods.

The Skeleton Layer. The skeleton layer concerned here is of course not the geometric skeleton layer used as basis for the design of an anatomic musculature, but the underlying skeleton structure allowing the animation of the model. This skeleton layer takes the form of a wireframe hierarchy of 1-DOF (degree of freedom) rotational joints. Though this approach is generally sufficient for most human joints, like the forearm joints for example, it does not easily lend itself to realistic animation, regarding the shoulder. Usually, the shoulder is modeled using one or two articulated segments, depending on whether the motion of the scapula is taken into account or not. The shoulder model currently used at the Computer Graphics Lab of EPFL (LIG) includes a two-segment shoulder model (Boulic 94, Huang 94). The arm segment is articulated with respect to the scapula, the scapular segment with respect to the clavicle, and the clavicular segment with respect to the spine skeleton. Though the model is improved, realistic animation of the shoulder is hardly achieved (Fig. 1.15).

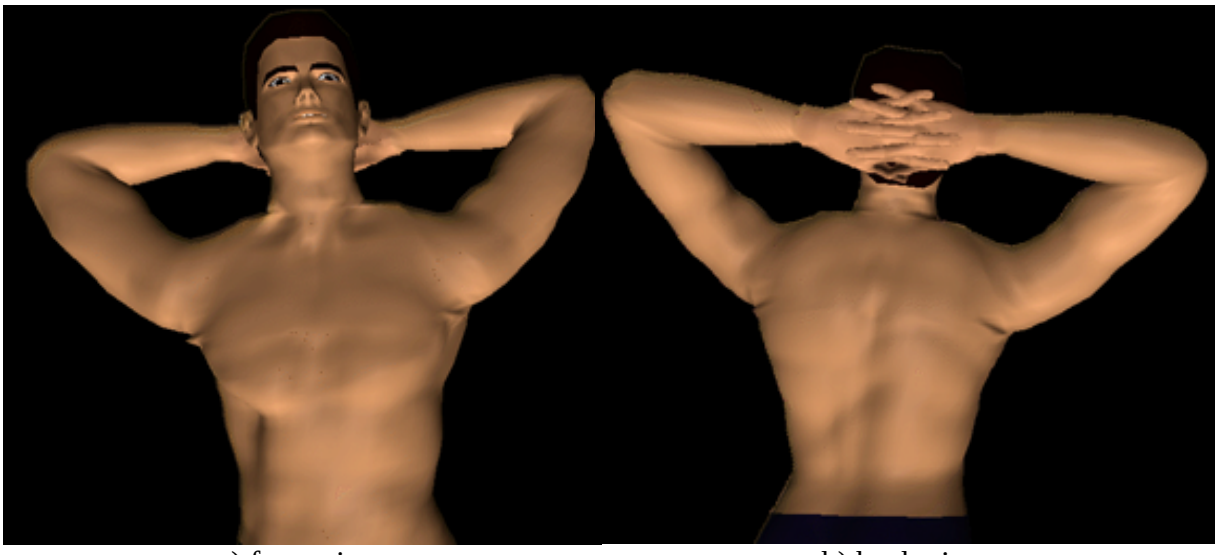

a) front view b) back view

Fig. 1.15. Unrealistic shoulder deformations currently obtained

This is due to the fact that it is difficult to simulate the simultaneous motions of the arm, scapula and clavicle, which occur in reality. This simultaneous motion is named the *shoulder rhythm*. An effort to account for this rhythm was investigated by Badler et al. who applied empirical results expressing the clavicular and scapular elevations as functions of the humeral abduction. The relationships however applies only for given movements (Badler 93). The realism achieved using such relationships with an anatomic model may thus be very limited. A more accurate investigation towards shoulder modeling is therefore necessary. An attempt in this direction is presented in the last chapters of this thesis (Chapters 6-7).

1.2 Biomechanical Musculoskeletal Modeling

1.2.1 Virtual Humans in Medicine

The Virtual Cadaver. Virtual Reality has great potential for simulation in medicine. This explains the growing interest from medical research in such applications. Evident primary interests are in the visualization of the anatomic components and the simulation of physiologic processes. Cadaver dissection, medical illustrations, and medical models have been used over four centuries to study human anatomy and to investigate the location and function of all major organs in the human body. Real cadavers are, however, expensive, difficult to obtain, and irremediably bound to destruction. These are strong limitations to the easy use of real specimens for educational practice. The availability of a pertaining standard 3-D virtual cadaver would incomparably increase the perpectives of representation and investigation of the human body. The Visible Human Project initiated in 1995 by the U.S. National Library of Medicine, represents a major advance in this direction. The 1-mm thick slice image data of the Visible Man has already led to many reconstruction and visualization programs (Fig. 1.16) (Schiemann 96).

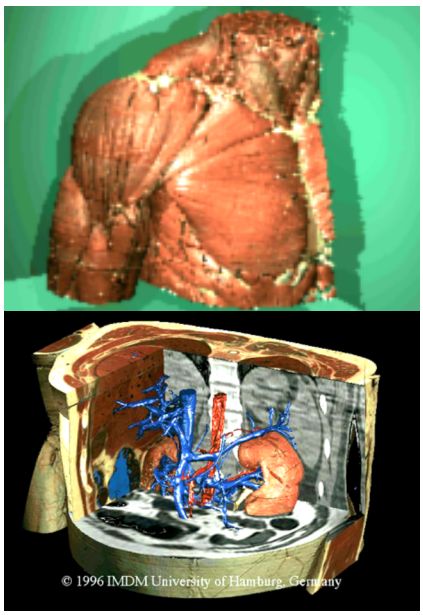

(Schiemann 96)

Fig. 1.16. Virtual dissection

Surgery Simulation. The emerging of three-dimensional representations of human organs has also led to the development of numerous surgery simulation applications. Surgery simulation systems can ideally provide an efficient, safe, realistic, and relatively economical method for training clinicians in a variety of surgical tasks (Fig. 1.17). This is particularly useful in the case of *minimally invasive surgery*. Endoscopic surgery requires the surgeons to be familiar with a new form of hand-eye coordination and skilled in the manipulation of instruments by looking at the endoscopic image projected on a video monitor. These skills are not intuitive and the optimization of the surgical procedures requires a considerable amount of training and experimentation before they can actually be applied in real operations. The realistic graphical modeling of the area of intervention therefore defines a virtual environment in which surgical procedures can be learned and practiced in an efficient, safe and realistic way. A number of simulation platforms already exist for heart, eye or arthroscopic surgery training (Kuhn 96, Sagar 94).

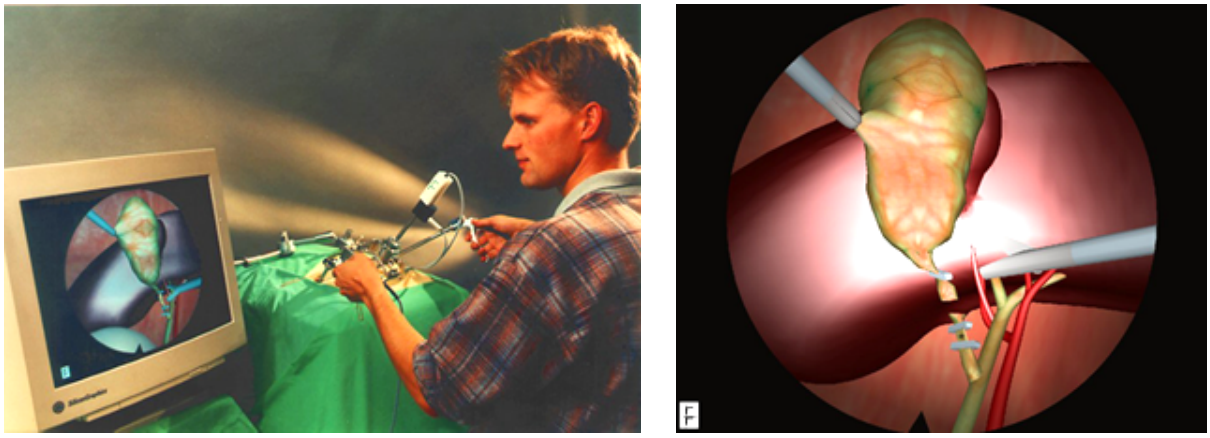

Fig. 1.17. Minimally invasive surgery (Kuhn 96)

Augmented Reality. Augmented reality proposes the combination of virtual reality displays with images of the real world. Applied to medicine, this technique would allow surgeons and physicians to see directly inside their patients (Fig. 1.18). The approach requires the use of a specific video see-through head-mounted display, with a high-performance graphics computer and fast imaging techniques, like ultrasound echography imaging, for allowing real time acquisition, reconstruction and matching of the virtual model with the real vision. Despite of these limitations, the technique has already been successfully applied in many cases such as obstetrics, diagnostic procedures such as needle-guided biopsies, cardiology, etc. (State 96, Fuchs 96, 98).

Telemedicine. The development of virtual reality brings new ways for communication and collaboration via virtual environments. Especially in medicine, the development of telepresence techniques would offer increased accessibility to specialists, allowing them to virtually assist operative surgery sessions or indirectly conduct robotic surgery from anywhere in the world. For example, the ARTEMIS project at the Karlsruhe Institute for Applied Informatics, features a complete telepresence system which allows the surgeon to perform minimally invasive surgery remotely via a man machine interface with multimedia capabilities (Fig. 1.19). The surgeon operates on a virtual representation of the patient, while his movements are translated by a computer that commands a robot operating on the live patient (Hunter 94, Voges 97).

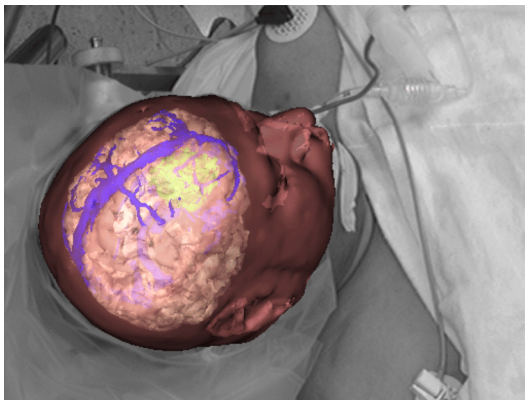

Fig. 1.18. Augmented reality (Fuchs 96)

Fig. 1.19. Telemedicine (Voges 97)

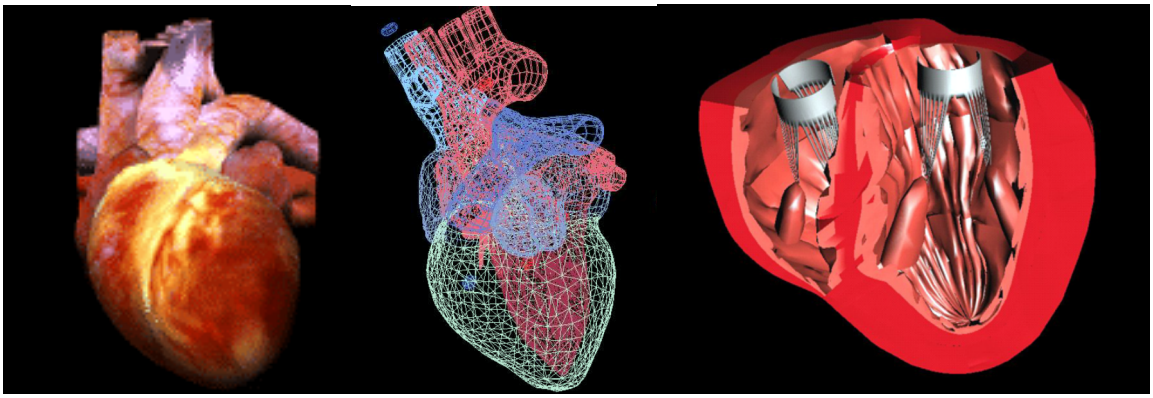

Fig. 1.20. Heart modeling for surgical planning and prosthesis design (Costa 94a,b)

Bioengineering. The development of 3-D computer graphics and animation techniques has also raised opportunities to experiment models of physiological phenomena. Complex neuro-chemical and biomechanical models for various organs may be experimented upon and applied to accurately simulate their behavior under specific conditions such as operative procedures. This also aids the prosthetic design process in allowing the simulation of the prosthesis behavior and comparison with that of the organ. The approach is currently widely applied to simulation of various organs such as the heart, arteries, lung, stomach, etc. as well as to the design of organ prosthesis such as heart valves (Fig. 1.20) (Hunter 88, Costa 94a,b).

Orthopaedics. The bioengineering approach may also be applied to the biomechanical simulation of the musculoskeletal system. The complexity of the musculature together with the lack of non-invasive investigation methods, prevents accurately identifying the function of each muscular component and also the consequences that would result from surgical intervention on their structure. Computer graphic modeling techniques offers new ways of investigating the musculoskeletal systems. The combination of motion analysis techniques with Three-Dimensional topological models of musculoskeletal systems allows the estimation of the force contribution of each muscle component during motion, the experimentation of modifications of the musculoskeletal topology as well as the comprehension of the complex motion coordination strategies (Fig. 1.21) (Delp 90, 95).

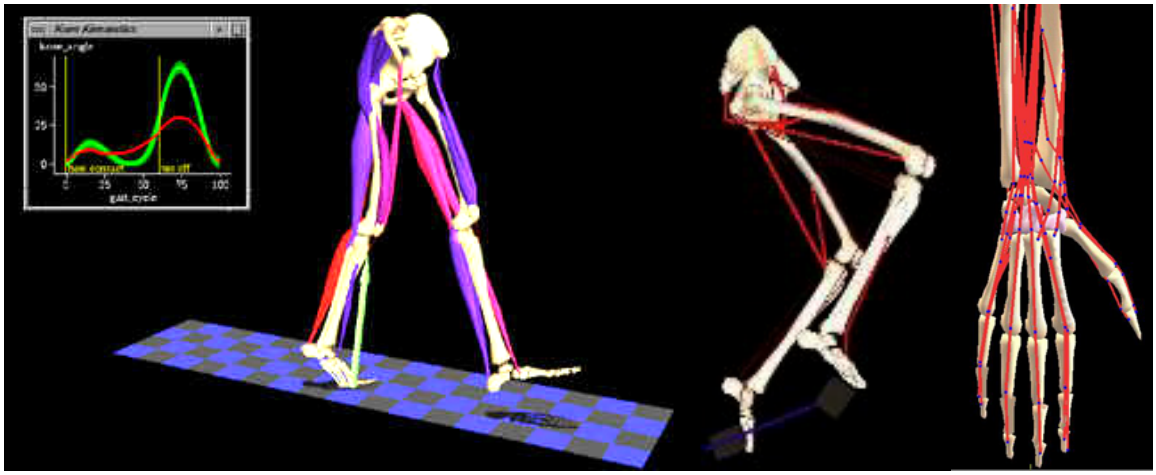

Fig. 1.21. Musculoskeletal simulation for orthopaedic rehabilitation (Delp 95)

1.2.2 Musculoskeletal Modeling Platforms

Early Works. Several studies have been led towards the musculoskeletal modeling of human articulations, in particular the ankle, knee, hip, shoulder, elbow and the hand. In most cases, as no specific simulation platform dedicated to the analysis of the human musculoskeletal system was available, numerical solving was achieved using commercial routines such as multi-body dynamics, finite element or optimization programs. The multi-body simulation programs ADAMS (Orlandea 77) and DADS (Wehage 82) were developed in the mid 70's to provide ability to formulate and solve the equations of motion of complex dynamic systems. The physical properties of connecting bodies and joints were modeled while numerical solutions were obtained after long computation in large digital main frames. Without the aid of computer graphics software permitting 3-D system visualization and interaction, it was difficult to interpret dynamics solutions and their implication to the system performance. This lack motivated a number of developments and product in this direction.

Interactive Graphic Systems. In 1990, Buford et al. developed a kinematic model of the hand that utilized interactive 3-D line drawings to facilitate tendon placement in finger digit control. The users of the software were allowed to interactively control the joint angle and view the spatial position of the hand (Buford 90). In the mean time, Delp et al. created an interactive computer graphic package to analyze the dynamics of the lower extremity. The software enabled modeling of different musculoskeletal joint systems using a 3-D shaded computer graphic display and allowed system parameters to be altered using a graphic interface (Delp 90). Neither, however, permitted a total interactive environment to alter system parameters, model configuration, and external forces for both kinematic and dynamic analyses, while able to display analysis results graphically. The development of such a fully interactive simulation/visualization package was then investigated by Chao et al. (Chao 93).

Their package allowed the creation of very detailed generic models based on anatomic and imaging data. A complete 3-D skeleton model was reconstructed from CT-scans and complemented with the centroid line data from each soft tissue unit, in order to accurately model their line of action in the dynamic analysis. In order to solve the complete static or dynamic problems including joint contact force, ligamentous tension, and muscle contractions, joint contact forces were assumed normal at the contact surface centroids, and optimization methods were applied to solve the indeterminate problem caused by the over-numerous lines of action. A discrete element analysis based on a rigid body spring model was used to determine the joint contact pressure distribution. The package and database developed were then used for selection and planning of total joint replacement operations, for joint osteotomy preoperative planning, and joint function simulation and rehabilitation (Chao 93).

Another software, called SIMM, developed to simulate the effects of reconstructive surgical procedures, was presented by Delp and Loan in 1995. It is a graphics-based program designed to aid in the creation of mathematical models of musculoskeletal structures for quantifying the effects of musculoskeletal geometry, joint kinematics, and muscle-tendon parameters on muscle-tendon lengths, moment arms, muscle forces, and joint moments. SIMM enables the analysis of the model by calculating the length, and the moment arm of each actuator, as well as to evaluate the force and moments it generates around a joint by simulating its contraction dynamics. The platform is however limited to visualization and interaction with the model. A compatible dynamic pipeline must be used separately to simulate forward and inverse rigid-body dynamics. Another limitation concerned the use of kinematic joint models instead of kinetic models accounting for forces in all ligamentous tissues and joint cartilages (Delp 95).

CHARM. In the mean time, the CHARM project, in the context of which this thesis has been developed, started. It was initiated in November 1993 under the ESPRIT Program with the support of the European Commission. The objective of CHARM was to develop a Comprehensive Human Animation Resource Model and a set of software tools, allowing the modeling of the human complex musculoskeletal system and the simulation of its dynamics, including the finite element simulation of soft tissue deformation and muscular contraction. Here, "database" means a numerical Three-Dimensional representation of the musculoskeletal system components, complemented with parameters and physical laws characterizing their macroscopic mechanical properties. To achieve this development, knowledge of anatomy and biomechanics was necessary: a biomechanical model of human musculoskeletal system including models and properties for bones, joints, muscles and soft tissues had to be designed as a basis for the tools and data structure implementation. For this purpose, the CHARM European team chose to focus on the upper limb, considering the fact that the shoulder is one of the most complex musculoskeletal structures of the human body (CHARM TR).

The development of a biomechanical model of the human upper limb was thus decided, and its responsibility was attributed to myself at the *Computer Graphics Lab* of EPFL (LIG) (Maurel 99). A Three-Dimensional upper limb model was constructed at the *University of Geneva* (UG) (Kalra 95) using the *Visible Human Data* provided by the *U.S. National Library of Medicine* (Gingins 96a,b). Biomechanical properties were then assigned to its components at LIG by myself (Maurel 96), using the interactive topological modeling tool developed at UG for this purpose (Beylot 96). A high-level interface allowing interactive motion control using linear, proportional-derivative and constraint-based control strategies (Multon 98), was then developed at the *Ecole des Mines de Nantes* (EMN) and the *Institut de Recherche en Informatique et Systemes Aleatoires of Rennes* (IRISA) on the basis of the equation dynamics of the model (CHARM D6, INRIA TR). Optimization analyses were then performed at the *Instituto Superior Técnico* of Lisbon (IST) using the model muscles topology, to compute, for specified movements, the respective muscle force contributions (Mateus 95, Engel 97). The resulting contraction forces were then used as input to the ABAQUS finite element code, in order to simulate soft tissue deformations and muscle contractions using biomechanical constitutive relationships for muscles, tendons, and skin (Martins 98). Finally, the photorealistic rendering of the simulation was achieved at the *Karlsruhe Universität* (UKA) following spatial spectra texture resynthesis approaches (CHARM D14) and a multi-modal matching interface was developed at the *Universitat de les Illes Balears* (UIB) for comparing synthetic animation with real motion sequences (CHARM D8).

Given the close relationship between my thesis and my own contribution in CHARM, the context of the project is furthermore described in the following section.

1.3 The CHARM Project

1.3.1 CHARM Originality

The human shoulder has been, and is still, the subject of numerous investigations aiming at modeling its structure, simulating its motion and determining the contribution of the different actuators involved. CHARM has been the first one to design its biomechanical modeling and

simulation to include the finite element simulation of soft tissue deformation and muscular contraction. In this context, the constraints on the model implementation and simulation have been different than those of other (partially similar) investigations. The achieved model may not be especially better than another that may have been formerly presented, but it has been more likely to succeed in the objectives of the project.

In general, biomechanical investigations are based on idealized physical representations of the musculoskeletal systems for which assumptions are done *a priori* and left for future validation. The considerations leading to these assumptions are rarely detailed. In our approach, the need was to find a compromise between accuracy and simplicity. This has been necessary for preserving the biomechanical validity of the model and easy interpretability of the parameters, as well as the interactivity of the application and feasibility of the subsequent analyses, especially the finite element simulation of soft tissue deformation. Therefore, I have found interesting to analyze the modeling procedure we have followed, and present, in the following section, the considerations justifying our choices with respect to the project constraints on the model implementation and simulation (Maurel 99).

1.3.2 General Approach

According to the theory of modeling, a model may be defined as an object, existential or abstract, which under investigation, provides information on a real object and an associated phenomenon. Thus, modeling consists of developing a representation of the properties of the object/phenomenon with respect to the goals of its analysis.

Physical modeling is a necessary first stage of the modeling procedure. It requires the establishment of the input/output signals and physical laws governing the phenomenon, as well as the establishment of the qualitative features, the quantitative characteristics and the assumptions simplifying both signals and the object/phenomenon itself. In mechanical engineering, this stage generally begins with the design of a graph featuring the system components as vertices connected by arcs representing their inter-relationships. In order to simplify the analysis, subsystems may be identified and modeled separately by converting their relationships to the rest of the system into external actions. Since the physical model is only a simplification of the reality, the real phenomenon differs from the behavior of the model. For this reason, the determination of the qualitative features of the model must be done with particular care, and with awareness of the consequences of any choice and any assumption.

Once the physical model has been established, its mathematically formalized description may be developed as a second stage of the modeling procedure. It usually consists of a set of equations with boundary conditions. It may be obtained directly by referring to the theoretical physical laws governing the phenomenon or empirically by applying an identification procedure based on experimental measures of the input/output signals. As a final stage, attempts must be made to validate the model and verify the assumptions by comparing the theoretical and original behaviors. In the case of inconsistencies, the physical model may require modifications (Arczewski 93).

Musculoskeletal Modeling. Considering the mechanics of musculoskeletal systems in the physiological ranges of motion and force handling, the set of components, which must be taken into account in the analysis, may be reduced to the macroscopic anatomical components

having noticeable contributions in the observed mechanical behavior. These are bones, muscles, tendons, ligaments, organs and skin. A bone-bone relation is commonly called a *joint*, a tissue-tissue relation a *connection*, a tissue-bone relation may be a *guide* or an *attachment*. The input/output signals may be identified as the muscular activations and the resulting motion/deformation while the physical laws involved are gravitation, the rigid body dynamics, and the mechanics of materials.

At this stage, the geometrical and mechanical topological graphs are identical – i.e. the anatomical structure and the mechanical relation follow the same topology. The most accurate approach would be to consider the dynamic analysis of each component, individually considered as a deformable body. However, given the respective material properties, in the relevant physiological ranges of motion and force handling, bones may be regarded as rigid bodies in contrast to soft tissues. This allows the isolation of the skeletal subsystem from the soft tissues by converting their relation to the bones into external actions. The *rigid body dynamic analysis* of the skeleton and *continuum dynamic analysis* of the soft tissues must however be performed *simultaneously*.

A consistent approach would be to follow the natural phenomenon of motion generation, i.e. to perform the continuum dynamic analysis of the soft tissues for specified muscular activations and the rigid body dynamic analysis of the skeleton for their resulting actions on the bones. However, natural motion always involves several muscles and the complex dynamic neuromuscular control strategies are still unknown. Specifying a dynamic muscular coordination scheme as input for the analysis is thus outside the realm of current ability, unless assumptions are made to avoid the indeterminacy. A method which achieves this simulation is to use the inverse approach, i.e. to *simultaneously* perform the rigid body inverse dynamic analysis of the skeleton for specified movements, and the continuum dynamic analysis of the soft tissues for the corresponding muscle forces. These may be obtained from the distribution of the resulting joint forces and torques on the different muscles by means of an optimization analysis accounting for their strength and topology.

Given the complexities of the musculoskeletal topology and of soft tissue mechanics, the continuum dynamic analysis may be expected to be time-consuming for the current numerical performance. The interdependency between the skeletal rigid body and the soft tissue continuum dynamic analyses may thus constitute an obstacle for simple control of the simulation. A rigid body dynamic analysis *independent* of the continuum dynamic analysis would be more appropriate for real-time control. For this reason, when anatomical segments including bones and soft tissues as a whole are distinguished, they are usually taken as articulated rigid bodies. The rigid body dynamic principles may then be applied to them, *independently* of a continuum dynamic analysis of their soft tissues. This procedure assumes that within each segment, bones and soft tissues have a similar rigid body motion, and that the soft tissue deformation does not significantly affect the rigid body properties of the segment as a whole. Then, if required, muscle forces may be obtained from the joint forces and torques by optimization analysis, and used as input to the continuum dynamic analysis for soft tissue deformation simulation.

Different results may thus be obtained depending on whether the modeling procedure aims at performing a *macroscopic* rigid body simulation, a *complete* musculoskeletal deformation simulation, or a *hybrid* rigid body/musculoskeletal deformation simulation. The latter alternative has been the goal of the CHARM project. The stages of the project are presented below with the emphasis placed on the constraints they imposed on the model development.

1.3.3 CHARM Specifications

Accounting for the above considerations, developments in CHARM have been planned as shown in Fig. 1.22:

- First, the *topological model*, combining a theoretical biomechanical model of a musculoskeletal system with its Three-Dimensional reconstruction, must be designed. Besides the development of the biomechanical model, this involves the development of a *labeling tool*, for medical image segmentation and 3-D reconstruction, as well as a *topological modeling tool*, for fitting biomechanical properties to the geometrical model.

- Then, *motion control* procedures, based on the rigid body dynamic analysis of the model, must be developed to allow the interactive generation of motion sequences. These include basic direct/inverse, and kinematic/dynamic controllers, as well as a *high level language interface*.

- Then, an *optimization* analysis is necessary to distribute the resulting joint efforts on the muscles, accounting for their topology and their dynamics.

- *Finite element* procedures are then proposed to compute the deformation of the soft tissues for the resulting muscle contraction forces.

- *Rendering* procedures are necessary to visualize the resulting 3D animations with various levels of depth and quality.

- To consider them as simulations, the modeling procedure needs *validation*. Corrections may concern the rigid body dynamic analysis, the optimization analysis, the soft tissue continuum dynamic analysis and the numerical methods applied for their resolution as well as the assumptions made on the biomechanical model and its mathematical formalization. The development of an interface allowing the matching of real and synthetic motions is thus necessary for comparative validation.

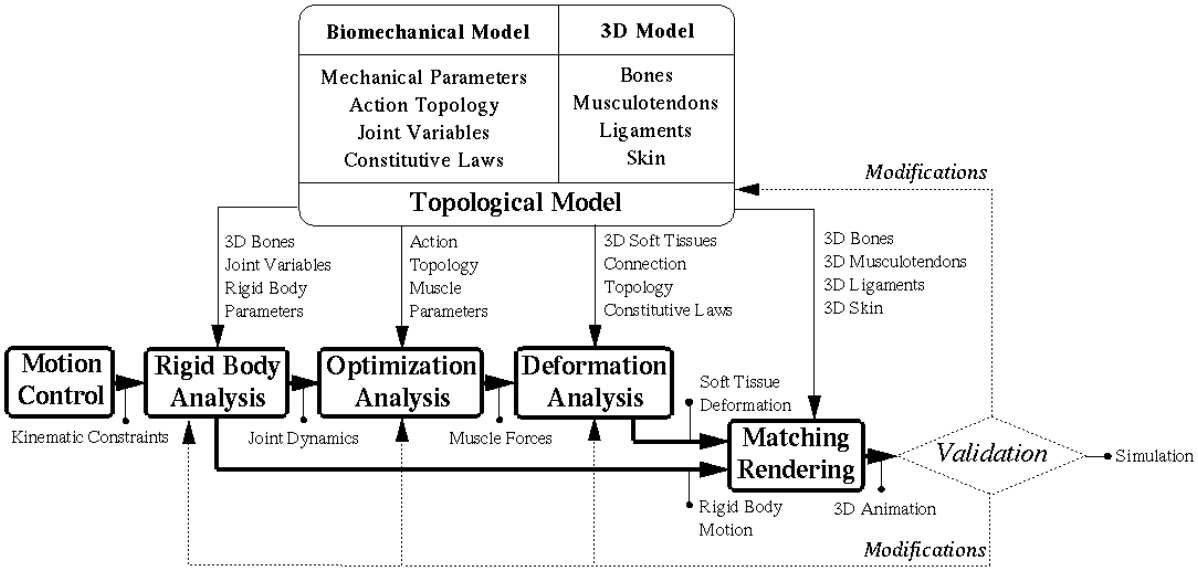

Fig. 1.22. CHARM synopsis (Maurel 99)

From this program, some specifications may be derived concerning the biomechanical model:

- As explained in § 1.3.2, for real time interactive motion control, the rigid body dynamic analysis is considered independently of the soft tissue finite element analysis. The biomechanical model must therefore combine a macroscopic rigid body representation with a semi-deformable musculoskeletal representation of the anatomic system.

- The motion control procedures require the definition of kinematic and dynamic parameters for motion description as well as mechanical parameters for the rigid body dynamic analysis.

- The optimization procedure requires the definition of the muscle topology and physiological cross sectional areas (PCSA) for action consideration.

- Finally, the finite element analysis requires the definition of the soft tissue topology as well as constitutive laws for soft tissue modeling.

Other constraints for the model may be derived from the specific requirements of the implementation and the application:

- Unless one variable prevails over the others, the variables that implement the data structure must be independent from each other in order to preserve its integrity.

- The definitions must also satisfy medical and biomechanical practice in order to allow interpretation of the parameters by the practitioners.

- They must simultaneously preserve the anatomical and biomechanical validity of the model and the feasibility of the subsequent analyses, especially the finite element simulation of soft tissue deformation.

- Finally, the definitions must also be compatible with the objective of interactive editing and motion control of the model, as well as that of an open implementation allowing corrections and future improvements of the model.

The human upper limb was therefore chosen to start with for its complexity, so as to ensure the generality of the developments proposed. In order to focus on large motion and to simplify the analysis, it was decided to ignore the wrist and hand mechanics. Hence, it is assumed that hand motion has negligible effect on the large motion dynamics of the upper limb. Therefore, the hand has been considered as a rigid extension of the forearm.

As stated previously, the responsibility of developing the biomechanical model of the human upper limb was attributed to the *Computer Graphics Lab* of EPFL (LIG), and to myself in particular. It is on the basis of this project that I engaged in the research presented in this thesis. My personal contribution in this direction is summarized in the next section, and therefore detailed in the following chapters.

1.4 Personal Contribution

1.4.1 Contribution in Biomechanics

My responsibility in CHARM has been to develop the biomechanical model of the human upper limb including models and properties for bones, joints, muscles and soft tissues. This has led me to investigate many disciplines, which are not usually related together. These are:

- the musculoskeletal anatomy and biomechanics of the human upper limb.
- the nonlinear dynamics of multi-body systems.
- the optimization analysis of redundant mechanical systems.
- the physiology and biomechanics of muscles and soft tissues.
- the nonlinear mechanics of continuous media.
- the incremental/iterative finite element methods.

On this basis, I have provided:

- qualitative and quantitative descriptions for modeling the upper limb joints.
- qualitative and quantitative descriptions for modeling the upper limb musculature.
- an extensive review of constitutive relationships for soft tissue modeling.

and made several propositions towards:

- the prediction of muscle forces using optimization analysis.
- the modeling and simulation of muscle contraction forces and dynamics.
- the constitutive modeling and finite element simulation of soft tissue deformation.

In practice, this responsibility has also conferred on me the advisory authority for specifying the implementation formats for the model parameters in the data structure as well as for designing the features to be provided on the topological modeler required for interactive editing of the model properties. More generally, this responsibility has put me in the privileged position of supervising the main technical aspects involved in the project as well as of coordinating the developments together with the other partners (see Chapter 5).

The originality of my contribution lays mainly in the synthesis and coordination of several highly theoretical disciplines which have formerly been deeply, but separately, investigated. This has already been demonstrated by the publication as a book by Springer (Maurel 98) of an extensive review of models and methods for the biomechanical simulation of soft tissues, and a journal paper whose originality mainly lays in the clarity of the synthesis and in the scrupulous justification of each choice, as presented previously in § 1.3 (Maurel 99).

1.4.2 Contribution in Computer Animation

On the basis of my investigations for CHARM, I investigated the possibility of improving the BODY *skeleton_* structure used at LIG in order to allow the realistic animation of the human upper limb skeleton. This has been agreed as part of an internal project aiming at the realistic anatomical modeling and animation of the human body using the tools and libraries developed in the lab. For this purpose, I have studied:

- *Scenelib*, the general purpose hierarchy animation library.
- *Bodylib*, the specialized vertebrate bodies animation library.
- *Keyframelib*, the keyframe animation library.
- *Inklib*, the inverse kinematics library.
- *Inventor*, the SGI C/C++ object oriented interactive 3-D graphics library.

and proposed:

- the proper adjustment of the shoulder and elbow joints on their anatomical topology.
- the adjunction of 1-DOF *_twisting joints_* to the *clavicle_* (SC) and *scapula_* (AC) *joints_*.
- the adjunction of one *n3d_* node representing the scapular node in contact with the thorax.
- the individual animations of the arm and shoulder using inverse kinematics.
- the modeling of realistic joint boundaries in the form of joint sinus cones.

On this basis, I have:

- designed an anatomical BODY *template_* with respect to the upper limb anatomy.
- developed an animation interface allowing the realistic animation of the arm and shoulder.
- implemented a library for handling joint sinus cones within *Scenelib* and *Inklib.*
- extended the *Skeledit* skeleton editor interface for joint sinus cone design and testing.

As a result, I have proposed an improved upper limb model appropriate for the realistic animation of the human body anatomic skeleton. The models and tools developed have allowed the generation of realistic animations which have been played back onto the anatomic body model designed by Thierry Michellod at LIG. As the skin layer may not be generated yet with this model, the improvement in the realism of the resulting skin deformations could not be tested. However, the realism of the resulting muscle deformations is manifest.

1.4.3 Plan of the thesis

As provided in the Preface, the present thesis is organized as follows:

- the next chapter investigates the biomechanics of the upper limb skeleton and proposes its modeling with respect to the CHARM constraints on its implementation and simulation.
- the third chapter investigates the biomechanics of the upper limb musculature and proposes its modeling and simulation in CHARM following earlier investigations.
- the fourth chapter investigates the biomechanics of soft tissues and proposes their modeling and simulation in CHARM following earlier investigations.
- the fifth chapter presents the developments and implementations achieved in CHARM by the whole consortium as effective applications of the theoretical models proposed before.
- the sixth chapter investigates and proposes the realistic modeling and animation of the human upper limb using the animation environment currently used at LIG.
- the seventh chapter investigates and proposes the modeling and handling of realistic joint boundaries in the form of joint sinus cones adjusted to the upper limb model.

The eighth chapter is provided as a conclusion to this work and an opening to future work.

Conclusion

Both computer graphics and medicine have a lot to gain from each other. The use of anatomical and biomedical knowledge for modeling and design of the human body may lead to major improvements in the realism of virtual humans. Conversely, computer animation techniques considerably extend the possibilities for experimentation and investigation of the human body. The European Project CHARM has aimed at joining both medical and graphical aspects in the development of improved techniques for biomechanical modeling and simulation of the human body. This has required the development of a biomechanical model of the human musculoskeletal system as a basis for tools and data structure implementation. Given the complexity of the human shoulder, the human upper limb was chosen to start with. The theoretical analysis I have led in this direction is presented in the first part of this thesis. On the basis of this study, an attempt is presented, as the second part, towards the improvement of the shoulder model currently used at the Computer Graphics Lab of EPFL (LIG). As the development of specific motion control techniques requires another long term investigation, the implementation has been limited to the demonstration of the approach.

2 Skeleton Modeling

Given the respective material properties, bones may be regarded as rigid bodies in contrast to soft tissues, with respect to the relevant physiological ranges of motion and force handling. This allows the isolation of the skeletal subsystem from the soft tissues by converting their relations with the bones into external actions. The upper limb kinematics and dynamics may then be analyzed and modeled in considering the skeletal components only. This is the purpose of this chapter. After a brief investigation into the anatomy and biomechanics of the human upper limb, the analysis I have led for modeling the upper limb kinematics is presented, on the basis of former investigations. In particular, the mobility of the human shoulder is investigated so as to explain the proposed modeling of the complex scapulo-thoracic joint. The rigid body model of the upper limb is finally developed and matched with the kinematic model.

2.1 Upper Limb Biomechanics

2.1.1 Upper Limb Description

Neglecting the hand, the human upper limb may be described as composed of five bones, the *clavicle*, the *scapula*, the *humerus*, the *ulna* and the *radius*, forming two mechanisms, the *shoulder* and the *elbow*. Their association allows a wide range of combined motions, and confers to the human arm the highest mobility in the human body (Kapandji 80, Grant 91).

Considering bones in pairs, seven joints may be distinguished (Fig 2.1):

- the *sterno-clavicular* (SC) joint,
  which articulates the clavicle by its proximal end onto the sternum.
- the *acromio-clavicular* (AC) joint,
  which articulates the scapula by its acromion onto the distal end of the clavicle.
- the *scapulo-thoracic* (ST) joint,
  which allows the scapula to glide on the thorax.
- the *gleno-humeral* (GH) joint,
  which allows the humeral head to rotate in the glenoid fossa of the scapula.
- the *ulno-humeral* (UH) and *humero-radial* (HR) joints,
  which articulate both ulna and radius on the distal end of the humerus.
- the *ulno-radial* (UR) joint,
  where both distal ends of ulna and radius join together.

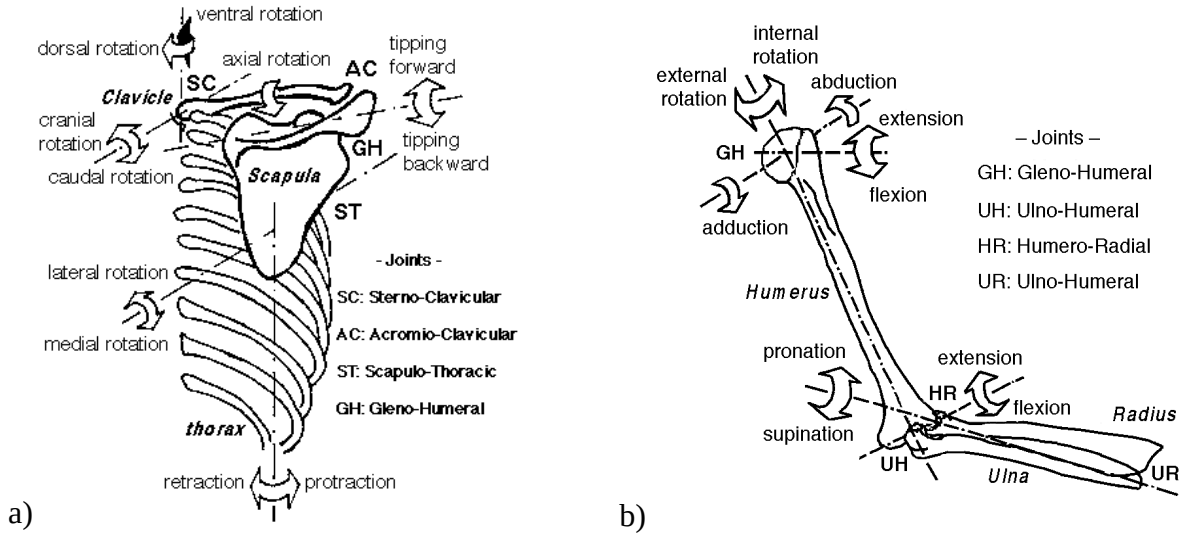

Fig. 2.1. The upper limb movements: a) shoulder, b) arm and forearm (Maurel 99)

2.1.2 Upper Limb Mobility

Considering translations negligible compared to rotations, each of these joints, except the scapulo-thoracic joint, is usually assumed to allow 3 *degrees of freedom* (DOF) in rotation. The scapulo-thoracic joint is a particular case since it does not properly involve articular structures between scapula and thorax. However, due to its surrounding muscles, the scapula is usually assumed constrained to glide on the thorax (Dvir 78).

The corresponding upper limb movements are usually referred to as (Chao 78, Kapandji 80):

- *ventral/dorsal*, *cranial/caudal* and *axial rotations* for the SC joint (3 DOF).
- *abduction/adduction*, *flexion/extension* and *axial rotation* for the GH joint (3 DOF).
- *elevation/depression*, *protraction/retraction*, *tipping forward/backward* and *medial/lateral rotations* for the ST joint (5 DOF).
- *flexion/extension* and *pronation/supination* movements for the forearm joints (2 DOF).

These movements are illustrated in Fig. 2.1. With the exception of the scapula which is maintained by its surrounding muscles, all these movements are restricted by passive structures like the joint capsule and the ligaments near the joint, which force rotations and translations when they become taut (Pronk 91).

2.1.3 Global Kinematics

As muscles never work in isolation, natural movements always involve the simultaneous motions of all the bones. Almost all investigations on the shoulder girdle motion are focused on the quantification of the scapulo-humeral rhythm during elevation. For example, in elevation, the humerus is limited to ca. 100° of angular displacement relative to the scapula.

However, maximum elevation is reached at ca.180° which means that the shoulder girdle has to contribute to the difference (Fig. 2.2). According to Inman et al., the ratio at the GH and ST articulations from almost the begining to the termination of the arc, is two to one, respectively. They also reported that, during elevation, the clavicle rotates in three directions in the SC joint. The combination of both the SC and the AC joints mobilities defines the motion of the shoulder girdle whose effect is to orientate the glenoid cavity and to place it in a particular position from which the arm movement will be performed (Inman 44, 46).

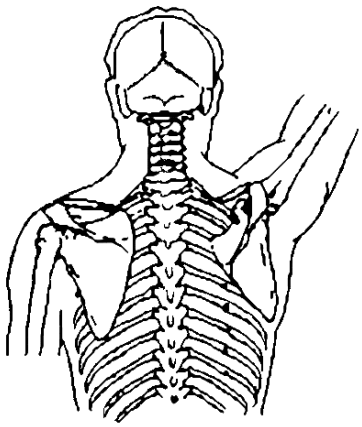

Fig. 2.2. Arm elevation (Thomson 64)

All the shoulder bones are also involved when the arm performs circumduction movements. This movement delimits the accessibility space where the hand can grab an object without moving the trunk (Hainaut 76, Kapandji 80).

In contrast to the shoulder, the forearm movements have been proved to be independent from each other (Youm 79).

For a complete analysis, it is necessary to consider the motion of the mechanism as a whole. As presented in the following section, many investigations have been made in this direction.

2.2 Former Investigations

2.2.1 Joint Models

Physiologically, no fixed axis or rotation centre can be recognized in a real joint. For most joints, the relative motion between bones is a combination of rolling and gliding with pressure on the contact areas (Fig. 2.3). An accurate joint model should account for all these movements as well as the forces and torques induced on the bones. A 2-D theoretical analysis was lead in this direction by Engin in 1984. The model described the relative motion between two bones, including both geometrical and material nonlinearities as well as the ligament and contact, forces and torques (Engin 84).

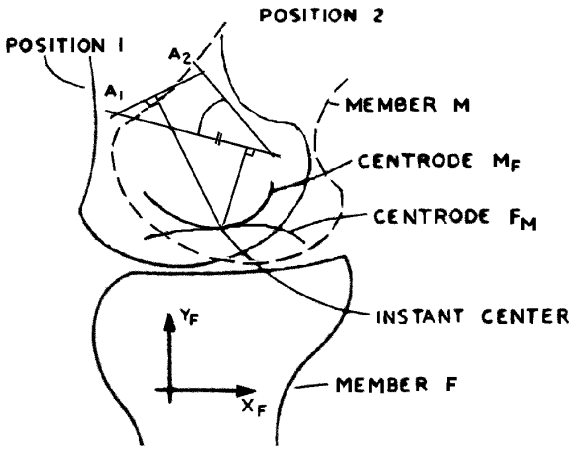

(Kinzel 83)

Fig. 2.3. Combined motion in a real joint

Another approach towards joint dynamics simulation was presented by Chao et al. with the musculo-skeletal simulation platform mentioned in § 1.2.2. The technique, named *Rigid Body Spring Model*, consisted of modeling the articular surface pressure with distributed

compressive springs. When subjected to tensile forces, the compressive springs were removed from the model (Fig. 2.4). An iterative scheme was thus used to solve the system for the equilibrium, whereas the spring redundancy was handled by energy optimization. It was applied to static analysis of the wrist and hand biomechanics (Chao 93).

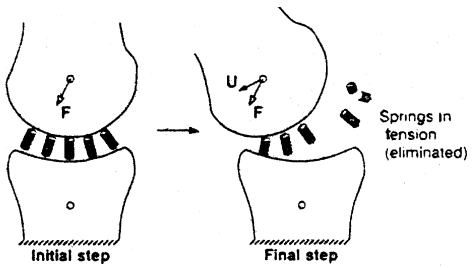

Fig. 2.4. Rigid Body Spring Model (Chao 93)

In most cases, however, translations appear negligible with respect to rotations, so that the model development and analysis may be simplified using idealized joints. In a 3-D space, an object may be characterized with respect to some reference coordinate system by 6 parameters: 3 Cartesian and 3 angular coordinates. The mobility of a mechanism corresponds to its number of *independent* kinematic parameters, therefore called *degrees of freedom* (DOF). Considering these definitions, the skeleton mobility may be completely described by analyzing the joint kinematics. The general procedure is to individually consider the true functional mobility of each joint before considering the interdependencies induced by loops. In most analyses (Engin 89a,b, Högfors 91, Raikova 92, Helm 94b), the upper limb joints were idealized in the form of 3-DOF *Ball_&_Socket* or 1-DOF *Hinge* rotational joints (Fig 2.5).

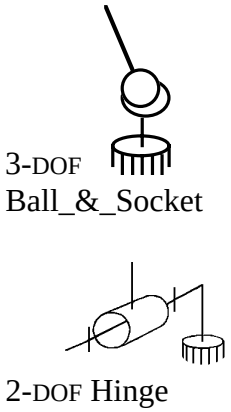

Fig. 2.5. Ideal Joints

2.2.2 Kinematic Models

Passive Resistance Characterization. In 1980, Engin started a research program for determining the three-dimensional passive resistive joint properties beyond the shoulder complex sinus. For this purpose, a global force applicator device was especially developed for applying various forces to the patient's upper arm, and the arm positions at which the subject could oppose the applied forces were measured using an exoskeletal device (ESD) (Fig. 2.6). Results were then provided in the form of 3D plots featuring the measured forces as a function of the arm orientation relative to the torso (Fig. 2.7) (Engin 80).

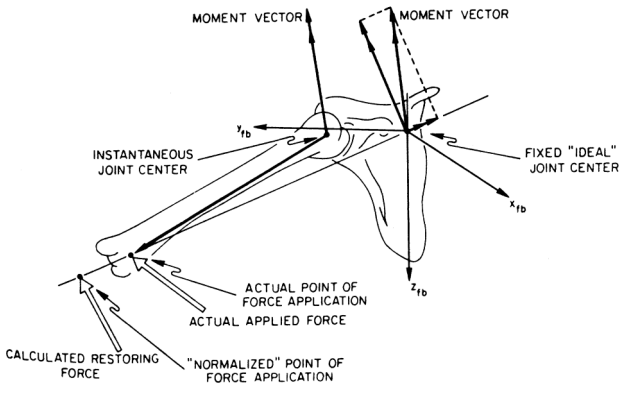

Fig. 2.6. Resistance measurement (Peindl 87)

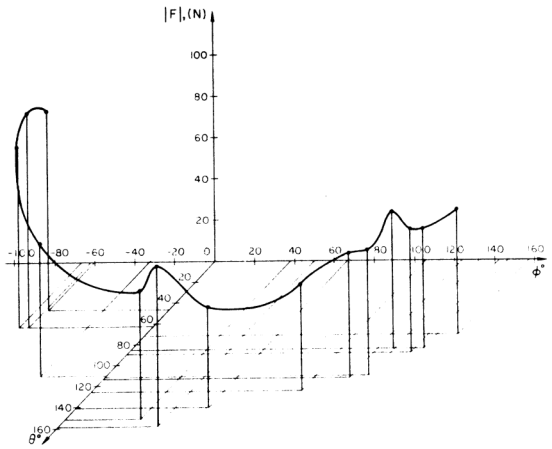

Fig. 2.7. Resistance vs orientation (Engin 80)

Passive vs Voluntary Resistance. In a second analysis, the approach was improved by the use of a sonic digitizing technique to determine the 3-D kinematics of the arm with a higher degree of accuracy (Engin 87, Peindl 87). The Euler angles describing the orientation of the arm with respect to the shoulder joint were then derived from those describing the arm orientation with respect to the fixed torso. Globographic representation was then used to determine the passive resistive properties beyond the shoulder complex sinus by comparison between voluntary movements and passive arm loading (Fig. 2.8).

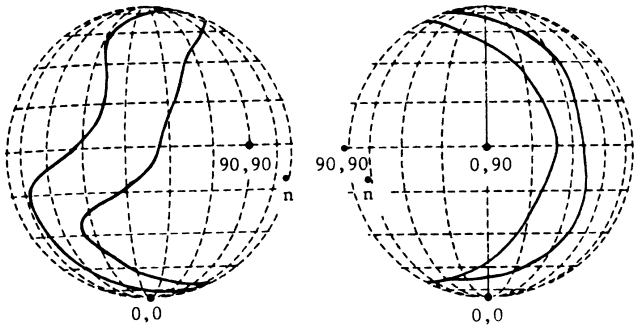

Fig. 2.8. Passive vs voluntary globographic representations (Peindl 87)

Sinus Cones Description. In a final analysis, Engin and Tumer focussed on the determination of the joint sinus cones for the three joints involved in the human shoulder. For this purpose, the shoulder was modeled as an open chain composed of three rigid links connected by 3-DOF rotational joints (Fig. 2.9).

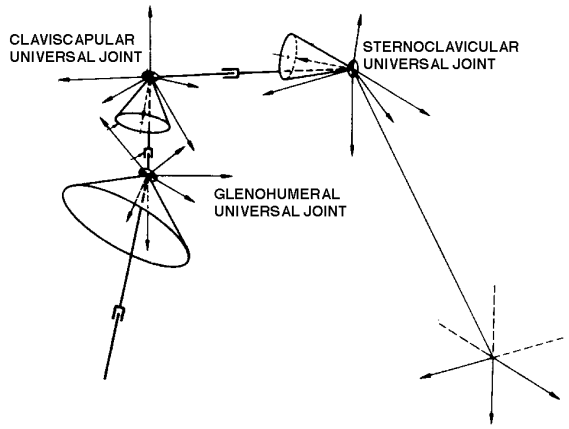

Fig. 2.9. Shoulder joint cones (Engin 89 a,b)

The cone model was assumed on an elliptic basis, and the joint sinus cones were obtained for each joint by least square fitting on a set of recorded arm postures on the voluntary shoulder complex sinus (Fig. 2.10).

As a result of this research, a shoulder model with quantitative descriptions of the individual joint sinus cones was provided. Although this is an improved description of the shoulder, the model does not provide information on the simultaneous motions of the shoulder bones, unless numerical optimization is applied (Engin 89a, b).

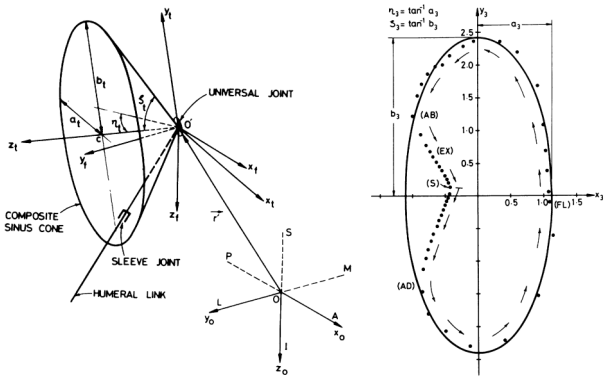

Fig. 2.10. Cone description (Engin 89 a,b)

Shoulder Kinematics. In 1987, another modeling program was initiated by Högfors et al. who applied optimization techniques to predict the forces in the muscles, modeled as straight or curved strings, as functions of the static arm position and the external loads (Högfors 87, 91, 95). Details on the force prediction part of this analysis are postponed to Chapter 3 (§ 3.1.3), which is especially concerned with muscle action modeling (Karlsson 92). The interesting point involved here is the approach that they followed towards determination of the shoulder 3-D kinematics.

For this purpose, spherical tantalum balls of 0.8 mm diameter were inserted percutaneously into the right shoulder bones of three specimen volunteers. The 3-D motions of these spheres during spiral-form arm lifting movements were then tracked using low dose roentgen-stereo-photogrammetry (Fig. 2.11).

The sphere motion data obtained were then converted into bone motion data with respect to the coordinate systems chosen to describe the shoulder kinematics. In particular, rotations were derived for each bone of the shoulder using Euler angles with respect to the torso fixed reference coordinate system (Fig. 2.12). For each recorded configuration of the upper limb, the values of the three Euler angles of each bone were then "plotted" with respect to the Euler angles of the humerus.

Three-Dimensional polynomial hypersurface fitting was finally used to identify the relation between the angular variables of each bone to the global orientation of the arm. The result was provided in the form of sets of equations expressing the Euler angles of each bone as functions of the arm angles with respect to the thorax (Eq. 2.1–2.3) (Högfors 91).

Contrary to the previous study, here the complete description of the shoulder kinematics was achieved. Dynamic modeling of the shoulder complex was then the next challenge.

Fig. 2.11. Shoulder markers (Högfors 91)

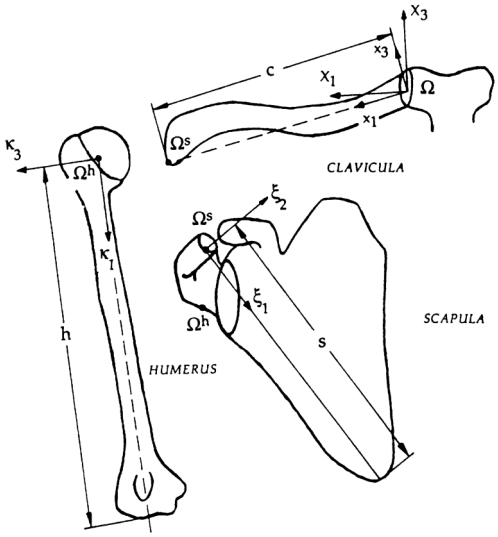

Fig. 2.12. Coordinate system (Högfors 91)

Humerus:
$$\gamma_h = -45 + \alpha_h\left[1 - (\beta_h + 90)/360\right] + (135 - \alpha_h/1.1)\sin\left(0.5(\beta_h + 90)(1 + \alpha_h/90)\right) \tag{2.1}$$

Clavicle:
$$\begin{cases} \alpha_c = -50 + 30\cos\left[0.75(\beta_h + 90)\right] \\ \beta_c = 24\left\{1 - \cos\left[0.75(\beta_h + 90)\right]\right\}(0.5 + \alpha_h/90) + 9 \\ \gamma_c = 15\left\{1 - \cos\left[0.75(\beta_h + 90)\right]\right\} + 3 \end{cases} \tag{2.2}$$

Scapula:
$$\begin{cases} \alpha_s = 200 + 20\cos\left[0.75(\beta_h + 90)\right] \\ \beta_s = -140 + 94\cos\left[0.75(\beta_h + 90)(1 - \gamma_h/270)\right] \\ \gamma_s = 82 + 8\cos\left\{(\alpha_h + 10)\sin\left[0.75(\beta_h + 90)\right]\right\} \end{cases} \tag{2.3}$$

2.2.3 Dynamic Models

In most approaches, the upper limb has been assumed to be composed of rigid bodies, including the bones and the soft tissues attached to them, connected by ideal (frictionless) kinematic joints. The rigid bodies have been assumed to possess fixed centers of gravity, and the joints, fixed axes or centers of rotation (Seireg 89, Raikova 92). In this direction, a major accomplishment was achieved by van der Helm who developed a complete dynamic model of the human shoulder using a finite element software (Fig. 2.13) (Helm 94b). In this approach, bones were modeled as usual as rigid segments connected by Ball_&_Socket joints. The originality here was in the modeling of the scapulo-thoracic joint in the form of a triangular structure constrained to be in contact with an ellipsoid. All muscles and ligaments were also included and modeled as straight or curved lines of action between their connections to the bones. A previous analysis had provided a discretization method for modeling the action of muscles with large attachment sites (§ 3.1.3) (Helm 91). Geometrical and mechanical parameters had also been collected to enable the kinematic and dynamic analysis of the shoulder (Veeger 91, Helm 91, 92, 94a).

From this analysis, a definitive description of the human shoulder was established by van der Helm and Pronk and validated on the basis of anatomical and practical criteria as well as on experimental result. For this purpose, bony landmarks were selected on the shoulder bones and a palpation technique was used in order to record their in vivo 3-D positions. As mentioned by van der Helm and Pronk: "*For the description of the rotations of local coordinate systems, a number of choices must be made. The orientation of the bones can be described with respect to the global coordinate system or with respect to the local coordinate system of the proximal bone. Rotation matrices describing rotations from one orientation to another, can be decomposed using Euler angles around the axes of the global coordinate system or Euler angles around axes of the local coordinate system of the bones. The initial position of the bone must be defined: the rest position or a well-defined virtual reference position. A clear statement of the choices made is necessary in order to enable comparisons between motion studies and to avoid confusion of the readers. Next the rotation matrices, can be decomposed into Euler angles around well defined axes*" (Helm 95).

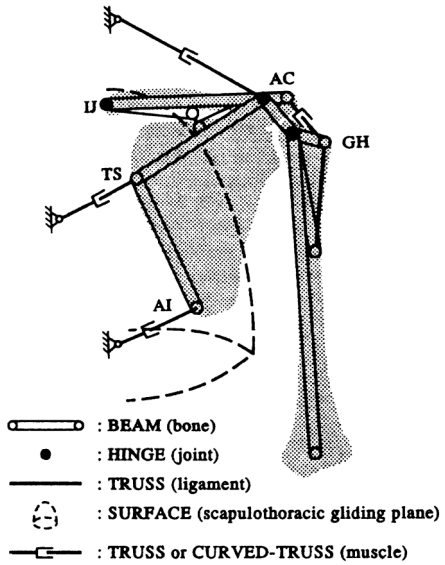

Fig. 2.13. Helm's shoulder model (Helm 94b)

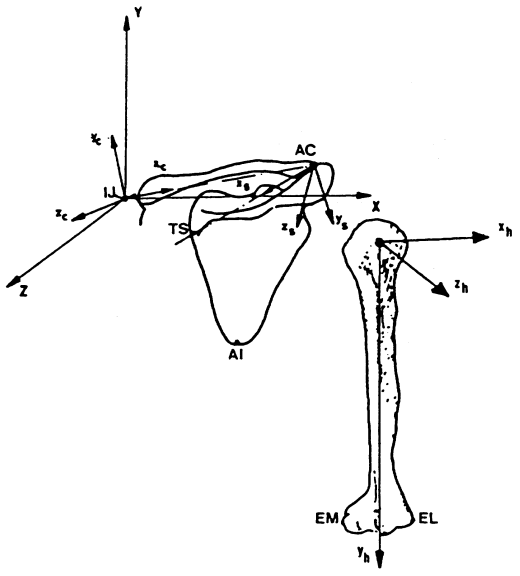

Fig. 2.14. Coordinate system (Helm 95)

In their analysis, only the right shoulder parameters were measured. The global reference coordinate system was chosen with its origin at the incisura jugularis (IJ), its X–axis pointing laterally, its Y–axis pointing cranially and its Z–axis pointing dorsally. The local coordinate system for each bone of the shoulder was chosen as follow (Fig. 2.14):

Thorax: y_t–axis: $(IJ - PX)/\|IJ - PX\|$;
x_t–axis: perpendicular to the plane $(IJ, PX, C7)$, pointing right;
Clavicula: x_c–axis: $(AC - IJ)/\|AC - IJ\|$;
z_c–axis: perpendicular to the x_c–axis and the global Y–axis, pointing dorsally;
Scapula: x_s–axis: $(TS - AC)/\|TS - AC\|$;
z_s–axis: perpendicular to the plane (AC, TS, AI), pointing dorsally;
Humerus: y_h–axis: logitudinal axis of the cuff, pointing caudally in the rest position;
z_h–axis: perpendicular to the plane defined by the y_h–axis and the line through the medial and lateral epicondyle, pointing ventrally at rest.

With the bony landmarks:

IJ: Incisura Jugularis (Sternum)
PX: transition from Sternum to Processus Xiphoideus (Thorax)
C7: 7^{th} cervical vertebra (Spine)
AC: most dorsal point on the acromioclavicular joint (Scapula)
TS: Trigonum Spinae (Scapula)
AI: Angulus Inferior (Scapula)

The z_t, y_c, y_s, and x_h –axes complete the above systems so as to be direct orthonormal, x_h pointing laterally at rest. Given that no well-defined anatomical rest positions exist for the thorax, clavicula, and scapula (they are different for each person), virtual reference positions were chosen to be oriented parallel to the axes of the global coordinate system.

The definition of joint rotations with respect to the local coordinate system of the proximal bone is common practice. However, van der Helm and Pronk noted that no flexion/extension, or abduction/adduction axes with respect to the proximal bone have been defined for the SC–, AC– and GH– joints. Therefore, they chose to describe joint rotations with respect to the global coordinate system. The rotation matrix decomposition into Euler angles was chosen to be closely related to medical definitions, so as to be reasonably interpretable. The analysis was finally applied to loaded and unloaded humeral abductions and anteflexion movements. The motion of the shoulder bones during these movements was then completely described, except for the clavicle axial rotation, which could not be recorded given that only two points were measured on this bone. It was therefore estimated by minimizing the AC joint rotations (Helm 95).

Benefiting from this background, I engaged in my turn into the modeling of the human upper limb with respect to the implementation requirements presented in § 1.3.3. Contrary to my predecessors, my contribution has been limited to theoretical considerations as no experimental program was planned in the context of CHARM (CHARM TR). The analysis I have led is presented in the following sections (Maurel 99).

2.3 Upper Limb Model Development

2.3.1 Kinematic Analysis

Following my predecessors (Engin 89a,b, Hogfors 91, Raikova 92, Helm 94b), I have considered joint translations negligible and modeled the SC, AC and GH joints as ideal 3-DOF rotational *Ball_&_Socket* joints, and the UH and UR joints as ideal 1-DOF rotational *Hinge* joints about the axes defined between their centres and the HR joint centre. Thus, the constraint induced by the HR joint in the triangle loop (HR–UH–UR) has been implicitly taken into account within the definitions of the UH and UR hinges. As presented in the following, the main challenge in human upper limb modeling is the modeling of the scapulothoracic constraint.

The ST joint is special since it does not properly involve articular structures between scapula and thorax. Almost totally covered by its surrounding soft tissues, the scapula possesses more or less any degree of freedom in space. However, its medial border has been described as constrained to glide on the thorax (Dvir 78). Therefore, three forms may be proposed to describe this constraint: a dot contact, a linear or a planar tangency onto the thorax. As these forms still involve a combination of gliding and rolling movements, equivalent idealized representations may be preferred, i.e. a 5-DOF top, a 4-DOF dipod or a 3-DOF tripod joint (Fig. 2.16). A definite choice for the ST joint may be further included when considering the shoulder assembly. Independently considered, the number of parameters describing the shoulder kinematics sums up to 9, 10 or 11 (SC+AC+ST), depending on the description chosen for the ST joint: 3-DOF in rotations for the SC joint, 3-DOF in rotations for the AC joint, and 3-DOF, 4-DOF OR 5-DOF for the ST joint.

However, the loop conformation of the trunk, the clavicle and the scapula induces interdependencies between these parameters, thus reducing the number of true DOF. Dvir and Berme have reported that "*during elevation of the arm, the scapula first rotates in the scapular plane around an ambiguous centre of rotation RS, which then progresses towards the glenoid and the acromio-clavicular joint*" (Fig. 2.15) (Dvir 78). According to Pronk, a description of the shoulder kinematics in terms of the helical axis may not be reliable for a scientific application (Pronk 91). Nethertheless, such a representation may help clarify the mobility of the assembly. I have therefore considered the shoulder mobility on the basis of a helical axis representation as presented in the following.

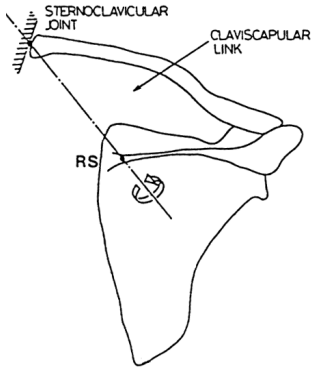

Fig. 2.15. Helical axis of the scapula (Dvir 78)

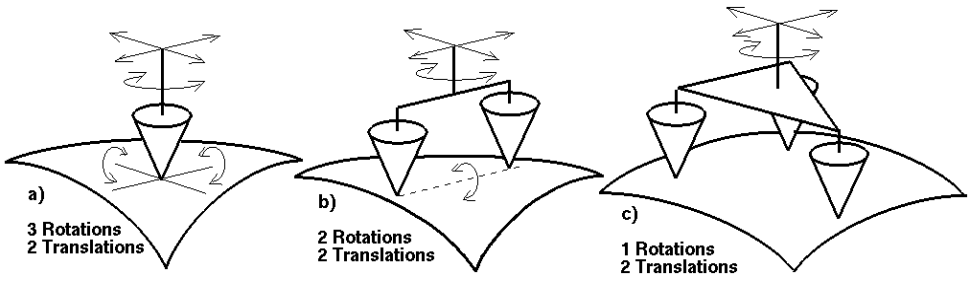

Fig. 2.16. Top (a), dipod (b) and tripod (c) models (Maurel 99)

Shoulder Mobility. Consider a helical axis pointing from the SC joint centre to a 5-DOF ST top joint as shown in Fig. 2.17b. Since the shape of the thorax does not fit that of a sphere centred on the SC joint, the gliding of the scapula on the thorax induces a translation of the scapula along this axis. This may be represented by a 4-DOF *linear ring* joint along the helical axis, as shown in Fig. 2.17a. In the plane containing the three joints, four distinct parameters may be distinguished: one extension λ and three rotations α, β, and γ. If any of them is kept constant, none of the others can vary. Hence there is *only one single DOF* in the plane of the assembly. Now, taking into account the shape of the thorax relates this single DOF to the 3-D orientation of the helical axis. Adding the clavicular and scapular rotations about themselves to the 3 DOF of the helical axis then raises the mobility of the assembly to 5 DOF. From a motion control point of view, this result is of interest since it establishes that the control of this axis fully determines the state of the whole shoulder girdle.

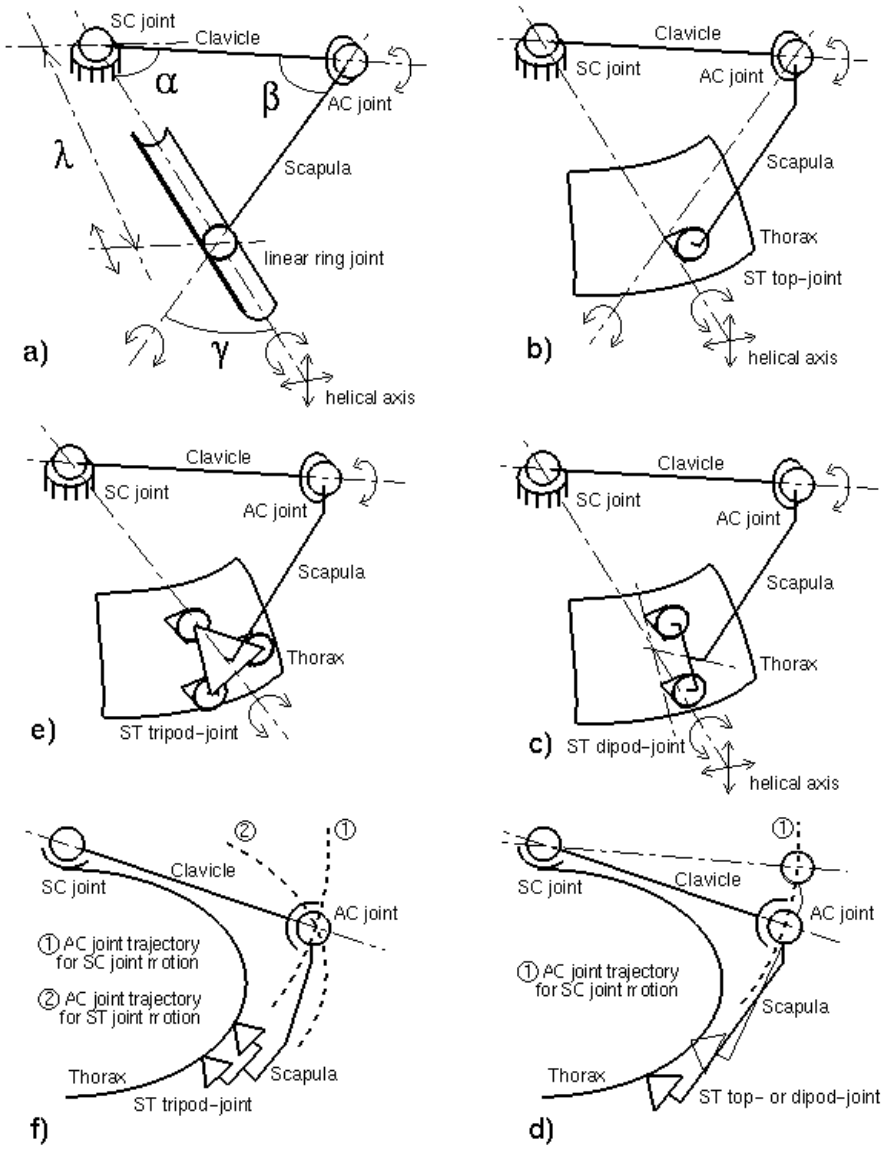

Fig. 2.17. Model comparative motion analysis (Maurel 99):
a) shoulder plane parameters
b) 5-DOF assembly
c) 4-DOF assembly
d) top view of a) or b)
e) 2-DOF assembly
f) incompatible trajectories

This result has been obtained with respect to the initial choice of a 5-DOF ST top joint (Fig. 2.17b). A 4-DOF ST dipod joint instead would add a dependency between the shape of the thorax and the rotation of the scapula about the (AC–ST) axis, thus reducing the number of DOF of the assembly to 4 (Fig. 2.17c). Similarly, a 3-DOF ST tripod joint would relate all the rotations of the scapula to the shape of the thorax (Fig. 2.17e). Since this shape is not compatible with the spherical motion of the acromio-clavicular joint, the assembly would jam itself (Fig. 2.17f) unless the scapula starts rolling on the thorax, thus breaking the tripod joint into an equivalent 5-DOF top or 4-DOF dipod joint (Fig. 2.17d). As a result, only the 5-DOF top or 4-DOF dipod joint may be used to model the ST joint (Maurel 99).

2.3.2 Upper Limb Model

In his analysis, van der Helm has opted for a 4-DOF gliding dipod on an ellipsoidal thorax (Fig. 2.18) (Helm 94b). This choice seems to be the most representative from the description Dvir and Berme have given for the motion of the scapula (Dvir 78). However, due to the loop conformation of the shoulder girdle, I have judged it inconvenient for the model implementation in CHARM. Taking into account the linear tangency constraint of the scapula on the thorax in the data structure, would have required maintaining two definitions of the orientation of the scapula: one with respect to the thorax in the ST joint and one with respect to the clavicle in the AC joint. These two definitions are likely to be incompatible unless a complex priority rule is implemented. Furthermore, it is more logical to include this linear tangency as a dynamic constraint in the motion control procedures than in the static data structure. Consequently, I have chosen to model the ST joint as a 5-DOF top joint, handling only the position of the scapula, and to leave the orientation of the scapula defined with respect to the clavicle by the AC joint, with a restricted range of rotation about the (AC–ST) axis (Fig. 2.16b). Nevertheless, the relation between the orientations of the clavicle and scapula and the position of the scapula – i.e. between the parameters $(\lambda, \alpha, \beta, \gamma)$ previously mentioned – is unavailable in practice. So, instead of 5 DOF, I have chosen to maintain the conformation of the shoulder bones described in terms of 9 interrelated parameters: 3 rotations for the SC joint, 3 rotations for the AC joint, 3 translations for the ST joint.

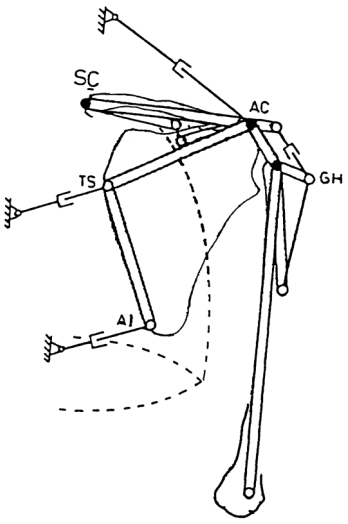

Fig. 2.18. Helm's model (Helm 94b)

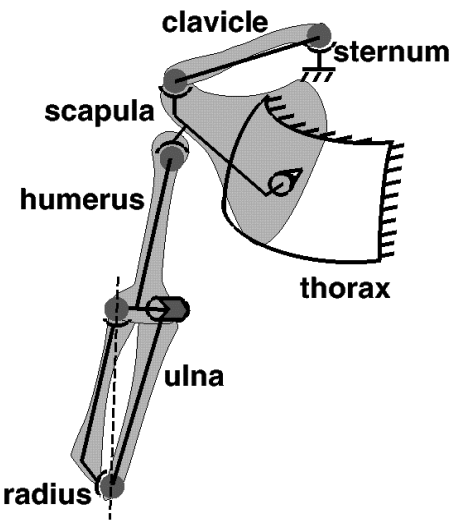

Fig. 2.19. My model (Maurel 96)

In order to solve the inherent redundancy, the coordinates of the ST contact may then be derived from the current position of the scapula, which is completely defined by the rotations of the SC and AC joints. Finally, following van der Helm, I have chosen to approximate the thorax by an ellipsoid for allowing the description of the scapulo-thoracic contact in terms of 2 independent ellipsoidal coordinates instead of three interrelated Cartesian coordinates.

The resulting upper limb model possesses a total of 10 DOF (Fig. 2.19) (Maurel 99):

- shoulder: 5 DOF
- arm: 3 DOF
- forearm: 2 DOF

obtained by the combination of 6 joints involving 13 parameters:

- SC: 3 angular parameters
- AC: 3 angular parameters
- ST: 2 angular parameters
- GH: 3 angular parameters
- UH: 1 angular parameter
- UR: 1 angular parameter

and 3 relations between the ST, SC and AC joint parameters.

Constraining the rotation of the scapula about the (AC–ST) axis would lead to van der Helm's result, i.e. a 7-DOF shoulder-arm model with a 4-DOF dipod joint (Helm 94b).

After developing the qualitative model of the upper limb, I investigated the formalization of joints in mathematical terms as required for handling the static description of the upper limb conformation in the CHARM data structure.

2.3.3 Joint Model

At the geometrical composition stage, no hierarchy or structural dependency exists between the bones. Each bone is obtained from the 3-D reconstruction in the form of a polygonal surface defined in its own *geometrical frame*, and its motion may be referred to any other frame by mean of a 4x4 transfer matrix defined between both frames (Fig. 2.20). As explained by van der Helm and Pronk, there are several methods for describing the skeleton kinematics: either *bone* or *joint* rotations may be considered with respect to either *global* or *local* coordinate systems and with reference to either a *rest* or a *virtual* position. Considering that *'no flexion/extension or abduction/adduction axes with respect to the proximal bone have been defined'* for the upper limb (§ 2.2.3), van der Helm and Pronk have chosen to describe joint rotations with respect to the global coordinate system, instead of the local coordinate system of the proximal bone (Helm 95). The parameters they consider therefore do not represent joint rotations. However, in practice, the upper limb anatomy is often described by considering the relative orientation of the bones. Furthermore, global parameters are not appropriate for describing the joint sinus cones restricting the motion of the bones (see § 2.2.2) (Engin 89a,b). These may be required for the accurate modeling of the upper limb. Although we did not consider the modeling of the joint sinus cones in CHARM, the possibility of bringing such improvements to the data structure in future had to be preserved, in conformity with the requirement of an open implementation. Therefore, I have chosen to describe the upper limb kinematics in terms of joint parameters defining a bone with respect to the coordinate system of the proximal bone of the joint (Maurel 99).

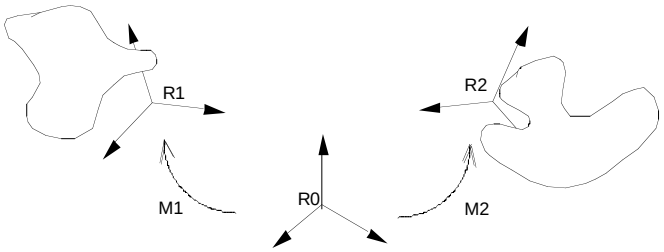

Fig. 2.20. Independent spatial composition

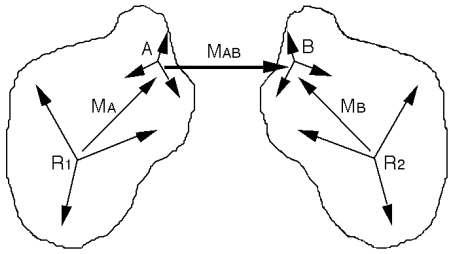

Fig 2.21. Joint mathematical definition.

Joint modeling requires the definition of the *reference* and *relative* coordinate systems on the reference bone and on the moving bone respectively (Fig. 2.21). The joint motion may then be described by means of Cartesian and angular coordinates representing the DOF of the joint. From the definition of the rotation sequence, a transfer matrix may be calculated which defines the *relative frame* with respect to the *reference frame*. Various methods may be used to describe the 3-D orientation of a coordinate system with respect to another, the most common being the Euler angles. In conformity with biomedical experience, I have chosen the gyroscopic Euler rotation composition. Due to the left/right symmetry of the human body, it is necessary to define different rotation sequences, one for each side, in order to respect the convention of *direct* coordinate systems as well as the anatomical rotation orders considered in practice.

Now, let $(R_0) \equiv (\mathbf{X}_0, \mathbf{Y}_0, \mathbf{Z}_0)$ and $(R_3) \equiv (\mathbf{X}_3, \mathbf{Y}_3, \mathbf{Z}_3)$ be the coordinate system of the moving bone *before* and *after* its rotation respectively. The intermediate successive rotations around local axes have been represented for the *left* arm and for the *right* arm in Figs. 2.22 and 2.23 respectively. In both cases, the transfer matrix from (R_0) to (R_3) is given by (Fig 2.24):

$$\mathbf{M}(\theta, \varphi, \psi) = \mathbf{M}(\theta)\mathbf{M}(\varphi)\mathbf{M}(\psi) \qquad \text{(column matrix)} \qquad (2.4)$$

and the coordinates in (R_0) of the image $\mathbf{V}'$ of any vector $\mathbf{V}$ due to the associated rotation may be obtained by:

$$\mathbf{V}' = \mathbf{M}(\theta, \varphi, \psi)\mathbf{V} \qquad (2.5)$$

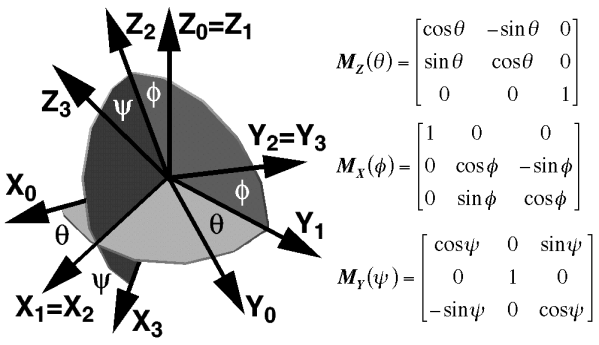

$$M_Z(\theta) = \begin{bmatrix} \cos\theta & -\sin\theta & 0 \\ \sin\theta & \cos\theta & 0 \\ 0 & 0 & 1 \end{bmatrix}$$

$$M_X(\phi) = \begin{bmatrix} 1 & 0 & 0 \\ 0 & \cos\phi & -\sin\phi \\ 0 & \sin\phi & \cos\phi \end{bmatrix}$$

$$M_Y(\psi) = \begin{bmatrix} \cos\psi & 0 & \sin\psi \\ 0 & 1 & 0 \\ -\sin\psi & 0 & \cos\psi \end{bmatrix}$$

Fig. 2.22. Left arm rotations (Maurel 99)

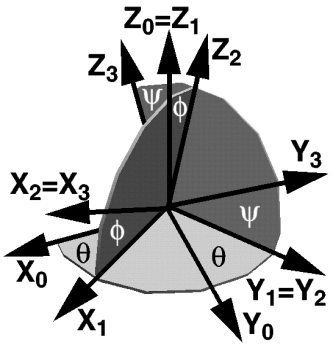

$$M_Z(\theta) = \begin{bmatrix} \cos\theta & -\sin\theta & 0 \\ \sin\theta & \cos\theta & 0 \\ 0 & 0 & 1 \end{bmatrix}$$

$$M_Y(\phi) = \begin{bmatrix} \cos\phi & 0 & \sin\phi \\ 0 & 1 & 0 \\ -\sin\phi & 0 & \cos\phi \end{bmatrix}$$

$$M_X(\psi) = \begin{bmatrix} 1 & 0 & 0 \\ 0 & \cos\psi & -\sin\psi \\ 0 & \sin\psi & \cos\psi \end{bmatrix}$$

Fig. 2.23. Right arm rotations (Maurel 99)

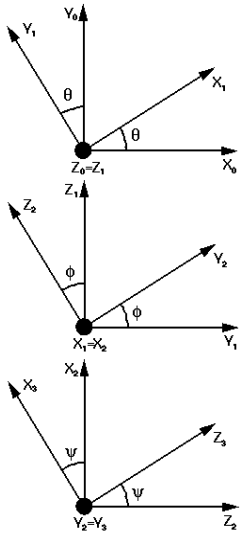

a) (0) –> (1) $\mathbf{V}_0 = \mathbf{M}_Z(\theta)\mathbf{V}_1$ $\mathbf{M}_Z(\theta) = \begin{bmatrix} \cos\theta & -\sin\theta & 0 \\ \sin\theta & \cos\theta & 0 \\ 0 & 0 & 1 \end{bmatrix}$

b) (1) –> (2) $\mathbf{V}_1 = \mathbf{M}_X(\varphi)\mathbf{V}_2$ $\mathbf{M}_X(\varphi) = \begin{bmatrix} 1 & 0 & 0 \\ 0 & \cos\varphi & -\sin\varphi \\ 0 & \sin\varphi & \cos\varphi \end{bmatrix}$

c) (2) –> (3) $\mathbf{V}_2 = \mathbf{M}_Y(\psi)\mathbf{V}_3$ $\mathbf{M}_Y(\psi) = \begin{bmatrix} \cos\psi & 0 & \sin\psi \\ 0 & 1 & 0 \\ -\sin\psi & 0 & \cos\psi \end{bmatrix}$

$\mathbf{V}_0$, $\mathbf{V}_1$, $\mathbf{V}_2$, $\mathbf{V}_3$: coordinates of vector $\mathbf{V}$ in $(\mathbf{X}_0, \mathbf{Y}_0, \mathbf{Z}_0)$, $(\mathbf{X}_1, \mathbf{Y}_1, \mathbf{Z}_1)$, $(\mathbf{X}_2, \mathbf{Y}_2, \mathbf{Z}_2)$, $(\mathbf{X}_3, \mathbf{Y}_3, \mathbf{Z}_3)$

Transfer matrix: $\mathbf{V}_0 = \mathbf{M}(\theta, \varphi, \psi)\mathbf{V}_3$ $\mathbf{M}(\theta, \varphi, \psi) = \mathbf{M}_Z(\theta)\mathbf{M}_X(\varphi)\mathbf{M}_Y(\psi)$

Rotation matrix: $\mathbf{V}' = \mathbf{R}(\theta, \varphi, \psi)\mathbf{V}$ $\mathbf{V}'$ image in $(\mathbf{X}_0, \mathbf{Y}_0, \mathbf{Z}_0)$ of $\mathbf{V}$ by $\mathbf{R}(\theta, \varphi, \psi)$:

$$\mathbf{R}(\theta, \varphi, \psi) = \mathbf{M}(\theta, \varphi, \psi) = \mathbf{M}_Z(\theta)\mathbf{M}_X(\varphi)\mathbf{M}_Y(\psi) = \mathbf{R}_Z(\theta)\mathbf{R}_X(\varphi)\mathbf{R}_Y(\psi)$$

Fig. 2.24. Joint transfer and rotation matrix for the left side (Maurel 99)

Upper Limb Joint Frames. From the analysis of their model, van der Helm and Pronk have defined the most appropriate coordinate systems for describing the motion of the human shoulder, validated on the basis of anatomical and practical criteria as well as experimental results (see § 2.2.3) (Helm 95). However, their definitions have appeared inappropriate for the developments in CHARM. First, their coordinate systems, published in 1995 were defined for a right shoulder while the reconstruction of the left arm of the Visible Human had been commenced since 1993 (Kalra 95, Gingins 96a,b). Secondly, some of their coordinate systems have axes penetrating the bones, which is inappropriate for the interactive editing and visualization of the model using the topological modeling tool (Beylot 96).

Therefore, I have defined my own coordinate systems, though on the basis of their definitions, while preserving the correspondences and the reasonable interpretability of the parameters. For each joint of the proposed upper limb model presented in § 2.3.2, I have defined reference and relative coordinate system on the corresponding bones. These are shown in Fig. 2.25a–f. Their interactive editing on the 3-D Visible Human model using the topological modeler is detailed in Chapter 5, which is devoted to the *CHARM Implementations* (Maurel 96).

As established in § 1.3.2 for dynamic simulation, the kinematic model must be complemented with a macroscopic articulated rigid body representation, in which rigid bodies include bones and soft tissues as a whole, in order to preserve the real-time motion control of the model. The rigid body model development is therefore presented in the following section.

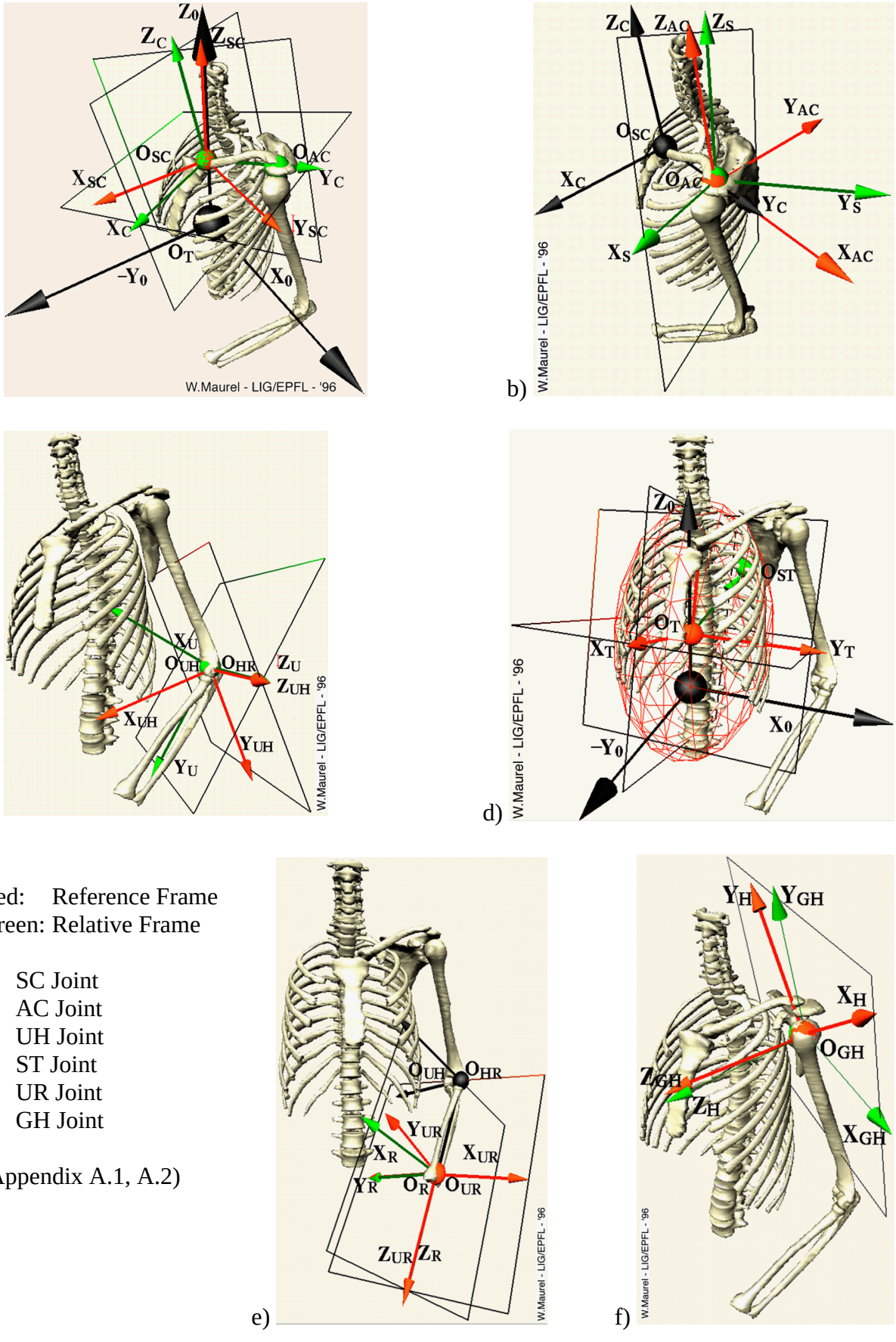

Red: Reference Frame
Green: Relative Frame

a) SC Joint
b) AC Joint
c) UH Joint
d) ST Joint
e) UR Joint
f) GH Joint

(Appendix A.1, A.2)

Fig. 2.25. Coordinate systems definition for the human upper limb joints (Maurel 96)

2.3.4 Rigid Body Model

Following my predecessors (Seireg 89, Raikova 92), I have considered the upper limb as a chain composed of three rigid bodies – the arm, the forearm and the hand – articulated on the rigid basis formed by the trunk and related by ideal rotational joints (Maurel 99). This representation relies on three assumptions:

- the mechanical behavior of the upper limb with respect to the trunk is independent of the rest of the human body
- within each segment, bones and soft tissues have similar rigid body motions
- the deformation of the soft tissues does not significantly affect the mechanical properties of a segment as a whole

The corresponding dynamic behavior may then be described by:

$$\sum_{i=1}^{3} \begin{Bmatrix} m_i \boldsymbol{\Gamma}^{G_i}_{i/0} = m_i \mathbf{g} + \mathbf{F}_{ext/i} \\ \mathbf{I}_{i/O_1} \mathbf{J}_{i/0} = \mathbf{M}^{O_1}_{ext/i} \end{Bmatrix} \quad \text{with:} \tag{2.6}$$

m_i, G_i, $\mathbf{I}_{i/O_1}$ mass, center of mass, and inertia matrix of body *i*

$\boldsymbol{\Gamma}^{G_i}_{i/0}$, $\mathbf{J}_{i/0}$ linear and angular acceleration vectors of body *i* with respect to *0*

$\mathbf{F}_{ext/i}$, $\mathbf{M}^{O_1}_{ext/i}$, $\mathbf{g}$ external force, torque and gravity vectors on body *i* with respect to O_1

Assuming the hand motion has a negligible effect on the large motion dynamics of the upper limb, I have taken the hand as a rigid extension of the forearm. Consequently, it has been necessary to determine a rigid body equivalent to the hand and forearm assembly to be substituted in the rigid body dynamic analysis (Fig. 2.26).

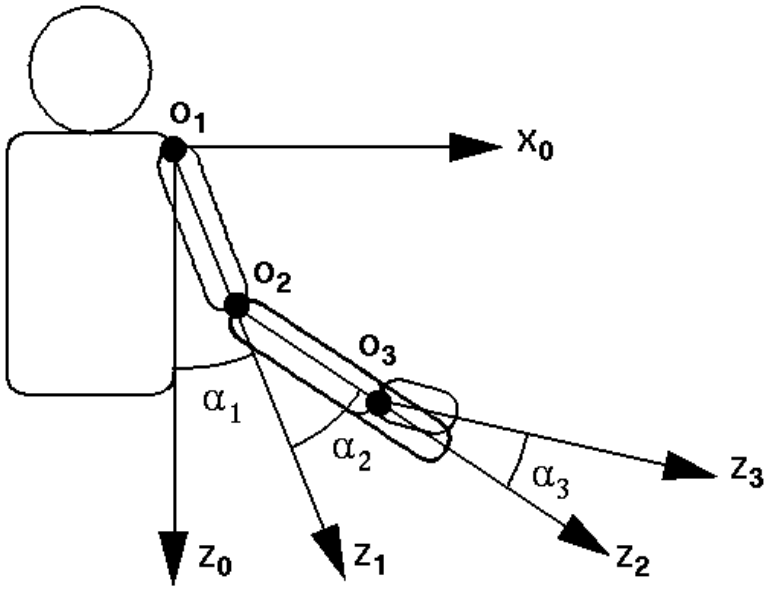

Fig. 2.26. The upper limb rigid body model (Maurel 99)

In order to further simplify the analysis, I have assumed the shape of the upper limb segments as more or less cylindrical and consequently modeled the arm and forearm bodies as rigid homogeneous cylinders. As a result, the mechanical properties of the equivalent hand-forearm cylinder may be obtained from those of the forearm and the hand using: (see Appendix A.3)

$$m_{II} = m_2 + m_3 \tag{2.7}$$

$$l_{II} = l_2\left(1 + \frac{m_3}{m_2 + m_3}\right) \tag{2.8}$$

$$r_{II} = \left[\begin{array}{l} \frac{m_2}{m_{II}}\left(r_2^2 + \frac{4}{3}l_2^2\right) - \frac{4}{3}l_{II}^2 + \\ \frac{m_3}{m_{II}}\left(r_3^2 + \frac{1}{3}l_3^2 + \left(2l_2 + l_3\right)^2\right) \end{array}\right]^{1/2} \tag{2.9}$$

where m_{II}, l_{II}, r_{II} are the mass, length, radius of the hand-forearm equivalent cylinder.

The resulting rigid body model is a rough model of the upper limb since it assumes that the rigid bodies are connected at their ends by rotational joints. This assumption is not compatible with the kinematic model of the upper limb skeleton developed in § 2.3.2. For consistency of the data structure, it has been necessary to align the rigid body model with the kinematic skeleton model (Maurel 99).

Regarding the shoulder, it appears that for an accurate model, the motion of the glenoid should be taken into account. However, clavicle and scapula are embedded in the flesh along with the trunk so that an equivalent anatomical rigid body segment is difficult to design. Furthermore, they are strongly maintained by their surrounding muscles so that their motion is usually regarded as quasi static. For these reasons, I have neglected their influence on the large motion dynamics of the upper limb and assigned mechanical properties to the arm segments only.

Regarding the hand-forearm segment, it appears that a single cylinder model is not compatible with the ulna/radius composition of the forearm. In order to fit compatible kinematic and rigid body models on the 3-D skeleton, it has been necessary to share the properties of the hand-forearm equivalent body between the radius and ulna. Consequently, I have split the hand-forearm cylinder into two equal cylinders between the ulna and radius.

The interactive fitting of those rigid body properties onto the 3-D upper limb model is also presented in the *CHARM Implemetations* chapter (Chapter 5).

Conclusion

The upper limb mobility may be completely described by analyzing the kinematics of its joints. These are the *sterno-clavi*cular (SC) between sternum and clavicle, the *acromio-clavicular* (AC) between clavicle and scapula, the *gleno-humeral* (GH) between scapula and humerus, the *ulno-humeral* (UH) between humerus and ulna, the *ulno-radial* (UR) between ulna and radius, and the *scapulo-thoracic* (ST) between thorax and scapula. The case of the *scapulo-thoracic* joint is special since this joint does not properly involve articular structures. The scapula has however been described as constrained to glide on the thorax. More or less following my predecessors, I have modeled all joints as ideal *Ball_&_Socket* and *Hinge* joints, except the ST joint which I have modeled as a gliding dot contact on an ellipsoid. For each joint, I have defined reference and relative coordinate systems so as to allow the description of joint rotations using Euler angles. In order to avoid redundancies, I have chosen to derive the ST joint parameters from the position of the scapula which is defined by the rotations in the SC and AC joints. Finally, I have developed the rigid body model in assuming the hand as a rigid prolongation of the forearm and the upper limb segments as rigid cylinders. I have then split in two the hand-forearm cylinder for the rigid body model to remain consistent with the kinematic model. The interactive editing of these properties onto the 3-D upper limb model is detailed in Chapter 5.

3 Muscle Action Modeling

The simulation of the upper limb motion can be achieved using *forward dynamics*. In this case, it is necessary to provide as input the muscle forces exerting on the skeleton. Conversely, the forces and torques required at the joints for performing a given motion may be obtained using *inverse dynamics*, and used for determining the required muscle forces. In both cases, a topological model of the musculature is necessary. The model I have developed for the upper limb is presented in this chapter. Given the complexity of the musculature, the determination of the individual muscle forces remains an indeterminate problem. This is due to the fact that a muscle never works alone but is always involved in a coordination scheme with several complementary/supplementary muscles. Furthermore, the tension in a muscle is not a constant parameter during motion but varies according to the muscle length, velocity and activation parameters. For accurate simulation, models for the muscle contraction dynamics are required. Suggestions in this direction are thus also provided here.

3.1 Muscle Topology Modeling

3.1.1 The Upper Limb Musculature

To perform movements (see § 2.1.2), the upper limb is equipped with not less than 22 muscle actuators, among which some divide into several bundles attached on different bones (Fig. 3.1). These muscles can be divided into several groups according to the bone they move and the DOF they control. The main ones are outlined below (Maurel 96).

Dvir and Berme noticed that most muscles acting on the scapula insert close to its medial border (Dvir 78). This concerns the *levator scapulae*, the *rhomboids*, the *serratus anterior*, the middle and the lower parts of the *trapezius*. These muscles make the scapula a strong basis for performing arm movements (Fig. 3.2).

The rotator cuff refers to the group of muscles which covers the humeral head and control some of its rotations. These are the *subscapularis/teres major* as opposed to the *infraspinatus/teres minor* for controlling the axial rotations, and the *supraspinatus/deltoideus* which handle the abduction (Kapandji 80).

The other actuators of the humerus are the *latissimus dorsi* and *pectoralis major*, which cooperate in its adduction, while they oppose each other in flexion/extension and axial rotation (Grant 91).

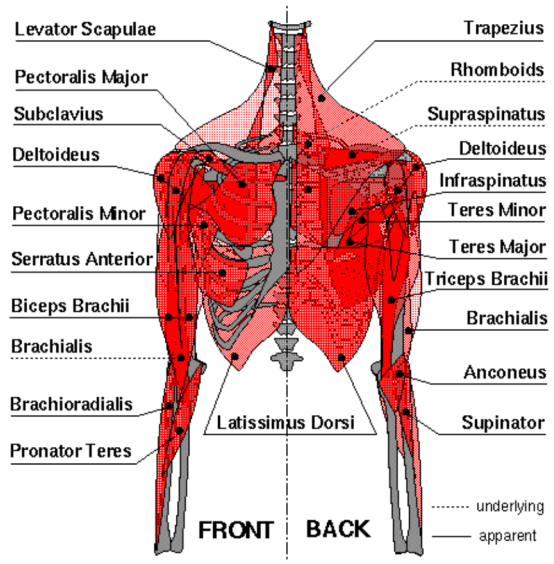

Fig. 3.1. The upper limb musculature (*Subscapularis* can not be seen) (Maurel 99)

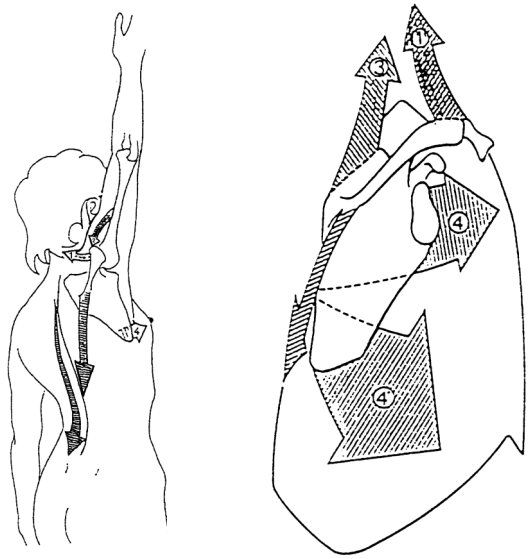

Fig. 3.2. Muscles of elevation: (Kapandji 80)
1) *trapezius* (upper and lower) 2) *deltoideus* (lateral)
3) *rhomboids* 4) *serratus anterior* (upper and lower)

With regard to the forearm, two prime antagonistic groups of muscles control the flexion/extension movements: the *brachialis* and *biceps brachii* for the flexion as opposed to the *anconeus* and *triceps brachii* for the extension.

When the *brachialis* is inactive, the *biceps brachii* also contributes for controlling the supination movement of the forearm, together with the *brachioradialis*, and in opposition to the *pronator teres*, which controls the pronation (Chao 78).

3.1.2 Modeling Approaches

There are basically two methods for modeling the actions of muscles on the skeleton.

- The first one is called the straight line approach. It consists of connecting the origin and insertion sites of a muscle (Seireg 89). This approach may be sufficient in many cases when the attachment sites of the muscle can actually be reduced to single points, when tendon fibers lie in prolongation of the muscle fibers with no pennation angle, and when the muscle fibers path is not constrained by neighbouring structures. However, it is often not the case, and the centroid-line approach is usually preferred.

- The centroid-line approach estimates the curved lines along which tension is developed, which are formed by the centroids of the muscle cross-sections (Jensen 75). Thus, it takes better into account the actual attachment areas and orientation of the fibers. Significant difference was observed between unit vectors colinear with the muscle forces obtained by straight-line modeling and centroid-line modeling. Though this method seems quite accurate for relatively long parallel fibred muscles, errors may occur, especially for relatively short muscles, when the slices are not properly taken perpendicular to the actual line of action of the muscle (Raikova 92).

The main drawback for both methods is that they refer to only one position of the model. An intermediate approach, called the *contour line* approach, realizes a balance between accuracy and simplicity in segmenting the bony contours followed by the muscles (Raikova 92).

In all cases, the *–line* approach assumes that the muscle line of action is representative of the muscle force direction at a cross-section and that the muscle exerts no moment around that line. This approximation is not always correct anatomically as well as mechanically (Zuylen 88). Some muscles have very broad attachments while some others divide in several bundles attached onto different bones. It has been observed that small changes in the direction of the forces can have large effects on the resulting moment vectors (Helm 91).

For this reason, van der Helm and Veenbaas developed a method for determining the number of muscle force vectors, capable of representing the mechanical effect of muscles with large attachment sites. This method takes into account the form and size of the attachments as well as the distribution of the fibres in the muscle. As detailed in the following section, it was applied for the accurate modeling of the shoulder musculature.

3.1.3 Former Models

Following one or the other approach, several musculoskeletal models have been proposed for the upper limb (Yamaguchi 95, Gonzalez 96, Johnson 96), the lower limb (Davy 87, Crowninshield 81, Pandy 90, 92) and even the whole body (Seireg 89). Two major studies should be outlined concerning the shoulder. The first one was presented in 1987 by Högfors et al. who considered 21 shoulder muscles and modeled their action using 33 action lines (Högfors 87). The action of most muscles was modeled by one straight line, except for the *latissimus dorsi*, the *pectoralis major*, the *serratus anterior*, the *trapezius*, the *deltoideus*, the *infraspinatus* and the *subscapularis*, which required several lines (Fig. 3.3). The model was applied by Karlsson and Peterson for force prediction in the human shoulder (Karlsson 92).

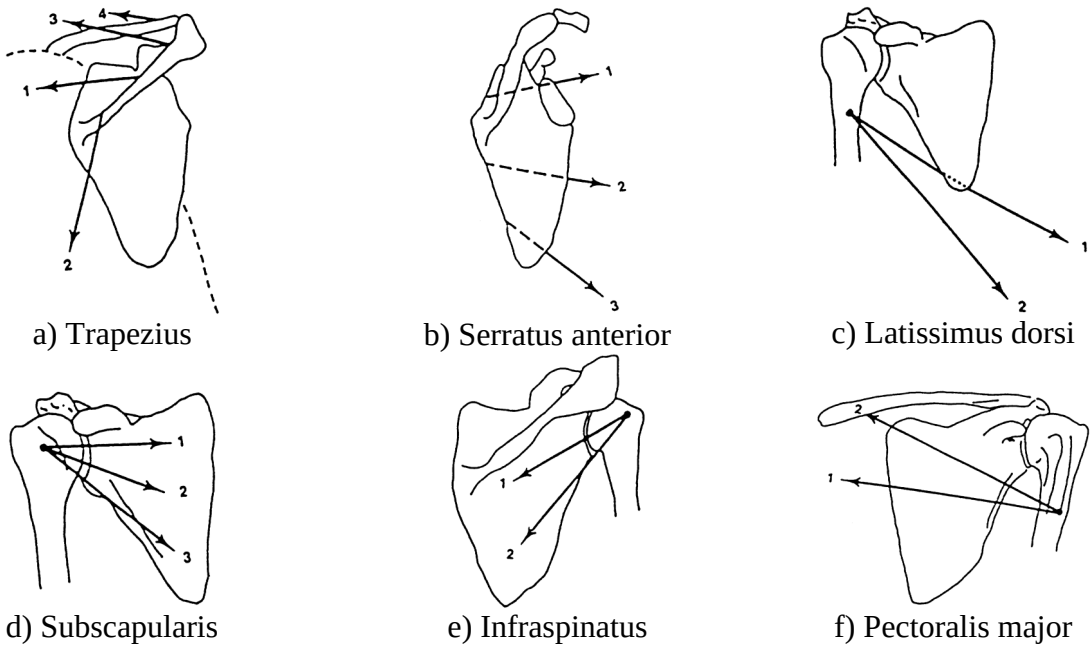

Fig. 3.3. Högfors' muscle models (Högfors 87)

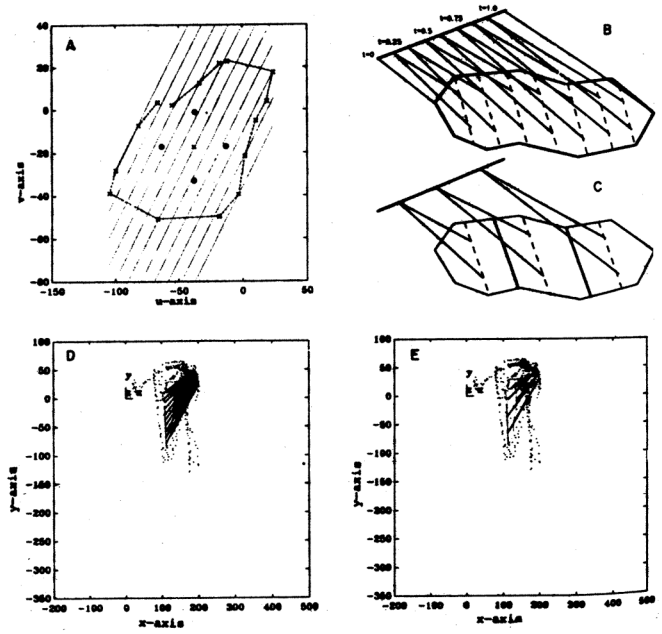

(Helm 91)

Fig. 3.4. Broad muscle automatic modeling

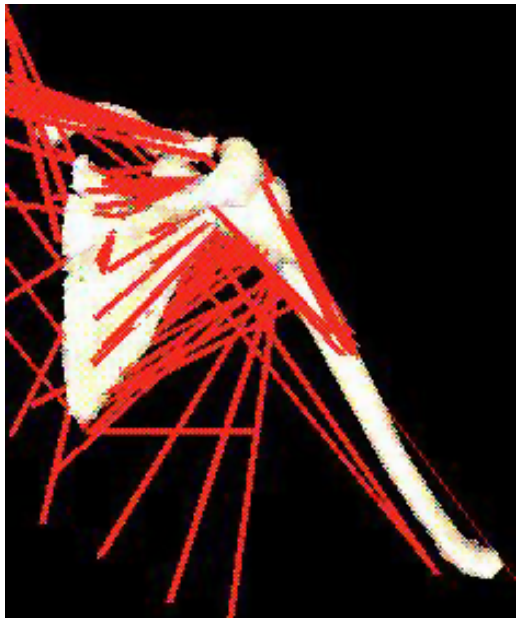

(Helm 91)

Fig. 3.5. Helm's shoulder model

The second major study was presented by van der Helm and Veenbaas who proposed, as mentioned before, a method for accurately modeling the mechanical effect of broad muscles (Fig. 3.4). For this purpose, the complete attachement site of the muscle was described mathematically, and a map of the fiber distribution from origin to insertion was derived. This map was then used to define an arbitrarily large enough (~200) number of force vectors to properly represent the mechanical effect of the muscle. A procedure was then developed to minimize the number of force vectors while keeping negligible the resulting error in the mechanical effect (Helm 91).

The method was applied to the accurate modeling of the *coracobrachialis*, the *deltoideus*, the *infraspinatus*, the *latissimus dorsi*, the *levator scapulae*, both *pectoralis major* and *minor*, the *rhomboideus*, the *serratus anterior*, the *subscapularis*, the *supraspinatus*, both *teres major* and *minor*, and the *trapezius*. Their analysis suggested that, for example, 6 force vectors are at least required to model the *trapezius*. This resulted in a highly refined musculoskeletal shoulder model, as shown in Fig. 3.5. It was applied for dynamic simulation of the human shoulder with the dynamic finite element model presented in § 2.2.3 (Fig. 2.13) (Helm 94b).

Following one or the other –line approach, it is thus possible to model the topology of the actions applied by the muscles to the skeleton. This topology may be used for simulating the dynamics of the musculoskeletal system under specified muscle actions (*forward dynamics*), or conversely for determining the muscle actions corresponding to specified motions (*inverse dynamics*). However, muscles always cooperate in complex agonist/antagonist schemes around the joints, so that, unless an equivalent isostatic model is derived from the topology, the individual determination of the muscle forces remains an indeterminate problem. Some methods have been developed towards its resolution and have been successfully applied for various simulations. This is presented in the following section.

3.2 Muscle Force Prediction

(The following review of optimization techniques (§ 3.2.1) is based on the one provided for CHARM at Instituto Superior Técnico by C. M. Matéus and G. Engel (CHARM D5–D10, Matéus 96, Engel 97))

3.2.1 Optimization Techniques

Given the complexity of the musculature, the determination of the individual muscle forces from the joint efforts is an indeterminate problem. The usual approach for solving such a problem is to perform an optimization analysis of the variables in excess involved in the problem. This approach, however, is limited because the obtained values are not exactly identified from the problem but rather estimated on the basis of a certain criterion. Talking about force *prediction* is therefore more appropriate than force *identification*.

The optimization approach assumes that at any instant during body motion the coordination of the involved muscles follows a rationale. An objective function is thus defined, which quantifies the rationale thought to be involved. A set of constraints must be added in order for the results to be physiologically acceptable. Values for the exerted forces at any instant can thus be obtained. The problem with optimization techniques is that the rationale by which the muscles act at any instant in the human body is not readily apparent. It is generally accepted as reasonable that the objective function used probably changes with the type of movement. However, it is still a research issue and also an object of controversy (CHARM D5).

There are two basic types of optimization techniques that may be applied to musculoskeletal systems: *static* optimization and *dynamic* optimization. Their presentation follows.

Static Optimization. Using static optimization, the muscle contraction is assumed to be a quasi-static phenomenon. Muscles are thus considered as instantaneously available actuators, whose force only depends on the current excitation signals, and the optimization can be independently performed at each instant of time. Linear optimization was first applied to muscle force prediction by Seireg and Arvikar (Seireg 73). This approach assumes that both the objective function and the model are linear. In this case, synergistic muscle activity may be considered only with the addition of interrelationships between the muscle forces or in assuming that some muscles are tetanized. For this reason, nonlinear optimization techniques appear more appropriate to the general prediction of muscle forces in complex musculoskeletal structures. Several criteria have been applied for this purpose. Among them, the following ones may be outlined (CHARM D5):

- the minimum sum of muscle stresses: $J = \sum_{i=1}^{n} \left(\frac{F_i}{A_i} \right)^p \quad p > 0$ (Crowninshield 81) (3.1)
- the minimum sum of muscle forces: $J = \sum_{i=1}^{n} \left(F_i \right)^p \quad p > 0$ (Seireg 89) (3.2)
- the minimization of muscle work: $J = \sum_{i=1}^{n} F_i \left| \Delta L_i \right|$ ΔL_i : *i*–th muscle elongation (3.3)

J: objective function F_i: *i*–th muscle force n: muscle number A_i: *i*–th muscle PCSA

Among these, the mostly used criterion is the muscle stress minimization for $p = 2$ or 3. A physiological basis was claimed by Crowninshield and Brand for this criterion for $p = 3$. (Crowninshield 81). Other criteria were used in specific analyses such as minimization of joint reaction forces or residual moments (Seireg 89), of metabolic energy consumption (Hard 78), of muscular fatigue (Hawkins 92), etc. Hybrid approaches, such as criterion combinations or combination with EMG measurements were also applied (Ringelberg 85) (CHARM D5).

Dynamic Optimization. As for static optimization, in the case of dynamic optimization, an optimization criterion is defined which can be minimized while accounting for the problem constraints. However, contrary to static optimization, dynamic optimization proposes to take into account the contraction dynamics of the muscles. In this case, the forces developed by the muscles are dependent not only on their present excitations, but also on their past excitations. For this reason, the objective functions generally take the form of an integral over time of the state and control variables. Among others, the following ones may be outlined (CHARM D5):

- the minimum jerk (acceleration derivative): $J = \frac{1}{2}\int_0^T \left(\frac{d^3\mathbf{x}}{dt^3}\right)^2 dt$ (Flash 85) (3.4)

- the minimum energy consumption $E(t)$: $J = \int_{t_0}^{t_f} [E(t)]dt$ (Davy 87) (3.5)

- the minimum tracking error: $J = \mathbf{z}(t_f)^T \cdot \mathbf{B} \cdot \mathbf{z}(t_f) + \int_{t_0}^{t_f} [\mathbf{z}(t)^T \cdot \mathbf{H} \cdot \mathbf{z}(t)]dt$ (Davy 87) (3.6)

  with: $\mathbf{z}(t) = \mathbf{x}(t) - \mathbf{x}^d(t)$ $\mathbf{z}(t)$: tracking error; $\mathbf{x}^d(t)$: desired trajectory

However, in order to achieve such analyses, the history of the muscle excitation signals over the period of interest, as well as a model of the muscle activation dynamics, must be provided. Several models have been developed for this purpose. These are presented in § 3.2.3.

3.2.2 Application Examples

Static Optimization. An analysis was presented by Karlsson et al. in which static optimization was applied to the prediction of muscle forces around the shoulder (Karlsson 92). The study was led using the musculoskeletal model developed by Högfors et al. and presented in § 3.1.3 (Högfors 87). The objective was to test if the model could be used to predict the internal forces acting on the humerus in different load situations. For this purpose, the sum of squared muscle stresses was considered as the criterion. The optimization problem consisted thus in minimizing:

$\min \sum \left(\frac{F_i}{A_i}\right)^2$ accounting for the constraints: $F_{imin} \le F_i \le F_{imax}$ with: $k = 0.7\ MNm^{-2}$ with: $F_{imax} = kA_i$ and: $F_{imin} = 0$ (3.7)

and the equilibrium equation: $\mathbf{AF} = -\mathbf{P}$ with: $\mathbf{A}$: constant matrix and: $\mathbf{F}$: vector of muscle forces; $\mathbf{P}$: vector of external load

In order to achieve this analysis, the evaluation of the *physiological cross-sectional area* (PCSA) A_i of each muscle considered was necessary. The PCSA corresponds to the area of the muscle cross-section actually sustaining the actuator tension. It is defined as the projection of the muscle cross-section on a plane perpendicular to the muscle force direction. This allows estimation of the force contributed by the muscle, accounting for its pennation angle. This practice is based on the assumption that the bigger a muscle is, the stronger it is (Winter 90).

However, except for muscles with strong pennation, the pennation angle is rarely taken into account and most PCSA are estimated with the following relation:

$$\text{PCSA} = S_0^M = \frac{V_0^M}{l_0^M} \qquad \text{with: } S_0^M,\ l_0^M,\ V_0^M \text{ the resting cross-sectional area, length, volume} \qquad (3.8)$$

Assuming then a constant material strength factor T^M, the maximum force F_{max}^M that the muscle can develop may be estimated using:

$$F_{max}^M = \text{PCSA} \times T^M \qquad \text{with} \qquad T^M = 0.4 - 1.0\ \text{MNm}^{-2} \qquad (3.9)$$

In the case of Karlsson's analysis, the material strength was taken as: $k = 0.7\ \text{MNm}^{-2}$.
The approach was applied to muscle force prediction for various loading situations (Fig. 3.6).

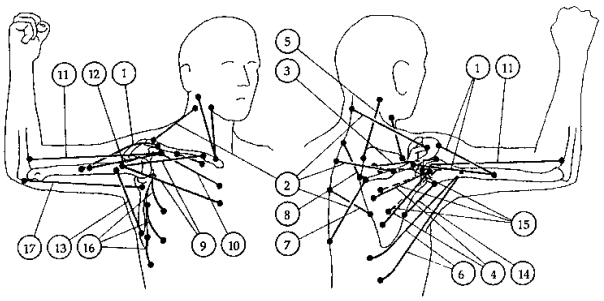

(1) deltoideus (three parts)
(2) trapezius (four parts)
(3) supraspinatus
(4) infraspinatus (two parts)
(5) levator scapulae
(6) latissimus dorsi (two parts)
(7) rhomboideus major
(8) rhomboideus minor
(9) pectoralis major (two parts)
(10) pectoralis minor
(11) biceps brachii (two parts)
(12) coracobrachialis
(13) teres major
(14) teres minor
(15) subscapularis (three parts)
(16) serratus anterior (three parts)
(17) triceps (part of)

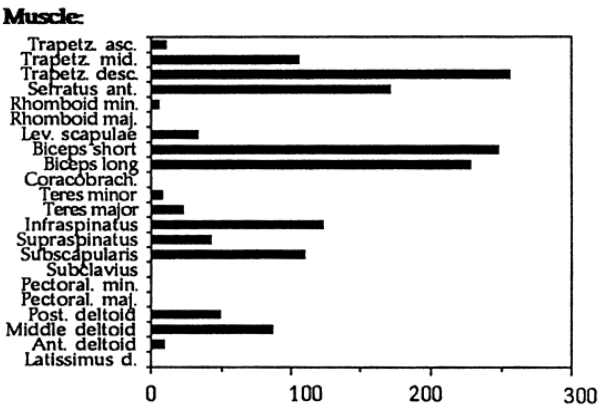

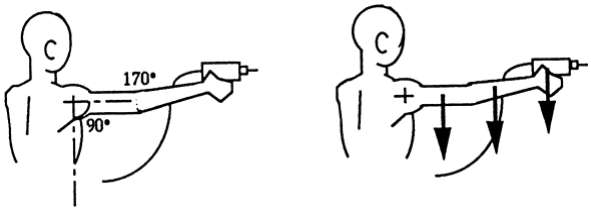

No	Muscle	Norm. CSA This study	Stand. dev.	CSA Veeger *et al.* (1991)
1	latissimus dorsi 1	2.620	0.090	8.64 (lat. dorsi)
2	latissimus dorsi 2	3.163	0.873	
3	pectoralis maj.-stern.	2.761	1.004	13.65 (pectoralis maj.)
4	pectoralis maj.-clav.	4.50	0.693	
5	deltoideus ant.	4.307	1.004	25.90 (deltoid)
6	deltoideus med.	5.653	1.921	
7	deltoideus post.	5.231	0.860	
8	coracobrachialis	1.918	0.411	2.51
9	infraspinatus 1	3.886	0.520	9.51 (infraspinatus)
10	infraspinatus 2	4.066	0.712	
11	subscapularis 1	3.143	0.661	13.51 (subscapularis)
12	subscapularis 2	2.831	0.949	
13	subscapularis 3	3.886	1.071	
14	supraspinatus	3.845	1.140	5.21
15	teres major	4.498	0.633	10.02
16	teres minor	1.898	0.202	2.92
17	biceps (long)	2.149	0.180	3.21
18	biceps (short)	1.898	0.620	3.08
19	triceps	8.906	1.647	6.84
24	trapezius 4	2.882	0.932	15.99 (trapezius)
25	trapezius 3	4.026	1.461	
26	trapezius 1	2.771	0.529	
27	trapezius 2	2.420	0.537	
28	levator scap.	1.918	1.211	2.82
29	rhomboid. maj.	2.319	0.509	6.27 (rhomboideus)
30	rhomboid. min.	1.145	0.384	
31	pectoralis min.	2.088	0.280	3.74
32	serratus ant. 1	3.032	0.589	13.93 (serratus ant.)
33	serratus ant. 2	2.560	0.972	
34	serratus ant. 3	4.167	0.825	
	Total	100		147.75

Fig. 3.6. Prediction of muscle forces around the shoulder during static loading (Karlsson 92)

Dynamic Optimization. Dynamic optimization was applied by Pandy et al. to analyse intermuscular control during maximum-height jumping (Pandy 90). The human lower limb was modeled as a four-segment, planar, articulated linkage using frictionless joints (Fig. 3.7). The mechanical behavior of muscle was described by a Hill-type contractile element, including both series and parallel elasticity (§ 3.3.1) (Hill 38). The optimal control problem was to maximize the height reached by the center of mass of the body, subject to body-segmental, musculotendon, and activation dynamics, a zero vertical ground reaction force at lift-off, and constraints which limit the magnitude of the incoming neural control signals to lie between zero (no excitation) and one (full excitation). The system dynamics were described using (Fig. .3.8):

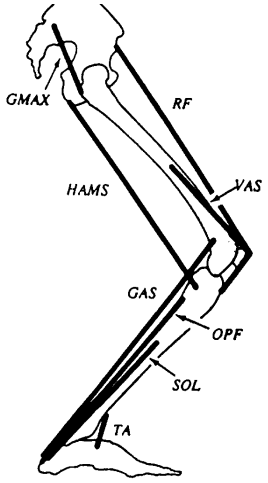

(Pandy 90)

Fig. 3.7. Pandy's model

$$\mathbf{A}(\boldsymbol{\theta})\ddot{\boldsymbol{\theta}} = \mathbf{B}(\boldsymbol{\theta})\dot{\boldsymbol{\theta}}^2 + \mathbf{C}(\boldsymbol{\theta}) + \mathbf{DM}(\boldsymbol{\theta})\mathbf{P}^T + \mathbf{T}(\boldsymbol{\theta},\dot{\boldsymbol{\theta}}) \qquad (3.10)$$

with:

$\boldsymbol{\theta}$, $\dot{\boldsymbol{\theta}}$, $\ddot{\boldsymbol{\theta}}$	vectors of limb angular displacement, velocity and acceleration
$\mathbf{T}(\boldsymbol{\theta},\dot{\boldsymbol{\theta}})$	vector of externally applied joint torques
$\mathbf{P}^T$	vector of musculotendon actuator forces $\mathbf{P}^T$
$\mathbf{A}(\boldsymbol{\theta})$, $\mathbf{M}(\boldsymbol{\theta})$	system mass and moment arm matrices
$\mathbf{C}(\boldsymbol{\theta})$	vector containing only gravitational terms
$\mathbf{B}(\boldsymbol{\theta})\dot{\boldsymbol{\theta}}^2$	vector describing both Coriolis and centrifugal effects
$\mathbf{D}$	matrix transforming joint torques into segmental torques

The contraction dynamics of the musculotendon actuators were expressed in the form:

$$\frac{dP^T}{dt} = f\left[P^T, l^{MT}, v^{MT}, a(t)\right] \qquad \text{with:} \qquad 0 < a(t) \le 1 \qquad (3.11)$$

and the optimization analysis was performed using the performance criterion: (3.12)

$$\max J = Y_c(t_f) + \frac{\dot{Y}_c^2(t_f)}{2g}$$

with:

g	gravitational acceleration constant
t_f	time instant at which lift-off occurs
$Y_c(t_f)$, $\dot{Y}_c(t_f)$:	center of mass position, velocity at t_f

Qualitative comparisons between the predictions and the reported findings indicated that the major features of a maximum-height squat jump were reproduced by the model (Pandy 90).

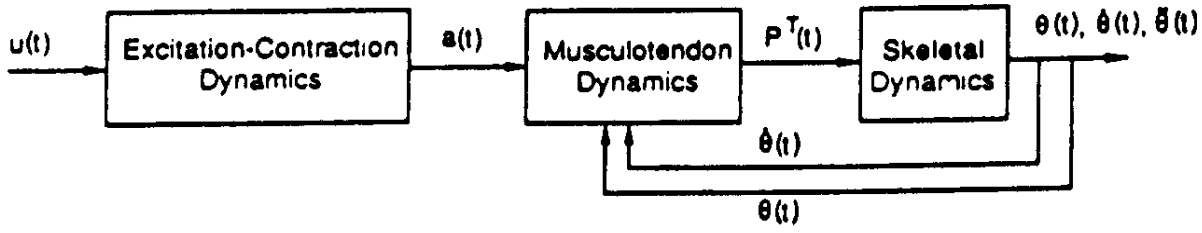

Fig. 3.8. Block diagram of the maximum height jump dynamic simulation (Pandy 90)

A similar analysis was led by Gonzalez et al. for the purpose of investigating the relationship among patterns of muscle excitation, individual muscle forces, and determining the effects of forearm and elbow position on the recruitment of individual muscles during a variety of ballistic movements (Gonzalez 96). The arm skeleton was composed of two segments, the arm and forearm, connected by revolute joints for flexion/extension and pronation/supination movements (Fig. 3.9).

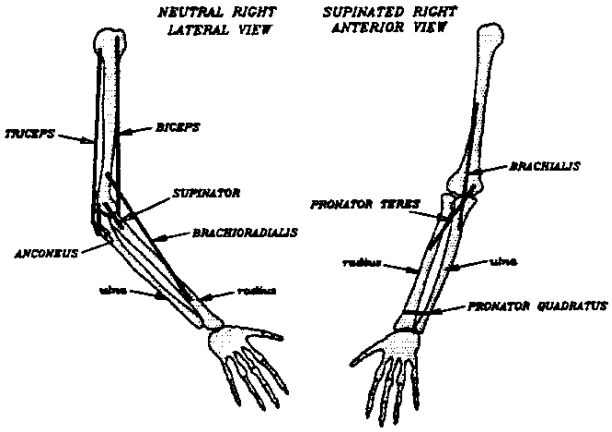

Fig 3.9. Gonzalez's arm model (Gonzalez 96)

As in Pandy's analysis, the musculoskeletal dynamics were expressed in the form:

$$\mathbf{A}(\mathbf{q})\ddot{\mathbf{q}} = \mathbf{B}(\mathbf{q})\dot{\mathbf{q}}^2 + \mathbf{C}(\mathbf{q}) + \mathbf{M}(\mathbf{q})\mathbf{F}^{MT} \tag{3.13}$$

with:	$\mathbf{q}$, $\dot{\mathbf{q}}$, $\ddot{\mathbf{q}}$	vectors of segmental displacement, velocity and acceleration
	$\mathbf{A}(\mathbf{q})$, $\mathbf{M}(\mathbf{q})$	system mass and moment arm matrices
	$\mathbf{B}(\mathbf{q})\dot{\mathbf{q}}^2$	vector describing both Coriolis and centrifugal effects
	$\mathbf{C}(\mathbf{q})$	vector containing only gravitational terms
	$\mathbf{F}^{MT}$	vector of the musculotendon force vector

and with actuator contractions dynamics described in the same form:

$$\dot{F}^{MT} = f\left[q, \dot{q}, F^{MT}, a(t)\right] \qquad \text{with:} \qquad 0 < a(t) \le 1 \tag{3.14}$$

By contrast, the criterion considered was the minimization of the performance time as:

$$\min J = \int_{t_0}^{t_f} dt \qquad \text{(Gonzalez 96)} \tag{3.15}$$

The experimental protocols consisted of various combinations of ballistic elbow flexion/extension and forearm pronation/supination movements. The model was partially verified using experimental kinematic, torque, and electromyographic data from volunteers. Predicted individual musculotendon forces for the eight actuators were analyzed to determine their contribution to the movements. Fig. 3.10 shows the block diagram of the simulation.

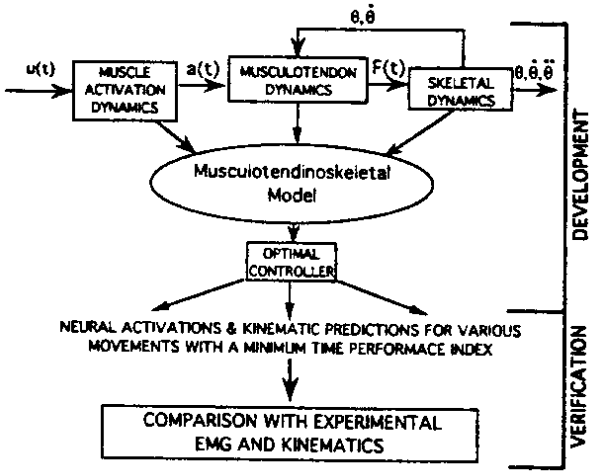

Fig. 3.10. Block diagram for optimal elbow flexion and forearm pronation (Gonzalez 96)

In both cases of static and dynamic optimizations, the contractile property of the musculotendon actuators must be taken into account. For static analysis, the concerned behavior may be limited to the force-length relationship of the actuator. For dynamic optimization, however, the contraction velocity and activation dynamics have also to be considered. Several models have been developed for this purpose. These are presented in the following section.

3.3 Musculotendon Actuators Modeling

3.3.1 Contraction Mechanics

Physiology. Skeletal muscles are composed of fascicles containing bundles of fibers, which are themselves composed of parallel bundles of *myofibrils*, the basic fibers of muscle. The *myofibril* consists of series of contractile units, named *sarcomeres*, composed of arrays of interdigitating *actin* and *myosin* myofilaments. These filaments constitute the basis for the sliding filament theory of muscle contraction (Huxley 57, 71, 74). The present understanding is that bulbous regions extending from the thick *myosin* filaments combine momentarily with the thin *actin* filaments, creating a shearing force between them, which tends to shorten the sarcomere. This connection is called *cross-bridge* (MacMahon 87). This architecture is shown in Fig. 3.11 (Winter 90).

Hill's Model. Long ago, Hill represented the muscle actuator as composed of three elements (Fig. 3.12): two elements arranged in series – one elastic element to account for the muscle elasticity in isometric conditions, and one contractile element, freely extendible at rest, but capable of shortening when activated – in parallel with one other elastic element to account for the elasticity of the muscle at rest (Hill 38). While it is recognized that the parallel element stands for the action of the intramuscular connective tissues surrounding the fibers, the series elastic element has mainly been attributed to the intrinsic elasticity of the cross-bridges.

Force-Length Relation. During isometric contraction (constant muscle length), the series elastic element lengthens slightly as the contractile element shortens. As the muscle lengthens, the parallel element is no longer loose and tension begins to grow in the non-linear fashion common to all soft tissues. The force-length characteristic of the muscle is a combination of the force-length characteristics of both active and passive components. Typical isometric active/passive force-length curves are drawn in Fig. 3.13 (Winter 90).

Force-Velocity Relation. The tension in a muscle also decreases as it shortens under load. The reasons for this appear to be the loss in tension as the cross-bridges in the contractile element break and then reform in a shortened condition, as well as the passive damping due to fluid viscosity in both the contractile element and the connective tissues (Winter 90). This phenomenon may be observed by measuring the velocity of shortening of a fully activated muscle submitted to constant loads. A force-velocity graph as shown in Fig. 3.14 may then be drawn to describe the mechanical power output that active muscle delivers (Zajac 89).

Activation. These interpretations concerning the force-velocity relationship are justified by the fact that the curve rate is affected by the activation rate. Besides, when the muscle is less than fully activated, the active force-length curve appears as a scaled version of the fully activated one, while the passive relationship is, of course, not affected (Winter 90).

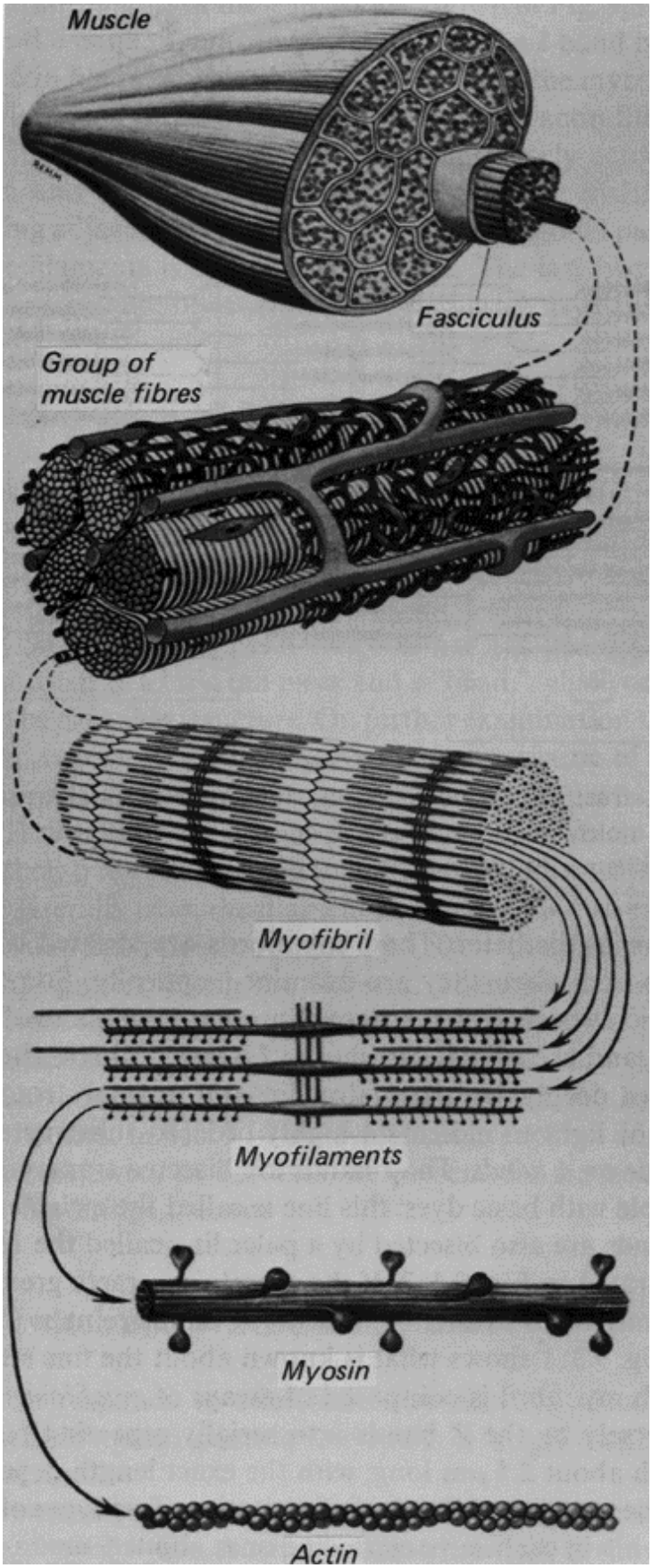

Fig. 3.11. Muscle structure (Warwick 73)

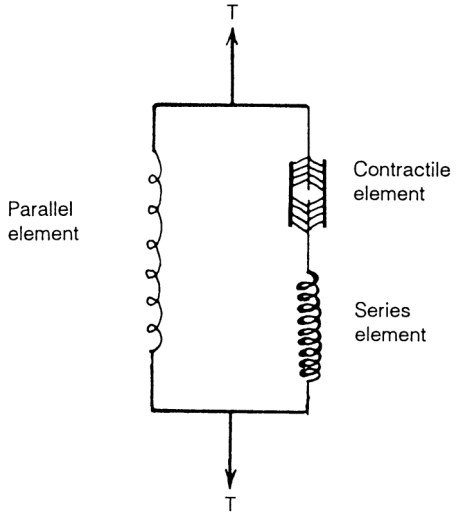

(Fung 93b)

Fig. 3.12. Hill's three element model

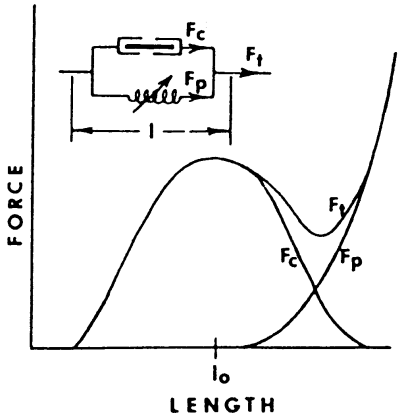

(Winter 90)

Fig. 3.13. Force-length relationships

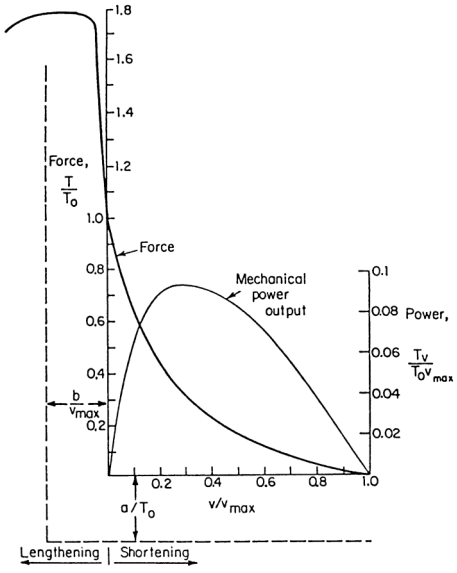

(Winter 90)

Fig. 3.14. Force-velocity relationship

Excitation. The contraction process is controlled neurologically. The smallest sub-unit that can be controlled is called a *motor unit* because it is innervated separately by a motor neuron. Each motor neuron may innervate many muscle fibers, though not all muscle fibers are excited at the same time, and the total contraction force of a muscle depends on how many fibers are stimulated. The muscle activation appears thus as an intermediate variable integrating the sequence of neural discharges and describing the level of contraction of the muscle (Fig. 3.15). An increase of tension can therefore be accomplished either by an increase in the stimulation rate for that motor unit or by the recruitment of an additional motor unit. The recruitment of motor units is accomplished according to the size principle, which states that the smaller units are recruited before the larger ones. Conversely, tension is reduced by releasing the motor units from the larger to the smaller ones (Winter 90).

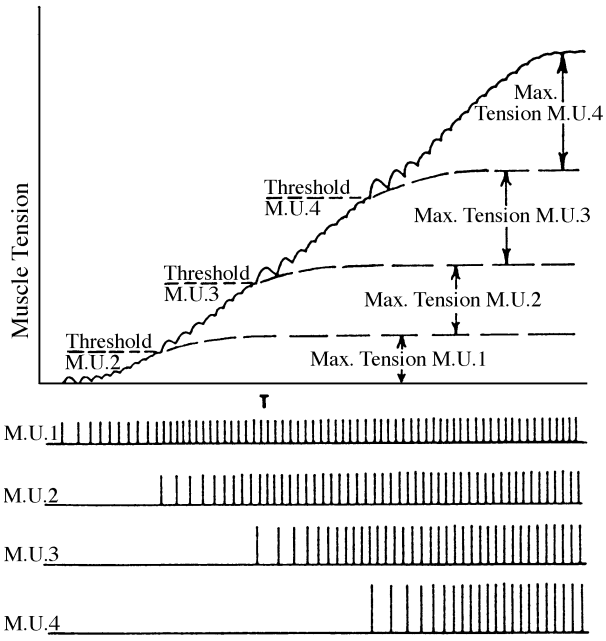

Fig. 3.15. Recruitment of motor units (M.U.)

As a result, the contraction dynamics of a skeletal muscle may be fully described in the form of Three-Dimensional surfaces representing the muscle output force as a function of its length, velocity, and activation level, complemented with a graph featuring the temporal evolution of its activation. Some models developed in this direction are presented in the following section.

3.3.2 Actuator models

Most investigations on muscle contraction modeling have been focussed on the force-length relationship. Otten's model may be shown as the main one (Otten 87). In his analysis, the force-length curve was fitted with the relation:

$$F = e^{-\left[\frac{(\varepsilon+1)^{\beta}-1}{w}\right]^{\rho}}$$ where: F is the normalized active force of a muscle actuator, ε is the muscle strain, β, ρ, w are the skewness, the roundness, the width factors (3.16)

The model was extended to muscles composed of several spindles by Baratta and Solomonow

$$F = \sum_{j} K_j \, e^{-\left[\frac{(\varepsilon+1)^{\beta_j}-1}{w}\right]^{\rho_j}}$$ with K_j relative contribution of each action line j to F (Baratta 93) (3.17)

An improvement of this relation was then proposed by Kaufman et al. to account for muscle pennation with an index of muscle fiber architecture i_a (Kaufman 89). This index of architecture was defined as the ratio of the mean fiber length to the muscle optimum length (Fig. 3.16), and incorporated in Otten's relation as:

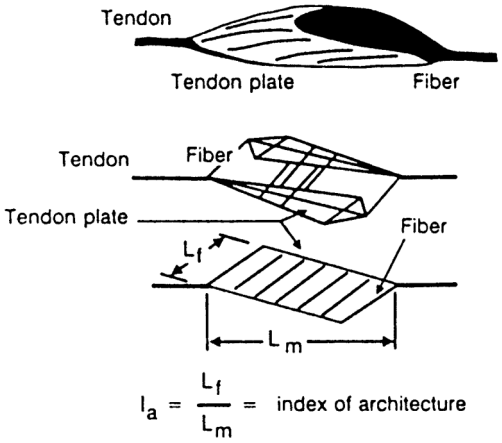

(Kaufman 89)

Fig. 3.16. Muscle architecture index

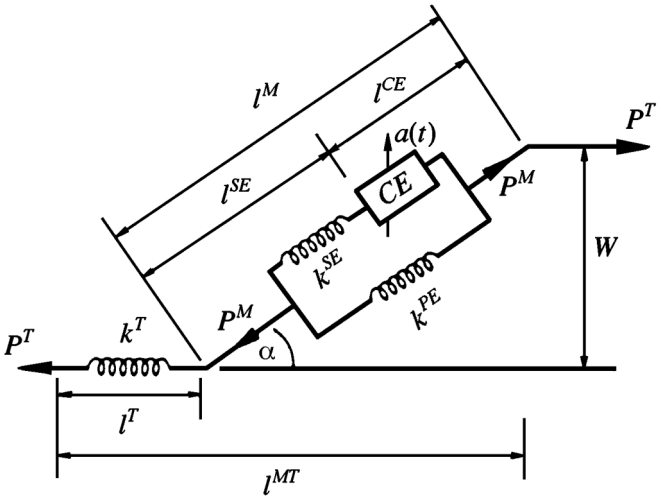

(Pandy 90)

Fig. 3.17. Zajac's musculotendon model

$$F = e^{-\left[\frac{(\varepsilon+1)^{\beta}-1}{w}\right]^{\rho}} \quad \text{with} \quad \begin{cases} \rho = 2 \\ \beta = 0.96343\left(1-\frac{1}{i_a}\right) \\ w = 0.35327\left(1-i_a\right) \end{cases} \quad \text{for} \quad i_a < 1 \qquad (3.18)$$

$$F = e^{-\left[2.727\times\ln(\varepsilon+1)\right]^2} \quad \text{for} \quad i_a = 1 \qquad (3.19)$$

This relation was applied to prediction of the muscle forces around the elbow (Kaufman 89).

Zajac et al. were the first to propose the complete modeling of the contraction dynamics accounting for the musculotendon architecture, the force-length and force-velocity relations, and the activation dynamics (Zajac 86, 89). In their analysis, the actuator was modeled as composed of a linear spring for tendon, in pennation with a Hill type model of muscle (see § 3.3.1): a series association of a contractile element and a non-linear spring, in parallel with another non-linear spring (Fig. 3.17). From the geometry and structure of the model, the relation describing the musculotendon actuator force-length-velocity relationship could be obtained in the form:

$$\frac{dP^T}{dt} = \frac{\left(k^{Ma}\cos\alpha\right)k^T}{\left(k^{Ma}\cos\alpha\right)+k^T}\left[v^{MT}-\left(\frac{k^{SE}}{k^{M\alpha}}\right)v^{CE}\right] \quad \text{with:} \quad \text{(Zajac 86)} \qquad (3.20)$$

$$k^M = k^{PE} + k^{SE} \quad \text{and:} \quad k^{Ma} = k^M\cos\alpha + \left(\frac{P^T}{l^M}\right)\tan^2\alpha \qquad (3.21)$$

with:

P^T	tendon tension
k^M, k^T	muscle and tendon stiffnesses
k^{PE}, k^{SE}	parallel and series elements stiffnesses
l^M, α	muscle length and pennation angle
v^{MT}, v^{CE}	musculotendon and contractile element velocities

In this model, some of the parameters need to be determined: k^M, k^{PE}, k^T, k^{SE} and v^{CE}.

The muscle stiffness k^M is determined by assuming the passive stiffness of the parallel element k^{PE} as being defined by the experimental force-length curves. The stiffnesses of the tendon k^T and of the serial spring element k^{SE} are assumed given by the equations:

$$k^T = \frac{1}{l_0^T}\left(\frac{P_0}{\varepsilon_0^T}\right) \qquad \text{and} \qquad k^{SE} = \frac{dP^{SE}}{dl^{SE}} = \frac{\left(100\, P^{SE} + 10\, P_0\right)}{l_0^M} \qquad \text{with:} \qquad P_0 = P_{fa}^{CE}\left(l_0^M\right) \tag{3.22}$$

the isometric contraction force of the fully activated muscle at optimal length l_0^M (Pandy 90). The last unknown in the model is v^{CE}, the velocity of shortening of the contractile element. Assuming first, the uncoupled contraction and activation mechanisms, Zajac expressed the effective isometric contraction force P_{iso}^{CE} as the experimental isometric contraction force of the fully activated muscle $P_{fa}^{CE}\left(l^M\right)$, scaled by its effective activation rate $a(t)$, giving:

$$P_{iso}^{CE} = a(t)\, P_{fa}^{CE}\left(l^M\right) \tag{3.23}$$

Zajac further investigated the muscle activation dynamics and provided a first order differential equation relating the activation rate $a(t)$ of the muscular contraction to the neural excitation signal $u(t)$ of the muscle as (Zajac 89):

$$\frac{da(t)}{dt} + \left[\frac{1}{\tau_{rise}}\left[\beta + \left[1-\beta\right]u(t)\right]\right] a(t) = \frac{1}{\tau_{rise}}\, u(t) \qquad \beta,\ \tau_{rise},\ \tau_{fall} \text{ constants} \quad \left(\tau_{fall} = \frac{\beta}{\tau_{rise}}\right) \tag{3.24}$$

In practice, considering the excitation as an on-off signal leads to reduce (3.24) to:

$$\frac{da(t)}{dt} = \frac{1}{\tau_{rise}}(1-a) \quad \text{for} \quad u(t) = 1 \qquad\qquad \frac{da(t)}{dt} = \frac{1}{\tau_{fall}}\left(a_{min} - a\right) \quad \text{for} \quad u(t) = 0 \tag{3.25}$$

in which a_{min} is a lower bound on muscle activation allowing the inversion of the force-velocity relationship as shown in (3.27). Further assuming uncoupled isometric force-length and force-velocity relationships, Zajac suggested normalizing the isometric contraction force P_{iso}^{CE} for scaling the force-velocity curve, in order to express the effective contraction force as:

$$P^{CE} = \left[\frac{P_{iso}^{CE}\left(l^M, a(t)\right)}{P_0}\right] P^{CE}\left(v^{CE}\right) \tag{3.26}$$

As a result of this development, the muscle contraction force P^{CE} appears as a function of the length l^M of the muscle, the velocity of shortening v^{CE} and the activation $a(t)$ of the contractile element. It is therefore possible to consider the inverse relation and express the velocity of shortening v^{CE} of the contractile element as a function of the musculo-tendon tension P^T, length l^{MT} and activation $a(t)$, as:

$$v^{CE} = v^{CE}\left[P^T, l^{MT}, a(t)\right] \tag{3.27}$$

Referring back to (3.20), the dynamics of the musculo-tendon actuator reduces finally to a function of its tension P^T, length l^{MT}, velocity v^{MT}, activation $a(t)$ as:

$$\frac{dP^T}{dt} = f\left[P^T, l^{MT}, v^{MT}, a(t)\right] \tag{3.28}$$

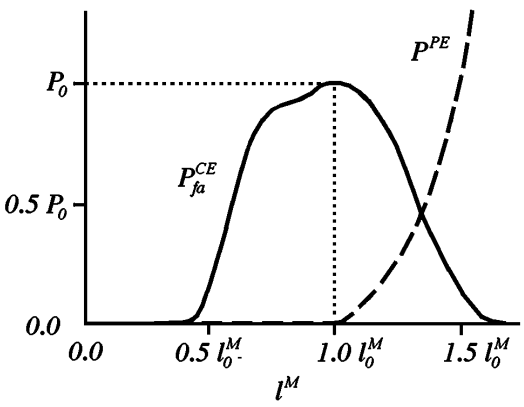

Fig. 3.18. Force-length curves (Pandy 90)

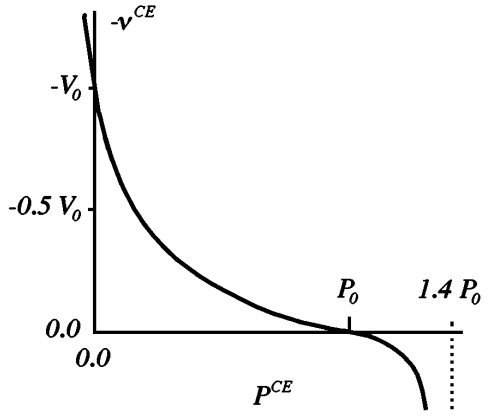

Fig. 3.19. Force-velocity curve (Pandy 90)

The corresponding set of required parameters are:

P_0: the peak isometric active contraction force $P_0 = P^{CE}_{fa}\left(l^M_0\right)$
l^M_0: the muscle length at which P_0 may be developed
l^T_0: the tendon slack length
ε^T_0: the tendon strain for $P^T = P_0$
α_0: the pennation angle for $l^M = l^M_0$

with the experimental isometric force-length and force-velocity curves (Fig. 3.18 – 3.19).

As the most complete musculotendon contraction dynamics model, Zajac's model has been used by many authors to perform optimization analyses on various musculoskeletal systems. This is actually the case of Pandy's and Gonzalez's analyses presented in § 3.2.2 (Pandy 90, Gonzalez 96). Fig. 3.20 illustrates the parameters used, the joint rotations and the excitation/contraction force histories of four muscles during maximum height jumping.

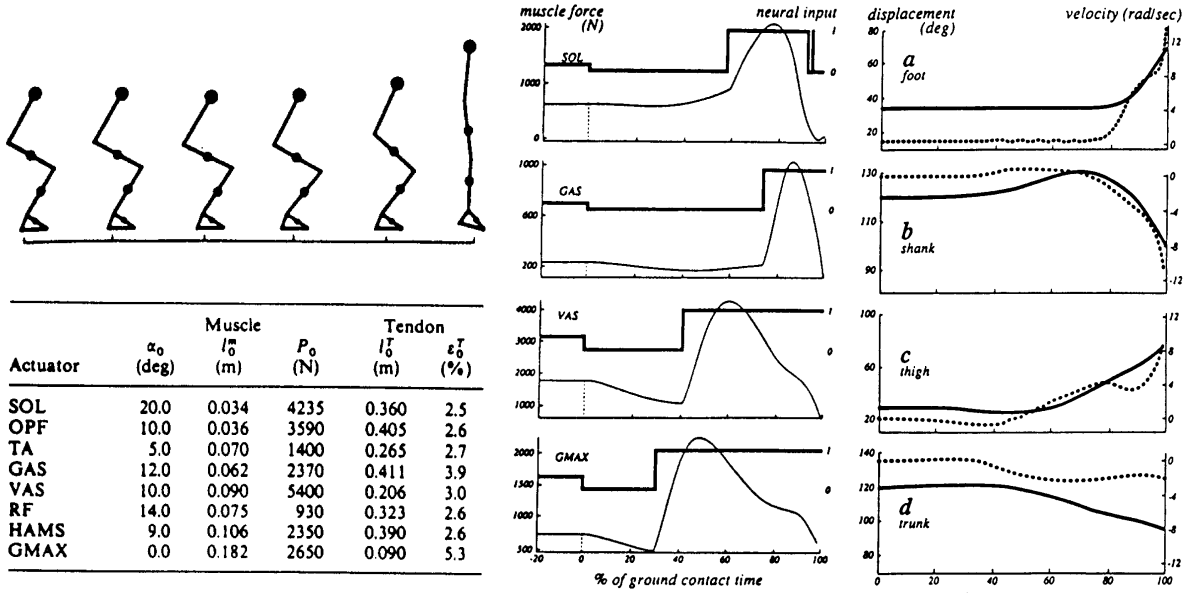

Actuator	α_0 (deg)	Muscle l^m_0 (m)	P_0 (N)	Tendon l^T_0 (m)	ε^T_0 (%)
SOL	20.0	0.034	4235	0.360	2.5
OPF	10.0	0.036	3590	0.405	2.6
TA	5.0	0.070	1400	0.265	2.7
GAS	12.0	0.062	2370	0.411	3.9
VAS	10.0	0.090	5400	0.206	3.0
RF	14.0	0.075	930	0.323	2.6
HAMS	9.0	0.106	2350	0.390	2.6
GMAX	0.0	0.182	2650	0.090	5.3

Fig. 3.20. Parameters and time histories for muscle actuators and limb segments (Pandy 90).

3.4 Model Development and Suggestions

3.4.1 CHARM Model

On the basis of these studies, I engaged on the modeling of the muscle actions on the upper limb skeleton. Ignoring the muscles involved in the motion of the hand and fingers, I have considered the 22 following muscles (Maurel 96):

anconeus	infraspinatus	rhomboids	trapezius
biceps brachii	latissimus dorsi	serratus anterior	teres major
brachialis	levator scapulae	subclavius	teres minor
brachioradialis	pectoralis major	long supinator	triceps brachii
coracobrachialis	pectoralis minor	subscapularis	
deltoideus	pronator teres	supraspinatus	

Though the number of muscles I considered is close to that of Högfors's model (Högfors 87, Karlsson 92), our respective models are not to be confused. Högfors et al. only considered the muscles controlling the human shoulder movements, whereas I also had to take into account the muscles controlling the forearm movements. I have thus considered four other muscles, the *anconeus*, the *brachioradialis*, the *pronator teres*, and the *long supinator*, which control the forearm pronation/supination movements. Besides, on the advice of Dr. P. Hoffmeyer of the Clinique Orthopédique of Geneva, I have neglected the actions of the *omohyoid*, *sternocleidomastoid* and *sternohyoid* muscles that Högfors et al. had considered.

For modeling muscle actions, the best choice, in terms of accuracy, would have been to rely on van der Helm's and Veenbaas's analysis, and model broad muscles following their results (Helm 91). However, this choice would have been inappropriate with respect to the objectives of the CHARM project of simulating human motion including soft tissue deformations. The complexity of their model could have compromised the feasibility of the following analyses, especially the finite element simulation of the corresponding muscle contractions.

I have therefore chosen to compromise between accuracy and simplicity and decided to apply muscle subdivisions based on anatomical considerations only (Maurel 96). All muscles have been modeled as single polylines, except the *biceps* and *triceps brachii*, the *pectoralis major*, the *deltoideus*, the *trapezius*, the *latissimus dorsi*, the *rhomboids* and the *serratus anterior*, which have been modeled using several polylines, as described below, in a way similar to the models proposed by Högfors et al. and Wood et al. (Högfors 87, Wood 89). That is:

- *Latissimus dorsi*: the latissimus dorsi may be modeled by mean of three polylines: one from the outer surface of the lower four ribs, one from the spine of the sacrum and the posterior part of the iliac crest, and one from the lower six thoracic and lumbar vertebras. All three lines wrap around the thorax and insert into the bottom of the intertubercular groove of the humerus.

- *trapezius*: similarly, the trapezius muscle may be modeled with three polylines: one from the medial third of the nuchal line to the AC joint, and two from the medial and inferior thoracic vertebras to the scapula along its spine.

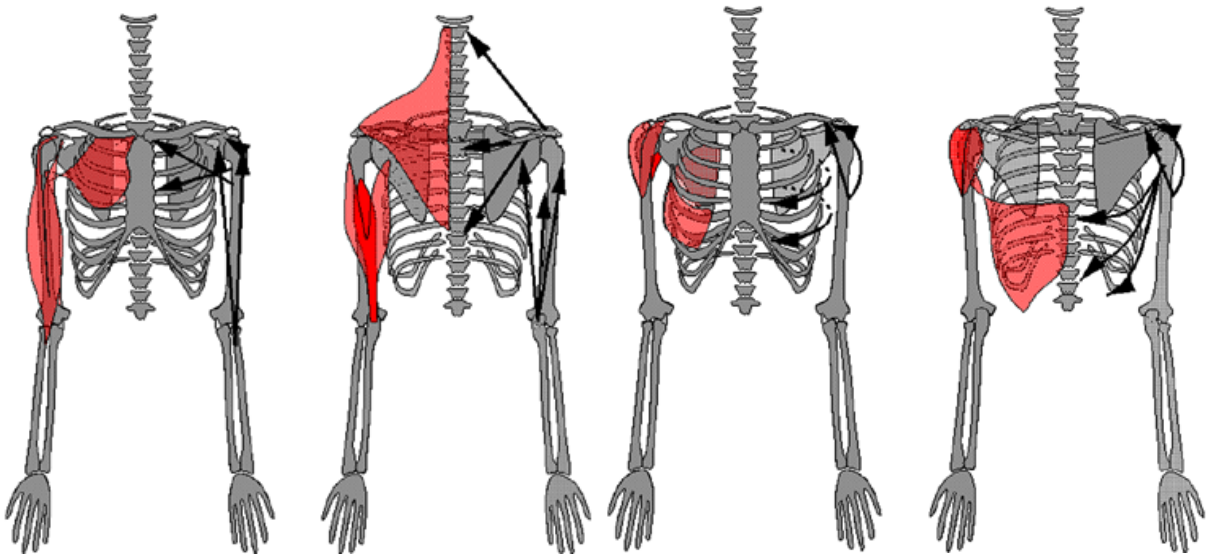

a) *pectoralis major, biceps* (front), *trapezius* and *triceps brachii* (back)

b) *serratus anterior* (front), *latissimus dorsi* (back) and *deltoideus* (both views)

Fig. 3.21. Topological models for some broad complex muscles (Maurel 99)

- *deltoideus*: the three heads of the deltoideus may be modeled by three polylines: the anterior one from the lateral third of the clavicle, the lateral one from the lateral margin of the acromion of the scapula, and the posterior one from the spine of the scapula. All three wrap around the humerus to insert into its deltoid tuberosity.

- *triceps brachii*: the three heads of the triceps brachii may be modeled by three straight lines: the long head from the infraglenoid tubercle of the scapula, the medial head and lateral head from the posterior surface of the humerus respectively below and above the radial groove. All three insert into the olecranon process of the ulna.

- *serratus anterior*: the serratus anterior may be modeled with two polylines wrapping backwards around the thorax from the eigth upper frontal ribs to the medial border of the scapula.

- *pectoralis major*: the pectoralis major is modeled with two straight lines: one from the clavicle, close to the anterior surface of the sternum, and one from the costal cartilages of the upper seven ribs. Both insert into the intertubercular groove of the humerus.

- *biceps brachii*: the biceps brachii may be modeled with two lines: a straight one from the coracoid process of the scapula, and a segmented one from the supraglenoid tubercle on the scapula and following the intertubercular groove of the humerus. Both insert into the radial tuberosity.

Fig. 3.21 illustrates the anatomy and modeling of these muscles in particular. The complete anatomical, biomechanical and topological description for each concerned muscle may be found in Appendix B (Maurel 96). Finally, the interactive editing of the topological model on the 3-D human upper limb model using the topological modeler is presented in Chapter 5.

3.4.2 Suggestions for Muscle Force Prediction

The determination of the muscle forces had been planned in CHARM as a necessary basis for simulating the muscle contractions. In this context, no specific constraint on the result or the analysis was defined.

Therefore, my suggestion was for CHARM to begin by following Karlsson's approach (Karlsson 92) and performing static optimization to the upper limb musculoskeletal structure using for criterion the minimum sum of the squared muscle stresses (§ 3.2.2):

$$\min \sum \left(\frac{F_i}{A_i} \right)^2 \quad \text{accounting for the constraints:} \quad \begin{matrix} F_{imin} \le F_i \le F_{imax} \\ F_{imax} = kA_i \end{matrix} \quad \text{with:} \quad \begin{matrix} k = 0.7\ MNm^{-2} \\ F_{imin} = 0\ N \end{matrix} \tag{3.29}$$

and the equilibrium equation: $\mathbf{AF} = -\mathbf{P}$ with: $\mathbf{F}$: vector of muscle forces, $\mathbf{A}$: constant matrix and: $\mathbf{P}$: vector of external load

Consequently, I have investigated the biomechanical literature in order to collect PCSA data as required for such an analysis. The PCSA values I have proposed are gathered in Table 3.1. They are based on data provided by Veeger et al. (Veeger 91) and Crowninshield and Brand (Crowninshield 81)

Since it is simpler, Otten's model could be applied at the first stage, so as to develop and test the optimization procedures (Otten 87). As a second stage, the analysis could be improved by performing dynamic optimization following Pandy et al. and Gonzalez et al. by using Zajac's model to fully take into account the contraction dynamics of the action line actuators of the upper limb model (§ 3.3.2) (Zajac 86, 89, Pandy 90, Gonzalez 96,). However, with lack of data for the upper limb muscles, no further suggestion/provision was made in this direction.

Table 3.1 PCSA values for the action lines of the CHARM model (Veeger 91)

Action line	PCSA (cm^2)	Action line	PCSA (cm^2)
Anconeus	2.50	Pronator teres	2.00
Biceps long head	3.21	Rhomboids lower head	3.14
Biceps short head	3.08	Rhomboids upper head	3.14
Brachialis	8.40	Serratus anterior lower head	7.00
Brachioradialis	4.70	Serratus anterior upper head	7.00
Coracobrachialis	2.51	Subclavius	2.00
Deltoideus anterior head	8.63	Subscapularis	13.51
Deltoideus lateral head	8.63	Supinator	3.00
Deltoideus posterior head	8.63	Supraspinatus	5.21
Infraspinatus	9.51	Teres major	10.20
Latissimus Dorsi lateral head	2.83	Teres minor	2.92
Latissimus Dorsi lower head	2.83	Trapezius lower head	5.30
Latissimus Dorsi upper head	2.83	Trapezius medial head	5.30
Levator scapulae	2.82	Trapezius upper head	5.30
Pectoralis Major lower head	6.80	Triceps brachii lateral head	2.30
Pectoralis Major upper head	6.80	Triceps brachii long head	2.30
Pectoralis minor	3.74	Triceps brachii short head	2.30

Conclusion

To fully explore the large mobility of the human upper limb described in § 2.1.2, 22 muscles at least are required. The actions of most of them may be easily modeled with straight action-lines. However, the upper limb also compounds several broad muscles, such as the *trapezius* and *latissimus dorsi* muscles, as well as muscles composed of several independent spindles, like the *deltoideus* and the *biceps* and *triceps brachii*. Thus, in order to properly model the upper limb muscular topology, no less than 34 action-lines are necessary. However, given the complexity of the musculature, the determination of the muscle force contributions is an indeterminate problem. The only possible way is to perform static or dynamic analyses accounting for muscle topology and actuator models in order to predict their values. The contraction dynamics of the muscle actuators also need to be modeled. Skeletal muscles are composed of bundles of contractile fibers. The basic contractile units along these fibers are called *sarcomeres* and are composed of sliding filaments which may combine under the electric control of the motor neurons. The muscle force appears thus to be a combination of passive and active mechanical properties. Several actuator models have been developed to account for these properties during musculoskeletal simulations. Zajac's model is probably the most complete one. The use of dynamic optimization techniques with such an elaborate model may currently be the most accurate approach for simulating the coordination of muscle force generation during motion. The predicted muscle forces may then be used as basis for muscle and soft tissue deformation simulation. Investigations in this direction are presented in the following chapter.

4 Soft Tissue Modeling

At this stage of the analysis, the 3-D displacement of the muscle attachements sites and the evolution of the muscle forces in the action-line is assumed available. The problem, now raised, is the generation of the corresponding soft tissue deformations, especially for musculotendons and skin. Soft tissues are clearly *quasi-incompressible, non-homogeneous, non-isotropic, non-linear viscoelastic materials* in *large deformation*. The general procedure consists of describing the evolution of the continuous medium using the continuum mechanics theory, approximating its geometry to a set of discrete finite elements, and simulating its evolution using incremental/iterative procedures. In this approach, the mechanical properties of the material must be provided in the form of a stress-strain constitutive relationship. Various such biomechanical relationships have been proposed for soft tissue modeling. Some are reported here for purpose of illustrating their form and diversity. Suggestions are then made for tendon, muscle and skin modeling using the finite element method.

4.1 Deformation Simulation

4.1.1 General Approach

In computer animation, physically-based modeling is commonly applied to simulate natural phenomenon. It combines physics and engineering disciplines with geometric modeling in order to produce realistic-looking behaviors. The general procedure is summarized by the pipeline shown in Fig. 4.1. The continuous physical problem may be described by a set of relations valid over finite continuous geometric domains and time intervals. In the general case, due to the geometrical and physical non-linearities involved in the problem, there is no solution method that allows carry out an analytic solution defining the system behavior as a continuous function of time. Therefore, geometric discretization methods such as the *finite element* method are first applied to approximate the continuous problem by a finite discrete system of equations in terms of the mesh nodes. Then, incremental/iterative methods are applied to linearize the equations over time intervals and achieve their temporal integration, so as to generate the incremental simulation of the phenomenon. The different stages of this pipeline are developed in the following.

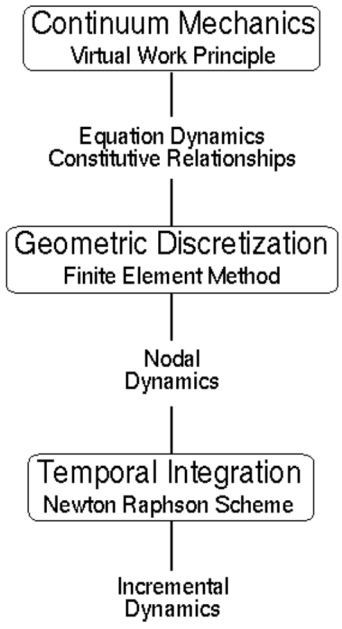

Fig. 4.1. Simulation pipeline

Continuum Mechanics. The main considerations involved in a mechanical problem are those of action and motion. In particular, the mechanical state of a continuous medium may be described in terms of stress and strain. The stress measures the internal tension in the material whereas the strain measures its local deformation. The dynamics of the medium may thus be fully described with an equation of motion relating these state variables to those representing the involved actions. The general form of this equation is given by the *Virtual Work* principle:

$$\delta\hat{W}^{acc} = \delta\hat{W}^{int} + \delta\hat{W}^{ext} \quad \text{(see Appendix C.1)} \qquad \text{with:} \quad \begin{array}{ll} \delta\hat{W}^{acc} & \text{virtual work due to the acceleration} \\ \delta\hat{W}^{int} & \text{virtual work due to the internal stresses} \\ \delta\hat{W}^{ext} & \text{virtual work due to the external actions} \end{array} \qquad (4.1)$$

Roughly speaking, this principle states that the acceleration energy exhibited by a continuous medium during its motion/deformation, results from the imbalance between its internal energy and the energy contributed by the external actions applied to it (Lemaitre 90).

In the general case, the continuous medium is likely to undergo large deformations: this introduces *geometric non-linearities* in the description of the phenomenon. Consequently, distinct formalizations must be considered depending on whether it is developed in terms of state variables referring to the current deformed *Eulerian* configuration or in terms of state variables referring to the reference undeformed *Lagrangian* configuration (Fig. 4.2) (Ogden 84).

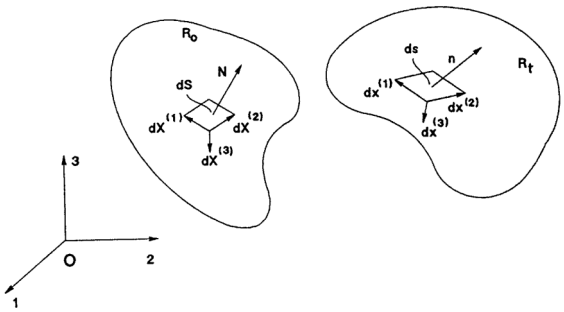

(Mal 91)

Fig. 4.2. Eulerian/Lagrangian configurations

With respect to the Eulerian configuration, the state variables to be considered are the *Cauchy* stress $\boldsymbol{\sigma}$ and the *Euler-Almansi* strain $\mathbf{e}$. With respect to the *Lagrangian* configuration, they are the *Piola-Kirchhoff* second stress $\mathbf{S}$ and the *Green-Lagrange* strain $\mathbf{E}$ (Fig. 4.3). These variables are all *second-order symmetric* tensors, which provide, in any case, measures of the same states of tension and deformation of the continuous medium, but with respect to different bases. When the deformation is small, the *Eulerian* and *Lagrangian* configurations are close, so that the stress and strain tensors of both configurations may no longer be distinguished: $\mathbf{E} \approx \mathbf{e} \approx \boldsymbol{\epsilon}$, $\mathbf{S} \approx \mathbf{T} \approx \boldsymbol{\sigma}$.

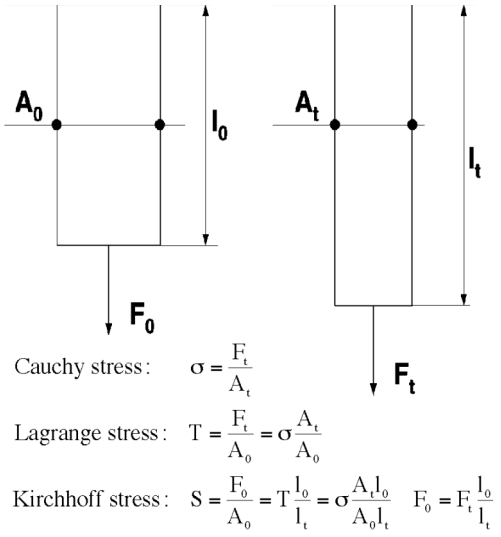

(Maurel 98)

Fig. 4.3. Relation between stresses

In any case, in order to determine the state of the system resulting from the applied actions, the obtained equation must be solved. However, as both state variables appear to be involved, this is not possible unless a supplementary equation relating stress and strain to each other is considered: the *constitutive relationship*. It is this relation that provides to the model the description of the specific material properties of the continuous medium. A reminder of the basic definitions for *elasticity* and *viscoelasticity* may be found in Appendix C.2.

Geometric Discretization. In principle, using the constitutive relationship of the material, the *Virtual Work* equation (4.1) may be solved for the stress or the strain, in order to determine the evolution of the continuous medium under the external actions applied to it. However, in practice, a general solution valid for any point of the continuous medium can be extracted only in singular cases, and not for arbitrary deformations. In such a case, solutions may be derived for a finite set of sample points only. Geometric discretization of the continuous medium is thus necessary, so as to approximate the solution of the general continuous problem to that of a finite number of equations defined for the mesh nodes.

Various discretization methods may be applied for this purpose. All, however, derive from the *finite element* method (Zienkiewicz 89). The basic idea of this method is to subdivide the continuous domain into smaller elements of various shape and size. In general, the elements have simple geometric shapes such as segments for curves, triangles or quadrilaterals for surfaces, tetrahedrons or parallelepipeds for volumes (Fig. 4.4). Any point in the continuous medium may thus be expressed within an element by interpolation between its nodes. The general interpolation relation then takes the form:

$$\mathbf{X} = \mathbf{H}\,\mathbf{N} \qquad \mathbf{H} \text{ tensorial shape-function,} \qquad \mathbf{N} \text{ nodal coordinate vector} \qquad (4.2)$$

In particular, this may be used to derive relations in terms of the nodal displacement vector $\mathbf{U}$. Thus, in the case of a non-linear viscoelastic material with a constitutive relationship of the form $\mathbf{S}\left(\mathbf{E}, \dot{\mathbf{E}}\right)$, the Virtual Work tensorial equation may be developed into the general form:

$$\mathbf{M}\,\ddot{\mathbf{U}} + \mathbf{\Pi}\left(\mathbf{U}, \dot{\mathbf{U}}\right) = \mathbf{L} \qquad \text{with:} \qquad \text{(see Appendix C.1–C.2)}$$

$$\begin{aligned} \mathbf{M} &= \int_V \rho_0 \mathbf{H}^T \mathbf{H}\, dV && \text{nodal mass matrix} \\ \mathbf{\Pi}\left(\mathbf{U}, \dot{\mathbf{U}}\right) &= \int_V \boldsymbol{B}^T \boldsymbol{S}\left(\mathbf{U}, \dot{\mathbf{U}}\right) dV && \text{nodal internal force vector} \\ \mathbf{L} &= \int_V \mathbf{H}^{f^T} \mathbf{f}^V\, dV + \int_S \mathbf{H}^{t^T} \mathbf{t}^S \mathbf{N}\, dS && \text{nodal external force vector} \end{aligned} \qquad (4.3)$$

which, in particular for a linear viscoelastic *Kelvin–Voigt* material ($\mathbf{S} = \mathbf{K}^M \mathbf{E} + \mathbf{D}^M \dot{\mathbf{E}}$), becomes:

$$\mathbf{M}\ddot{\mathbf{U}} + \mathbf{D}\dot{\mathbf{U}} + \mathbf{K}\mathbf{U} = \mathbf{L} \qquad \text{with:}$$

$$\begin{aligned} \mathbf{D} &= \int_V \boldsymbol{B}^T \boldsymbol{D}^V \boldsymbol{B}\, dV && \text{nodal damping matrix} \\ \mathbf{K} &= \int_V \boldsymbol{B}^T \boldsymbol{K}^E \boldsymbol{B}\, dV && \text{nodal stiffness matrix} \end{aligned} \qquad (4.4)$$

As a result of this geometric discretization stage, the dynamic response of the mesh under the defined external nodal loads may be analyzed by solving the finite second-order differential system for the nodal displacements vector $\mathbf{U}$. This way, the solution of the continuous deformation problem is approximated to the solutions obtained for the nodes of the mesh which approximates the continuous domain.

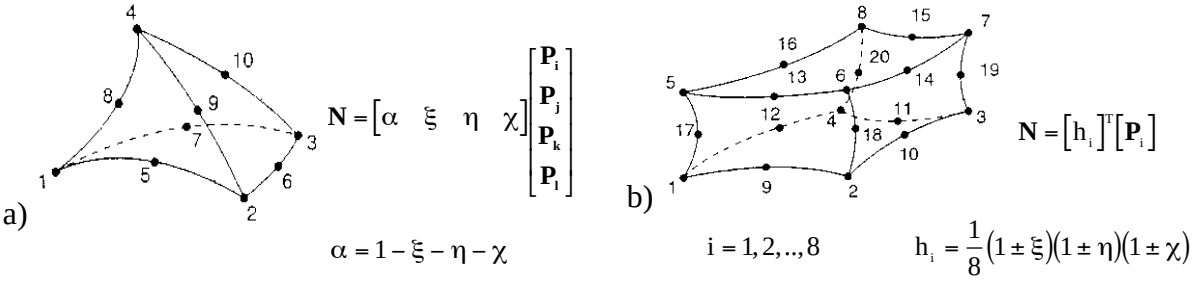

Fig. 4.4. 3D linear interpolation using: tetrahedrons (a), parallelepipeds (b) (Ansys Manual)

Temporal Integration. Though geometric discretization has led to geometric linearization of the problem, there, however, remain physical non-linearities, due in particular to the non-linear physical properties of the material. Due to a lack of resolution methods, still no solution can be carried out directly from the discrete equation of motion, and the solution can only be approximated step-by-step by means of incremental/iterative methods. It is therefore necessary to convert the time-continuous equation of motion and constitutive relation into incremental forms, so that within each time interval the problem may be handled as linear.

In practice, the *Updated Lagrangian* approach, which refers the state variables to the recently computed configuration and updates them after each step, has proved to be the more general and computationally efficient (Fig. 4.5). The other approches are the *Total Lagrangian* approach, referring to the initial configuration, or the *Eulerian* approach, referring to the current configuration, which is usually the unknown (Argyris 80). As a result of the incremental formulations, the time-continuous problem is replaced by a finite system of tensorial equations, linear within each respective interval, of the form (Kleiber 89):

$$\mathbf{M}_n \Delta\ddot{\mathbf{U}} + \mathbf{D}_n \Delta\dot{\mathbf{U}} + \mathbf{K}_n \Delta\mathbf{U} = \Delta\mathbf{L} \qquad \text{over } [t_n, t_{n+1}] \qquad \text{i.e.:} \qquad (4.5)$$

$$\mathbf{M}_n \ddot{\mathbf{U}}_{n+1} + \mathbf{D}_n \dot{\mathbf{U}}_{n+1} + \mathbf{K}_n \Delta\mathbf{U} = \mathbf{L}_{n+1} - \mathbf{R}_n \qquad \text{where:} \qquad \mathbf{R}_n = \mathbf{L}_n - \mathbf{M}_n \ddot{\mathbf{U}}_n + \mathbf{D}_n \dot{\mathbf{U}}_n$$

with

$\Delta\mathbf{U} = \mathbf{U}_{n+1} - \mathbf{U}_n$	nodal displacement increment vector
$\Delta\mathbf{L} = \mathbf{L}_{n+1} - \mathbf{L}_n$	nodal external force increment vector
$\mathbf{R}_n$	nodal internal force vector
$\mathbf{M}_n,\ \mathbf{D}_n,\ \mathbf{K}_n$	tangent mass, damping, stiffness matrix

In this scheme, all components are assumed known up to step n, except $\Delta\mathbf{U}$ which is sought for updating to step n+1. Several incremental methods exist, which allow the incremental simulation of the system behavior. The main ones are presented in Appendix C.3.

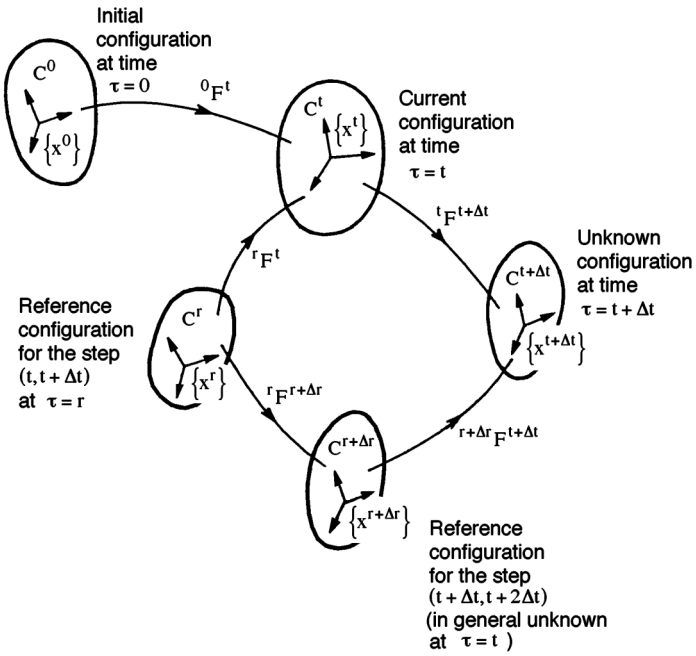

Fig. 4.5. Incremental description of the deformation process (Kleiber 89)

4.1.2 Former Applications

Finite Element Models. Various applications have made use of this general methodology for the simulation of soft tissue deformations in computer graphics. Several models for skin and muscle have been proposed following the linear finite element approach. Larrabee et al. applied the finite element method to simulate the effect of skin flap design. Skin was modeled as a linear elastic membrane with regularly spaced nodes, connected by linear springs to subcutaneous attachments (Larrabee 86). Gourret et al. applied the finite element method to grasping simulation including deformation of the grasped objects and of the skin of the fingers (Fig. 4.6) (Gourret 89). Essa et al. proposed the use of the linear finite element mode superposition method to simulate the objects deformations as linear combinations of their deformation modes (Fig. 4.7) (Essa 93). In this approach, they considered the body as a linear viscoelastic isotropic incompressible Kelvin-Voigt material:

$$\boldsymbol{\sigma} = \mathbf{K}^{E}\boldsymbol{\epsilon} + \mathbf{D}^{V}\dot{\boldsymbol{\epsilon}} \qquad \text{with: } \mathbf{K}^{E},\ \mathbf{D}^{V} \text{ constant matrix} \tag{4.6}$$

with as elastic component ($\mathbf{K}^{E}$), a linear elastic isotropic incompressible material defined by *Young* modulus E and *Poisson* coefficient ν, and a viscous component ($\mathbf{D}^{V}$) based on *Rayleigh damping* principle, which consists of choosing the global damping matrix $\mathbf{D}$ by combination of the mass and stiffness matrix $\mathbf{M}$ and $\mathbf{K}$. The discrete equation of motion was then obtained in the form:

$$\mathbf{M}\ddot{\mathbf{U}} + \mathbf{D}\dot{\mathbf{U}} + \mathbf{K}\mathbf{U} = \mathbf{L} \quad \text{with:} \quad \mathbf{D} = \alpha\mathbf{M} + \beta\mathbf{K} \quad \text{and: } \alpha,\ \beta, \text{ parameters controlling stability} \tag{4.7}$$

in which $\mathbf{M}$, $\mathbf{D}$, $\mathbf{K}$ are constant matrices obtained from finite element discretization of the system mechanical properties.

The equation of motion was then converted into the modal form:

$$\ddot{\mathbf{V}} + \boldsymbol{\Lambda}\dot{\mathbf{V}} + \boldsymbol{\Omega}^{2}\mathbf{V} = \tilde{\mathbf{L}} \quad \text{with:} \quad \boldsymbol{\Psi}\text{: modal transfer matrix composed with the eigenvectors} \tag{4.8}$$

$$\tilde{\mathbf{M}} = \boldsymbol{\Psi}^{T}\mathbf{M}\boldsymbol{\Psi} \equiv \mathbf{I} \qquad \tilde{\mathbf{D}} = \boldsymbol{\Psi}^{T}\mathbf{D}\boldsymbol{\Psi} = \boldsymbol{\Lambda} \qquad \tilde{\mathbf{K}} = \boldsymbol{\Psi}^{T}\mathbf{K}\boldsymbol{\Psi} = \boldsymbol{\Omega}^{2} \qquad \tilde{\mathbf{L}} = \boldsymbol{\Psi}^{T}\mathbf{L}$$

which was solved using common algorithms for linear algebraic systems (Essa 93).

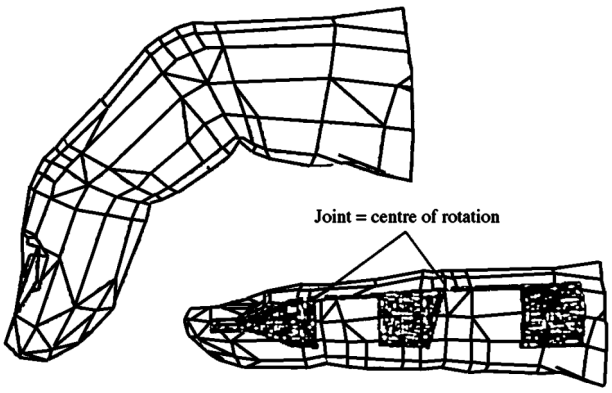

Fig. 4.6. Finite element model of finger (Gourret 89)

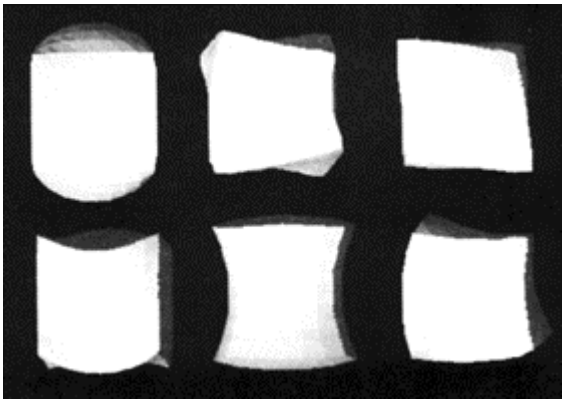

Fig. 4.7. Deformation modes of a 27-node finite element cube (Essa 93)

Following this approach, Chen et al. developed a linear finite element model of skeletal muscle for computer animation, including a contraction process based on Zajac's muscle force model. For simplification, the finite element analysis was performed on a prismatic bounding box embedding the muscle object, and the resulting deformations were mapped onto the muscle using the free-form deformation principle (FFD) introduced by Sederberg and Parry (Sederberg 86). Assuming the contraction forces greater than the passive response in the physiological range of functioning, Chen et al. neglected the passive non-linearities, and considered muscle as a homogeneous, incompressible, linear, isotropic, viscoelastic material. Muscle contraction was then simulated by incrementally applying biomechanically-based loads on the mesh (Fig. 4.8) (Chen 92). Bro-Nielsen et al. also presented a linear finite element modeling approach, including common computational improvements such as matrix condensation techniques, in order to achieve real-time surgery simulation (Bro-Nielsen 96).

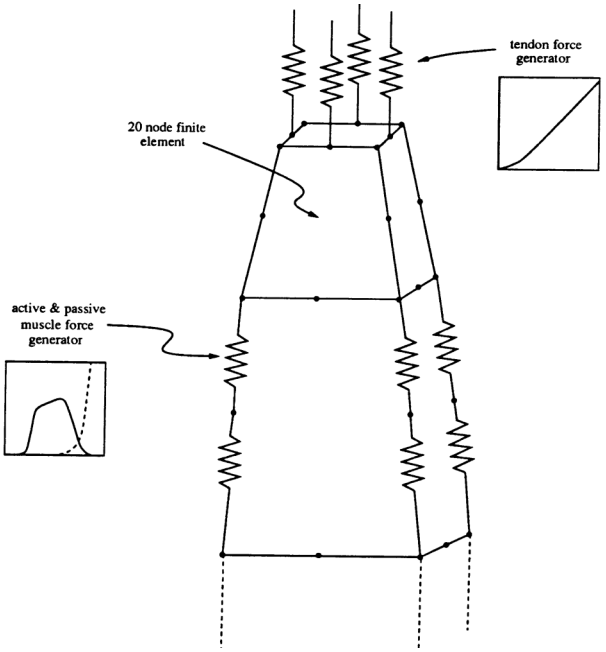

(Chen 92)

Fig. 4.8. Chen's finite element muscle model

Physically-Based Models. Other approaches have been proposed for soft tissue modeling in computer animation. Platt and Badler developed a facial animation model, in which skin was represented as a warped tension net, with nodes connected together by Hookean springs, and muscles as macroscopic fibers connecting the skin nodes to the underlying bone. Facial expressions were thus simulated by applying forces on the skin mesh by means of the muscle fibers (Platt 81). Waters et al. improved this approach in designing muscle vectors following the major direction and insertion of the real facial muscle fibers. Three types of muscles were modeled: linear, sphincter, and sheet. The linear and sheet muscle contractions were designed as vectors, while the sphincter muscle contraction was designed as elliptical (Waters 87).

The first and most famous physically-based approach for realistic deformation simulation in computer animation was proposed by Terzopoulos et al. (Terzopoulos 87). Instead of the Virtual Work Principle, their model was based on the *Lagrange Formalism.* Though the formulation is different, the mechanical problem stays the same. Assuming a constant uniform mass density ρ and an isotropic hyper-viscoelastic material with constant uniform damping densities η, the Lagrange equation of motion was obtained as: (see Appendix C.4)

$$\frac{d}{dt}\left(\rho\frac{dq_i}{dt}\right)+\eta\frac{dq_i}{dt}+\frac{\partial W_{elast}^{int}}{\partial q_i}=f_{q_i}^{ext} \qquad \text{(Terzopoulos 87)} \qquad (4.9)$$

where: $W_{elast}^{int}=\int_V \left\|\mathbf{C}-\mathbf{C}^0\right\|_\alpha^2 dV$ strain energy function of the hyperelastic material

$f_{q_i}^{ext}$ projections on q_i of the external force vector

$\mathbf{C}$ Cauchy-Green right dilation tensor of the deformation

Terzopoulos et al. proposed the general strain energy function in the form of control continuity generalized spline kernels allowing the modeling of inelastic behaviors such as visco-plasticity, fracture, etc. For linear behavior, the strain energy function was taken as:

$$W_{elast}^{int} = \int_L (\alpha.\text{stretching} + \beta.\text{bending} + \gamma.\text{twisting})\,dl \qquad \text{for a curve} \qquad (4.10)$$

$$W_{elast}^{int} = \int_S (\alpha.\text{stretching} + \beta.\text{bending})\,ds \qquad \text{for a surface} \qquad (4.11)$$

Spatial discretization was then achieved following the *finite difference method*, i.e. applying a grid discretization with a linear finite element interpolation (see Appendix C.4), leading to an equation of motion of the form:

$$\mathbf{M}\ddot{\mathbf{U}} + \mathbf{D}\dot{\mathbf{U}} + \mathbf{K}(\mathbf{U})\mathbf{U} = \mathbf{F}^{ext} \quad \text{with:} \quad \begin{array}{ll} \ddot{\mathbf{U}},\ \dot{\mathbf{U}},\ \mathbf{U}: & \text{nodal acceleration, velocity, displacement vectors} \\ \mathbf{M},\ \mathbf{D}: & \text{mass and damping diagonal matrix} \\ \mathbf{K}(\mathbf{U}) & \text{deformation dependent stiffness matrix} \\ \mathbf{F}^{ext} & \text{external nodal force vector} \end{array} \qquad (4.12)$$

The nonlinear ordinary differential system was then converted into a sequence of linear algebraic systems by means of a *finite difference* time discretization and were integrated through time using a *semi-implicit* integration procedure as: Δt time step (4.13)

$$\mathbf{A}_n\mathbf{U}_{n+1} = \mathbf{L}_{n+1} - \mathbf{Y}_n \quad \text{with:} \quad \ddot{\mathbf{U}}_n = \frac{\mathbf{U}_{n+1} - 2\mathbf{U}_n + \mathbf{U}_{n-1}}{\Delta t^2} \qquad \dot{\mathbf{U}}_n = \frac{\mathbf{U}_{n+1} - \mathbf{U}_{n-1}}{2\Delta t} \qquad \mathbf{V}_n = \frac{\mathbf{U}_n - \mathbf{U}_{n-1}}{\Delta t}$$

$$\mathbf{A}_n = \mathbf{K}_n + \frac{1}{2\Delta t}\mathbf{D} + \frac{1}{\Delta t^2}\mathbf{M} \qquad \mathbf{Y}_n = -\left(\frac{1}{\Delta t^2}\mathbf{M} + \frac{1}{2\Delta t}\mathbf{D}\right)\mathbf{U}_n - \left(\frac{1}{\Delta t}\mathbf{M} - \frac{1}{2}\mathbf{D}\right)\mathbf{V}_n \qquad \mathbf{U}_n = \mathbf{U}(t_n)$$

The model was later extended to inelastic behavior such as *viscoelasticity*, *plasticity* and *fracture* by means of a general strain energy function in the form of control continuity generalized spline kernels (Terzopoulos 88).

Following this approach, Gascuel and Verroust proposed a model of skin with spring-like muscles, in which the skin layer was represented by a B-spline surface attached by its control points (Gascuel 91). Terzopoulos and Waters modeled facial tissues using a trilayer spring lattice structure, each layer representing respectively the skin, the subcutaneous tissue, and the underlying muscle layers, with different stiffness parameters according to the relevant tissue (Terzopoulos 90, 91). Celniker and Gossard proposed an approach for free form shape design using deformable curve and surface finite elements. Their approach is entirely based on Terzopoulos's linear Lagrangian approach, with the only difference being that they used the finite element discretization with the squared interpolation function instead of the finite difference discretization. Shape design may be interactively achieved by applying forces on the finite element mesh, and smoothness is automatically obtained from the underlying physically based model (Celniker 91). Pieper et al. used a linear model of skin to perform simple facial surgical simulation (Pieper 92). In their approach, both the skull and skin surfaces extracted from CT images were mapped into cylindrical coordinates, and a home-grown static displacement-based method was used to solve the equilibrium equation. Wu et al. modeled skin as a thin membrane connected to strong spring-like muscles by means of soft bilinear springs representing the respective contributions of elastin and collagen fibers to the elastic behavior of the subcutaneous tissues (Fig. 4.9) (Wu 95).

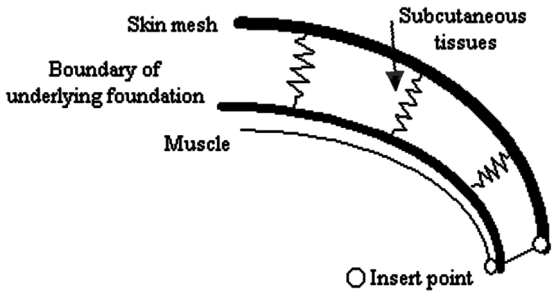

(Wu 95)

Fig. 4.9. Skin underlying connections

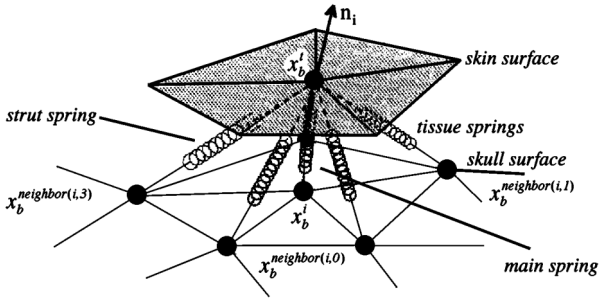

(Koch 96)

Fig. 4.10. Spring mesh between skin and skull

Koch et al. applied the general approach for finite element curve and surface free-form shape design, proposed by Celniker and Gossard, to surgical planning and prediction of the human facial shape after craniofacial and maxillofacial surgery. They followed Terzopoulos's approach except for the use of finite element primitives instead of a finite difference discretization, with as strain energy function:

$$W^{int} = \int_{\Omega} \left(\alpha.\text{stretching} + \beta.\text{bending}\right) d\Omega \qquad \alpha \text{ and } \beta \text{ smoothness parameters} \qquad (4.14)$$

Interactive control of the shape is then achieved by parametrizing the shape with sculpting loads or geometric constraints. The facial surface and inner structures (bones or muscles) were obtained from the patient's CT or MRI data, and the effect of the subcutaneous tissue was simulated by connecting the finite element skin surface nodes with nodal springs to the skull as shown in Fig. 4.10 (Koch 96).

Though each of these investigations has lead to the generation of realistic deformations of the soft-tissue layers, a major criticism may be raised on the basis that these models do not take into account the real biomechanical properties of soft tissues. They, consequently, can not accurately reproduce the very nature of their behavior. The originality of CHARM has been to lead investigations in this direction. This is presented in the following section.

4.2 Soft Tissue Biomechanics

4.2.1 Soft Tissue Physiology

Soft tissues may be distinguished from other body tissues like bones for their flexibility, their soft mechanical properties. This concerns the connective tissues, the muscles, the organs and the brain (Lee 82). In this section, we are mainly concerned with the mechanical properties of the soft tissues involved in body motion and deformation, i.e., skeletal muscles, tendons, ligaments, and skin. Skeletal muscles are responsible for generating forces to move the skeleton. The detailed analysis of their mechanical properties was presented in § 3.3.1. The role of tendons is to transmit these forces to the bones, whereas that of ligaments is to handle the stability of joints and restrict their ranges of motion. Among other functions, skin supports internal organs and protects them from injury while allowing considerable mobility.

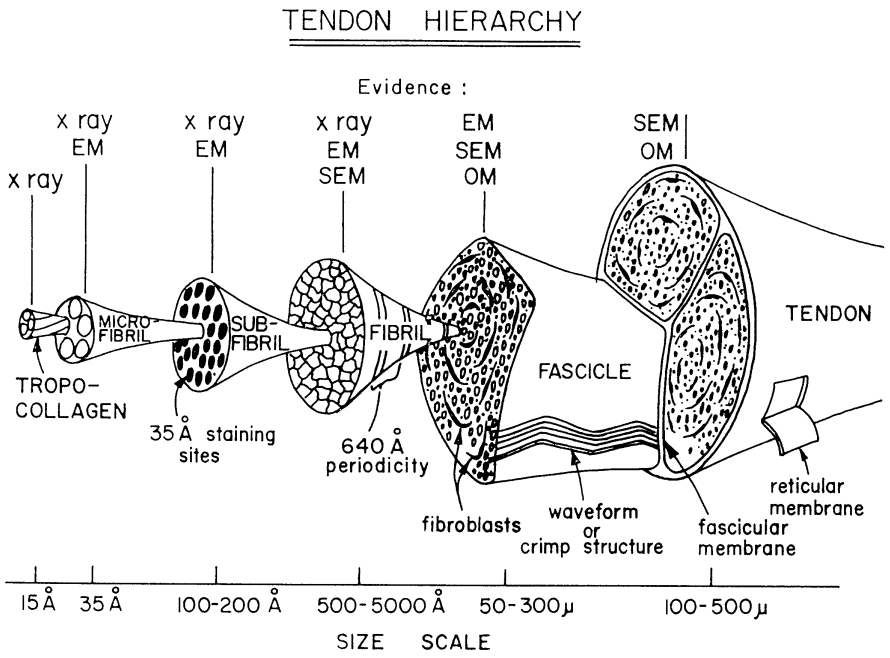

Fig. 4.11. The fibrous structure of tendon (Kastelic 78)

Soft tissues are all essentially composed of *collagen*. Elliott had reported that collagen represents among 75% dry weight in human tendons (Elliott 65). The remaining weight is shared between *elastin, reticulin,* and a hydrophilic gel called *ground substance* (Fung 72). However, soft tissues exhibit large differences in their mechanical properties (Crisp 72). This observation has led to the conclusion that the mechanical properties of soft tissues are due to their structure rather than to the relative amount of their constituents (Fung 87). As described in Fig. 4.11, the tendon fascicles are organized in hierarchical bundles of fibers arranged in a more or less parallel fashion in the direction of the effort handled. A close look at the fiber networks shows that this parallel arrangement is more irregular and distributed in more directions for ligaments than for tendons (Fung 93a).

In addition, skin is organized into two biaxial membranes: a relatively thin layer of stratified epithelium called the *epidermis,* and a thicker layer of disordered wavy coiled collagen and elastin fibers called the *dermis* (Fig. 4.12) (Danielson 73). The elastin fibers play an important role in the skin's response at low strains: they are the first stretched when the tissue is strained whereas the collagen fibers are still crimped. They are also considerably more pliant but can be reversibly stretched to more than 100 per cent (Lanir 87). The epidermis and dermis are also connected by collagen fibers to a subcutaneous fatty tissue, called the *hypodermis*. This layer is sometimes considered as a third layer of skin. It appears as a honeycomb fat container structure connected to the fascia which surrounds the muscle bundles. It is the hypodermis that provides the skin's loose flexible connection with the other internal soft tissues, whereas the upper layers are more resistant to protect from injuries.

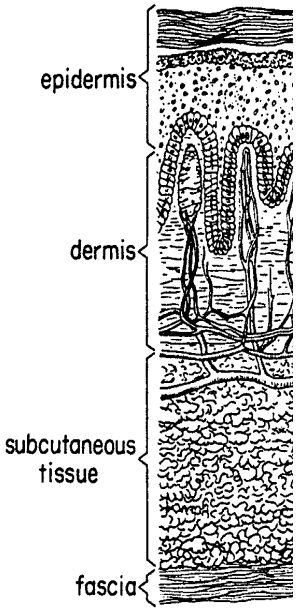

Fig.4.12. The skin layers (Danielson 73)

4.2.2 Mechanical Properties

Nonlinear Elasticity. The main property of soft tissues may be outlined as being their nonlinear elasticity. Kwan described the phenomenon as follows: *"Under uniaxial tension, parallel-fibered collagenous tissues exhibit a non-linear stress-strain relationship characterized by an initial low modulus region, an intermediate region of gradually increasing modulus, a region of maximum modulus which remains relatively constant, and a final region of decreasing modulus before complete tissue rupture occurs. The low modulus region is attributed to the removal of the undulations of collagen fibrils that normally exist in a relaxed tissue. As the fibrils start to resist the tensile load, the modulus of the tissue increases. When all the fibrils become taut and loaded, the tissue modulus reaches a maximum value, and thereafter, the tensile stress increases linearly with increasing strain. With further loading, groups of fibrils begin to fail, causing the decrease in modulus until complete tissue rupture occurs*." A typical tensile curve is shown in Fig. 4.13. From a functional point of view, the first parts of the curve are more useful since they correspond to the physiological range in which the tissue normally functions (Kwan 89).

Viscoelasticity. The above experiment reveals the relationship between stress and strain in the static case. However, when the equilibrium is not reached, a history-dependent component exists in the mechanical behavior of living tissues (Fung 72). When measured in dynamic extension, the stress values appear higher than those at equilibrium, for the same strain. The resulting tensile curve appears steeper than the one at equilibrium (Fig. 4.14). When a tissue is suddenly extended and maintained at its new length, the stress gradually decreases slowly against time. This phenomenon is called *stress relaxation* (Fig 4.15a). When the tissue is suddenly submitted to a constant tension, its lengthening velocity decreases against time until equilibrium. This phenomenon is called *creep* (Fig. 4.15b). Under cyclic loading, the stress-strain curve shows two distinct paths corresponding to the loading and unloading trajectories. This phenomenon is named *hysteresis* (Fig. 4.15c). As a global statement, the stress at any instant of time depends not only on the strain at that time, but also on the history of the deformation. These mechanical properties, observed for all living tissues, are common features of a physical phenomenon named *viscoelasticity* (Fung 93a).

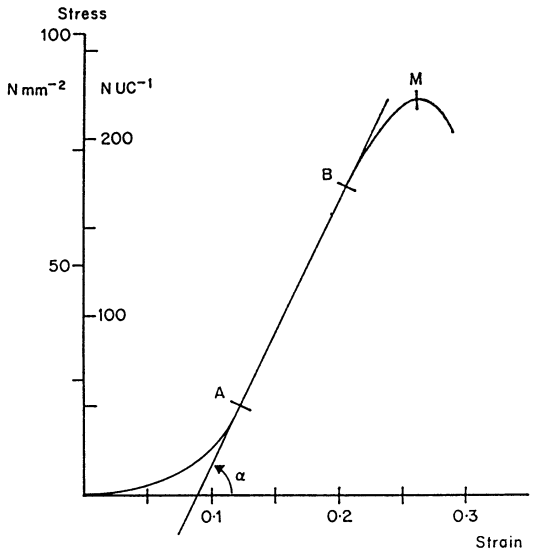

(Viidik 80)

Fig. 4.13. Load-extension curve

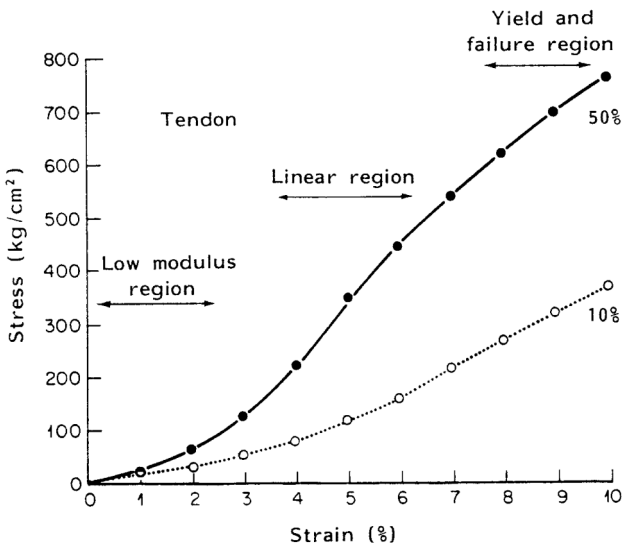

(Birk 91)

Fig. 4.14. Influence of the train rate

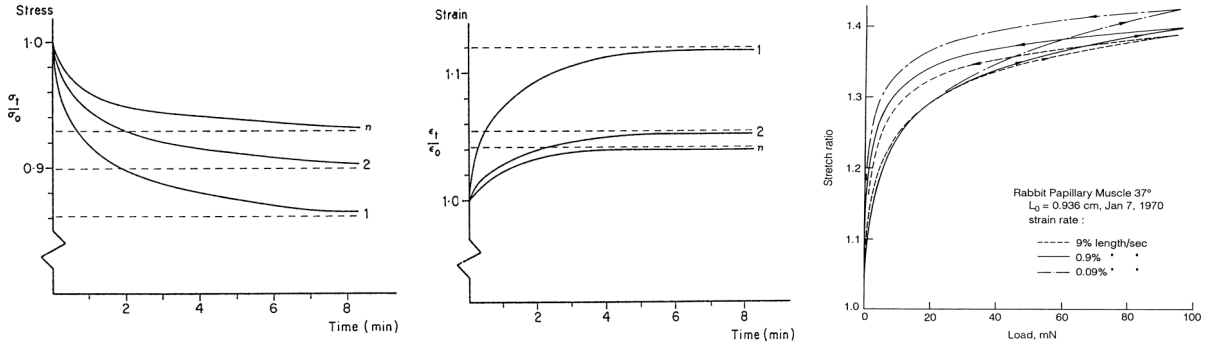

a) stress-relaxation (Viidik 80) b) creep (Viidik 80) c) hysteresis (Fung 72)

Fig. 4.15. Viscoelastic behaviors

Other Properties. The compressibility of soft tissues has been investigated very little. Soft tissues are however usually assumed to be incompressible materials (Audu 85). Besides, when loading-unloading cycles are applied on the tissue successively up to the same stress level, the stress-strain curve is gradually shifted to the right. After a number of such cycles, the mechanical response of the tissue enters a stationary phase and the results become reproducible from one cycle to the next. This phenomenon is due to the changes occurring in the internal structure of the tissue, until a steady state of cycling is reached. This initial phase of behavior common to all living tissues is usually used as *preconditioning* of the tissues prior to experimentation (Fig. 4.16) (Viidik 87).

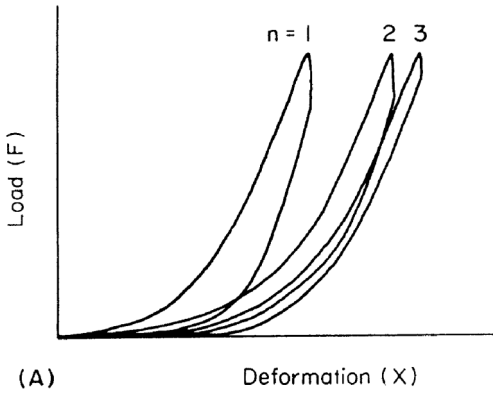

Fig. 4.16. Preconditioning (Viidik 73)

A further property may be outlined as the propensity to undergo large deformations. In normal tensile tests, graphs are plotted for the Lagrangian stress T with respect to the Lagrangian strain ε. Sometimes, this Lagrangian stress is taken for the true stress (Cauchy stress) σ in the resulting constitutive equation. It must be emphasized that this substitution is valid only for strains smaller than 2% of the resting length. However, soft tissues are likely to exceed this limit in their physiological range of functioning, so that, in most cases, this assumption no longer applies. For example, a common strain for tendons is around 4% but they may extend up to 10% of their original length. One then talks about *finite strain,* or *large deformation*.

Summarizing, soft tissues may be characterized as *quasi-incompressible, non-homogeneous, non-isotropic, non-linear viscoelastic materials* likely to undergo *large deformations*. Though with different proportions depending on the tissue, these properties may be attributed to all soft-tissues, passive muscle included. Numerous investigations have been lead towards the constitutive modeling of these materials. The main approaches which have been followed in this direction are overviewed in the following section.

4.3 Constitutive Modeling

4.3.1 Generalities

Considering the numerous approaches which have been followed for soft tissue modeling, as well as the specific nature and conditions of the experiments, it is probably not possible to present one model as more reliable for any case than any other. It is also not possible to collect and review all the existing biomechanical models without losing understanding of the natural mechanical behavior common to all of them. The purpose of this section is therefore not to point at *the* model to apply, but rather to outline as far as possible the different forms they can take. Suggestions for application in CHARM are made on this basis in the next section.

Soft tissue models may be distinguished with respect to several criterions, whether they are *uniaxial* or *multi-dimensional*, *elastic* or *viscoelastic*, *phenomenological* or *structural*, as well as depending on the tissue they model. Phenomenological modeling essentially consists of fitting mathematical equations to experimental tensile curves. This approach is convenient for generalization, and behavior prediction in independent tests. By contrast, structural models are based on the assumed behavior of the structural components of the tissue. They are thus formulated in terms of structural parameters. Such models appear more appropriate for relating the microstructure of the tissues to their mechanical behavior (Woo 93, Maurel 98).

4.3.2 Uniaxial Models

Elastic Models. The early models of soft tissue were essentially developed in the form of uniaxial constitutive relationships relating the Lagrange stress T $(\equiv F/S_0)$ to the infinitesimal strain ε $(\equiv L - L_0/L_0)$ or the extension ratio λ $(\equiv 1+\varepsilon)$. Various similar relationships were derived from tensile curves, fitting experimental data or based on continuum mechanics, like:

(Wertheim 47)	(Carton 62)	(Kenedi 64)	
$\varepsilon^2 = a\,T^2 + b\,T$ for tendons	$\varepsilon = a\left(1 - e^{bT}\right)$ for elastic fibers	$T = a\,\varepsilon^b$ for skin	(4.15)

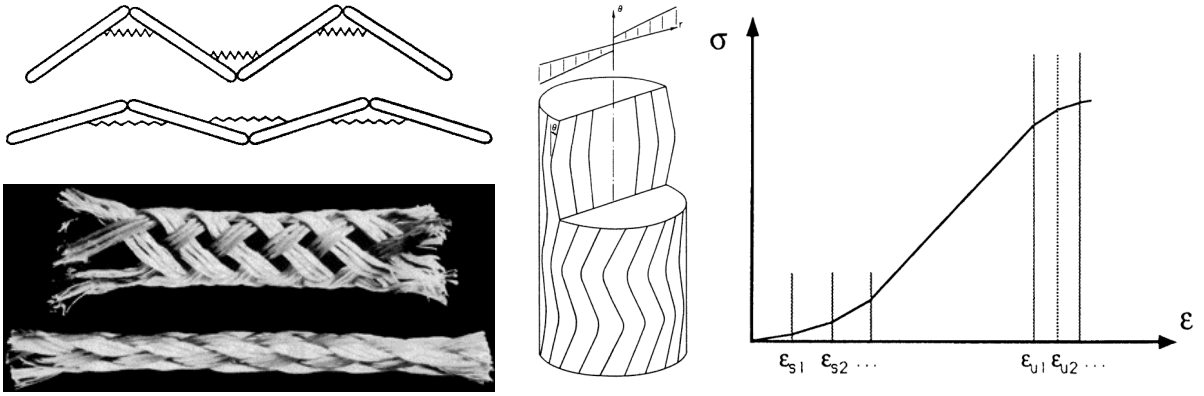

Fig. 4.17. Various structural representations for modeling soft tissue nonlinear elasticity (Diamant 72, Crisp 72, Kastelic 80, Kwan 89, Maurel 98)

Relations of other types were also obtained, based on various representations of the tissue structure, such as in the form of series of slender crimp arms medially connected by springs for tendon (Diamant 72), of a hollow cylinder braided with inextensible fibers arranged in a helical pattern (Beskos 75), or of groups of fibers described by bilinear tensile curves (Kwan 89), or as sinusoidal beams (Kastelic 80), etc., all generating nonlinear tensile curves similar to those of the real tissues (Fig. 4.17).

Viscoelastic Models. Most viscoelastic models were developed following the discrete element combination approach (Fig. 4.18). Buchthal and Kaiser described the continuous relaxation spectrum of soft tissues by the combination of an infinite number of Voigt and Maxwell elements (Buchthal 51). Viidik proposed an idealized model composed of Hooke, Newton, Coulomb, and Maxwell elements to fully describe the non-linear viscoelastic behavior of soft tissues (Viidik 68, Frisen 69a,b). Capelo et al. used a three-element model composed of two exponential springs and one hyperbolic sinusoidal dashpot to model passive muscle (Capelo 81). Constitutive relations were usually obtained in differential form like (Galford 70):

$$T + p_1 \frac{dT}{dt} + p_2 \frac{d^2T}{dt^2} = q_1\dot{\varepsilon} + q_2\ddot{\varepsilon} \quad \text{with:} \quad \eta_3 = \frac{q_1 q_2}{p_1 q_1 - q_2 - \frac{q_1^2 p_2}{q_2}} \quad \eta_2 = q_1 \quad E_3 = \frac{q_1}{p_1 - \frac{q_2}{q_1} - \frac{q_1 p_2}{q_2}} \quad E_1 = \frac{q_2}{p_2} \qquad (4.16)$$

which were integrated for specific experimental boundary conditions (Fig 4.18).

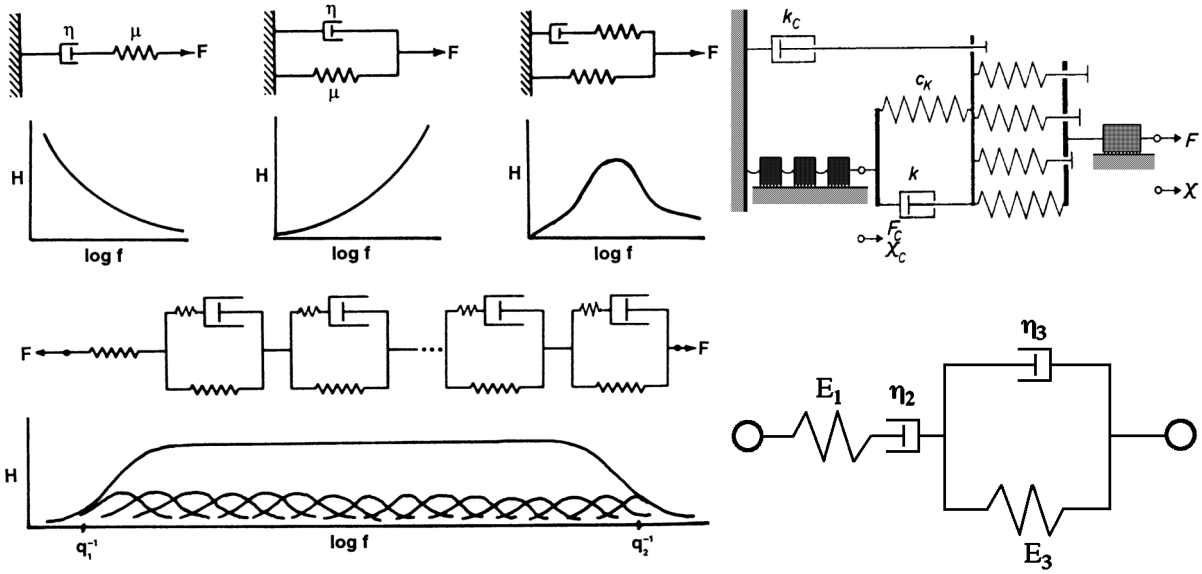

Fig. 4.18. Various structural representations for modeling soft tissue viscoelasticity (Viidik 68, Galford 70, Fung 93a, Maurel 98)

The Quasi Linear Viscoelasticity Theory. Fung has been the first to propose a general description based on continuum mechanics, which can be indifferently applied for the characterization of any soft tissue. According to him, it is reasonable to expect that for oscillations of a small amplitude about an equilibrium state, the theory of linear viscoelasticity should apply. For finite deformations, however, the non-linear stress-strain characteristics of living tissues must be taken into account (Fung 72).

Thus, he has developed a theory he has called *quasi-linear viscoelasticity* (QLV), by assuming the *relaxation function* as composed of a *reduced relaxation function* $G(t)$ and an *elastic response* $T^{(e)}(\lambda)$ – not especially linear – such that:

$$T(t) = \int_{-\infty}^{t} G(t-\tau)\frac{\partial T^{(e)}\left[\lambda(\tau)\right]}{\partial \tau}\,d\tau \qquad \text{with:} \qquad G(0) = 1 \tag{4.17}$$

which may be seen as the sum of the contributions of all the past changes, each governed by the same reduced relaxation function $G(t)$ (hence the name *quasi-linear viscoelasticity*).

Observing that, after preconditioning, the steady-state stress-strain loop of soft-tissues is repeatable and not very sensitive to strain rate, Fung pointed out that the *loading* and *unloading* tensile curves may be characterized separately using the elasticity theory – a property he called *pseudoelasticity* – and may be approximated by the tensile stress responses in loading/unloading experiments with sufficiently high rates of loading/unloading. Any stress-strain relationship is thus suitable as elastic response for the QLV theory (Fung 72).

Fung outlined the exponential form of the stress–strain relationship of tissues as:

$$\frac{dT}{d\lambda} = a(T+b) \qquad \text{leading to:} \qquad T = \left(T_0 + b\right)e^{a\left(\lambda-\lambda_0\right)} - b \qquad \text{with:} \qquad b = \frac{T_0\, e^{-a\left(\lambda_0-1\right)}}{1-e^{-a\left(\lambda_0-1\right)}} \tag{4.18}$$

for strains up to 30% resting length, where (λ_0, T_0) is an arbitrary point on the curve (Fung 67). This relation was applied by many investigators or used as a basis for deriving others as:

$$T = a\left[e^{b\varepsilon} - 1\right] \text{ for heart (Feit 79)} \qquad T = a\left(\varepsilon - \varepsilon^2\right)e^{b\varepsilon} \text{ for ligaments (Haut 69)} \tag{4.19}$$

Besides, observing the fact that the stress-strain loop is almost independent of the strain rate with several decades of the rate variation, Fung also suggested applying a reduced relaxation function of the form (Fung 72):

$$G(t) = \frac{1+\int_0^{\infty} S(\tau)e^{-\frac{t}{\tau}}\,d\tau}{1+\int_0^{\infty} S(\tau)\,d\tau} \qquad S(t) = \begin{cases} \frac{c}{t} + S_0 & \tau_1 \le t \le \tau_2 \\ 0 & t < \tau_1, t > \tau_2 \end{cases} \qquad \text{i.e.:} \tag{4.20}$$

$$G(t) = \frac{1 + c\left[E\left(\frac{t}{\tau_2}\right) - E\left(\frac{t}{\tau_1}\right)\right]}{1 + c\ln\left(\frac{\tau_2}{\tau_1}\right)} \qquad E(y_1) = \int_{y_1}^{\infty} \frac{e^{-y}}{y}\,dy \qquad \begin{cases} y = \frac{t}{\tau} \\ y_1 = \frac{t}{\tau_1} \end{cases} \qquad \text{i.e.:} \tag{4.21}$$

$$G(t) \approx \frac{1 - c\,\gamma - c\ln\left(\frac{t}{\tau_2}\right)}{1 + c\ln\left(\frac{\tau_2}{\tau_1}\right)} \qquad \gamma = 0.5772 \qquad \tau_1 << t << \tau_2 \qquad \text{i.e.:} \tag{4.22}$$

$$G(t) = \alpha\ln(t) + \beta \qquad \alpha = -\frac{c}{1 + c\ln\left(\frac{\tau_2}{\tau_1}\right)} \qquad \beta = \frac{1 - c\,\gamma + c\ln(\tau_2)}{1 + c\ln\left(\frac{\tau_2}{\tau_1}\right)} \tag{4.23}$$

Many investigators have applied the QLV theory with:

$$T^{(e)} = a\left(e^{b\varepsilon} - 1\right) \quad \text{and:} \quad G(t) = \alpha \ln(t) + \beta \quad \text{with:} \quad \alpha\left(c, \tau_1, \tau_2\right) \quad \text{and:} \quad \beta\left(c, \tau_1, \tau_2\right) \tag{4.24}$$

Among others, Woo applied it to model the medial collateral ligament (Woo 82), Trevisan to model human tendons and ligaments (Trevisan 83), Kwan et al. to model the anterior cruciate ligament (Kwan 93), Best et al. to model live skeletal muscle (Best 94) (Maurel 98).

4.3.3 Multi-Dimensional Models

Elastic Models. Stress-strain relationships reveal, more than constitute, the mechanical properties of materials: they are only material responses to given mechanical constraints. Hence the idea: to assume soft tissues as hyperelastic materials and to model them using a strain energy formulation, from which the 3-D stress-strain relationships may be derived (Appendix C.2). Various strain energy functions existed with polynomial forms for modeling incompressible polymers. The first thoughts were to extend them to the constitutive modeling of soft tissues (Mooney 40, Blatz 69, Allaire 77, Peng 78). Snyder presented how Fung's uniaxial exponential relation could be integrated in order to obtain a strain energy function in terms of the extension ratio λ as:

$$W_1 = \frac{B}{A^2}\left[e^{A(\lambda-1)} - A\lambda\right] \qquad T = \frac{B}{A}\left[e^{A(\lambda-1)} - 1\right] \qquad \text{(Snyder 72, 75)} \tag{4.25}$$

From then, various other similar exponential forms have been developed for soft tissues (Gou 70, Veronda 70, Demiray 72, Janz 74, Vawter 80). The generalization of this form was achieved by Tong and Fung in terms of the Green–Lagrange strain components E_{ij} (Tong 76):

$$W = \frac{1}{2}\sum_{i,j,k,l=1}^{3}\alpha_{ijkl}E_{ij}E_{kl} + \beta_0\sum_{m,n,p,q=1}^{3}\beta_{mnpq}E_{mn}E_{pq}e^{\left(\sum_{i,j=1}^{3}\nu_{ij}E_{ij} + \frac{1}{2}\sum_{i,j,k,l=1}^{3}\gamma_{ijkl}E_{ij}E_{kl} + \cdots\right)} \qquad \alpha_{ijkl}, \beta_{mnpq}, \nu_{ij}, \gamma_{ijkl}, \beta_0 = \text{cste} \tag{4.26}$$

This relation has been applied to biaxial experiments on skin in the form:

$$W = f(\alpha, \mathbf{E}) + \frac{c}{2}e^{F(a,\mathbf{E})} \qquad f(\alpha, \mathbf{E}) = \frac{1}{2}\left(\alpha_1 E_{11}^2 + \alpha_2 E_{22}^2 + 2\alpha_4 E_{11}E_{22}\right) \tag{4.27}$$

$$F(a, \gamma, \mathbf{E}) = a_1 E_{11}^2 + a_2 E_{22}^2 + a_3 E_{12}^2 + 2a_4 E_{11}E_{22} + \gamma_1 E_{11}^3 + \gamma_2 E_{22}^3 + \gamma_4 E_{11}^2 E_{22} + \gamma_5 E_{11}E_{22}^2$$

where α_i, a_i, γ_i and c are experimental constants. In practice, the third-degree terms are assumed negligible with no significant loss of accuracy. This leads therefore to the simplified strain energy function:

$$W \approx f(\alpha, \mathbf{E}) + \frac{c}{2}e^{F(a,\mathbf{E})} \qquad \begin{cases} f(\alpha, \mathbf{E}) = \frac{1}{2}\left(\alpha_1 E_{11}^2 + \alpha_2 E_{22}^2 + 2\alpha_4 E_{11}E_{22}\right) \\ F(a, \mathbf{E}) = a_1 E_{11}^2 + a_2 E_{22}^2 + a_3 E_{12}^2 + 2a_4 E_{11}E_{22} \end{cases} \tag{4.28}$$

Fung's relations have since been used by many authors as basis for the development of various 3-D constitutive relationships for soft tissues (Chuong 83, Huang 90, Guccione 91). The main refinement left to bring to the modeling approach was to compose full 3-D strain energy functions on the basis of structural representations of the soft tissues, as shown below.

An interesting multi-dimensional theory for fibrous connective tissue modeling was proposed by Lanir on the basis of microstructural and thermodynamic considerations. Assuming tissues as composed of several networks of different types of fibers embedded in a fluid matrix, he has developed a strain energy function including their structural properties such as their angular and geometrical non-uniformities. For a unit volume of tissue, the distortional energy W_1 was expressed as the sum of the strain energies of the different fiber types (Lanir 83a):

$$W_1 = \sum_k W_k \qquad \text{with} \qquad W_k = \int_\Omega S_k R_k(\mathbf{u}) w_k(\lambda)\, d\Omega \tag{4.29}$$

where S_k is the volumetric fraction of unstrained k-type fibers
$R_k(\mathbf{u})$ is the density of fibers with unit direction $\mathbf{u}$
$w_k(\lambda)$ is the k-type fibers uniaxial strain energy function
λ, Ω are the individual fiber stretch ratio and the range of fiber orientations

The model was then extended to account for the non-uniform undulation of each k-type fiber along its direction $\mathbf{u}$ by means of a fiber strain-energy function $w_k^*(\lambda)$ incorporating an undulation density distribution function $D_{k,\mathbf{u}}(X)$. Further extensions concerned viscoelastic behavior and non-homogeneities by means of theoretical functionals introduced in the fiber strain energy functions. Following this approach, Lanir has developed a biaxial incompressible viscoelastic model for skin assumed as a membranous tissue composed of a ground substance and planar collagen and elastin fibers (Lanir 79). The advantage of this structural model lies in the fact that the non-homogenous non-linear anisotropic properties of the skin components may be included while avoiding ambiguity in material characterization and offering an acute insight into their structure, mechanics, and function. A similar formulation has also been applied to model the lung tissue (Lanir 83b).

Horowitz et al. led an interesting application of Lanir's fibrous description to model the anisotropic properties of the myocardial muscle (Horowitz 88c). Here also, the cardiac tissue was assumed to be composed of muscle fibers and collagen fibers embedded in a gelatinous ground substance. Assuming incompressibility, the stress tensor $\mathbf{S}$ was defined as:

$$\mathbf{S} = \frac{\partial W_1}{\partial \mathbf{E}} + L\frac{\partial I_3}{\partial \mathbf{E}}$$

W_1: fiber distortional energy function from Lanir
L: Lagrange multiplier for the matrix hydrostatic pressure
I_3: 3-rd invariant of the Cauchy–Green right dilation tensor $\mathbf{C}$ (4.30)

Assuming a fiber waviness distribution function $D_{k,\mathbf{u}}$ and a straight fiber constant stiffness C_k, the wavy fiber's stress-strain relations were expressed in the form (Fig. 4.19):

$$f_k^*(\varepsilon') = \int_0^{\varepsilon'} D_{k,u}(x)\, f_k(\varepsilon)\, dx \quad \text{where: } f_k(\varepsilon) = C_k\varepsilon \text{ is the stress-strain relation for straight fibers.} \tag{4.31}$$

$\varepsilon = \dfrac{\varepsilon' - x}{1 + 2x}$ true wavy fiber strain

$\varepsilon' = \dfrac{\partial \xi^r}{\partial \xi_1'}\dfrac{\partial \xi^s}{\partial \xi_1'} E_{rs}$ total fiber strain

E_{rs} global tissue strain component

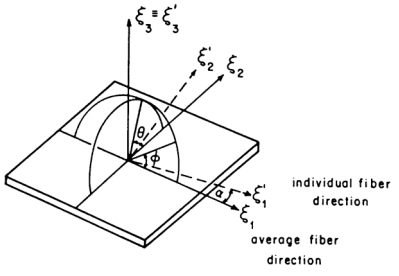

Fig. 4.19. Orientations of the fiber coordinate systems (Horowitz 88c)

Then, considering the wavy fiber stress f_k^* as deriving from the strain energy $w_k^*(\varepsilon)$, the global tissue stress tensor could be developed into the form:

$$\mathbf{S} = \int_\Omega S_k R_k(\mathbf{u})\, f_k^*(\varepsilon') \frac{\partial \varepsilon'}{\partial \mathbf{E}}\, d\Omega + L \frac{\partial I_3}{\partial \mathbf{E}} \qquad f_k^*(\varepsilon') = \frac{\partial w_k^*(\varepsilon)}{\partial \varepsilon'} \tag{4.32}$$

With assumptions on the fiber waviness distribution functions, the model was applied to Two– (Horowitz 88a) and Three– (Horowitz 88b) Dimensional finite element modeling of passive myocardium and ventricle.

Viscoelastic Models. A major advantage of Fung's QLV theory (4.17) was its extendibility to the development of Three-Dimensional constitutive relationships in the form:

$$\mathbf{S}(t) = \mathbf{G}(t)\mathbf{S}^{(e)}(0) + \int_{-\infty}^{t} \mathbf{G}(t-\tau) \frac{\partial \mathbf{S}^{(e)}[\mathbf{E}(\tau)]}{\partial \tau} d\tau \quad \text{with:} \quad \begin{array}{ll} \mathbf{S}(t) & \text{second } \textit{Piola-Kirchhoff} \text{ stress tensor,} \\ \mathbf{S}^{(e)}[\mathbf{E}] & \text{pure elastic response of the material} \\ \mathbf{G}(t) \equiv G(t) & \text{reduced relaxation function} \end{array} \tag{4.33}$$

An interesting application was achieved by Shoemaker et al. for human skin modeling using Lanir's model with Fung's QLV theory (Shoemaker 86). Like in Horowitz's model (Horowitz 88c), the stress was assumed composed of a compliant component due to the gelatinous matrix and a fibrous component due to the fibers. The Piola–Kirchhoff second stress tensor $\mathbf{S}$ was then expressed as:

$$\mathbf{S} = \mathbf{S}^F + \mathbf{S}^C \quad \text{with:}$$

$$\mathbf{S}^F = \int_{-\frac{\pi}{2}}^{\frac{\pi}{2}} D(\theta) S_f \frac{\partial E_f}{\partial \mathbf{E}}\, d\theta \quad \text{fibrous stress}$$

$$\mathbf{S}^C = \mathbf{\Lambda} \int_{-\infty}^{t} g(t-\tau) \frac{\partial \mathbf{E}(\tau)}{\partial \tau} d\tau \quad \text{compliant stress}$$

$D(\theta)$: the fiber orientation distribution function
θ: the angle of a fiber with respect to the **x** axis
S_f: the fiber stress measure
$g(t)$: the reduced relaxation function
E_f: the fiber strain measure
$\mathbf{\Lambda}$: a constant tensor (4.34)

The fiber stress measure S_f was also assumed to be a viscoelastic function of E_f:

$$S_f = \int_{-\infty}^{t} G(t-\tau) \frac{\partial E_f(\tau)}{\partial \tau} d\tau \quad \text{with:} \quad G(t) = G_0 g(t) \qquad g(t) = \frac{1 + a\int_0^\infty f(\tau) e^{-\frac{t}{\tau}} d\tau}{1 + a\int_0^\infty f(\tau)\, d\tau} \qquad f(t) = e^{-pt} \qquad \text{a, constant}$$

$$E_f = \frac{1}{\lambda_0^2}\left[(1-b)\,\Sigma + b\,\Sigma^- - \Sigma_0\right] \quad \text{for:} \quad S_f > 0 \quad \text{with:} \quad \Sigma = \frac{1}{2}(\lambda^2 - 1) \qquad \lambda_0 = \sqrt{2\Sigma_0 + 1} \tag{4.35}$$

where: Σ and λ are the fiber strain and stretch ratio
Σ_0 and λ_0 the effective straightening fiber strain and stretch ratio
Σ^- the perpendicular line strain, G_0 and b constants $(0 \le b \le 1)$

Various other such complex combinations of structural representations with 3-D strain energy formulations and/or with the QLV assumption have been developed by Humphrey et al. (Humphrey 87, 90), Zeng et al. (Zeng 87), Huyghe et al. (Huygue 91a-b), Johnson et al. (Johnson 92), Pioletti (Pioletti 97). The application of such relationships to the finite element simulation of the soft tissues is briefly described in the following section.

4.3.4 Finite Element Formulation

Numerous non-linear finite element models have been developed for soft-tissue simulation, mainly for lungs (Liu 78, Pao 78, Vawter 80, Karakaplan 80, Lee 83) and ventricles (Janz 74, Christie 80-82, Needleman 83, Huang 90, Huygue 91a-b, Taber 91a-b). An incremental dynamic analysis has also been presented by Deng et al. who developed a non-linear thick shell model including a skin layer, a sliding layer, and a muscle layer, to simulate the closure of skin excisions on facial tissue (Deng 88). Usually, the material tangent stiffness matrix $\mathbf{K}_n^M$ of the incremental constitutive relationship is obtained by second-order derivation of a strain energy function W with respect to the strain tensor $\mathbf{E}$:

$$\Delta\mathbf{S} = \mathbf{K}_n^M \Delta\mathbf{E} + \mathbf{S}_n^R \qquad \text{with:} \qquad \mathbf{K}_n^M = \frac{\partial^2 W}{\partial \mathbf{E}_n^2} \tag{4.36}$$

Horowitz et al. presented an extended development of such incremental formulation as they led for 2-D (Horowitz 88a) and 3-D (Horowitz 88b) finite element heart muscle modeling with the fibrous constitutive model presented in the previous section (Horowitz 88c). For an incompressible ventricular wall segment, the stress tensor $\mathbf{S}$ was obtained as:

$$\mathbf{S} = \frac{\partial W_1}{\partial \mathbf{E}} + L\frac{\partial I_3}{\partial \mathbf{E}} \quad W = W_1(I_1, I_2) + W_2(I_3) \quad W_1 = \sum_k W_k = \sum_k S_k \int_\Omega R_k(\mathbf{u}) w_k^*(\gamma'_n)\, d\Omega \quad W_2 = L(I_3 - 1) \tag{4.37}$$

where I_3 is the third invariant the Cauchy–Green right dilation tensor $\mathbf{C}$, and L is a Lagrange multiplier accounting for the hydrostatic pressure of the incompressible embedding matrix. The stress $\mathbf{S}_n$ and stress increment $\Delta\mathbf{S}$ at n were then derived from (4.32) as:

$$\mathbf{S}_n = \frac{\partial W_1}{\partial \mathbf{E}_n} + L_n \frac{\partial I_3}{\partial \mathbf{E}_n} \qquad \Delta\mathbf{S} = \frac{\partial \mathbf{S}_n}{\partial \mathbf{E}_n}\Delta\mathbf{E} + \frac{\partial \mathbf{S}_n}{\partial L_n}\Delta L = \left(\frac{\partial^2 W_1}{\partial \mathbf{E}_n^2} + L_n \frac{\partial^2 I_3}{\partial \mathbf{E}_n^2}\right)\Delta\mathbf{E} + \frac{\partial I_3}{\partial \mathbf{E}_n}\Delta L \tag{4.38}$$

$$\Delta\mathbf{S} = \left(S_c \int_{-\frac{\pi}{3}}^{\frac{\pi}{3}} \int_0^{2\pi} \int_0^{\pi} f_c^*(\varepsilon'_n) R_c(\alpha,\theta,\phi) \frac{\partial^2 \varepsilon'_n}{\partial \mathbf{E}_n^2} J\, d\phi d\theta d\alpha + L_n \frac{\partial^2 I_3}{\partial \mathbf{E}_n^2}\right)\Delta\mathbf{E} + \frac{\partial I_3}{\partial \mathbf{E}_n}\Delta L$$

As a result, the tangent elastic stiffness matrix $\mathbf{K}_n^M$ required for the incremental stress-strain formulation was obtained in the form:

$$\mathbf{K}_n^M = \frac{\partial^2 W}{\partial \mathbf{E}_n^2} = \frac{\partial^2 W_1}{\partial \mathbf{E}_n^2} + L_n \frac{\partial^2 I_3}{\partial \mathbf{E}_n^2} \qquad \mathbf{K}_n^M = S_c \int_{-\frac{\pi}{3}}^{\frac{\pi}{3}} \int_0^{2\pi} \int_0^{\pi} \left[\int_0^{\varepsilon_c} \frac{D_c(x)}{1+2x} dx\right] R_c(\alpha,\theta,\phi) \frac{\partial^2 \varepsilon'_n}{\partial \mathbf{E}_n^2} J\, d\phi d\theta d\alpha + L_n \frac{\partial^2 I_3}{\partial \mathbf{E}_n^2} \tag{4.39}$$

The resolution of the equation of motion was then performed using a finite element incremental-iterative modified Newton–Raphson scheme, in which the tangent stiffness matrix $\mathbf{K}_n$ was updated after each load increment only. The approach was applied to finite element modeling of canine myocardial strips (Horowitz 88a,b).

On the basis of this review (Maurel 98), I have proposed a selection of constitutive relationships for the modeling, in CHARM, of tendons, ligaments, passive skeletal muscle and skin together with practical suggestions with respect to their finite element implementation and simulation. This is presented in the next section.

4.4 Suggestions for Simulation

4.4.1 Constitutive Modeling and Implementation

On the basis of the theories, models and methods reviewed in the previous sections, I have proposed considering constitutive relationships for soft tissues in the general form (Fung 93):

$$\mathbf{S}(t) = \mathbf{G}(t)\,\mathbf{S}^{(e)}(0) + \int_{-\infty}^{t} \mathbf{G}(t-\tau)\frac{\partial \mathbf{S}^{(e)}\left[\mathbf{E}(\tau)\right]}{\partial \tau}\,d\tau \quad \text{with:} \quad \begin{array}{ll} \mathbf{S}(t) & \text{second Piola–Kirchhof stress tensor,} \\ \mathbf{S}^{(e)}[\mathbf{E}] & \text{elastic response of the material} \\ \mathbf{G}(t) & \text{tensorial reduced relaxation function} \end{array} \tag{4.40}$$

Considering the lack of experimental data to fully determine the terms of the tensorial reduced relaxation function $\mathbf{G}(t)$, I have assumed $\mathbf{G}(t) \equiv G(t)$ as a scalar function, and proposed using the form as suggested by Fung (Fung 72):

$$G(t) = \alpha \ln(t) + \beta \qquad \text{with:} \qquad \alpha = -\frac{c}{1 + c\ln\left(\frac{\tau_2}{\tau_1}\right)} \qquad \beta = \frac{1 - c\,\gamma + c\ln(\tau_2)}{1 + c\ln\left(\frac{\tau_2}{\tau_1}\right)} \tag{4.41}$$

Concerning the elastic response, I have suggested modeling soft tissues as isotropic incompressible hyperelastic materials, using a strain energy function of the form (Oden 89):

$$W = W_1(I_1, I_2) + L(I_3 - 1) \qquad \text{leading to a stress tensor of the form:} \tag{4.42}$$

$$\mathbf{S}^{(e)}[\mathbf{E}] = \frac{\partial W_1(I_1, I_2)}{\partial \mathbf{E}} + L\frac{\partial I_3}{\partial \mathbf{E}} \qquad \text{with } L \text{ Lagrange multiplier accounting for hydrostatic pressure,}$$

and to formulate the incremental tangent stiffness matrix as: $\mathbf{K}_n^M = \frac{\partial^2 W}{\partial \mathbf{E}_n^2} = \frac{\partial^2 W_1(I_1, I_2)}{\partial \mathbf{E}_n^2} + L_n \frac{\partial^2 I_3}{\partial \mathbf{E}_n^2}$

Suggestions for tendon, ligaments, skin and passive muscle modeling are presented below.

Tendons and Ligaments. Due to the parallel orientation of their fibers, most of the constitutive relationships for tendons and ligaments have been developed for uniaxial tensile experiments. A few 3-D models for tendons and ligaments have been recently arising in the form of pseudo-elastic strain energy functions. However, considering that tendons always work in extension, and that the transverse constriction is small compared to the extension, it is possible to use a one-dimensional finite element model, and to assume incompressibility in order to insure the volume deformation on the 3-D tendon object. Among the available models, Fung's exponential form remains the most common for soft tissues. I have, therefore, suggested modeling tendons and ligaments with a constitutive relation of the form:

$$T(t) = \int_0^t G(t-\tau)\frac{\partial T^{(e)}\left[\varepsilon(\tau)\right]}{\partial \tau}\,d\tau \quad \text{with:} \quad T^{(e)}(\varepsilon) = a\left(e^{b\varepsilon} - 1\right) \quad \text{as the elastic function,} \tag{4.43}$$

with values provided by Woo (Woo 82), by Trevisan (Trevisan 83) or Kwan et al. (Kwan 93) for the elastic response $T^{(e)}$ and the reduced relaxation function $G(t)$.

Passive Skeletal Muscle. Skeletal muscles have rarely been investigated in the biomechanical literature from a constitutive modeling point of view. As extensive as my investigations have been, I have found only a few uniaxial relations (Glantz 74, 77, Capelo 81). However, a strain energy formulation allowing a 3-D non-linear deformation simulation seems more convenient since visible body deformation mainly arises from skeletal muscles. Therefore, I have suggested using one of the strain energy functions developed for ventricles, though skeletal muscles may have a slightly different mechanical behavior, in structure, strength, and stiffness. Among these, my preference has been Horowitz's constitutive description (Horowitz 88a, b, c) for the structural properties that the model includes and because it has already been applied to finite element modeling: (4.44)

$$W = \sum_k W_k = \sum_k S_k \int_\Omega R_k(\mathbf{u}) w_k^*(\gamma'_{11})\, d\Omega \qquad \mathbf{K}_n^M = S_c \int_{-\frac{\pi}{3}}^{\frac{\pi}{3}} \int_0^{2\pi} \int_0^{\pi} \left[\int_0^{\varepsilon_c} \frac{D_c(x)}{1+2x}\, dx \right] R_c(\alpha,\theta,\phi) \frac{\partial^2 \varepsilon'_n}{\partial \mathbf{E}_n^2} J\, d\phi d\theta d\alpha + L_n \frac{\partial^2 I_3}{\partial \mathbf{E}_n^2}$$

I have also suggested Humphrey's models as substitute in case the implementation of the Horowitz model proved to be too difficult (it actually happened to be the case, as shown in Chapter 5). Meanwhile, for any model selected, I have suggested applying Best's data for the QLV formulation since these have been especially investigated for skeletal muscles (Best 94).

Skin. In contrast to tendons and skeletal muscles, numerous strain energy functions have been proposed for skin modeling. As both Horowitz's and Shoemaker's models are based on Lanir's structural description, I have thought that some of the constitutive finite element routines to be implemented could be common for both muscle and skin tissues, and I have therefore suggested to using Shoemaker's model for skin simulation with (Shoemaker 86):

$\mathbf{S} = \mathbf{S}^F + \mathbf{S}^C$ with: (4.45)

$\mathbf{S}^F = \int_{-\frac{\pi}{2}}^{\frac{\pi}{2}} D(\theta) S_f \frac{\partial E_f}{\partial \mathbf{E}}\, d\theta$ fibrous stress similar to Lanir's form

$\mathbf{S}^C = \mathbf{\Lambda} \int_{-\infty}^{t} g(t-\tau) \frac{\partial \mathbf{E}(\tau)}{\partial \tau} d\tau$ compliant stress similar to Fung's QLV form

$S_f = \int_{-\infty}^{t} G(t-\tau) \frac{\partial E_f(\tau)}{\partial \tau} d\tau$ with: $G(t) = G_0 g(t)$ and:

$g(t) = \frac{1 + a\int_0^{\infty} f(\tau) e^{-\frac{t}{\tau}} d\tau}{1 + a\int_0^{\infty} f(\tau)\, d\tau}$ with: $f(t) = e^{-pt}$ and: a, constant

As stated above for skeletal muscle, in case this model would appear too complex for a finite element implementation, I have suggested the alternative choice of Tong's exponential biaxial constitutive relationship (Tong 76):

$$W = f(\alpha, \mathbf{E}) + \frac{c}{2} e^{F(a,\mathbf{E})} \qquad f(\alpha, \mathbf{E}) = \frac{1}{2}\left(\alpha_1 E_{11}^2 + \alpha_2 E_{22}^2 + 2\alpha_4 E_{11} E_{22}\right) \tag{4.46}$$

$$F(a, \gamma, \mathbf{E}) = a_1 E_{11}^2 + a_2 E_{22}^2 + a_3 E_{12}^2 + 2a_4 E_{11} E_{22} + \gamma_1 E_{11}^3 + \gamma_2 E_{22}^3 + \gamma_4 E_{11}^2 E_{22} + \gamma_5 E_{11} E_{22}^2$$

or Allaire's human vivo skin model (Allaire 77): $\begin{cases} W = C_1(I_1 - 3) + C_2(I_2 - 3) + g(I_3) \\ g(I_3) = C_3(I_3 - 1)^2 - (C_1 + 2C_2)(I_3 - 1) \end{cases}$ (4.47)

4.4.2 Finite Element Meshing

The choice of the element type for finite element meshing depends on the type of analysis to be performed and the expected level of precision. The common finite element software provides extended libraries of element types, depending on the number of geometrical and integration nodes, as well as on their disposition and associated properties. The meshing procedure is therefore closely related to the intrinsic properties of the material and consists of an entire step in the modeling approach. On this basis, I have made suggestions regarding the way soft tissue meshing and simulation could be achieved.

Volume Meshing. Our goal in CHARM was Three-Dimensional modeling of the skeletal soft-tissues, so volume element meshing seems appropriate. Principally two kinds of shapes are available for volume elements: tetrahedrons and hexahedrons (Fig. 4.4). Given the complex shapes of muscles, I have suggested the use of tetrahedron elements.

Line Meshing. The deformation of the tendon is strongly oriented in the direction of the fibers. Its volume is also reduced compared to muscle volume. Therefore, in compatibility with the choice of a 1-D constitutive relationship, I have suggested applying a 1-D meshing in the direction of the tension, and to generate volume deformation in assuming incompressibility using a constriction coefficient such as the Poisson ratio ν.

Surface Meshing. The specification of skin modeling is more difficult because of the great variability of its structure and properties around the body. Furthermore, constitutive equations for skin usually account for the epidermis and dermis only: because of its low resistance to tension, in mechanical experiments, the hypodermis is often removed from the upper layers. A simple approach would have been to apply the skin constitutive relationship to the three layers considered as a whole. However, as the mechanical properties of the hypodermis are quite different from those of the upper layers, and have significant influence on the overall behavior of skin, it would be more convenient to distinguish between the constitutive relationships of the upper and subcutaneous layers in the model. I have therefore suggested using two-layered thick composite shell elements with a different constitutive relationship for each of the layers (Fig. 4.20). Besides, no relationship is available for hypodermis. I have consequently proposed using a simple incompressible linear viscoelastic law or the same relation as the one for epidermis and dermis, with different parameters. Concerning the geometry, I have suggested considering a uniform thickness for the upper layer, while specifying a nodal thickness for the hypodermis layer so as to account for variations of its thickness.

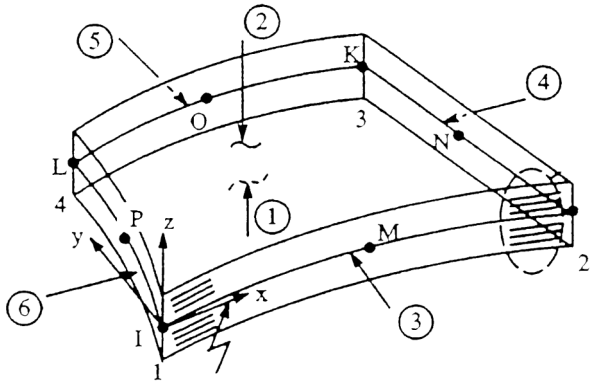

Fig. 4.20. 3D-shell finite element for skin (Ansys Manual)

Interconnections Modeling. In real motion, the in-vivo deformation of the different anatomical structures do not occur successively: they happen simultaneously and depend on each other. The deformation of an isolated contracting muscle will not be the same as that of a muscle connected to bones by tendons, and compressed by other deforming muscles. Therefore, the deformation computation must be performed simultaneously on the different muscles involved in the motion. For this purpose, common finite element software usually provides a set of interface elements allowing the resolution of contact dynamics. Mainly two cases appear: *static contacts*, for which nodes on both socks may be matched together, and *sliding contacts* which involve friction and relative displacements of surfaces. In the human anatomical structure, although some may be separated more easily than others, all layers appear more or less tied to their neighbours by a network of infiltrating collagen fibers. Hence, epidermis, dermis, hypodermis, fascia, muscles, tendons and bones are all embedded in the same continuous collagenous network. Therefore, I have suggested using *static interface* elements for the simultaneous deformation of the different structures.

However, given the complexity of the analysis, I have suggested a simplification when considering the insignificance of skin tension on muscle deformation. Skin is much more flexible and lighter than the other soft tissues. It may be assumed that it will just adjust to the deformation of the other stronger soft tissues rather than produce a change in their equilibrium state. My suggestion has therefore been to compute the deformation of all involved muscles together, and post-process the deformation of skin for each step of the analysis so as to fit onto the outer surface of all internal objects. Instead of using interface elements and specifying loads as input, the constraints for skin deformation analysis would thus be the nodal displacements so as to fit onto the deformed envelope of muscles.

4.4.3 Muscle Contraction Simulation

Muscle effective modeling requires taking into account its specific contractile properties. The activable stresses induced in the muscle body (depending on its length and shortening velocity) must be modeled by accounting for their actual fiber-oriented distribution through the volume as well as for their resulting force at the tendon extremity.

Two types of muscle contraction models may be found in the literature. One considers the macroscopic effects of contraction at the extremity of the tendon – for example Zajac's model (Zajac 86, 89) – while the other one considers the internal contractile mechanism at the sarcomeral level – for example Huxley's model (Huxley 57, 71, 74) – and formulates its force on the basis of its kinetics. These models are complementary. In CHARM, both properties are required. On one hand, the coincidence of the model output force with the measured muscle force is a priority, as a basis for skeletal motion simulation, but on the other hand the accurate modeling of the internal contraction stress is the basis for a realistic simulation of the muscle deformation.

As far as I have investigated the literature, I have not found a muscle model integrating both aspects of the real contraction phenomenon. For this reason, I have developed and suggested an alternative approach, with full respect to the finite element implementation perspectives, for modeling the muscle fiber contraction stress in relating the macroscopic and structural aspects of this phenomenon. This approach is described in the following (Maurel 98).

Considering the fact that, in the muscle, the fibers are organized resembling a flow, similar in a way to the flow-lines considered in fluid mechanics or in electromagnetism, the structural properties of muscle may be described by means of a mathematical approach.

Muscle may be viewed as a continuous deforming Three-Dimensional object $\mathcal{M}$, in which each point may be described with respect to the local coordinate system $(\mathbf{x}_1, \mathbf{x}_2, \mathbf{x}_3) \equiv (\mathbf{x}, \mathbf{y}, \mathbf{z})$ of the muscle. The deformation may be also described with respect to a global reference frame $(\mathbf{X}_1, \mathbf{X}_2, \mathbf{X}_3)$ corresponding to the reference configuration of the muscle. For a given muscle, the fibrous structure may be described by means of a vector field function **d**, defining for each point P of the muscle $\mathcal{M}$, the unitary tangent vector to the fiber f.

Considering the different pennate configurations represented in Fig. 4.21, I have globally assumed three types of muscle fiber distribution: *fusiform*, *triangular*, and *spiral* (Fig. 4.22-4.24) (Maurel 98).

The Contraction Force Function. In a muscle, the fibers may have, at a given time, different strengths (resp. cross-section) as well as different activation rates. According to Winter, the smaller units are recruited before the larger ones, and released in the reverse order. The inner fibers are usually powerful, while the outer ones generally stand for refining the force developed by the actuator (Winter 90). Thus, it may be interesting to describe the strength, activation and contraction force distributions as mathematical functions of the muscle geometric space.

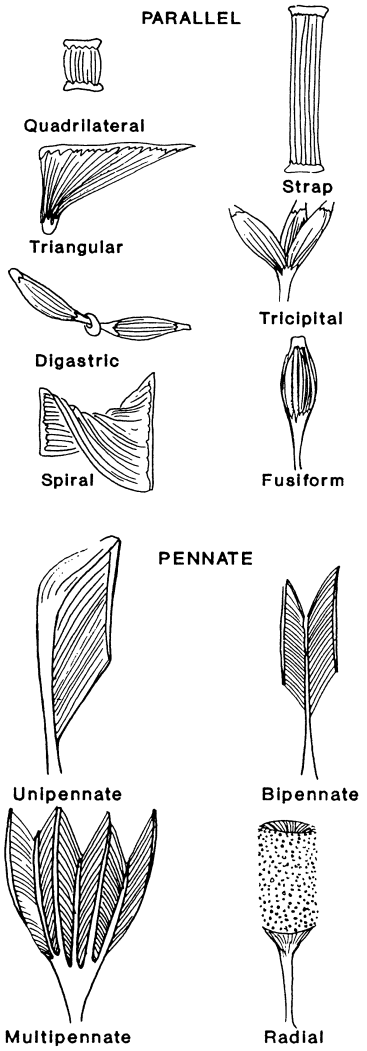

(Cutts 93)

Fig. 4.21. Muscle pennations

For this purpose, I have defined the contraction force vector at a point P, as a function $\mathbf{f}^C$ as:

$$\forall P \in \mathcal{M} \qquad \mathbf{f}^C(P) = -f^C(P)\,\boldsymbol{\delta}(P) \qquad \text{with:} \qquad f^C(P) = a(P)\,s(P)\,f^M(l^M, v^M) \tag{4.48}$$

where: $s(P)$ and $a(P)$ are the *strength scale* and *activation scale* distribution functions
$\boldsymbol{\delta}(P)$ is the unitary vector along the local contraction force direction
f^M is the *uniform contraction force* at maximum activation

The uniform contraction force f^M may be defined as the muscle contraction force value on the force-length-velocity diagram invoked in § 3.3.1. It is assumed uniform across the muscle and only depends on the muscle length and shortening velocity, since it does not include the fiber direction, strength and activation. Approximately, f^M may be estimated using the force-length and force-velocity diagrams (see Fig. 3.18, 3.19) as: (4.49)

$$f^M = \frac{P^M\left(l^M, v^M\right)}{V_0^M} \qquad \text{with:} \quad P^M\left(l^M, v^M\right) \text{ force defined by the force-length-velocity diagrams}, \quad V_0^M \text{ initial muscle volume}$$

Fusiform. As shown in Fig. 4.22, the fibers of a fusiform muscle may be represented by parabolic curves, with the equation in cylindrical coordinates (ρ,θ,z) (Maurel 98): (4.50)

$$\rho(z)=\rho_0\left(1+a_F z^2\right) \quad \text{for} \quad (\theta,z)\in[0,2\pi]\times[-h,h] \quad \text{with:} \quad (\rho_0,\theta_0)\in[0,r_2]\times[0,2\pi] \quad \text{and:} \quad a_F=-\frac{r_2-r_1}{r_2 h^2}$$

Then, the fiber direction at a point $P(\rho,\theta,z)$ may be defined by the function: (4.51)

$$\mathbf{d}:\ P(\rho,\theta,z)\mapsto \mathbf{d}(P)=\begin{bmatrix} d_\rho=\dfrac{2a_F\rho z}{1+a_F z^2} \\ d_\theta=0 \\ d_z=1 \end{bmatrix}$$

with: $$\rho_0=\frac{\rho}{1+a_F z^2}$$

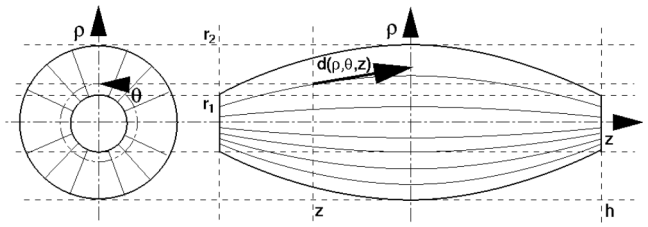

Fig. 4.22. Fusiform muscle description (Maurel 98)

Triangular. As shown in Fig. 4.23, the fibers of a triangular muscle may be represented by straight lines with the equation in Cartesian coordinates (x,y,z) (Maurel 98): (4.52)

$$y(z)=y_0\left(1+a_T z\right) \quad \text{for} \quad (x,z)\in\left[-\frac{e}{2},\frac{e}{2}\right]\times[0,h] \quad \text{with:} \quad (x_0,y_0)\in\left[-\frac{e}{2},\frac{e}{2}\right]\times[0,r_1] \quad \text{and:} \quad a_T=\frac{r_2-r_1}{r_1 h}$$

Then, the fiber direction at a point $P(x,y,z)$ may be defined by the function: (4.53)

$$\mathbf{d}:\ P(x,y,z)\mapsto \mathbf{d}(P)=\begin{bmatrix} d_x=0 \\ d_y=\dfrac{a_T y}{1+a_T z} \\ d_z=1 \end{bmatrix}$$

with: $$y_0=\frac{y}{1+a_T z}$$

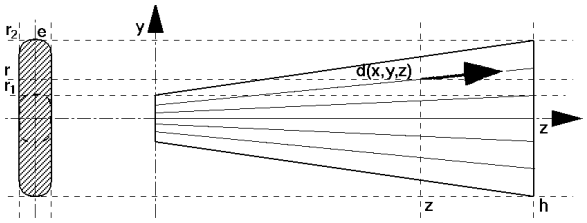

Fig. 4.23. Triangular muscle description (Maurel 98)

Spiral. As shown in Fig. 4.24, the fibers of a spiral muscle may be represented by straight lines, with equation in cylindrical coordinates (ρ,θ,z) (Maurel 98): (4.54)

$$\begin{cases}\rho=\dfrac{\rho_0}{\cos\theta} \\ z=a_S\left(\theta-\theta_0\right)\end{cases} \quad \text{with:} \quad \begin{cases}\theta_0=-\dfrac{\alpha}{2} & \text{for} \quad \theta\in\left[-\dfrac{\alpha}{2},\dfrac{\alpha}{2}\right] \\ \theta_0=\pi-\dfrac{\alpha}{2} & \text{for} \quad \theta\in\left[\pi-\dfrac{\alpha}{2},\pi+\dfrac{\alpha}{2}\right]\end{cases} \quad \text{with:} \quad a_S=\frac{h}{\alpha} \quad \text{and:} \quad \rho_0\in[0,r]$$

Then, the fiber direction at a point $P(\rho,\theta,z)$ may be defined by the function: (4.55)

$$\mathbf{d}:\ P(\rho,\theta,z)\mapsto \mathbf{d}(P)=\begin{bmatrix} d_\rho=\rho\tan\theta \\ d_\theta=\rho \\ d_z=a_S \end{bmatrix}$$

with $$\rho_0=\rho\cos\theta$$

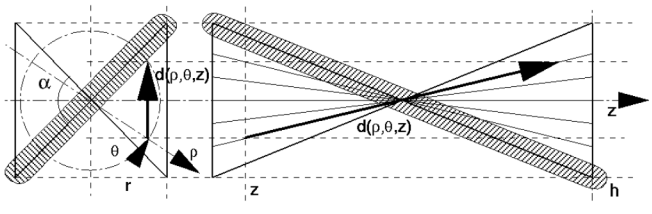

Fig. 4.24. Spiral muscle description (Maurel 98)

Considering the physiological and structural properties, as well as the previous mathematical descriptions, the following statements arise: (a^f, s^f, f^f) fiber constants at current time

$$\forall P \in \mathcal{M} \qquad \boldsymbol{\delta}(P) = \frac{\mathbf{d}(P)}{\|\mathbf{d}(P)\|} \qquad \text{and:} \qquad f^M(l^M, v^M) = f^{\mathcal{M}} \text{ ("uniform")} \tag{4.56}$$

$$\forall P \in f \qquad a(P) = a^f \qquad s(P) = s^f \qquad \mathbf{f}^C(P) = a^f s^f f^M(l^M, v^M) = f^f \tag{4.57}$$

Thus, the fibers may be viewed as the *iso-strength*, *iso-activation*, and *iso-tension* lines of the muscle, to which the contraction force vector $\mathbf{f}^C$ is always tangent, and to which the strength and activation gradient vectors are always normal (Maurel 98):

$$\forall P \in f \qquad \mathbf{f}^C(P) = f^f \boldsymbol{\delta}(P) \qquad f^f \text{: constant at current time} \tag{4.58}$$

$$\forall P \in \mathcal{M} \qquad \nabla a(P)\, \boldsymbol{\delta}(P) = 0 \qquad \nabla s(P)\, \boldsymbol{\delta}(P) = 0 \tag{4.59}$$

These properties may be used to formulate the contraction force,strength and activation scales distribution functions for muscle contraction simulation. For simplicity, in the following, I have grouped the strength and activation scales distribution functions $s(P)$, $a(P)$, under the same factor $\omega(P)$ that may be named the *active strength scale*, so that:

$$\forall P \in \mathcal{M} \qquad \mathbf{f}^C(P) = \omega(P)\, f^M(l^M, v^M)\, \boldsymbol{\delta}(P) \qquad \text{with:} \quad \omega(P) = a(P)\, s(P) \quad \nabla\omega(P)\, \boldsymbol{\delta}(P) = 0 \tag{4.60}$$

Fusiform: $\omega(P)$ must be a positive, decreasing function of ρ. I have suggested:

$$\frac{2a_F \rho z}{1 + a_F z^2} \frac{\partial\omega(P)}{\partial\rho} + \frac{\partial\omega(P)}{\partial z} = 0 \qquad \text{from (4.51) and (4.60), leading to:}$$

$$\omega_F(\rho, \theta, z) = \omega_F^0 + \Omega_F e^{-\left(\frac{\varpi_F y}{1 + a_F z^2}\right)^{\eta_F}} \qquad \text{with:} \quad \left(\omega_F^0, \Omega_F, \varpi_F, \eta_F\right) \equiv \text{constants at t} \tag{4.61}$$

Triangular: $\omega(P)$ must be a positive, decreasing function of y. I have suggested:

$$\frac{a_T y}{1 + a_T z} \frac{\partial\omega(P)}{\partial y} + \frac{\partial\omega(P)}{\partial z} = 0 \qquad \text{from (4.53) and (4.60), leading to:}$$

$$\omega_T(x, y, z) = \omega_T^0 + \Omega_T e^{-\left(\frac{\varpi_T y}{1 + a_T z}\right)^{\eta_T}} \qquad \text{with:} \quad \left(\omega_T^0, \Omega_T, \varpi_T, \eta_T\right) \equiv \text{constants at t} \tag{4.62}$$

Spiral: $\omega(P)$ must be a positive, decreasing function of ρ, and independent on z, since for spiral muscle, z is proportional to θ whichever the point. I have suggested:

$$\rho \tan\theta \frac{\partial\omega(P)}{\partial\rho} + \frac{\partial\omega(P)}{\partial\theta} + a_S \frac{\partial\omega(P)}{\partial z} = 0 \qquad \text{from (4.55) and (4.60), leading to:}$$

$$\omega_S(\rho, \theta, z) = \omega_S^0 + \Omega_S e^{-(\varpi_S \rho \cos\theta)^{\eta_S}} \qquad \text{with:} \quad \left(\omega_S^0, \Omega_S, \varpi_S, \eta_S\right) \equiv \text{constants at t} \tag{4.63}$$

Finally, for any type of muscle, time-dependency may be introduced in the active strength scale $\omega(P)$ by means of factor functions $\omega_m^0(t)$, $\Omega_m(t)$, $\varpi_m(t)$, $\eta_m(t)$. Suggestions towards finite element implementation for contraction simulation are presented in the following.

Application. Taking into account the geometric nature of the contraction force description, profit may be made of the finite element discretization by applying on the mesh nodes, contraction forces calculated from the discretized contraction force distribution. For this purpose, it is necessary to refer back to the original formulation of the equation of motion. Given the structural and functional constitution of muscles described in § 3.3.1, the active contraction phenomenon appears as arising from multiple contractile mechanisms, microscopically inserted within the passive constituents of the muscle material. Thus, the contraction force appears as internal stresses distributed through the muscle volume, though it rather belongs, in nature, to the group of external actions applied onto the muscle material. Under these microscopic actions, the muscle deforms by involving its passive elastic and viscoelastic properties. As a result of this description, the equations of motion may be written as follows:

Force balance: $$\int_v \rho \boldsymbol{\Gamma}^v \, dv = \int_v \mathbf{f}^v \, dv + \int_s \mathbf{t}^s \, ds + \int_v \mathbf{f}^c \, dv \tag{4.64}$$

Moment balance: $$\int_v \rho \boldsymbol{\Gamma}^v \wedge \mathbf{x} \, dv = \int_v \mathbf{f}^v \wedge \mathbf{x} \, dv + \int_s \mathbf{t}^s \wedge \mathbf{x} \, ds + \int_v \mathbf{f}^c \wedge \mathbf{x} \, dv \tag{4.65}$$

where $\boldsymbol{\Gamma}^v$ is the acceleration of point P, $\mathbf{t}^s$ the external stress on ds
$\mathbf{f}^v$ is the external body force, $\mathbf{f}^c$ the contraction force (see 4.48)

Following § 4.1.2, the Lagrangian virtual work equation may be developed as:

$$\delta\hat{W}^{acc} = \delta\hat{W}^{ext} + \delta\hat{W}^{int} \quad \text{with:} \quad \begin{aligned} \delta\hat{W}^{acc} &= \int_V \delta\hat{\mathbf{u}}^T \rho \boldsymbol{\Gamma}^V \, dV && \text{inertial virtual work} \\ \delta\hat{W}^{int} &= -\int_V \mathrm{Tr}\left(\delta\mathbf{E}^T\mathbf{S}\right) dV = -\int_V \delta\hat{\boldsymbol{E}}^T \boldsymbol{S} \, dV && \text{internal virtual work} \\ \delta\hat{W}^{ext} &= \int_V \delta\hat{\mathbf{u}}^{fT}\left(\mathbf{f}^V + \mathbf{f}^C\right) dV + \int_S \delta\hat{\mathbf{u}}^{tT}\mathbf{t}^S\mathbf{n} \, dS && \text{external virtual work} \end{aligned} \tag{4.66}$$

with: $\mathbf{f}^V$, $\mathbf{f}^C$, $\mathbf{t}^S$ Lagrangian equivalents of the Eulerian forces $\mathbf{f}^v$, $\mathbf{f}^c$, $\mathbf{t}^s$: $\mathbf{f}^C = J\,\mathbf{G}\,\mathbf{f}^c$

The incremental formulation may then be developed for the contraction force $\mathbf{f}^C$ in the form:

$$\mathbf{f}^C_{n+1} = \mathbf{f}^C_n + \Delta\mathbf{f}^C \quad \text{with:} \quad \Delta\mathbf{f}^C(P) = \Delta\mathbf{f}^\omega(P) + \Delta\mathbf{f}^M(P) + \Delta\mathbf{f}^\delta(P) \quad \text{and:} \quad \boldsymbol{\partial}_n = \mathbf{G}_n\boldsymbol{\delta}_n \tag{4.67}$$

with $\boldsymbol{\partial}$: Lagrangian equivalent of the fiber direction $\boldsymbol{\delta}$ (see 4.56)

$\Delta\mathbf{f}^\omega(P) = J_n\Delta\omega(P)\,f_n^M\left(l^M, v^M\right)\boldsymbol{\partial}_n(P)$ due to the active strength scale change

$\Delta\mathbf{f}^M(P) = J_n\omega_n(P)\,\Delta f^M\left(l^M, v^M\right)\boldsymbol{\partial}_n(P)$ due to the uniform force change

$\Delta\mathbf{f}^\delta(P) = J_n\omega_n(P)\,f_n^M\left(l^M, v^M\right)\Delta\boldsymbol{\partial}_n(P)$ due to the fiber direction change

and a corresponding incremental finite element virtual work equation may be formulated as:

$$\mathbf{M}_n\ddot{\mathbf{U}}_{n+1} + \left(\mathbf{K}_n^L + \mathbf{K}_n^{NL}\right)\Delta\mathbf{U} = \mathbf{L}_{n+1} - \mathbf{R}_n + \Delta\mathbf{R}_n^\omega + \Delta\mathbf{R}_n^M + \Delta\mathbf{R}_n^\delta \quad \text{with:} \quad \Delta\mathbf{R}^i = \int_V \mathbf{H}^T\Delta\mathbf{f}^i\left(\mathbf{U}, \dot{\mathbf{U}}\right) dV \tag{4.68}$$

Finally, in applying parallel finite element discretizations, over the muscle mesh, of the fiber direction, active strength scale and uniform contraction force distribution functions, $\boldsymbol{\partial}$, ω and f^M, it would be possible to express $\Delta\mathbf{f}^M(P)$ and $\Delta\mathbf{f}^\delta(P)$ as functions of $\Delta\mathbf{U}$, whereas the nodal active strength scale increment vector $\Delta\mathbf{w}$ could be left as open variable for the control of the contraction.

As a result, the contraction process could be simulated following a manner similar to reality. A change of activation yields an active strength scale increment Δw, which itself yields an increment $\Delta \mathbf{f}^c$ of the contraction force, which exerts on the passive muscle tissue along distributed fiber directions and produces the deformation. Simultaneously, the deformation yields a change in the internal passive stress, as well as a change in the uniform contraction force f^M that the sarcomeres can develop. The system then deforms so that the passive stress equilibrates the contraction force and the external loads. As opposed to the simulation of passive behavior, though increments of external load may still be added at each step, the real input here would be the change of activation by means of the nodal active strength scale increment vector $\Delta \mathbf{w}$. This would then leave to the user the responsibility of learning how to activate the muscle model for exerting a load or controlling its contraction, in the same way humans learn how to control their force and to refine their gestures (Maurel 98).

Model Limitation. Though the proposed approach may be convenient in practice for simulating muscle contraction, its appropriateness for effectively representing the mechanical phenomena involved in a real contraction must be declared *relative*. The reason is given here. As described in Chapter 3, muscle is a composite material composed of passive tissues and activable contractile fibers. On this basis, the internal state of stress is bound to be different whether it is considered in one tissue component or the other. In particular, during an active contraction, the stress inside the contractile fibers is bound to increase in tension whereas the stress inside the surrounding passive tissues is bound to increase in compression. This opposite stress evolution depending on the location in the muscle may be easily described by referring to Hill's three-element model: during active contraction, the series element SE tends to be extended by the shortening of the contractile element whereas the parallel element PE tends to shorten (Fig. 3.12).

In order to take this phenomenon into account in the simulation, it would be necessary to distinguish, throughout the muscle volume, the geometric domains representing the respective components and to apply to them distinct respective constitutive relationships. This way, the contractile fibers and passive tissues could be distinctly modeled, in the mesh geometry as well as in the mechanical behavior, particularly by using for the contractile fibers a specific constitutive relationship accounting for the active behavior. Consequently, the simulation of muscle contraction would result from a different process than the one I proposed in this section. Instead of taking the form of an external contractile force applied to a fully passive tissue, the contraction would result from an internal change in the mechanical state of the contractile fibers, induced by a change of activation. This change of internal state of stress of the contractile fibers would affect the equilibrium of the medium, which would then evolve and stabilize by compressing the surrounding passive tissues.

Though accurate, such an approach is particularly complex as it requires to handle the continuity between the distinct continuous media. In our case, although the modeling of the active and passive behaviors of muscle was intended, the modeling of the internal, fibrous, composite structure of the tissues was out of our scope in CHARM. Although this does not prevent from distinctly modeling the respective constitutive behaviors of the active and passive components of the muscle material, the assumption of a continuous muscle material prevents from their distinct simulation: *the state of stress in a point of the medium is unique, and cannot correspond to a state of tension and compression at the same time*. Furthermore, given the purpose of contraction simulation, the evolution of the state of stress in the muscle must be towards a reduction of the state of tension or an increase of the state of compression.

On this basis, the accurate approach would consist of distinguishing in the global constitutive relationship the stress contributions of the contractile fibers and surrounding passive tissues, with care to the fact that the resulting behavior during simulation should be the one described in the previous sentence. This is actually the approach which has been followed by the IST partners in CHARM, which is detailed in § 5.4.2. By contrast, this is not the case of the approach I have proposed in this section for muscle contraction simulation. With respect to the analysis developed here, my approach does not properly describe the real phenomenon of contraction. It represents the contraction as resulting from external compressive forces applied on a fully passive material, whereas the contraction is a complex phenomenon, which operates by modifying the mechanical state of the material from the inside. Following this, it must be borne in mind that my approach does not actually model the contraction phenomenon as it happens in reality, but only proposes to obtain equivalent deformations in accounting for anatomical and biomechanical data.

Conclusion

It is not possible to collect and review all the existing biomechanical models without losing the understanding of the natural mechanical behavior common to all of them. The purpose of this chapter was rather to outline more or less the different forms they can take. Distinction may be made whether they are *uniaxial* or *multi-dimensional, elastic* or *viscoelastic, phenomenological* or *structural*, and with respect to the tissue they model. Most of the approaches followed could have been applied indiscriminately to tendon, passive muscle, passive heart, skin, lung... The Quasi-Linear Viscoelasticity theory proposed by Fung and its application with Three-Dimensional structural hyperelastic constitutive relationships, however, emerge from this analysis as the most general forms to be used for an appropriate simulation of the soft tissue biomechanics. Following the real deformation phenomenon, muscle contraction may then be simulated step-by-step within an incremental process generating muscle shortening, tendon lengthening, skeletal motion, and skin deformation. The effective selection, implementation and finite element simulation made by the IST partners of biomechanical models for muscle, tendon, and skin, are presented in the following chapter together with the presentation of the other technical implementations achieved in CHARM.

5 CHARM Implementations

As a demonstration of my contribution to CHARM, the practical developments which have been achieved by the CHARM European team on the basis of my theoretical investigations, are presented in this chapter. This chapter has consequently been composed using the technical reports and publications provided by the concerned partners. The three-dimensional construction of the upper limb model achieved at the *University of Geneva* (UG) using the *Visible Human Data* of the *U.S. National Library of Medicine* is first presented. The presentation of the topological data structure and modeling tool implemented at UG with my collaboration then follows with that of the biomechanical topological model that I have designed at the *Ecole Polytechnique Fédérale de Lausanne* (EPFL) with the assistance of orthopedic specialists. This is followed by the presentation of the high-level interface developed at the *Ecole des Mines de Nantes* (EMN) and at the *Institut de Recherche en Informatique et Systèmes Aléatoires* (IRISA) for allowing the dynamic simulation of the model and the interactive control of its motion using various control strategies. Finally, the optimization analyses and finite element implementations achieved at the *Instituto Superior Técnico* of Lisbon (IST) for soft tissue deformation and muscle contraction simulation are presented. Brief descriptions of the developments led at the *Universitat de les Illes Balears* (UIB) for multi-modal matching and at the *Karlsruhe Universität* (UKA) for photorealistic rendering then conclude the chapter, illustrating the simulation achieved in the project.

5.1 3-D Reconstruction at UG

(This section has been composed using the reports and publications provided by UG)

5.1.1 The Visible Human Data

The first of the developments achieved in CHARM was the 3-D modeling of the human upper limb. This has been the responsibility of the *University of Geneva* (UG). The *Visible Human Data* from the *U.S. National Library of Medicine* was used for this purpose. This was decided so as to avoid data acquisition problems as well as benefiting from a complete standard data model. The data was provided in the form of low-resolution MRI frontal views, high resolution transverse CT images and cross-sectional colored cryosections of a male cadaver at an average interval of 1mm. These data could have been used as a sophisticated Voxel representation of the anatomy (Lorensen 95, Sims 96, Tiede 96). However, Voxel representation can not provide information on the structure and geometry of the anatomical components. The 3-D surface segmentation of the data was therefore engaged in order to identify on the images the spatial extents of the organs of interest. This concerned the bones, the musculotendons, the skin and the deep fascia (Fig. 5.1).

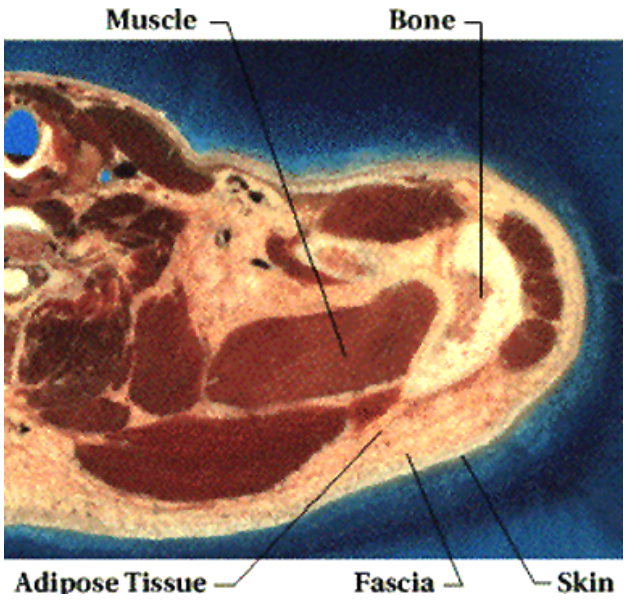

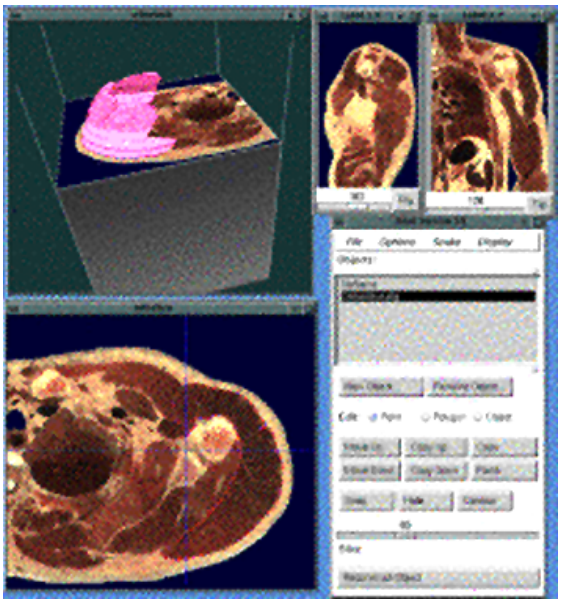

Fig. 5.1. A VHD cryosection (Gingins 96a,b) **Fig. 5.2.** The labeling tool (Gingins 96a,b)

5.1.2 Surface Reconstruction

The process of surface reconstruction may be divided into many steps: *preprocessing*, *labeling*, *reconstruction*, and *post-processing* (Baker 90, Udupa 91, Pommet 94). Preprocessing is necessary to convert the data into readable image files, reduce their resolution, and enhance them by filtering. These images may then be interpreted and labeled to identify the contours of the organs of interests. For this purpose, a labelling tool was developed, which allows the interactive semi-automatic segmentation of the anatomical components (Fig. 5.2) (Kalra 95). This tool compounds two main viewers, one for the 2-D images, called the *slice viewer*, and the other for the stack of images, called the *stack viewer*. The reconstruction axis may be chosen between axial, frontal or saggital, so that any organ may be extracted across its major axis. Other axial projections may be displayed in separate windows to help the interpretation. For interpretation, the user successively designs the contours in the form of closed polygons on the selected slices. These contours roughly correspond to the cross-sectional profile of the anatomical component considered. The exact fitting is then automatically achieved using *discrete snakes*, which realize the fitting of the contours to the maximum contrast neighbour points.

Snakes are useful in many circumstances, particularly in the presence of high contrast such as bones on CT images. They are characterized by a few parameters (such as elasticity, rigidity, and speed) (Kass 87). In order to ease manipulation, they are provided in the labelling tool with predefined settings dedicated to particular contouring problems (skin, bones, etc.). As contours are modeled as closed polygons, the discrete snake model was used. A 3-D generalization of the Sobel operator, combining edge detection and low-pass filtering, was applied to estimate the gradient of the image (Gonzalez 93). Besides this, structures present in successive slices were re-enforced by the contours of the neighbouring slices. The weight of the gradient component transverse to the slice was allowed to be tunable or even neglected in order to avoid confusing fittings to structures not visible in the current slice.

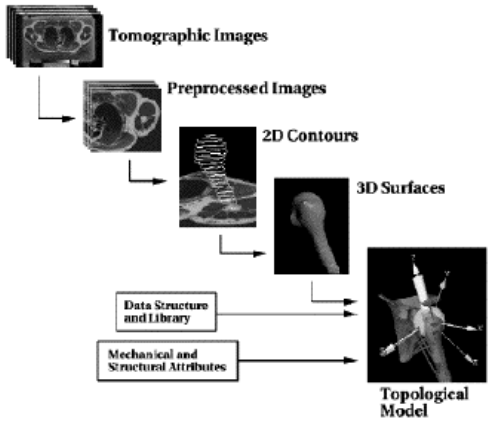

(Gingins 96a,b)

Fig. 5.3. Topological modeling pipeline

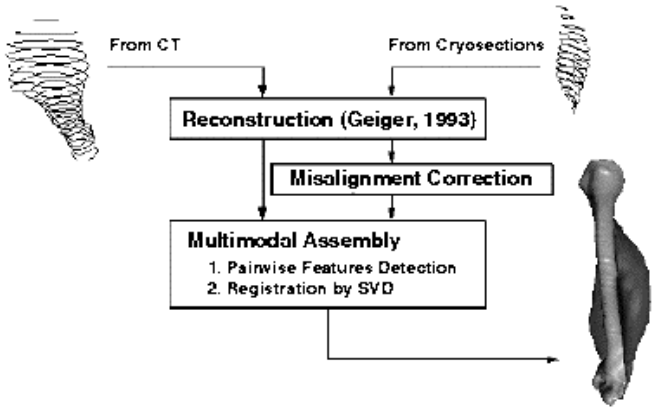

(Gingins 96a,b)

Fig. 5.4. 3D reconstruction and matching process

5.1.3 3-D Matching

Once a sufficient number of contours is defined, 3-D reconstruction is achieved by joining the contours of all the pertinent slices, yielding a 3-D surface of the anatomical component considered (Fig. 5.3) (Geiger 93, Elsen 93). Because of their high contrast, CT images were more appropriate for identifying bones and the outer skin surface, whereas the anatomical cryosections were especially used for soft tissues, which can not be extracted from the other modalities. As labelling was performed on different subregions of the complete dataset, *multi-modal matching* was then necessary as post-processing for correcting misalignments, insuring the consistency of the units and assembling the reconstructed components in the same space. For this purpose, a single global affine transform was determined from a set of corresponding feature points between the frozen CT and the cryosections, and applied to each reconstruction from the CT (Fig. 5.4).

Fig. 5.5 illustrates the reconstructed components of the left upper limb using the VHD. It includes all the vertebras, ribs, the shoulder and forearm bones and muscles as well as the skin and deep fascia in the elbow area. Despite the high resolution, distinction between adjacent muscles have relied on texture, fiber orientation, and sometimes pure anatomical knowledge.

The segmentation of the deep fascia needed for evaluating the local skin thickness, was achieved by tracing the surface of the muscle. In the absence of underlying musculature, some indirect criteria such as epifascial veins were used. The segmentation of the outer skin was more easily obtained from using the CT or the cryosections as the embedding medium is in clear contrast to the color of the skin (Gingins 96a,b).

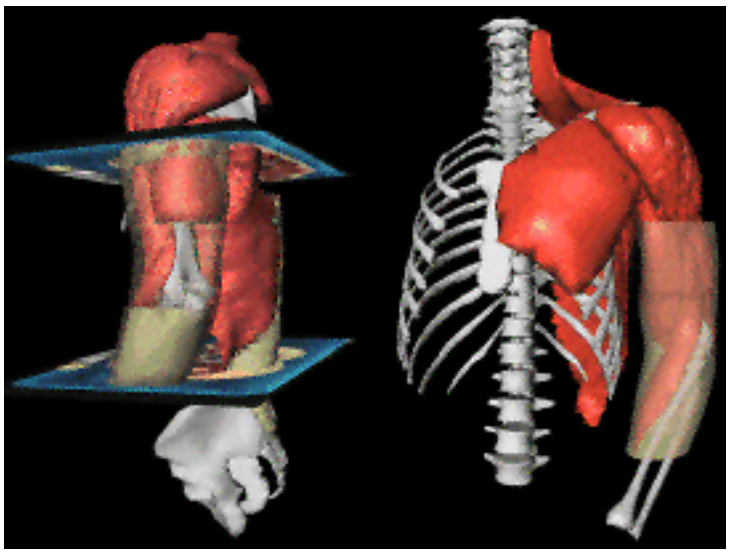

Fig. 5.5. The 3-D upper limb model

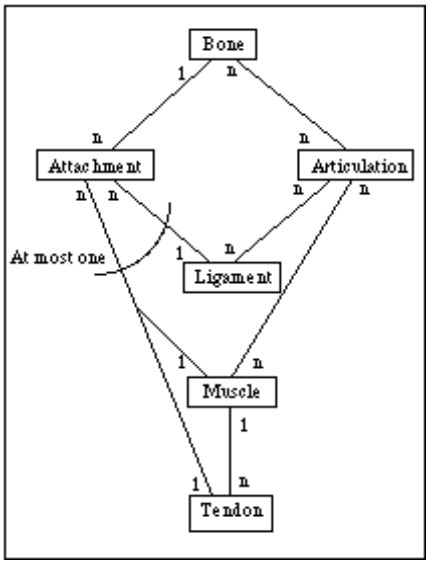

(Kalra 95)

Fig. 5.6. Classes cardinality

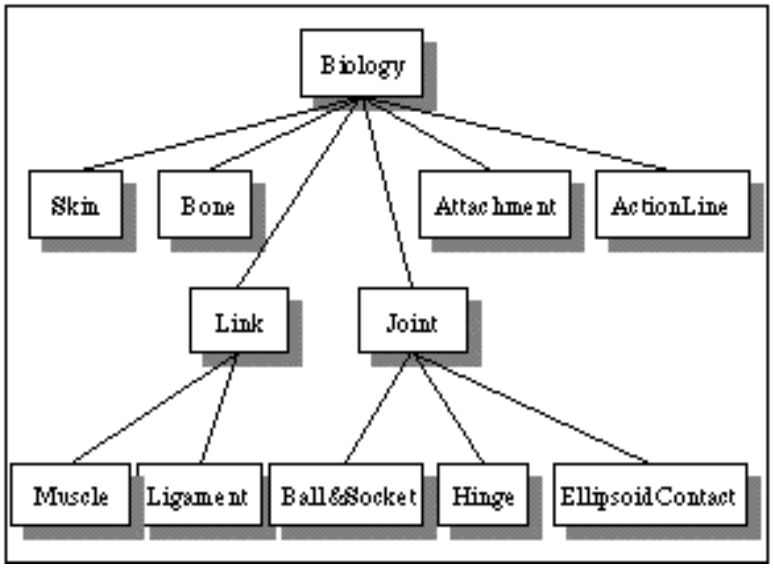

(Gingins 96a,b)

Fig. 5.7. Extended topological data structure

5.1.4 Data Structure Implementation

Once the 3-D reconstruction of the upper limb was achieved, an object-oriented database was developed on the basis of the theoretical biomechanical model presented in previous chapters, in order to associate mechanical and topological information to the geometric anatomical components. *Topology* in this context is defined as a 3-D connectivity graph of anatomical elements for a given body part (e.g. arm). It contains the reference for all the topological elements and their relations to each other. The topological relation in terms of connectivity of the elements can be drawn as shown in Fig. 5.6. The number shown on the arc connecting two different elements indicates the cardinality of the relationship, i.e. the manner in which the two elements are related. For example, there may be several attachments (n) on a same bone whereas there is only one bone (1) for an attachment. Besides this, the hierarchical relation provides the dependency constraints on the motion between the components of a body part. For example, the arm motion is subsequent to the motion of the shoulder (Kalra 95).

Mainly, six basic classes were thus implemented for encompassing the geometrical and physical attributes of the entities involved in the biomechanical model. These are the *Joint*, *Attachment*, *Action-Line*, *Muscle*, *Bone* and *Skin* Classes. A generic Class called *Biology* encompassing them all was also created, collecting the access functions common to all of them. Figure 5.7 shows the overall hierarchy. In order to allow the interactive creating, editing and saving of the database, an interactive interface, the topological modeler *tm*, was developed using the *Open Inventor* toolkit and the *Motif* widget library. The Open Inventor toolkit provides a library of methods for building and rendering 3-D scenes as well as for interacting with its components. The Motif library provides various widgets such as buttons, draggers and manipulators allowing the building of 2-D user interfaces. The topological modeler thus developed provides the user with an extensive 3-D visualization of the model as well as with the direct manipulation and interaction with its components (Beylot 96). The demonstration of the implemented data structure and topological modeler is detailed in the next section along with the presentation of the design of the topological model of human upper limb.

5.2 Topological Modeling at EPFL

5.2.1 Topological Modeling

The 3-D reconstructed skeleton remains a collection of independent geometrical bones in the database unless mechanical properties are attributed to them and interrelationships are defined between them. This involves the specification of kinematic parameters for joints, dynamic parameters for rigid-bodies, and muscle action topology. Following the development of the theoretical biomechanical human upper limb model, the conception of the data structure was done in collaboration with UG (Beylot 96) and the design of the topological model was achieved by myself at the *Ecole Polytechnique Fédérale de Lausanne* (EPFL) (Maurel 96) using the topological modeler *tm* developed at UG for this purpose. This is described below.

5.2.2 Joints

In § 2.3.3, the joint kinematics were described with three Cartesian and three Euler parameters, defining a 4x4 transformation matrix between reference and relative joint frames defined on the respective bones. In the database, the *Joint* class was thus designed to store:

- 3 Cartesian coordinates together with their minimum, maximum and resting values.
- 3 Euler angles together with their minimum, maximum and resting values.
- a *left*/*right* side status with the corresponding matrix calculation functions.
- 4x4 rigid transformation matrix defining each joint frame with respect to the bone frame together with its *reference*/*relative* status.

On the basis of the upper limb kinematic model (§ 2.3.2), three types of joints were derived:

- the *Ball_&_Socket* joint, owning 3 independent rotational parameters.
- the *Hinge* joint, owning 1 rotational parameter.
- the *Ellipsoid* joint, owning 3 independent rotational parameters and 2 angular latitude and longitude parameters defining the Cartesian position of the contact on the ellipsoid.

The interface of the topological modeler was thus designed so as to allow the creation of each of these joint types. The procedure for creation using tm is common to all of them: it is necessary, first, to place the *reference* (blue) and *relative* (pink) coordinate systems with respect to the associate bone anatomy, then to adjust the minimum, maximum and resting values of the parameters. The definition of the joint frames is approximate, since interactive. However, the interface offers adjustment features, like the permutation of a frame on its axes, or its alignment with respect to another existing frame, which aids error minimization in the design process. Besides this, sliders were made available for helping the setting of the extremum values of the parameters, by allowing the simulation of the range of motion of the joint (Maurel 96).

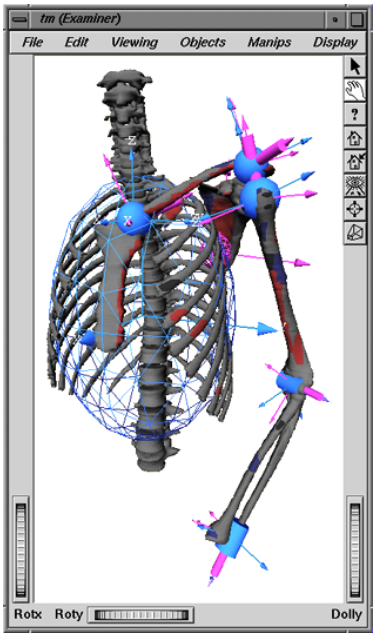

Fig. 5.8. Kinematic model (Maurel 99)

Proceeding with joints design, I have first adjusted coordinate systems for the thorax, the clavicle, the scapula, the humerus, the radius and the ulna for the left arm on the basis of van der Helm's and Pronk's definitions. I have then interactively fitted joints onto the 3D skeleton following the upper limb kinematic model presented in § 2.3.2 (Fig. 5.8, 5.9):

a) b) c)

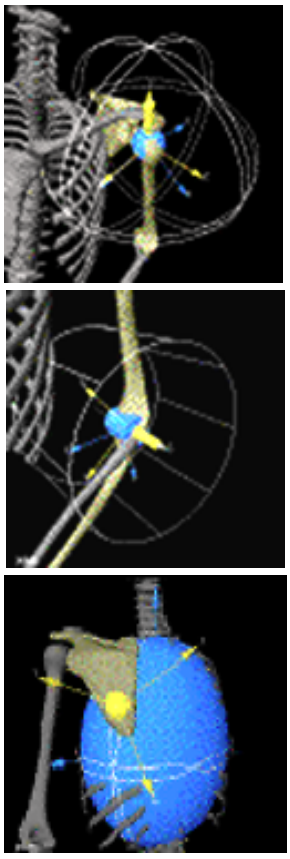

(Beylot 96)

Fig. 5.9. Joint models

- *Ball_&_Socket* joints (Fig. 5.9a) for the SC, AC and GH joints
- *Hinge* joints (Fig. 5.9b) for the UH and UR joints
- *Ellipsoid* joint (Fig. 5.9c) for the ST constraint

I have positioned the SC, AC, GH, UH and UR joints on their estimated anatomical *centers* on the respective bones, then successively aligned and derived their *reference* (blue) and *relative* (pink) coordinate systems by permutations and local rotations from those of the precedent joints or of the relevant bones (Maurel 96).

My coordinate systems differ thus from van der Helm and Pronk's definitions (Helm 95) only in the fact that I have orientated them so as to make them visible, unlike some of theirs. Concerning the forearm, as explained in § 2.3.1, I have implicitly taken the HR joint into account in the modeling of the UH and UR joints: their respective rotation axes were aligned through the anatomical location of the HR joint. Thus, this joint was not modeled. Concerning the ST joint, as the ST constraint has never been defined anatomically, I have followed van der Helm's finite element approach (Helm 94b), and fitted onto the thorax an ellipsoid joint bent backwards with respect to the sagital plane. I have finally defined boundary values for the parameters on the basis of anatomical data from the literature, whereas the resting state of the skeleton was automatically derived from the skeleton assembly. Corresponding joint data are collected in Appendix A.1.

5.2.3 Action Lines

In § 3.4.1, models for the action of the upper limb muscles were suggested in the form of action-line subdivisions. A basic *Action-Line* class was therefore implemented to model the lines along which muscle, tendons and ligaments develop forces. An action line consists of a set of successive arcs connecting the attachment sites of a spindle on the bones. The local direction of the force applied on a bone may thus be determined from the direction of the incident arcs. The Action-Line thus, contains:

- the ordered collection of arcs and attachments
- the mass parameter for finite element analysis
- the activation parameter of the muscle spindle
- the PCSA for the optimization analyses

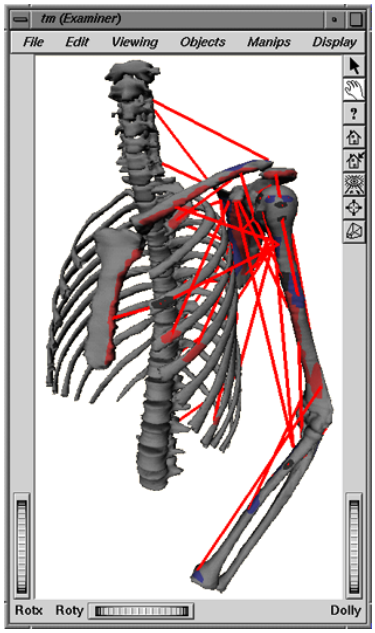

Fig. 5.10. Muscle action topology (Maurel 99)

The above implementation of the Action-Line class called for another one, the *Attachment* class. Attachments are the areas where tendons, ligaments and some muscles, are connected onto the bones. The Attachments terminating an action-line are called *origin* and *insertion.* They can be common to several action-lines of the same muscle as for the biceps and triceps insertions. An Attachment may also be a *guide*, constraining the path of an action-line without effective binding to the bone. This is the case for contact on the intertubercular groove of the humerus of the biceps long head tendon for example. The Attachment class thus includes:

- the geometry of the attachment as a collection of triangular facets of the 3-D bone
- the centroid point of attachment and its type: ORIGIN, INSERT, GUIDE, NONE

As a result of both implementations, a general *Muscle* class could be defined for representing structures involving one or more Action-Lines. The Muscle class was thus conceived as a collection of Action-Lines connecting Attachments defined on the bones. In some cases, a Muscle just consists of one single Action-Line. In order to save confusion between both structures, a distinction was forced by attributing to the Muscle class the parameters common to its action-lines. A Muscle Instance thus includes:

- the collection of its Action-Lines.
- the material strength parameter measuring the intrinsic strength of the muscle tissue.

For topological modeling of the muscle actions, I have preliminary defined for each Action-Line the Attachment sites by selecting sets of triangles on the bones and labelling them as *origin*, *insertion* or *guide.* I have then created the Action-Lines by the ordered selection of their defined Attachments, and complemented them with mass, strength and PCSA parameters based on biomechanical data. Muscles were then created on the basis of the defined Action-Lines and complemented with the material strength parameter (Maurel 96).

Following this procedure, I have modeled the action of all 22 muscles as defined in § 3.4.1 in the form of 34 Action-Lines as shown in Fig. 5.10 and Fig. 5.11. Two Action-Lines were designed for the *biceps brachii*, *serratus anterior*, *rhomboids* and *pectoralis major*, whereas the *deltoideus*, *triceps brachii*, *trapezius*, and *latissimus dorsi* muscles needed three. Besides this, several overlapping muscles required the definition of guiding areas on intermediate bones in order to consider the deviation of their Action-Lines between their origin and insertion sites. This concerns *the biceps long head*, the *deltoideus*, the *serratus anterior*, the *trapezius*, the *latissimus dorsi*, the *pronator teres* and the *anconeus*. Finally, as required by the optimization analysis, I have complemented the topological description with biomechanical data based on Veeger's data for mass, PCSA and material strength (Veeger 91). Data for the created action-line topology may be found in Appendix B.

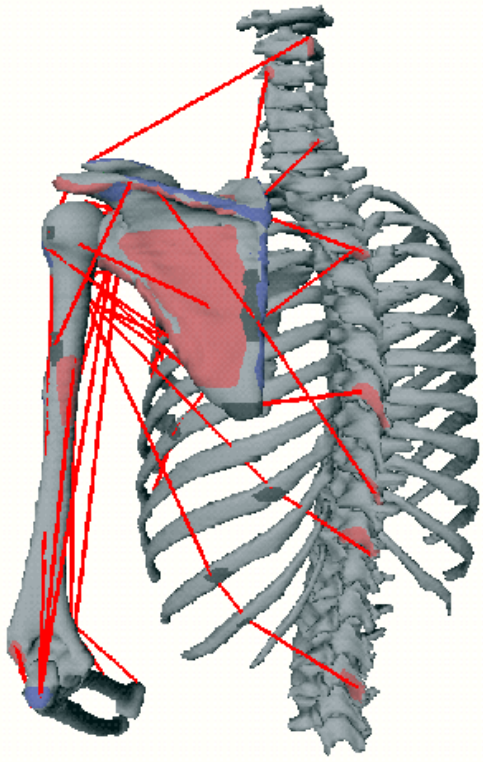

Fig. 5.11. Action-lines topology (Maurel 96)

5.2.4 Rigid Bodies

The rigid body analysis requires the definition of the mass and inertia matrix of the rigid body components as presented in § 2.3.4. However, these components do not appear as such in the data structure. The development of an overlaying rigid body class would have required implementing the relationships between their kinematics and those of the constituent bones. As these relationships are specific to the musculoskeletal system and the way it has been modeled, an interface allowing the entry of user defined functions to handle them would have been required. This alternative was rejected because it was too complex whereas the sharing of the rigid body properties among the constituent bones is much simpler. Besides this, a *Bone* class had been implemented to encompass the geometry of the bones as well as to provide a structural entity as a basis for Joints and Muscles construction. Rigid body properties have therefore been attributed to the Bone class, which thus contains (Maurel 96):

- the collection of Joints, Attachments and Action-Lines connected to it.
- the mass and inertia moduli parameter of the embedding rigid body.
- the 3x3 inertia matrix and the 4x4 transformation matrix defining the inertial frame with respect to the geometrical frame of the bone

Furthermore, it was assumed in § 2.3.4 that the rigid bodies associated to the arm and forearm bones could be modeled as rigid cylinders. A specific cylinder type of the bone class was then derived and made available in the topological modeler interface. This class therefore also accepts cylinder radius and height parameters for automatic calculation of the inertia matrix. I have thus modeled the rigid body properties for the arm and forearm by the interactive fitting of cylinders on each bone of the arm (Fig. 5.12). The mass, radius and height parameters were then adjusted with biomechanical data accounting for relations in § 2.3.4 (see Appendix A.3).

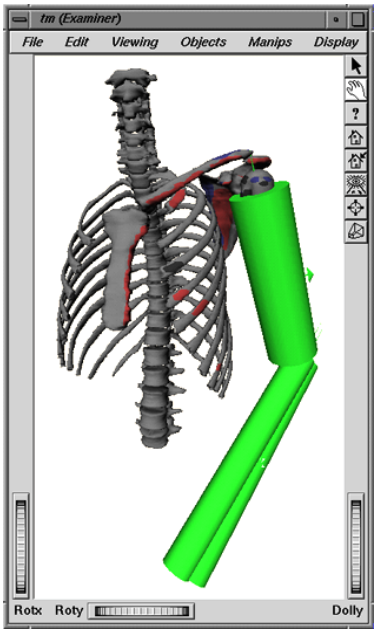

Fig. 5.12. Rigid body model (Maurel 99)

5.2.5 Skin

As skin is a continuous envelope of the musculo-skeletal body components, the design of a *Skin* class could have been complex if information concerning its connections had to be stored. In our case, we considered that the interface between skin and the underlying body components would be handled in the finite element deformation analysis of the soft tissues. Therefore, skin has been conceived as a single object composed of the reconstructed inner and outer surfaces, allowing the calculation of its local thickness for finite elements, and no specific setting feature for skin has been developed in the topological modeler (Beylot 96).

5.3 High-Level Motion Control at EMN/IRISA

(This section has been composed using the reports and publications provided by EMN/IRISA)

5.3.1 Dynamic Model Generation

Following the design of the 3-D topological human upper limb model, the development of a high level interface allowing the interactive motion control of the model was engaged under the responsibility of the *Ecole des Mines de Nantes* (EMN) and the *Institut de Recherche en Informatique et Systèmes Aléatoires* (IRISA). In order to allow the automatic derivation of the equations of motion of the model, two conversion processes were applied on the data, so as to fit with the requirements of the *NMECAM* dynamic simulator of IRISA (INRIA TR).

Hierarchical Representation. The first conversion consisted of derivating the hierarchical representation of the model from the database. A specific feature was thus added to the interface of the topological modeler, for allowing the specification of the hierarchy by giving the tree-like succession of joints. In such representations, loop conformations are not allowed. For this reason, it was necessary to break the closed-loop formed by the shoulder bones. The most natural approach was to open the loop at the scapulo-thoracic joint, remembering to further consider its influence in the motion control strategies as a constraint on the mechanism. Then, given that the database contains the global transformation of each bone with respect to the scene coordinate system, and the joint frame transformations with respect to the respective bone frames, the successive transformation matrices of the hierarchical structure were easily obtained. Figure 5.13 provides an example of hierarchical conversion of an open chain containing three bones.

The hierarchical structure is related to the non-hierarchical one by the relationships:

$$M_2 = N_1.N_{A1}.N_A.N_{A2} \qquad M_2.M_{B2} = N_1.N_{A1}.N_A.N_{AB} \tag{5.1}$$

$$M_3 = N_1.N_{A1}.N_A.N_{AB}.N_B.N_{B3} \qquad M_3.M_{C3} = N_1.N_{A1}.N_A.N_{AB}.N_B.N_{BC} \tag{5.2}$$

Taking into account that: $N_1 = M_1$ $N_A = M_A$ $N_{A1} = M_{A1}$ $N_{A2} = M_{A2}^{-1}$ $N_{B3} = M_{B3}^{-1}$

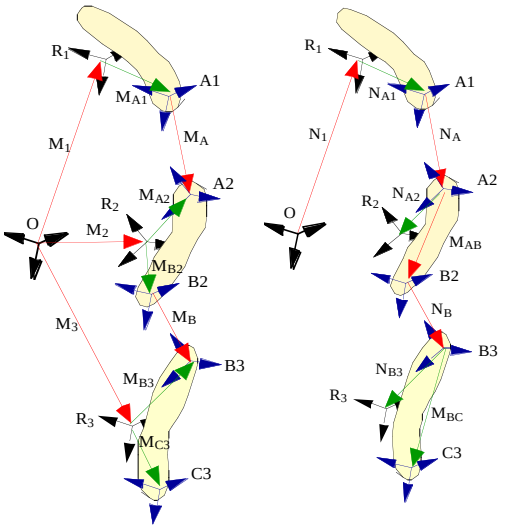

the matrices N_{AB}, N_{BC}, N_{A2} and N_{AB}, defining the position and orientation of the *son-frames* with respect to their *father-joints* may be extracted. The principle may be applied to any frame attached to the bones, in particular the geometrical, inertial and joint frames. Conversely, invoking that bones are linked by:

$$M_2.M_{A2} = M_1.M_{A1}.M_A \qquad M_3.M_{B3} = M_2.M_{B2}.M_B \tag{5.3}$$

it is possible with the given relationships to convert the hierarchical structure backward into a general non-hierarchical data structure representation.

Fig. 5.13. Equivalence between hierarchical (left) and non-hierarchical structure (right)

Muscle/Torque Conversion. The second requirement for using the NMECAM simulator was to represent muscle actions in the form of *equivalent torques* about respective joints (Fig. 5.14). The equivalent torque is the resulting torque engendered by a set of lineic forces around a joint. This conversion requires the determination of the effective moment arms of the forces. This information was easily derived from the designed muscle action topology presented in § 5.2.3. The complex architecture of the real musculature could thus be approximated around each joint by a unique equivalent muscle and the joint torques linearly related to the muscle forces using the matrix form (Meek 90):

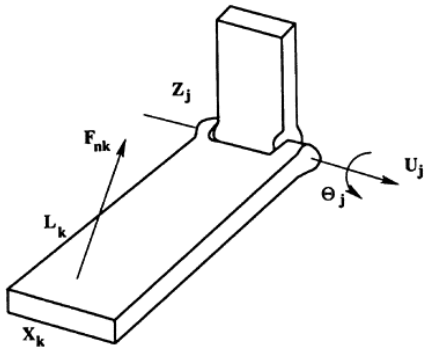

Fig. 5.14. Muscle acting about a Hinge

$$\boldsymbol{\tau} = \mathbf{A}(\mathbf{q})\mathbf{F} \qquad \text{with:} \qquad A_{jk} = \left[\left(\mathbf{x}_k - \mathbf{z}_j\right) \wedge \mathbf{l}_k\right] \cdot \mathbf{u}_j \qquad \text{(Multon 98)} \qquad (5.4)$$

where: $\mathbf{A}(\mathbf{q})$ is the anatomy matrix containing the muscle instantaneous moment arms
$\mathbf{x}_k$ is the point of attachment of the k-th muscle
$\mathbf{z}_j$ locates in space the unit vector of revolution $\mathbf{u}_j$ of the j-th joint
$\mathbf{l}_k$ is a unit vector of the effective line of action of the k-th muscle.

As a result of both conversions, the human body could be considered as a hierarchical model of rigid bodies linked with rotary joints suitable for a dynamic simulation with the NMECAM system. The major interest of this system is that the dynamic model and the associated parameters – like the kinetic energy or the kinematics values – are all computed in symbolic form. Based on the Lagrangian formulation, a set of second-order nonlinear differential equations was automatically generated together with efficient numerical C/C++ code. The provided topological and mechanical data such as joint frames, masses, inertias and muscle topology were fully taken into account in this process (Cozot 96).

ST Constraint Modeling. An interesting point to outline concerning the use of the NMECAM simulator is how the ST constraint has been taken into account in the model. Such constraints, like kinematic closed-loop structures, imply that additional forces exerted at the contact point must be taken into account. Two approaches may be followed for this purpose:

$$Q_i - \frac{d}{dt}\left(\frac{\partial C}{\partial \dot{q}_i}\right) + \frac{\partial C}{\partial q_i} + L_i \qquad \text{with } L_i \text{ in the form:} \qquad \text{(INRIA TR)} \qquad (5.5)$$

- The Lagrange multipliers: $L_i = \lambda \frac{\partial f}{\partial q_i} + \mu \frac{\partial g}{\partial \dot{q}_i}$ (5.6)

- The penalty scheme: $L_i = k \cdot \sum_h f \frac{\partial f}{\partial q_i} + k \cdot \sum_h g \frac{\partial g}{\partial q_i}$ (5.7)

where:

C, k	kinetic energy, penalty constant
L_i	sum of kinetic and potential energies relative to q_i
$q \equiv (q_i)_{i=1,n}$	generalized Lagrangian coordinates of the multibody system
Q_i	generalized given external effort relative to q_i
f, g	(holonomic, non holonomic), constraints

However, the Lagrange multiplier method has the major drawbacks of adding some unknowns to the system and of failing when antagonist constraints are applied to the mechanism. The penalty scheme method, more general and efficient, was therefore chosen. The ST constraint was thus included in the model in a form similar to that of an elastic link tending to reduce the distance of the scapular contact point to the thoracic ellipsoid. The model equation dynamics implemented, specific controllers adequate to the simulation of human arm motion were left to be designed (INRIA TR).

5.3.2 Motion Controlers Development

After reviewing the control theory and the various control schemes available, the different types of motions exhibited by the human arm were classified and identified with known control patterns, namely the *kinematic tasks*, the *reflex-like behavior* and *the dynamic servoing*. For each of these, a workable control scheme was suggested. Such control strategies consists of abstract classes that the experimenter can overload with its own computation methods or gain matrix. The resulting classes may then be used to develop plug-ins intended for an open simulation platform (Multon 98).

Kinematic Tasks. Kinematic tasks refers to slow movements that require accurate positioning of the hand. For such movement, the dynamic parameters of the arm do not matter in the sense that any intermediate configuration of the arm limbs can be considered quasi-static. The definition of the control strategy is included into the definition of the mechanical model by inserting the constraint expressions. Thus, the controller module only consists of activating or not the constraints and providing the goals in the Cartesian frame. Given the instant position and orientation of the end-effector, an (constrained) inverse kinematics (IK) algorithm can be used to compute the joint angle values corresponding to the arm configuration which satisfies the goal. The relation between the variation of the effector position and the joint angle values is defined by:

$$\Delta\boldsymbol{\alpha} = \mathbf{J}^{+}\Delta\mathbf{x} + \left(\mathbf{I} - \mathbf{J}^{+}\mathbf{J}\right)\Delta\mathbf{z} \qquad \text{(Boulic 92)} \qquad (5.8)$$

where: $\mathbf{J}^{+}$ is the so-called pseudo-inverse of non-square Jacobian matrix $\mathbf{J}$
$\Delta\boldsymbol{\alpha}$ represents the vector collecting the angular coordinates of the arm,
$\Delta\mathbf{x}$ represents the 6-DOF vector of the hand
$\Delta\mathbf{z}$ describes a secondary task in the joint variation space

In the case of kinematically redundant mechanisms such as the arm, a secondary task may be defined and optimized. The term "secondary-task" refers to the fact that minimization of $\left(\mathbf{I} - \mathbf{J}^{+}\mathbf{J}\right)$ does not alter fulfillment of the primary task (hand positioning). For example, various positions of the elbow are possible for the same hand position. Several criteria, such as minimum jerk, maximum comfort, or minimum torque variations have been suggested for expressing the natural motion of the human arm (Bruwer 87, Kawato 90). Depending on the arm redundancy, cascaded criteria can be used. Alternatively, experimental data suggest what kind of natural IK algorithm (input-output relationship) may be hardwired into the motor control units. For example, for increased realism, time-parametrization of the IK-generated trajectories may also be employed a posteriori whereas the tradeoff speed-precision of typical arm movement can also be emulated with "real-time" IK algorithms (Bullock 88, Multon 98).

Reflex-like Behavior. Since the beginning of the century, the so-called Motor Programs have been theorized to be the underlying representation of rapid movement. More recently, generalized motor programs have been proposed to account for the production of human movements with qualitative invariant features (Young 91). Evidence for units of motor control and provision for motor programs is that the time response of sensory feedback loops are too slow to be involved in the production of rapid movements. Hence, the idea that some central neural structure must be responsible for storing and flushing the gesture. One important feature of these motor program units is that the engendered motions are able to expand or contract in a number of dimensions (time, amplitude) while maintaining some invariant characteristics (relative timing). Motor programs can be considered by approximating pre-recorded angular trajectories that can be modified using, for example, signal processing techniques. In such a case, the input of the design pattern is the identifier of the motion and its parameters. The outputs are the joint angle values provided to the visualization module. Motor programs may thus be regarded as joint torque information. In this case, the mechanical model works as a dynamic filter. The actual reflex motion is thus obtained applying this filter to the input torque sequence associated with the motor program (INRIA TR).

Dynamic Servoing. From the point of view of the control theory, the human arm is a *multi-input multi-output* (MIMO) dynamic system with high-dimensionality defined by its state-space equation:

$\dot{\mathbf{x}} = h(\mathbf{x}, \mathbf{u})$

- $\mathbf{x}$ represents the system's state vector (built-up by collecting all DOFs together with their respective angular velocities),
- $\mathbf{u}$ is the vector made of all externally applied generalized forces

(5.9)

The system exhibits coupling between DOF as well as strong non-linearities. As such, the model is a tough system to control, although nonlinear control theory provides alternative and workable control strategies. One solution to the problem would be to consider a set of operating points around which a linearized model of the arm could be extracted:

$\dot{\mathbf{x}} = \mathbf{A}\mathbf{x} + \mathbf{B}\mathbf{u}$ $\mathbf{A}$ and $\mathbf{B}$ matrices calculated from the Jacobians $\frac{\partial \mathbf{h}}{\partial \mathbf{x}}$ and $\frac{\partial \mathbf{h}}{\partial \mathbf{u}}$ (5.10)

By doing so, the initial nonlinear control problem can make use of the powerful tools provided by the linear control theory. For instance, for each operating point of the human arm, one may consider designing an *optimum time-invariant linear feedback controller* which would minimize a weighable tradeoff between energy consumption and tracking accuracy (Massaquoi 93). An alternative approach would be to regard the nonlinear system as a linear system associated with an uncertainty due to its nonlinear components. Application of *Proportional Derivative* controllers could thus also be applied. However, such solutions may yield a combinatory explosion in the number of operating points to be sampled, unless a very simple model of the arm is considered. This would be up to the biomechanicians to decide what form of control law $\mathbf{u} = -\mathbf{G}(\mathbf{x})$ should be implemented for the simulation (INRIA TR).

5.3.3 Motion Control Interface

Following these considerations, an open simulation toolbox was designed to allow simulation of the upper limb motion by automatic generation of the simulation code and provision of various types of motion controllers. A natural language interface was designed to allow the user to specify the movement in qualitative terms (such as "raise the arm slowly") (Fig. 5.15).

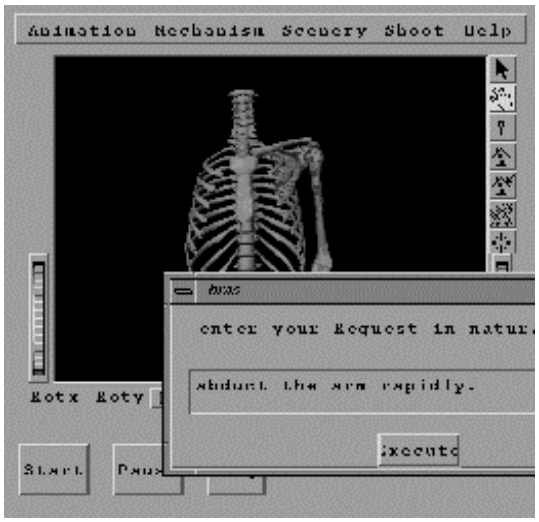

(INRIA TR)

Fig. 5.15. High level control interface

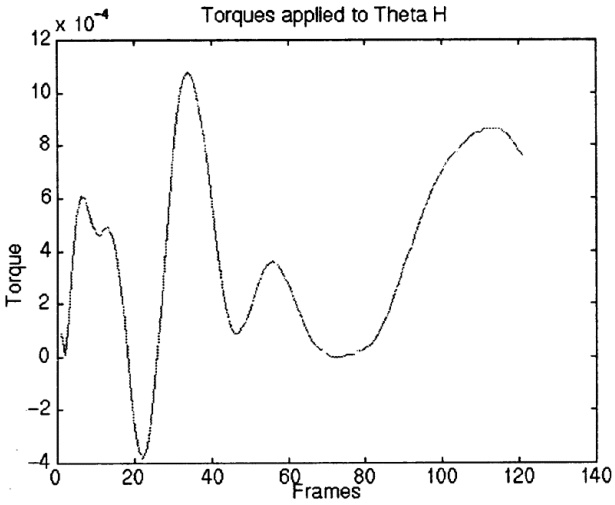

(INRIA TR)

Fig. 5.16. Torque history from inverse dynamics

Orders are then lexically, syntaxically and semantically analyzed and translated using tools coming from *fuzzy logic* theory into functions that modify the control parameters. A planner decomposes the complex movements into elementary motions and converts the orders expressed in the Cartesian frame into orders expressed in the joint frames (or conversely) depending on the controller patterns. Then the system calls the simulation code and the selected controller to execute the motion. Interactive control features were also implemented allowing the user to drive a part of the skeleton to a given position. The controller takes the end position and orientation specified by the user and makes the arm move to this goal. A database containing the state of the model and its controller is shared between the controller and the planner. The controller fills in this shared database during the simulation to ensure the other components of the platform know the state of the system (Multon 98).

To this end, two main control strategies were tested: a simplified *dynamic servoing* (PID) and a *constraint-based control* (kinematic task). Within the control design software, the upper limb model appears as a black box where the inputs are the driving angular torques, and the outputs are the arm DOFs. In this design, the 11-DOF model exhibits strong coupling and non-linearities. A PID controller was then designed for each DOF of the model. However, the penalty scheme employed to ensure constraint-fulfillment at runtime cannot provide joint torque information as required for muscle force optimization analysis. Contrary to this, a constraint-based control strategy allows a control similar to inverse-kinematics – except that motion is generated by the dynamical simulator – and provides valuable information about the actual joint torques needed to produce the constrained motion. Hence a simplified 5-DOF model of the arm with no closed kinematic loop, was adopted and complemented with a constraint-based control strategy allowing joint torque extraction. The user can then control the wrist trajectory by interactive specification of its goal Cartesian position and torques may be automatically computed during the simulation (Fig. 5.16) (INRIA TR).

The application of the resulting joint dynamics to the determination of the muscle contraction forces and the simulation of soft tissue deformation is developed in the following section.

5.4 Soft Tissue Simulation at IST

(This section has been composed using the reports and publications provided by IST)

5.4.1 Muscle Force Prediction

From the dynamic simulation of the 3-D human upper limb model, the angle trajectories and torque histories of the upper limb joints could be derived. On this basis, both static and dynamic optimization analyses were performed at *the Instituto Superior Técnico* of Lisbon (IST) for the determination of the muscle contraction forces. Several constitutive relationships for tendon, muscle and skin were also implemented in the ABAQUS finite element software for the simulation of muscle contraction and of soft tissue deformation. This is shown below.

Static Optimization. As stated in § 3.2.1, in the case of static optimization, muscles are considered as instantaneously available actuators whose force depends only on the current excitation signal. Static optimization analyses were thus performed independently at each instant of time using Zajac's model, proposed in § 3.3.2 (Zajac 86, 89), by considering the force-length property only. The objective function $J(F^T)$ was then minimized in considering:

- the simple bounds: $0 \le F_i^T \le F_{i\,max}^T \qquad (i = 1,\dots m)$ (5.11)
- the model equation dynamics: $\mathbf{M}(\mathbf{q})\dot{\mathbf{v}} = \mathbf{A}(\mathbf{q})\mathbf{F}^T + \mathbf{F}^E(\mathbf{q}) - \mathbf{I}(\mathbf{q},\mathbf{v})$ (5.12)
- the nonlinear constraints: $C_i(F_i^T) \equiv \dfrac{F_i^T}{F_i^{PE}(F_i^T)\cos\left[\alpha_i(F_i^T)\right]} \ge 1$ (5.13)

with: $\mathbf{v}$, $\dot{\mathbf{v}}$ first and second time derivatives of $\mathbf{q}$ vector of the DOFs: $\dot{\mathbf{q}} = \mathbf{B}(\mathbf{q})\mathbf{v}$
$\mathbf{M}(\mathbf{q})$, $\mathbf{A}(\mathbf{q})$ system mass $(p \times p)$ and moment arm $(p \times m)$ matrix,
$\mathbf{I}(\mathbf{q},\mathbf{v})$ $(p \times 1)$ vector describing the Coriolis and centrifugal effects
$\mathbf{F}^E(\mathbf{q})$ p-vector of the generalized external applied forces (CHARM D5, D10)
$\mathbf{F}^T = [\mathbf{F}_i^T]$ vector of the forces in the tendons (Matéus 96, Engel 97)

The problem was applied to arm abduction and forearm flexion movements of the upper limb model reduced to 5-DOF (fixed clavicle and scapula) and 25 action-lines. As proposed in § 3.2.2, the minimum muscle stress sum criterion was adopted, but following Crowninshield and Brand (Crowninshield 81) instead of Karlsson (Karlsson 92):

$$J = \sum_{i=1}^{m}\left(\frac{F_i^T}{A_i}\right)^3$$ m: number of muscles F_i^T, A_i: i^{th} muscle force and PCSA (5.14)

The problem was solved using the E04UCF NAG Fortran Library optimization algorithm (NAG 91). For each movement a minimum-jerk-type history was prescribed. The time histories of the normalized forces F_i/F_{max} for the most important muscles parts are presented in Fig. 5.17 and Fig. 5.18. A load was applied in both cases to exert a force against the motion. The time interval [0, 1] was discretized into 21 nodal points (CHARM D5, D10, Matéus 96, Engel 97).

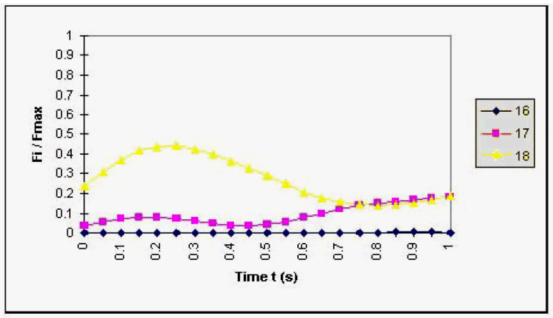

Figure I - FOREARM FLEXION : Biceps Brachii (16, 17), Brachioradialis (18)

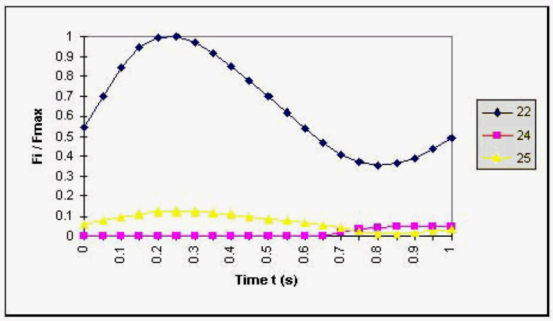

Figure II - FOREARM FLEXION : Brachialis (22), Supinator (24), Pronator Teres (25)

Fig. 5.17. Forearm Flexion (Engel 97)
The movement consists of a rotation carried out from an angle of -19º (rest position) to an angle of -109º with an additional mass in the hand. The main contributors are the *brachialis* (22) helped by the *brachioradialis* (18) and by the *biceps brachii* (17). The *pronator teres* (25) and the *supinator* (24) are both exerting some force on the radius. The humerus-flexor *pectoralis major* (not shown) also appeared to be slightly active so as to balance out the humerus.

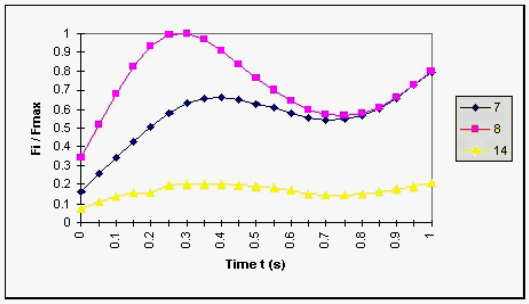

Figure III - ABDUCTION : Deltoideus (7, 8), Subscapularis (14)

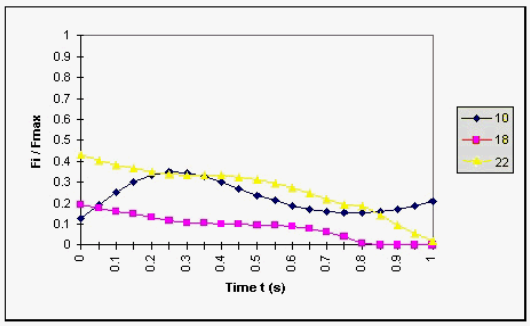

Figure IV - ABDUCTION : Supraspinatus (10), Brachioradialis (18), Brachialis (22)

Fig. 5.18. Arm Abduction (Engel 97)
The motion was carried out in 1s from 15º (rest position) to 60º with an additional mass in the hand. The abductors *deltoideus* (8), *supraspinatus* (10) and *subscapularis* (14) appeared to be supplying the largest forces. Significant forces also appeared exerted by the first part of the *deltoideus* (7) which is a flexor of the arm. Less important forces appeared, contributed by the *brachioradialis* (18) and by the *brachialis* (22) which are flexors of the forearm.

Dynamic Optimization. As stated in § 3.2.1, performing dynamic optimization requires taking into account the muscle force histories over the period of interest. This time, Zajac's model, proposed in § 3.3.2 (Zajac 86, 89), was fully applied. The problem then consisted of minimizing the performance criterion $J(F^T)$, taking into account (CHARM D10, Engel 97):

- the musculotendon equation of motion: $\dot{F}^T = f\left[F^T, l^{MT}, v^{MT}, a\right]$ (5.15)
- the model equation dynamics: $\mathbf{M}(\mathbf{q})\dot{\mathbf{v}} = \mathbf{A}(\mathbf{q})\mathbf{F}^T + \mathbf{F}^E(\mathbf{q}) - \mathbf{I}(\mathbf{q},\mathbf{v})$ (5.16)
- the muscle activation dynamics: $\dot{a} = \frac{1}{\tau_{rise}}(u-a)u + \frac{1}{\tau_{fall}}\left[u - (a - a_{min}) - (u-a)u\right]$ (5.17)
- the boundary conditions (i.e., $\mathbf{q}(t=t_0)$, $\dot{\mathbf{q}}(t=t_0)$, $a(t=t_0)$, $F^T(t=t_0)$) (5.18)
- inequality constraints on the neural excitation signals: $0 \le u_i(t) \le 1 \quad (i = 1,\ldots,m)$ (5.19)

The objective function was chosen so as to combine a minimum stress criterion like for static optimization with a minimum tracking error criterion (CHARM D10, Matéus 96, Engel 97):

$$J = C_1 \int_0^{t_f} \sum_{i=1}^{m} \left(\frac{F_i^T(t)}{A_i} \right) dt + \int \left[\mathbf{z}^T(t) \mathbf{C}_2 \mathbf{z}(t) + \dot{\mathbf{z}}^T(t) \mathbf{C}_3 \dot{\mathbf{z}}(t) \right] dt \qquad (5.20)$$

with: C_1, $\mathbf{C}_2$, $\mathbf{C}_3$ weighting factors or matrices
$(\mathbf{z}(t), \dot{\mathbf{z}}(t)) = (\mathbf{q}(t) - \mathbf{q}^d(t),\ \dot{\mathbf{q}}(t) - \dot{\mathbf{q}}^d(t))$ characterizes the tracking error of the solution relatively to a desired (given) motion $(\mathbf{q}^d(t),\ \dot{\mathbf{q}}^d(t))$

In this case, the excitation signals are the controls of the optimal control problem. Such a problem is defined as a *free final-time* problem by adding the final time t_f to the control parameters. The solution was found by converting this optimal control problem into a parameter optimization problem as proposed by Pandy et al. (Pandy 90). The neural excitation values of the muscles at each node of the discretized time interval [0, t_f] form a set of unknown variables in the resulting optimization problem. For purpose of dynamics integration, the continuous excitation history for each muscle was reconstructed by linear interpolation between the control nodes. As for static optimization, the E04UCF NAG Fortran Library optimization algorithm was used to solve the problem (CHARM D10, Engel 97).

The approach was applied to the forearm flexion movement of a reduced 1-DOF model of the upper limb including three action lines: the long head of the *biceps brachii*, the *brachialis* and the *brachioradialis*. The flexion was performed in the range of 45° to 135° in a time period of 1 s with an additional mass of 10 kg in hand. A desired minimum jerk type motion was given, and a negligible tracking error achieved. The time evolution of the forces in the three muscles turned out to be close to the one that was numerically and analytically obtained for the corresponding static optimization problem under the same motion (Fig. 5.19). The solution of the static optimization problem allows the confirmation and complete interpretation of the results in terms of the physiological cross-sectional areas of the three muscles and the time evolution of their moment arms. In addition to the time evolution of the musculotendon forces and of the kinematic variables, the dynamic optimization furnishes also the time evolution of the other state variables (the activation levels $a_i(t)$) and the control variables $u_i(t)$. However, this is to the detriment of the computation time and simplicity of the problem to solve. It was therefore concluded that applying dynamic optimization is much more expensive than static optimization whereas little difference may be observed between their results (CHARM D10).

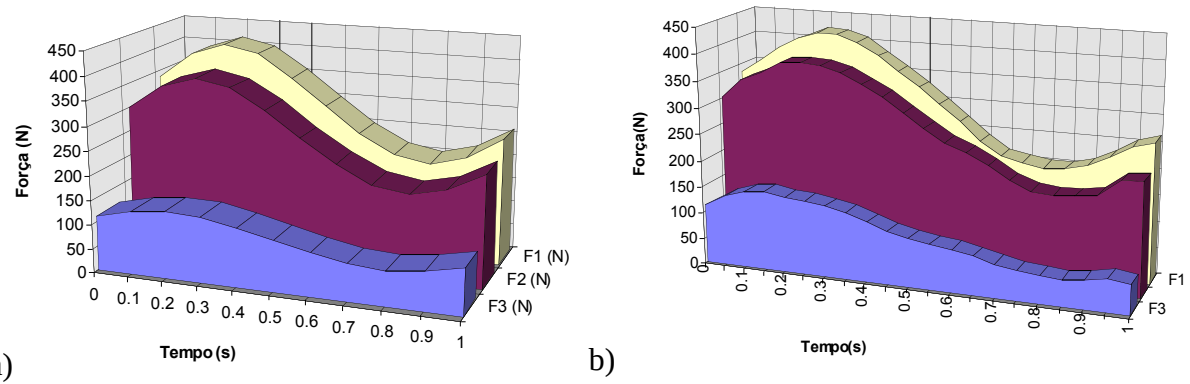

a) b)

(Mateus 96)

Fig. 5.19. Muscle force evolution during forearm flexion: a) static b) dynamic optimizations

5.4.2 Finite Element Modeling

To achieve the deformation analysis of the soft tissues, use was made of a standard finite element code named ABAQUS. This general code is appropriate for the analysis of solids that may undergo arbitrarily large deformations. Though the ABAQUS constitutive library offers a wide variety of material models, the constitutive relationships of soft tissues are too complex and too specific to be found in this general purpose library. Nevertheless, the ABAQUS code allows extension to other material models in the form of user-defined material subroutines. As shown below, several constitutive relations for the passive behavior of human soft tissues like tendons, ligaments, skin and for the passive/active behavior of skeletal muscles were therefore analyzed and implemented in ABAQUS (CHARM D10, Martins 98).

Tendons and Ligaments. As explained in § 4.4.1, because of the parallel orientation of their fibers and the consequent unixial behavior, there is no three-dimensional constitutive equation available for tendons and ligaments. These tissues were therefore modeled as suggested in § 4.4.1, by using a 1-D non-linear viscoelastic constitutive relationship with 1-D bar elements and with the assumption of incompressibility in order to obtain cross-sectional deformations. For this purpose, Fung's QLV approach was chosen, as proposed in § 4.4.1 (Fung 72):

$$T(t) = \int_{-\infty}^{t} G(t-\tau)\frac{dT^{(e)}}{d\tau}d\tau \qquad \text{with:} \quad G(t) \approx \frac{1 - c\gamma - c\ln(\tau/\tau_2)}{1 + c\ln(\tau_2/\tau_1)} \text{ relaxation function} \qquad (5.21)$$

with the model of elastic response proposed by Fung and modified by Trevisan (Trevisan 83):

$$T^{(e)} = A\left(e^{B(\lambda-1)} - 1\right) - AB(\lambda - 1) \qquad \text{with:} \quad \lambda\text{, stretch ratio, and A, B, constants} \qquad (5.22)$$

For implementation in ABAQUS, the relaxation function was further approximated in the form of Prony series (CHARM D10):

$$G(t) = 1 - \sum_{\alpha=1}^{N} g_\alpha\left(1 - e^{-t/\tau_\alpha}\right) \qquad \text{with:} \quad g_\alpha \text{ relative moduli and } \tau_\alpha \text{ relaxation times} \qquad (5.23)$$

and the constitutive Jacobian for the elastic response was obtained in the form (CHARM D10)

$$\frac{d\Delta\sigma}{d\Delta\varepsilon} = \lambda(t+\Delta t)\left[T(t+\Delta t) + \lambda(t+\Delta t)(1 - D_v)AB\left(e^{B(\lambda(t+\Delta t)-1)} - 1\right)\right] \qquad \text{with:} \quad \sigma = \lambda T \qquad \varepsilon = \ln\lambda \qquad (5.24)$$

Skin. Two of the models proposed in § 4.4.1 were considered for skin modeling. The first one is the isotropic hyperelastic constitutive relationship proposed by Veronda et al. which leads to a strain energy function in terms of the first two strain invariants:

$$W = c_1\left[e^{\beta(I_1-3)} - 1\right] + c_2(I_2 - 3) + g(J) \qquad \text{with:} \quad c_1,\ c_2,\ \beta\text{, constants} \quad \text{(Veronda 70)} \qquad (5.25)$$

This relation is the simplest relationship modeling the isotropic hyperelastic behaviors since it allows the independent modification of the different components of the energy. It was furthermore chosen for its compatibility with ABAQUS which provides a UHYPER subroutine for modeling hyperelastic materials. No specific implementation was therefore necessary. To adjust the model to the format requirements of this subroutine, incompressibility was assumed ($J = 1,\ g(1) = 0$) and the principal partial derivatives of W were obtained as (CHARM D10):

$$\frac{\partial W}{\partial I_1} = c_1\beta e^{\beta(I_1-3)} \qquad \frac{\partial W}{\partial I_2} = c_2 \qquad \frac{\partial^2 W}{\partial I_1^2} = c_1\beta^2 e^{\beta(I_1-3)} \qquad \text{(the others being taken null)} \tag{5.26}$$

The second model adopted for skin modeling was the one proposed by Tong and Fung as:

$$W = \frac{1}{2}\left(\alpha_1 E_{11}^2 + \alpha_2 E_{22}^2 + \alpha_3 E_{33}^2 + \alpha_3 E_{21}^2 + 2\alpha_4 E_{11}E_{22}\right) + \qquad \text{(Tong 76)} \tag{5.27}$$

$$+ \frac{1}{2} c e^{a_1 E_{11}^2 + a_2 E_{22}^2 + a_3 E_{12}^2 + a_3 E_{21}^2 + 2a_4 E_{11}E_{22} + \gamma_1 E_{11}^3 + \gamma_2 E_{22}^3 + \gamma_4 E_{11}^2 E_{22} + \gamma_5 E_{11} E_{22}^2}$$

For implementation in ABAQUS, the constitutive Jacobian was developed in the form:

$$\frac{\partial \Delta\sigma_{ij}}{\partial \Delta\varepsilon_{rs}} = -\delta_{rs}\sigma_{ij} + \delta_{ir}\sigma_{sj} + \sigma_{ir}\delta_{js} + \frac{1}{J} F_{ik}\left(\frac{\partial^2 W}{\partial \mathbf{E}^2}\right)_{klmn} F_{rm} F_{sn} F_{jl} \qquad \text{with} \tag{5.28}$$

Details of the derivation may be found in Appendix D.1 (CHARM D10).

Skeletal Muscle. Among the models reviewed in § 4.3, the incompressible transversely isotropic hyperelastic model provided by Humphrey and Yin for passive cardiac tissues was chosen, for suitability reasons with ABAQUS, as basis for the development of the constitutive model for the passive and active behavior of skeletal muscle (Humphrey 87, 90). The model developed in § 4.4.3 for muscle contraction simulation was not considered to the benefit of the development of a more appropriate model generalizing Humphrey's model so as to make it compatible with the 1-D model of Zajac used in the optimization analyses (Zajac 86, 89). Originally, the quasi-incompressible version of Humphrey's model for the passive cardiac muscle was given in the form:

$$W = W_f(I_1) + W_f(\lambda_f) + W_J(J) \qquad \text{with: } (c,\ b,\ A,\ a,\ D) \text{ constants} \qquad \text{(Humphrey 87,90)} \tag{5.29}$$

$W_I = c\left(e^{b(I_1-3)} - 1\right)$ strain energy of the embedding isotropic matrix

$W_f = A\left(e^{a(\lambda_f-1)^2} - 1\right)$ strain energy of each muscle fiber family

$W_J = \frac{1}{D}(J-1)^2$ strain energy associated with the volume change.

The model was then modified to allow prescription of an active contractile strain ζ^{CE} compatible with the contractile element of Zajac's musculotendon model (Zajac 86, 89). The modification hold on the expression of the fiber strain energy as: (Pires 97, Martins 98)

$$W_f = W_f(\lambda_f, \zeta^{CE}) = W_{PE}(\lambda_f) + W_{SE}(\lambda_f, \zeta^{CE}) \qquad \text{with:} \quad \begin{aligned} W_{PE}(\lambda_f) &= T_0^M \int^{\lambda_f} f_{PE}(\lambda) d\lambda \\ W_{SE}(\lambda_f, \zeta^{CE}) &= T_0^M \int^{\lambda_f} f_{SE}(\lambda, \zeta^{CE}) d\lambda \end{aligned} \tag{5.30}$$

The complex material tangent operator was finally derived as: $\mathbf{H} = \frac{\partial^2 W}{\partial \mathbf{E}^2} = \frac{\partial \mathbf{S}}{\partial \mathbf{E}}$ (5.31)

Details on the model composition and derivation are provided in Appendix D.2 (CHARM D10, Pires 97, Martins 98).

3D QLV for Soft Tissues. As stated in § 4.3.3, Fung's 1-D QLV formulation could be generalized to 3-D so as to complete the implementation of the above 3-D models with viscoelastic behavior (Fung 72, 93a). The generalized 3-D QLV equation was thus written as:

$$S_{ij}(t) = \int_{-\infty}^{t} G_{ijkl}(t-\tau)\frac{\partial S_{kl}^{(e)}\left[\mathbf{E}(\tau)\right]}{\partial \tau}d\tau \qquad \text{with:} \qquad G_{ijkl}(t) = G(t)(\mathbf{1})_{ijkl} \tag{5.32}$$

As for 1-D modeling, the relation was approximated using Prony series, and derived to get:

$$\Delta S_{ij} = (1-D_v)\Delta S_{ij}^{(e)} - (S_v)_{ij} \qquad \text{with:} \tag{5.33}$$

$$Dv = \sum g_\alpha\left[1-\frac{\tau_\alpha}{\Delta t}\left(1-e^{-\Delta t/\tau_\alpha}\right)\right] \qquad (S_v)_{ij} = \sum_{\alpha=1}^{N}\left(1-e^{-\Delta t/\tau_\alpha}\right)\left(S_{ij}^{(e)}(t) - A_{ij}^{\alpha}(t)\right) \tag{5.34}$$

$$\text{The tangent was obtained as: } \frac{\partial \Delta S_{ij}}{\partial \Delta E_{kl}} = \frac{\partial \Delta S_{ij}}{\partial \Delta S_{mn}^{(e)}}\frac{\partial \Delta S_{mn}^{(e)}}{\partial \Delta E_{kl}} = (1-D_v)\frac{\partial \Delta S_{ij}^{(e)}}{\partial \Delta E_{kl}} \quad \text{(CHARM D10)} \tag{5.35}$$

Application. Following the ABAQUS implementations described above, all the selected constitutive relationships were successfully applied to the deformation simulation of cylinder beams. Application of these material routines to the deformation simulation of the reconstructed anatomical components provided by UG was then initiated with the *brachialis*. This muscle was discretized into a mesh of 4050 hybrid 4-node tetrahedra with a total of 1029 nodes (Fig. 5.20). In a first loading phase, an increasing traction force was imposed at the right end of the muscle at rest ($\zeta^{CE} = 0$**)**. An extension of 5 mm (about 2.5 %) was reached for a traction up to 588 N. In a second loading phase, the traction was maintained constant at this maximum value and a contractile strain was applied up to –7.5 %. A contraction of about 8 mm resulted from this activation. A similar loading experiment was then simultaneously applied to the *brachialis* and *biceps brachii* together with the motion of the arm and forearm bones, each in contact with each other (Fig. 5.21). Similar deformations were obtained whereas important differences were observed concerning the stresses. However, the simulation was time and memory consuming, and some finite elements extremely distorted revealed meshing problems inherited from the original 3-D reconstructed mesh which was not especially adjusted to the mechanical analysis to perform. This prevented further extension of the simulation. Also, no skin deformation was generated. Nevertheless, the ability to simulate the passive/active behavior of muscles and soft tissues in contact with each other and with the underlying bones was demonstrated (CHARM D10, Pires 97, Martins 98).

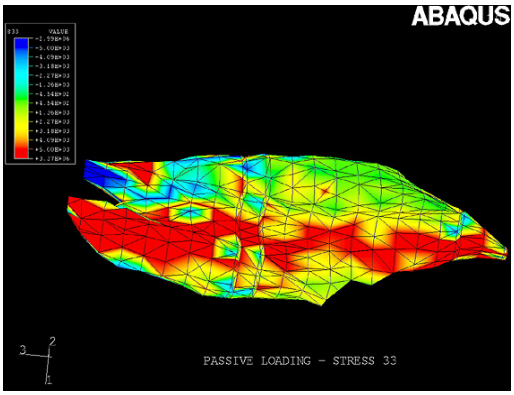

Fig. 5.20. Stresses in the brachialis

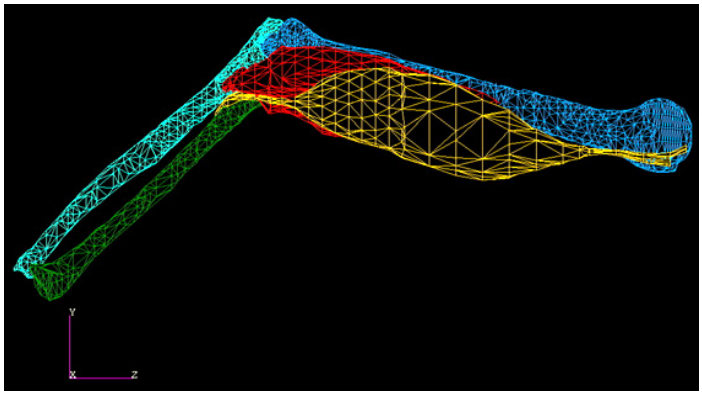

Fig. 5.21. Biceps and brachialis finite element meshes

Conclusion

The application of the investigation I have led for CHARM was presented in this chapter. The theoretical biomechanical human upper limb model was used as a basis for implementing the data structure, developing the topological modeler *tm*, and designing the 3D topological upper limb model reconstructed from the Visible Human Data. This model was then applied for developing various motion control strategies and performing the optimization analyses providing, for a given motion, the muscle forces histories required for contraction simulation. The approaches and models I have suggested for muscle force prediction in § 3.4 and soft tissue finite element modeling in § 4.4 were not all adopted, essentially for insuring the feasability of the whole simulation. In particular, this is the case of Horowitz's muscle and Shoemaker's skin models (Horowitz 88a,b,c, Shoemaker 86), which were thought too complex for implementation in ABAQUS. The applied models were chosen from among the alternative suggestions I had made. Besides, the technical limitations encountered in the simulation tended to justify this prudence. The complexity of the proposed models could have compromised the success of the enterprise. Indeed, the efficiency of the methods implemented and the effectiveness of the overall CHARM pipeline were demonstrated. Photo-realistic rendering of the simulation was then achieved in UKA and an interface for multi-modal matching were developed in UIB for comparing the simulation to real motion sequences. Fig. 5.20 illustrates the realism of the rendering achieved for the simulation. As a conclusion to CHARM, it may be said that the achieved developments constitute an initial step for further advances in research. Anatomists have found the VHD model to be a gold standard for structure identification and labeling. The models developed could be of use for medical education, as well as clinical applications like surgical simulation. Orthopedicians and sports scientists consider our developments as offering unprecedented insights into the complex kinematics of the articulations and into the unknown neuro-muscular control strategies. Finally, from the point of view of the computer graphics research community, CHARM constitutes an outstanding contribution towards the realistic physically-based modeling and animation of the human body. The project objectives were therefore fulfilled.

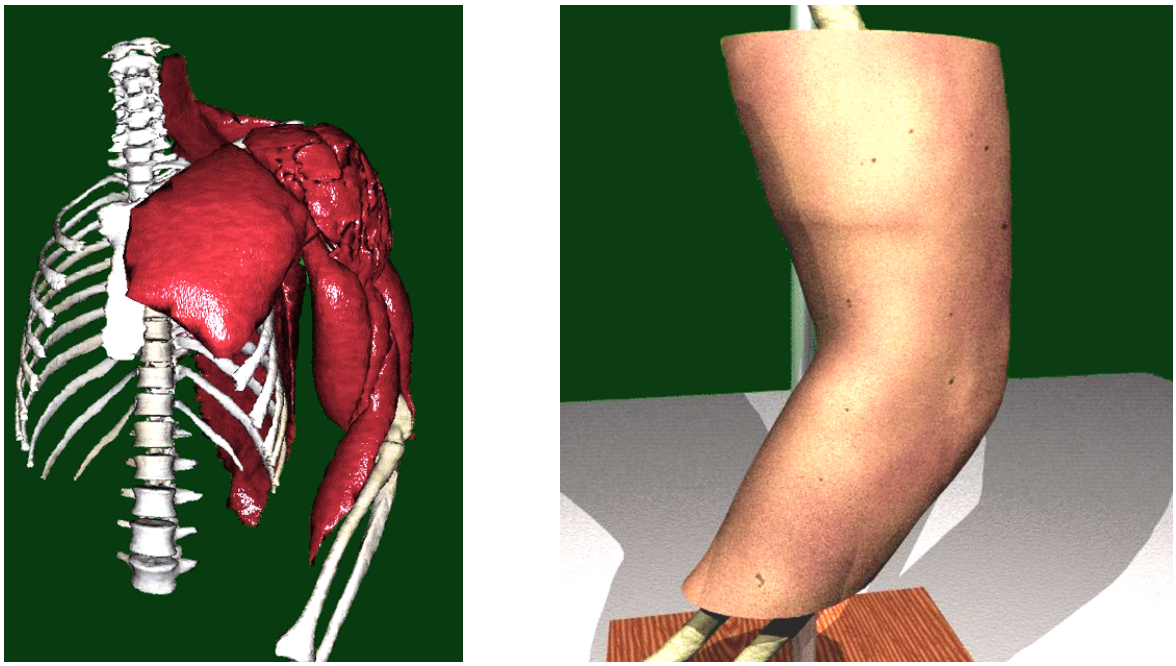

Fig. 5.22. Photo-realistic rendering of bones, muscles and skin achieved for CHARM (UKA)

6 BODY Upper Limb Modeling

In computer animation, virtual characters are composed of several layers, each one handling one component of the global deformation: the skeleton, muscle and skin layers. An incorrect animation of the basic skeleton layer is thus bound to lead to unrealistic animation and deformation of the overlaying layers. This is the case for the forearm and the shoulder, especially when common keyframe sequences are played back with anatomically correct body models: the radius dislocates from the humero-radial (HR) joint whereas the scapula is easily seen flying away from the thorax or penetrating into it. In this chapter, an attempt towards the improvement of the BODY *skeleton_* structure currently used at the Computer Graphics Lab in EPFL (LIG) is presented, based on the experience gained from the investigations of CHARM. It evaluates the possible adjustment of the upper limb structure to the anatomical joint topology as well as its extension with *_scapulo-thoracic* (ST) nodes so as to allow the proper animation of the shoulder following the natural process of shoulder motion. The idea is to constrain the scapula motion against the thorax and derive the corresponding rotations in the SC and AC joints using inverse kinematics. The automatic adjustment of the shoulder motion to the upper limb movements is however not investigated.

6.1 The BODY Framework

6.1.1 Animation Environment

Virtual Body Modeling. In practise, virtual characters are composed of several layers, each one handling one component of the global deformation. The basic layer is a wire articulated skeleton composed of joints providing the rigid body motion of the character. Key posture sequences composed of joint rotation sequences may then be played back on the skeleton to generate its rigid body animation (Steketee 85, Boulic 94). A basic approach to designing the character consists then of dressing it with a skin layer composed of rigid surface patches directly tied to the skeleton segments and deformable surface patches connecting them around the joints. Though this approach may be efficient and sufficient for designing simple characters, it hardly leads to realistic animation with respect to the human body (Thalmanns 87, 88, Chadwick 89). The approach is therefore usually improved by inserting between the skin and the skeleton an intermediate layer composed of soft objects, similar to the muscles and soft tissues underneath the skin. A better smooth skin layer may then be generated as the envelope of the underlying soft objects. The most common approach is to use blending/unblending deformable Metaballs distributed around the skeleton so as to reproduce the anatomical deformations of the body (Yoshimoto 92, Shen 93, 95, Thalmann 96).

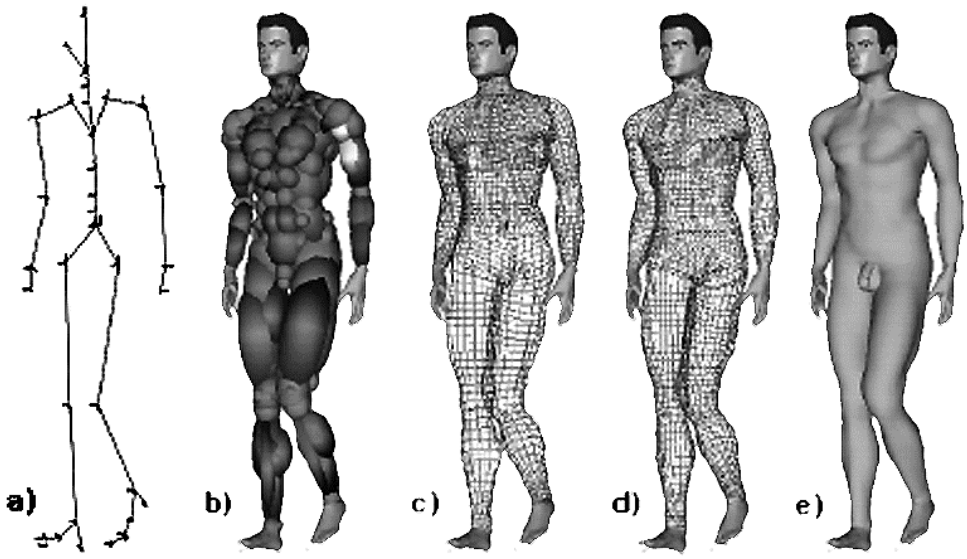

(Shen 93, 95, Thalmann 96)

Fig. 6.1. Virtual body generation: a) skeleton, b) Metaballs, c) envelope, d) mesh, e) skin

Again, two approaches are available whether the Metaballs distribution refers to the real anatomical muscular composition or not. The realism of the result finally depends on the refinement of the model. The closer the model is to the real anatomical constitution of the body the more realistic it is. This may however be to the detriment of the interactivity and the computing efficiency. If fast or real-time processing is necessary, a reduced model may therefore be preferential.

In LIG, there is no standard model with respect to the Metaball constitution: various body models have been designed depending on the sex of the character and its individual corpulence. The *BodyBuilder* interface, developed by Jianhua Shen for this purpose, constitutes a very flexible tool, allowing the design of any human body morphology (Fig. 6.1, 6.2). There is also no standard template with respect to the underlying skeleton since different character sizes may be required as well, depending on their age or their individual corpulence again. All bodies are however built on the same animation library infrastructure shown in Fig. 6.3 (Boulic 95).

LIG Libraries. BodyBuilder is mainly based on the *SkinLib* library, which, in user applications, handles the simultaneous realistic deformation of multiple virtual characters. SkinLib allows automatic generation of the skin envelope from the current shape and configuration of the underlying Metaballs and skeleton layers. As the Metaballs deformations themselves depend on the skeleton conformation, SkinLib is directly built on top of the *BodyLib* library, which handles the human skeleton structure, and which itself is built on the *SceneLib* library, which handles the basic scene hierarchy. The proper animation of the skeleton is thus essential for the generation of realistic human body deformations.

The SceneLib library handles a low-level structure, the *scene*, which maintains the general purpose hierarchy and allows the multiple positioning of complex functional entities without duplication of data. Each entity in the scene is thus distinguished from the others by its specific *unit_*. This allows for example the creation of a scene including several characters, although they are all built on the same structural model. SceneLib provides thus a flexible means for the modeling of a heterogeneous environment (Boulic 91).

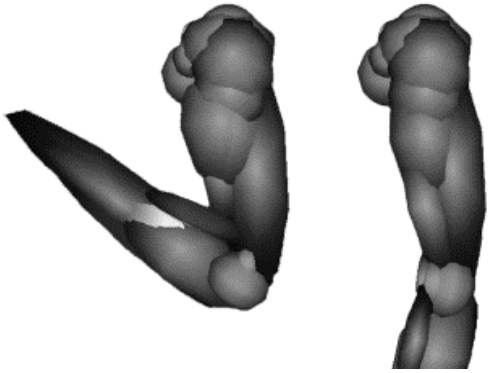

(Shen 93, 95)

Fig. 6.2. Biceps Metaball deformation

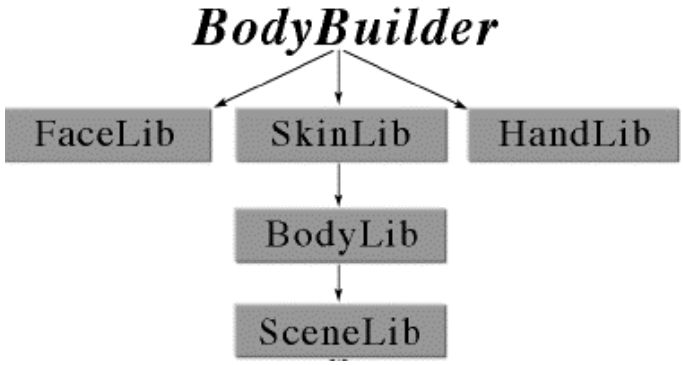

(Shen 93, 95)

Fig. 6.3. LIG's animation library infrastructure

The basic structuring component of the scene is the node (*n3d_*). It retains all the geometric, topological and display information needed to set a frame in 3-D space. This allows therefore the construction of any kind of n-ary tree hierarchy. Furthermore, additional functions can be associated to the *n3d_* through the binding of typed structures. In particular, *n3ds_* may be extended to translational or rotational *joints_*, by complementing them with limit and motion data. The word "joint" is here a bit excessive in the sense that the corresponding data structure only carries the information of one degree of freedom (DOF).

Nevertheless, it is easy to obtain more complex joints by instanciating the appropriate combinations of several elementary *joints_*. An arbitrary choice has retained the ***z axis*** of the local node coordinate system as the rotation axis of the *joint_* (standard convention from Robotics). This is however, not limiting, since each *n3d_* may be freely orientated with respect to its parent node. Combining joints and nodes, it is thus possible to develop 3-D hierarchical articulated structures for modeling and animating any specialized vertebrate characters. In particular, this is true for the skeletal structure of the virtual human bodies used in LIG, which have been built this way (Boulic 91).

BODY *Skeleton_* Structure. The skeletal structure of the virtual human bodies used in LIG is based on the BodyLib library, which maintains the topological tree structure for vertebrate bodies with predefined mobility. The major purpose of the BODY data structure is to retain the basic information of the geometric characterisation, the mass distribution and the deformation entities for a general topology composed of a trunk connected to four limbs and a head. This allows the modeling of various populations of virtual humans as well as vertebrate animals based on the same topological structure.

The human BODY model used in LIG is a 3-D articulated hierarchy composed of 74 joints, plus 30 others for each hand. Its *skeleton_* structure may be customized either at a high level using a small set of scaling parameters (mass, sizes) or at a low level using a BODY *template_* file (*.tpl*) defining the position and orientation of the different joints. The rest position of the body has been defined as standing up with dangling arms oriented such that the palmar surface of hand lies in the sagital plane with medial orientation. In the rest position, all DOFs have a zero value except the *_shoulder_flexion* and *_elbow_flexion* (-5 degrees and 5 degrees respectively) in order to provide a more natural posture (Huang 94, Boulic 94, 95).

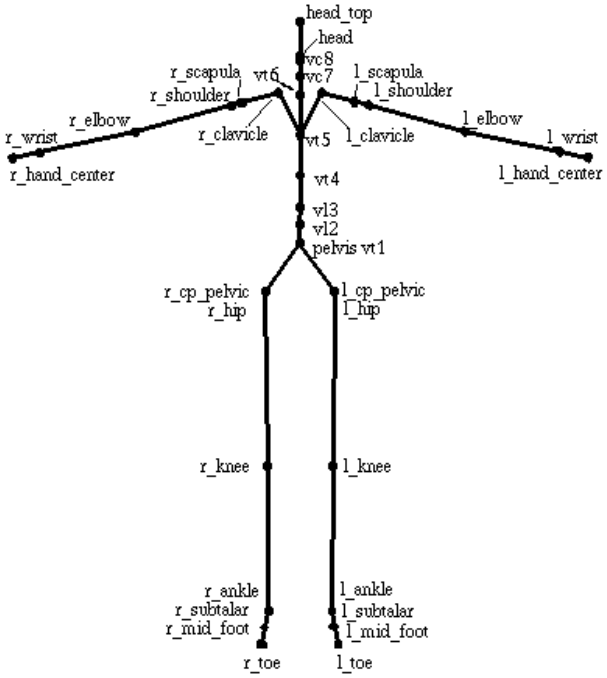

(Huang 94, Boulic 94)

Fig. 6.4. The BODY *skeleton_* structure

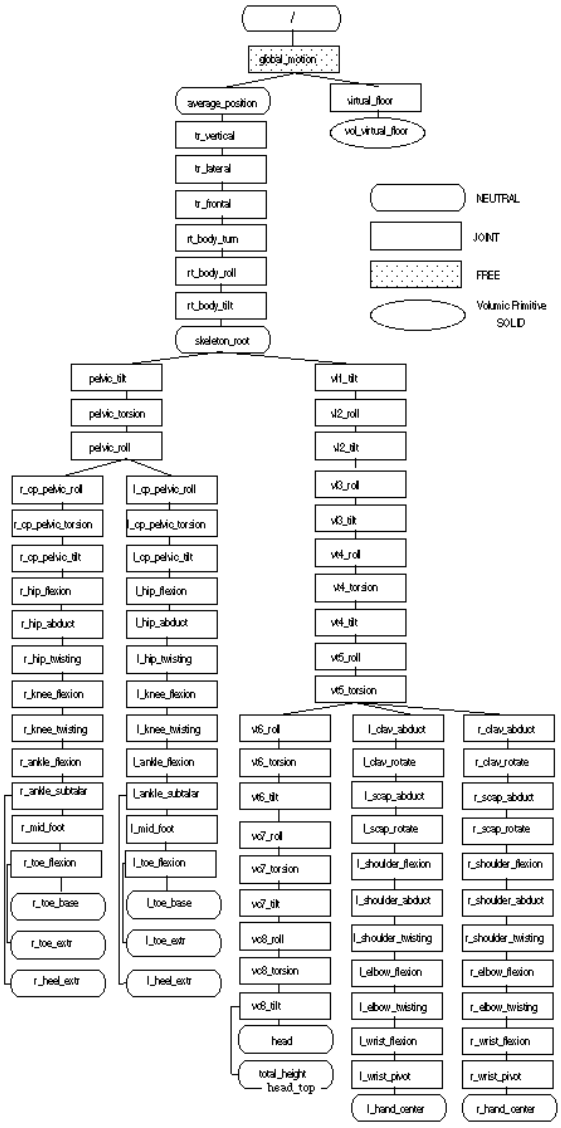

(Huang 94, Boulic 94)

Fig. 6.5. *Skeleton_* hierarchy

According to the Computer Graphics community, the default orientation of the body in the world coordinate system is called BODY_Y_UP:

- the body vertical axis is along the world y axis.
- the body lateral right side axis is along the world x axis.
- the body frontal axis is along the world -z axis.

However, in order to describe the BODY parameters in a more natural way, a permutation of the axes is instanciated at the skeleton root, so that within the hierarchy:

- the body lateral x axis points to the *right side*.
- the body frontal y axis points to the *front side*.
- the body vertical z axis points to the *head*.

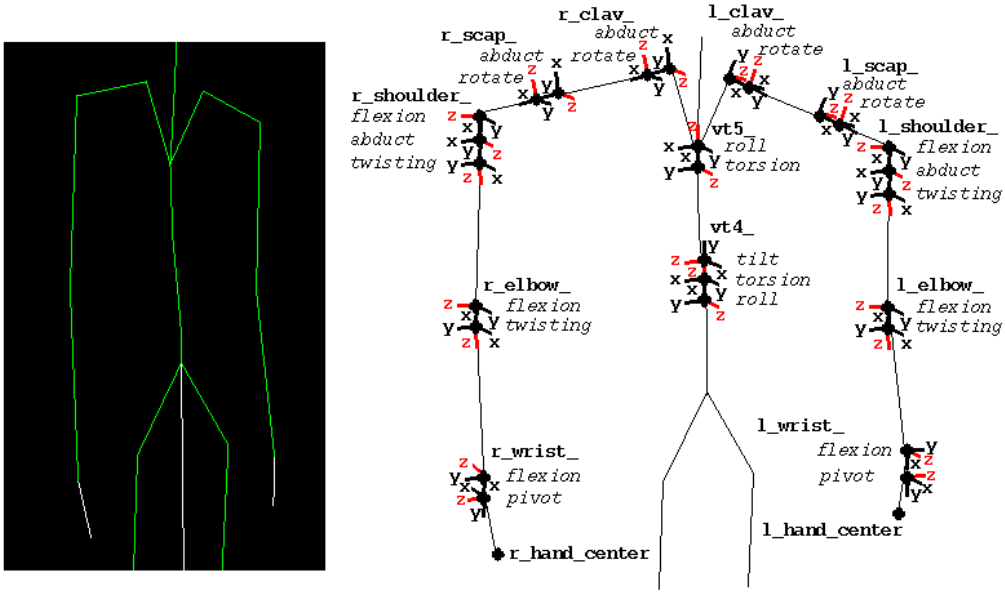

Fig. 6.6. The upper limb skeleton in rest position.

6.1.2 Upper Limb Model Extension

The upper limbs of the virtual humans used in LIG are currently modeled with 11 joints and 4 segments each, the clavicle, the scapula, the arm and the forearm. These are hierarchically attached to the spine as child branches of the fifth vertebra and both terminated by hand structures. As shown in Fig 6.6 and detailed in Table 6.1, the *_clavicle_* (SC) and the *_scapula_* (AC) *joints_* have both been attributed *only* 2 DOFs in rotation around their transversal axes. The twisting movements around these two segments are therefore not included. Besides this, the *_elbow_flexion* and *_twisting joints_* have been joined on the same location at the arm end. The *_twisting joint_* axis is therefore not to be assimilated to the radius pronation/supination axis. Furthermore, the upper limbs joints have been simply organised in almost the same plane, which does not properly represent the 3-D joint topology of a real human upper limb. Finally, it may also be noted that the joint coordinate systems between the left and right arms are identical, though flexion movements would require them to be opposed so as to take into account the symmetry between both sides.

Table 6.1. The upper limb DOF

joint	DOF	Description
clavicle	_clav_abduct	up and down motion in the coronal plane (y BODY)
	_clav_rotate	rotation in the transverse plane (z BODY)
scapula	_scap_abduct	up and down motion in the coronal plane (y BODY)
	_scap_rotate	rotation in the transverse plane (z BODY)
shoulder	_shoulder_flexion	forward-backward motion in the sagital plane (x BODY)
	_shoulder_abduct	sideward motion in the coronal plane (y BODY)
	_shoulder_twisting	along the forearm axis
elbow	_elbow_flexion	flexion-extension of the arm in the sagital plane (x BODY)
	_elbow_twisting	along the arm axis.
wrist	_wrist_flexion	rotation of the hand in the coronal plane (y BODY)
	_wrist_pivot	rotation of the hand in the sagital planes (x BODY)

To use this infrastructure to perform a biomechanical simulation of the upper limb motion, several modifications of the BODY model would be necessary:

- Skeleton anatomic fitting:
  - The virtual joint topology does not properly follow the anatomic one.
    The joint locations need to be adjusted onto that of a realistic 3D skeleton model.

- Joint frames setting:
  - The joint parameters are arbitrary and do not correspond to those usually considered.
    The coordinate systems need to be aligned with biomechanical definitions.

- Structure extension:
  - The twisting of the *_clavicle_* (SC) and *_scapula_* (AC) *joints_* are not taken into account. These joints need to be complemented with one DOF each.
  - The radius pronation/supination axis is not properly modeled. The *_elbow_twisting* axis need to be shifted and reoriented.
  - The scapulo-thoracic (ST) constraint is not modeled. A specific development is necessary to take this constraint into account.

In my case, however, the perspective of such modifications is confronted by the drawback that any slight modification of this the standard BODY structure may finally require the updating of all the overlaying tools and libraries developed for years on this basis at LIG. In order not to compromise the potential interest in my development, I have focussed on remaining compatible with the existing framework.

Besides this, the biomechanical simulation of the upper limb model was the objective of CHARM. Here, I have focussed on another purpose: the realistic modeling of the human shoulder for computer animation. This was planned as part of an internal project, recently launched in LIG, towards the anatomic modeling of the human body, as shown in Fig. 6.7. In this context, the extensive biomechanical modeling of the upper limb was not necessary.

(Thierry Michellod) (Nedel 98a,b)
Fig. 6.7. Anatomic body models

Body Builder has been extended to allow the disposition of several ellipsoids along contour lines as well as the association of several ellipsoids into independent muscle entities. A complementary development has been initiated by Luciana Porcher-Nedel who proposed the modeling of the human body using physically-based deformable muscle components (Nedel 98a,b). In both cases, the model development required the use of a 3-D skeleton model as the basis for realistic anatomical modeling. For this purpose, a rough, but complete, 3-D human skeleton model was chosen. In this context, our development found its main purpose in the proper modeling and animation of the underlying shoulder skeleton model, as basis for the realistic deformation of the overlaying musculature.

6.2 BODY Modification

6.2.1 Anatomic Fitting

As shown in § 6.1.2, the default BODY template is inaccurate with respect to the joint topology of the real human skeleton. In particular with respect to the upper limb, the default template sets all joints in the saggital plane. Though this configuration is sufficient for common virtual bodies, it is not compatible with the purpose of anatomic modeling. The first step in the model implementation is therefore to fit the BODY hierarchy to the joint topology of a realistic 3-D skeleton model. The geometric model used for this purpose is a rough, low resolution model of the upper limb in *Inventor* format. It compounds *spine*, *sternum*, *thorax*, *clavicle*, *scapula*, *humerus*, *ulna*, *radius* and *hand* independent Inventor bone objects.

To identify the different joint coordinates with respect to the reference origin, small Inventor spheres have been created and interactively fitted onto the 3-D skeleton at the estimated anatomic joint locations. In particular, the localization of the center of the thorax has been achieved by fitting onto the thorax an ellipsoid obtained by the scaling of an Inventor sphere object. This interactive session was performed using the 3-D editing features of the *SGI Showcase Design Software*. Once converted into Inventor ASCII format, the resulting Inventor file provides the 3-D coordinates of the different objects contained in the scene, in particular the centers of the Inventor spheres and ellipsoid, representing the estimated joint centers of rotation (Fig. 6.8).

The next step in the model implementation is to fit a standard BODY *template_* on the joint topology defined by the above joint centers. This has been achieved using the *nedit* hierarchy editor developed by Tom Molet in LIG. This tool operates at the SceneLib level. It allows the manipulation of all SceneLib components and the interactive composition of any kind of scene hierarchy. Using this interface, an initial scene has been composed with a standard BODY *skeleton_* hierarchy and with independent *n3d_* nodes positioned on the sphere centers obtained previously (Fig. 6.9).

Approximate uniform scaling and shift were then applied in the resulting *.n3d* file on the coordinates of the independent nodes so as to make them become a realistic substitute position for the upper limb nodes of the BODY standard hierarchy. The limb lengths and joint values of the standard BODY *template_* were then interactively adjusted one after the other, proceeding down the upper limb hierarchy, so as to fit onto the independent nodes.

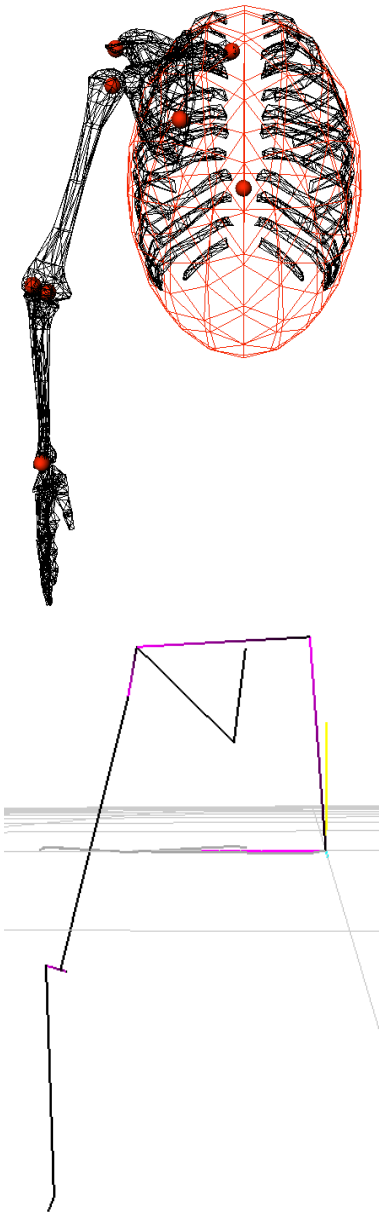

Fig. 6.8. Anatomic fitting

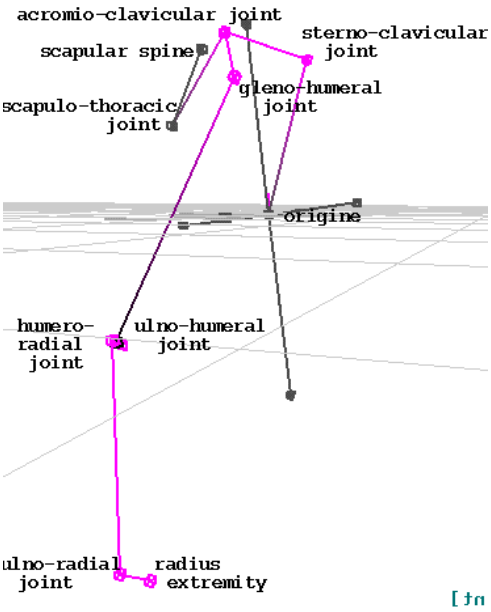

Fig. 6.9. Anatomic upper limb topology

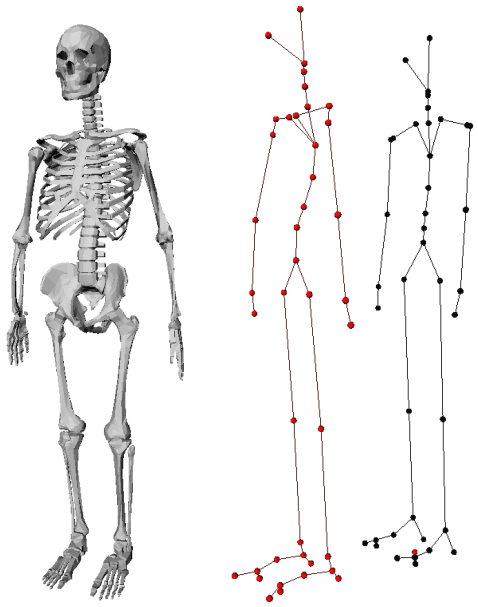

(Nedel 98b)

Fig. 6.10. BODY template evolution

The coordinate vectors could finally be derived from the resulting *.n3d* file, and substituted to the standard ones in the standard BODY *template_* file leading to an anatomically correct template with respect to the geometric model used. The approach was later extended to the whole body by Luciana Porcher-Nedel for anatomic modeling of the human body (Fig. 6.10) (Nedel 98b). To this end, no modification of the BODY *skeleton_* structure was necessary, but only modifications of values in the template file (*.tpl*), in Table 6.2.

Table 6.2 Template file organization for the upper limbs

```
[19.424742, 83.896637, 77.841187],     /* vertebra 5 to right clav origin */
[-19.425478, 83.896667, 77.841187],    /* vertebra 5 to left clav origin  */
[-1.285471, -1.145968, -1.483492],     /* right clav orientation          */
[0.118648, -2.025823, -2.071134],      /* left  clav orientation          */
[136.570251, -0.000023, -0.000122],    /* right clav to scap origin       */
[0.000038, 136.570282, -0.000122],     /* left clav origin to scap origin */
[-1.456047, -0.189408, 0.167290],      /* right scapular orientation      */
[0.190635, 1.435479, -0.164896],       /* left  scapular orientation      */
[50.670410, 0.000000, 0.000000],       /* right scap to shoulder origin   */
[0.000015, 50.670532, -0.000031],      /* left  scap to shoulder origin   */
[-0.011693, -0.136994, -0.111902],     /* right shoulder orientation      */
[-2.020111, -2.260689, -0.131137],     /* left  shoulder orientation      */
[0.000004, 0.000061, 281.141296],      /* right shoulder to elbow origin */
[0.000031, -0.000122, 281.141113],     /* left  shoulder to elbow origin */
[-0.038254, 2.006382, 2.330884],       /* right elbow orientation         */
[-0.038175, 2.324522, 2.004682],       /* left  elbow orientation         */
[0.000092, -0.000687, 242.189331],     /* right elbow to wrist origin     */
[0.000031, -0.000261, 242.189270],     /* left  elbow to wrist origin     */
[-1.057000, -1.300000, -1.057000],     /* right wrist orientation         */
[1.057000, -1.300000, 1.057000],       /* left wrist orientation          */
[12.312910, 70.473083, 0.171967],      /* right wrist to hand center      */
[-12.367798, 70.458801, 0.836884],     /* left  wrist to hand center      */
[0.000000, 0.000000, 0.000000],        /* right hand center orientation   */
[0.000000, 0.000000, 0.000000],        /* left  hand center orientation   */
```

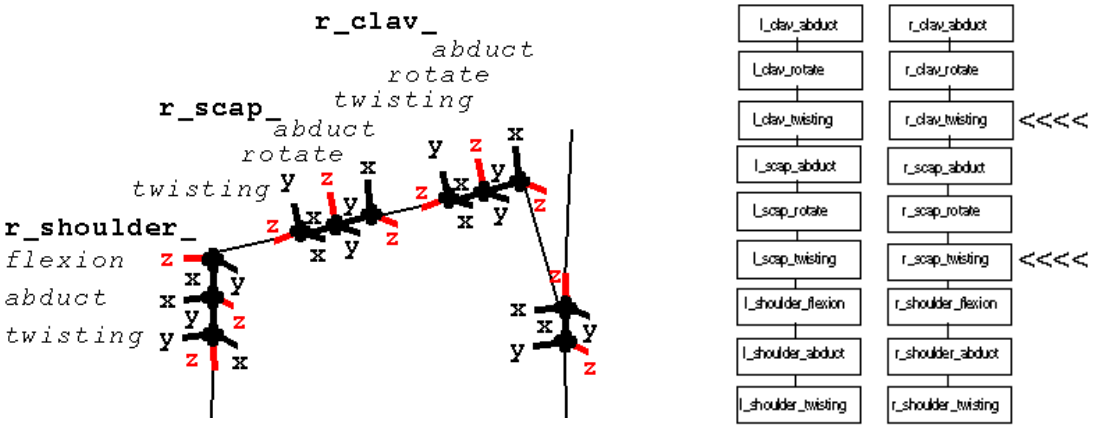

Fig. 6.11. Addition of twisting DOFs to clavicle and scapula

6.2.2 Structure Extension

DOFs Addition. In the BODY upper limb structure, the *_clavicle_* (SC) and *_scapula_* (AC) joints have originally only two degrees of freedom each. The reason for this is probably that they were considered redundant with the three rotations of the *_shoulder_* joint (GH). Though this may be sufficient to generate any arm posture with the common virtual bodies, it may be compromising with respect to the realistic animation of an anatomic skeleton. The extension of the BODY *skeleton_* structure with the two *_twisting* DOFs consists of inserting two supplementary joints into the hierarchy (Fig. 6.11). This change does not require structural modifications to the *template_* file, but corrections of the following orientations (`clav_to_scap, scap_to_shoulder`), so as to take into account the axis permutations they induced. However, these additions imply structural changes in the associate *joint_* file (*.jts*) which defines the default joint minimum, maximum and rest values as shown in Table 6.3. These structural changes therefore compromise the compatibility with the whole animation environment. Because of this, it has been necessary to handle separate versions of BodyLib, with or without the relevant *_twistings*, so as to compare the resulting animations at the end, and to evaluate the influence of these DOFs on the realistic animation of the upper limb. If they proved to be indispensable, a decision about updating the whole animation environment or not would have to be taken.

Table 6.3 Joint file organization and additions for the left upper limb

min *rest* *max*	*joint_*	
`[-0.087266, 0.349066, 0.349066],`	`/* l_clav_abduct */`	
`[-0.174533, 0.300000, 3.140000],`	`/* l_clav_rotate */`	
`[-0.174533, 0.000000, 0.174533],`	`/* l_clav_twisting */`	`<<<<`
`[-3.140000, -1.500000, 0.523599],`	`/* l_scap_abduct */`	
`[-1.523599, -0.500000, 0.523599],`	`/* l_scap_rotate */`	
`[-0.523599, 0.000000, 0.523599],`	`/* l_scap_twisting */`	`<<<<`
`[-3.140000, -1.550000, 3.141594],`	`/* l_shoulder_flexion */`	
`[-0.349066, 0.850000, 3.141594],`	`/* l_shoulder_abduct */`	
`[-1.570797, -0.500000, 1.570797],`	`/* l_shoulder_twisting */`	
`[0.000000, 0.400000, 2.617995],`	`/* l_elbow_flexion */`	
`[-1.570797, 0.000000, 1.570797],`	`/* l_elbow_twisting */`	
`[-1.570797, 0.000000, 1.570797],`	`/* l_wrist_flexion */`	
`[-1.047198, 0.000000, 1.047198],`	`/* l_wrist_pivot */`	

Forearm Modeling. The modeling of the forearm mobility in the BODY *skeleton_* structure also requires attention. In the anatomic fitting stage (§ 6.2.1), the *_elbow_ n3d_* nodes were fitted onto the anatomic elbow at the end of the humerus (Fig. 6.12a). The axis of the *_elbow_twisting joint_* therefore can not fit that of the forearm pronation/supination. Consequently, when a twisting of the elbow occurs, the radius dislocates from the humero-radial joint anatomic location. Therefore, the alignment of the elbow on a biomechanical description is necessary. In § 2.3.1, the forearm mobility was modeled using two hinge joints, the UH and UR joints, respectively localized at the elbow and at the end of the ulna, both with their axis going through the anatomic center of the HR joint (Fig. 6.12b).

Applied to the BODY model, this representation would require moving the *_elbow_twisting joint_* to the end of the forearm at a distance from the elbow. At least, it could be placed on the same location as the *_wrist_ joints_* (Fig. 6.12c). This would, in any case, require modifying the *skeleton_* structure and *template_* file so as to take into account the shift between the *_elbow_flexion* and *_twisting joints_*. Furthermore, the resulting forearm segment between the *_elbow_flexion* and *_twisting joints_* would not materialize the forearm pronation/supination axis, which may be a bit confusing. Considering the fact that the center of a Hinge joint can be placed anywhere along its axis, an easier solution would consist of placing the *_elbow_twisting joint_* on the anatomic HR joint center, and aligning its axis with the end of the ulna. This way, the forearm segment materializes the pronation/supination axis and the forearm bones articulate properly (Fig. 6.12d).

However, in order to avoid the instanciation of a shift between the *_elbow_flexion* and *_twisting joints_*, the *_elbow_flexion* must follow the positioning of the elbow twisting joint and take place on the anatomic HR joint center. This is achieved at no expense to the flexion mechanics, since the displacement of this Hinge joint would be done along its axis. But the segment joining the *_shoulder_ joints_* to the *_elbow_ joints_* could no longer be assimilated to the longitudinal axis of the arm (Fig. 6.12e). This is an issue left to decide in LIG, whether it is important that this segment remains the arm axis or not. Therefore, I have applied this correction locally in my development, in order not to compromise the anatomic modeling approach in the lab. The correct positioning of the *_elbow_ joints_* only affected the "`shoulder_to_elbow`" vectors in the *template_* file (see Table 6.2).

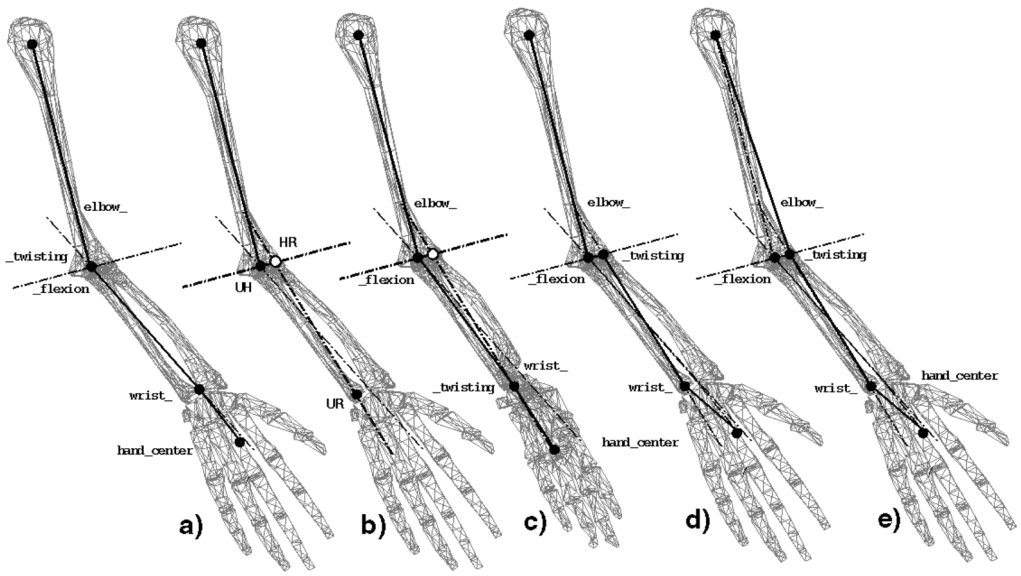

Fig. 6.12. Modeling the radius pronation/supination axis with the BODY standard

Shoulder Modeling. With the *_clavicle_* and *_scapula_ _twistings joints_*, the BODY shoulder joints possess all the DOFs of a real shoulder. This way, nothing should prevent the design of realistic animation of the shoulder. In practice, this is difficult given that nothing constrains the scapula to stay on the thorax, as is the case with real shoulders (Fig 6.13). Consequently, when old keyframe files are played on the 3-D skeleton model, the scapula is easily seen penetrating the thorax or conversely floating away from it. The process of shoulder animation would gain much from an extension of the BODY model to take into account the scapulo-thoracic (ST) constraint. This is therefore my proposal here.

Fig. 6.13. Flying scapulas

Considered independently, the DOFs of the *_clavicle_* and *_scapula_ joints_* are difficult to coordinate to animate the shoulder properly. Benefit could be made of the analysis of the real motion of the shoulder, in remembering that most of the shoulder muscles act on the scapula so as to make it a strong basis for performing arm movements. The way the different parameters of the shoulder are related to each other was described in § 2.3.1. In the plane containing the SC, AC and ST joints, all rotations were observed, depending on the 3D orientation of the helical axis going through the SC and ST joint centers (Fig. 6.14). An easy way to properly animate the shoulder would therefore consist of controlling the orientation of this helical axis, i.e. controlling the motion of the ST joint. The motion of the scapula could thus be constrained to move on the thorax and proper rotations could then be derived for clavicle and scapula.

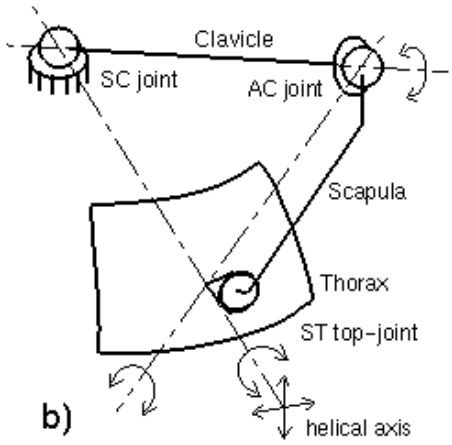

Fig. 6.14. The shoulder loop

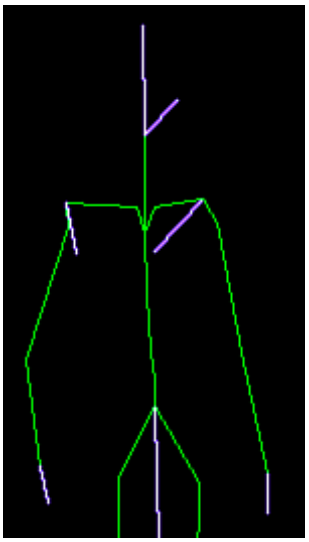

For this purpose, it is necessary to add to the BODY shoulder model a node representing the point of the scapula constrained to stay in contact with the thorax. This node must be inserted as the child of the *_scapula_ joints_*, i.e. as the brother of the *_shoulder_ joints_* (Fig. 6.15). As this node is not spatially superimposed on the *_scapula_ joints_* location, it must be introduced with a specific translation vector in the template file (*.tpl*). As it is not a *joint_* node, but a *neutral_*, no modification of the joint file (*.jts*) is necessary.

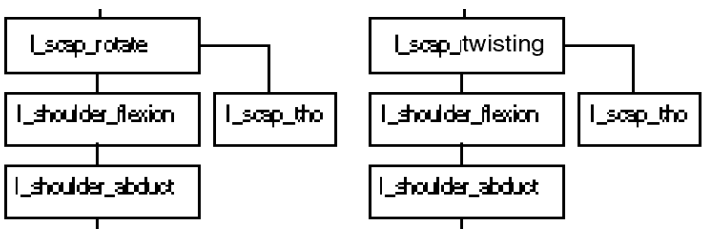

Fig. 6.15. Insertion of *_scapulo-thoracic* (ST) nodes in the BODY *skeleton_* structure

Such an extension of the structure is, however, not welcome, as any modification of the template and structure compromises their general use with the animation environment. Nethertheless, contrary to the insertion of the *_clavicle_* and *_scapula_* *_twisting* DOFs, the ST nodes may be regarded as *optional* plugs on, offering a more natural approach to shoulder motion control, without affecting the integrity of the basic *skeleton_* structure. Thus, it is possible to operate the plugging of such nodes from within the applications requiring it, so as to leave the BODY *skeleton_* structure unchanged. In particular, in view of an animation interface devoted to shoulder animation, the *_scapulo-thoracic* (ST) nodes could be added by the interface when the template is loaded, whereas keyframe files could be generated for the original *skeleton_* structure only. This is therefore the approach I followed.

6.3 Model Implementation

6.3.1 Inverse Kinematics Control

In real motion, two situations may be distinguished which involve movements of the shoulder. On one hand, the shoulder is moved so as to place the glenoid-cavity in a position appropriate for performing intended arm movements. In this case, the control of shoulder motion may be regarded as secondary and depends on the arm movement to be achieved. On the other hand, the shoulder muscles allow the performance of shoulder movements independently of the arm motion. In such cases, the control of shoulder motion is intended and must be disconnected from the motion of the rest of the arm. For the realistic motion control of the shoulder, these two aspects should be taken into account. On one hand, it should be possible to control shoulder movements independently from the arm trajectory; on the other hand, it should be possible to avoid direct control of the shoulder and leave shoulder movements automatically adjusted to the arm trajectories. The first approach is direct and may be quite easily implemented. By contrast, the second one requires a specific investigation on motion control techniques for loop mechanisms. This is outside the scope of the current study. Therefore, I have only investigated the first approach. It is presented in the following work. This does not compromise the perspective of a future extension in that direction.

Shoulder Kinematics. Considering the first approach, the principle is to derive the rotations in the *clavicle_* (SC) and *scapula_* (AC) *joints_* from the position of the *_scapulo-thoracic* (ST) node. For this purpose, the geometric relation within the loop may be written in terms of the Euler angles of the SC and AC joints as (Fig. 6.16):

$$\mathbf{OS} = \mathbf{OC} + \mathbf{CS} = f\left(\theta_{SC}, \varphi_{SC}, \psi_{SC}, \theta_{AC}, \varphi_{AC}, \psi_{AC}\right) \tag{6.1}$$

Given its non-linearity, this relation is difficult to apply. Its linearized form may be prefered, and may be obtained in considering the relation between velocities:

$$\mathbf{V}_S = \mathbf{V}_C + \boldsymbol{\Omega}_{S/C} \wedge \mathbf{CS} \qquad \mathbf{V}_C = \mathbf{V}_O + \boldsymbol{\Omega}_{C/O} \wedge \mathbf{OC}$$

$$\mathbf{V}_S = \boldsymbol{\Omega}_{C/O} \wedge \mathbf{OC} + \mathbf{V}_C + \boldsymbol{\Omega}_{S/C} \wedge \mathbf{CS} \tag{6.2}$$

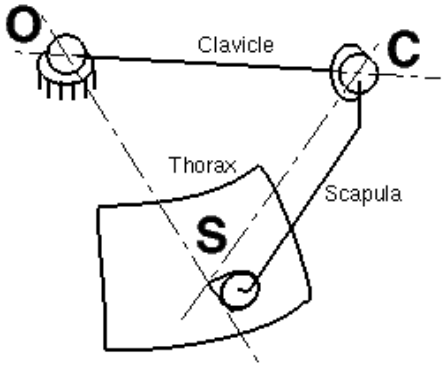

Fig. 6.16. Loop geometric relation

Developed with respect to the axis of the world coordinate system, this relation may be converted into matricial form in terms of the joint angular rotations:

$$\mathbf{V}_S = \begin{bmatrix} \dot{x}_1 & \dot{x}_2 & \dot{x}_3 \end{bmatrix}^T = \begin{bmatrix} \dot{\theta}_{SC} & \dot{\varphi}_{SC} & \dot{\psi}_{SC} & \dot{\theta}_{AC} & \dot{\varphi}_{AC} & \dot{\psi}_{AC} \end{bmatrix}^T \mathbf{J}_S^T \qquad \text{with:} \quad \mathbf{J}_S = \left[\frac{\partial x_i}{\partial \alpha_j} \right] \tag{6.3}$$

where $\mathbf{J}_S$ is the Jacobian matrix of the assembly motion $\left(\alpha_j \equiv \theta_j, \varphi_j, \psi_j\right)$.

From this relation, an incremental relation may be obtained as:

$$\Delta\mathbf{S} = \begin{bmatrix} \Delta x_1 & \Delta x_2 & \Delta x_3 \end{bmatrix}^T = \begin{bmatrix} \Delta\theta_{SC} & \Delta\varphi_{SC} & \Delta\psi_{SC} & \Delta\theta_{AC} & \Delta\varphi_{AC} & \Delta\psi_{AC} \end{bmatrix}^T \mathbf{J}_S^T \tag{6.4}$$

which expresses the displacement increments of the *_scapulo-thoracic* (ST) node in terms of the angle increments of the *_clavicle_* and *_scapula_ joints_*. Inverting this relation would allow the determination of the *joint_* angle increments corresponding to displacement increments of the *_scapulo-thoracic* (ST) node. However, this relation is not bijective: the Jacobian matrix $\mathbf{J}$ counts more columns than lines, and its inversion would not lead to a unique solution. Physically, this may be observed in Fig. 6.16, as the *_scapula_ joint_* (C) may lay anywhere on a circle centered on the OS axis, without affecting the position of the *_scapulo-thoracic* (ST) node. This is due to the fact that there are more angular parameters than necessary to determine the Cartesian position of the *_scapulo-thoracic* (ST) node. This problem is the typical concern of the inverse kinematics commonly used in robotics.

Inverse Kinematics. The inverse-kinematics technique proposes the determination of the joint rotations of an articulated manipulator given the position and orientation of its end with respect to the reference coordinate system. The approach is based on a linearization of the geometric model of the chain at the current state of the system. As a consequence, its validity is limited to the neighborhood, of the current state and, as such, any desired motion has to comply with the hypothesis of small movements. The discrete form of the general solution provided by inverse kinematics may be written as (Boulic 91):

$$\Delta\boldsymbol{\alpha} = \mathbf{J}^+\Delta\mathbf{x} + \left(\mathbf{I} - \mathbf{J}^+\mathbf{J}\right)\Delta\mathbf{z} \qquad \text{where:} \tag{6.5}$$

- $\Delta\boldsymbol{\alpha}$ is the vector of unknown joint angles (dim. n)
- $\Delta\mathbf{x}$ is the vector of the Cartesian position of the main task (dim. m)
- $\mathbf{J}$ is the Jacobian matrix of the linear transformation, representing the differential behavior of the controlled system over the dimensions specified by the main task
- $\mathbf{J}^+$ is the unique pseudo-inverse of $\mathbf{J}$ providing the minimum norm solution which realizes the main task.
- $\mathbf{I}$ is the identity matrix of the joint variation space $(n \times n)$
- $\left(\mathbf{I} - \mathbf{J}^+\mathbf{J}\right)$ is the projection operator on the null space of the linear transformation $\mathbf{J}$. Any element belonging to this joint variation subspace is mapped by $\mathbf{J}$ into the null vector in the Cartesian variation space.
- $\Delta\mathbf{z}$ describes a secondary task in the joint variation space. This task is partially realized via the projection on the null space. In other words, the second part of the equation does not modify the achievement of the main task for any value of $\Delta\mathbf{z}$. Usually $\Delta\mathbf{z}$ is calculated so as to minimize a cost function.

This situation is illustrated on a 2-D example in Fig. 6.17.

- In (a), the main task requested is that the end-effector follows the horizontal. The joint rotations are then computed for a minimum norm solution.

- In (b), an arbitrary secondary task is imposed, whereas no main task is requested. The joint rotations leave the end-effector unaffected.

- In (c), the initial main task is requested again together with an arbitrary secondary task. The main task is fullfilled whereas the secondary task is approximated.

Inverse kinematics has been successfully applied to the design of complex postures by interactively moving some end-effector(s) attached to the articulated structure. It is possible to control only the end-effector position or its orientation (Girard 85, Zeltzer 88, Maciejewski 90, Boulic 94, 96).

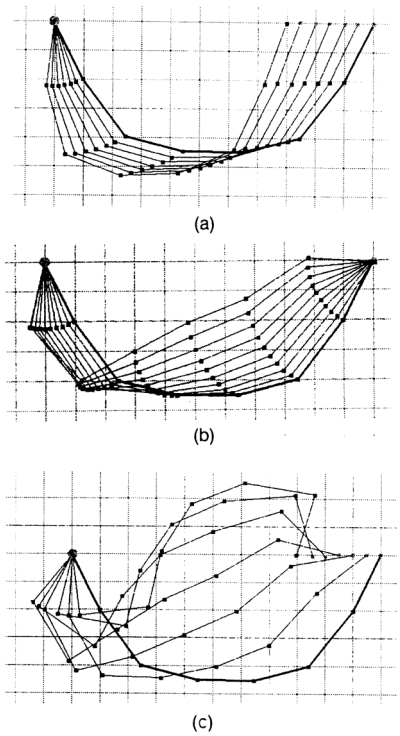

Fig. 6.17. Inverse kinematics (Boulic 91)

Another approach considers the simultaneous position control of multiple end effectors attached at any place on the human tree structure. The resulting posture is a compromise depending on the relative weights, which are also associated with each end effector. This method has been extended further to include combinations of position and orientation control under the generic name of goals. In fact these goals are constraints analogous to mechanical joints as point on point, point on line, point on plane, as well as plane on plane, ball and socket, etc.

Double Control. The inverse kinematics technique may therefore be applied to the animation of the human limbs. A similar incremental development as the one presented for the shoulder loop may thus be established for the whole upper limb. The incremental relation would be then obtained as:

$$\Delta \mathbf{H} = \mathbf{J}_{\mathrm{H}} \Delta \boldsymbol{\alpha} \tag{6.6}$$

with: $\Delta \mathbf{H}$ displacement increment vector for the *_hand_center* end-effector node
$\Delta \boldsymbol{\alpha}$ rotation angle increments vector for all joints in the upper limb
$\mathbf{J}_{\mathrm{H}}$ Jacobian matrix between the Cartesian space and the joint space

In particular, this relation involves the contribution of the *clavicle_* and *scapula_ joint_* rotations to the displacement of the end effector. These rotations are however not constrained in this case, so that the scapula is free to move without respect to the thorax. Here again, the two approaches to shoulder motion control invoked previously emerge. On one hand, a solution would be to specialize $\mathbf{J}_{\mathrm{H}}$ so as to constrain the *_clavicle_* and *_scapula_ joints_* rotations so as to maintain the scapula on the thorax. This approach requires a long term investigation of motion control techniques and is hence outside the realm of this study.

On the other hand, another solution would be to simultaneously apply the inverse kinematics technique to both the *_hand_center* node and the *_scapulo-thoracic* (ST) node, so as to constrain the scapula on the thorax independently. In this case, both the upper limb and the shoulder appear as independent open chains, though with joints in common. The hand-center end-effector node may then be requested to follow arbitrary trajectories, whereas the *_scapulo-thoracic* (ST) end-effector node may be requested to stay in contact with the thorax. This approach corresponds to the use of inverse kinematics with multi-end-effector chains. On this basis, (6.3) and (6.6) may be assembled to obtain a global relation for the upper limb including the shoulder as:

$$\begin{bmatrix}\Delta\mathbf{S}\\ \Delta\mathbf{H}\end{bmatrix} = \begin{bmatrix}\mathbf{J}_S\\ \mathbf{J}_H\end{bmatrix}\Delta\boldsymbol{\alpha} \qquad \text{with:} \quad \mathbf{J}_S \text{ Jacobian matrix of the open clavi-scapular chain} \qquad (6.7)$$

whose inverse allows the simultaneous control of both the arm and shoulder end-effectors.

6.3.2 Animation Interface

A basic application, devoted to the control of the human upper limbs and shoulders, has been developed to demonstrate the principle and the model. It is based on the multi-end-effector inverse kinematic algorithm developed by Paolo Baerlocher at the Computer Graphics Lab (LIG) in EPFL (Baerlocher 98). The algorithm may be summarized as shown in Fig. 6.18. First, the root and end-effectors of the sketeton hierarchy must be specified in order to build the structures involved in the inverse kinematics process.

Goal increments along the straight paths to the specified targets are then calculated for both end-effectors. The Jacobian may then be computed and inversed for the current configuration of the skeleton. The resulting virtual new configuration is then compared with respect to the joint boundaries. An improved approach would be to set the values of the bound joints to their reached boundaries, and to recompute and inverse a new Jacobian corresponding to this new configuration. This process is however time-consuming, so that another approach is commonly preferred, which consists of setting the values of the bound joints to their previous values, and removing these joints in the next computation (Boulic 97). A new goal increment may then be computed for performing a new step. The Jacobian matrix is thus gradually filled with zeros, until the targets are reached without any joint over its boundaries, or until a compromise configuration is found in case one or both targets cannot be reached.

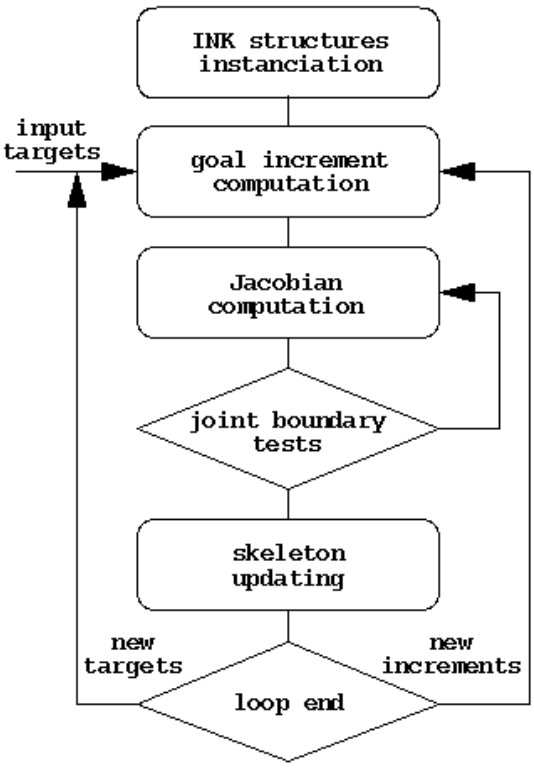

Fig. 6.18. Inverse kinematics algorithm

The interface of the application is composed of a *main viewer* and a *control panel* including two reduced viewers (Fig. 6.20). The main viewer allows the control of the trajectories of both hands, whereas the reduced viewers are devoted to the local control of the shoulders. Five distinct *keyframe* animation files may be given as input or saved: one for the whole body animation, and four for reading pre-recorded end-effector goal trajectories for the right and left hands and scapulas (Fig. 6.21).

Besides this, the end-effector target 3-D trajectories may be generated or modified interactively using the 2-D mouse trackball and saved as keyframe files to be played back. For this purpose, the position of the hand-center end-effector target was chosen as defined by the intersection of the ray perpendicular to the screen through the mouse cursor, with the plane parallel to the screen through the current hand-center position (Fig. 6.19). For the scapulo-thoracic end-effector target, the position chosen was defined by the intersection of the ray perpendicular to the screen through the mouse cursor, with an ellipsoid approximating the thorax shape. The involvement of each end-effector in the inverse kinematics process may also be activated or deactivated with the control panel toggles. This interface thus allows the animator to read and/or to generate independent/combined animations for the body, arms and shoulders, in order to add or correct the shoulder animation of existing keyframes.

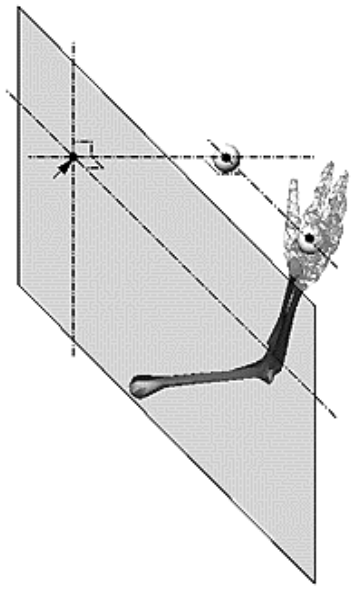

Fig. 6.19. End-effector control

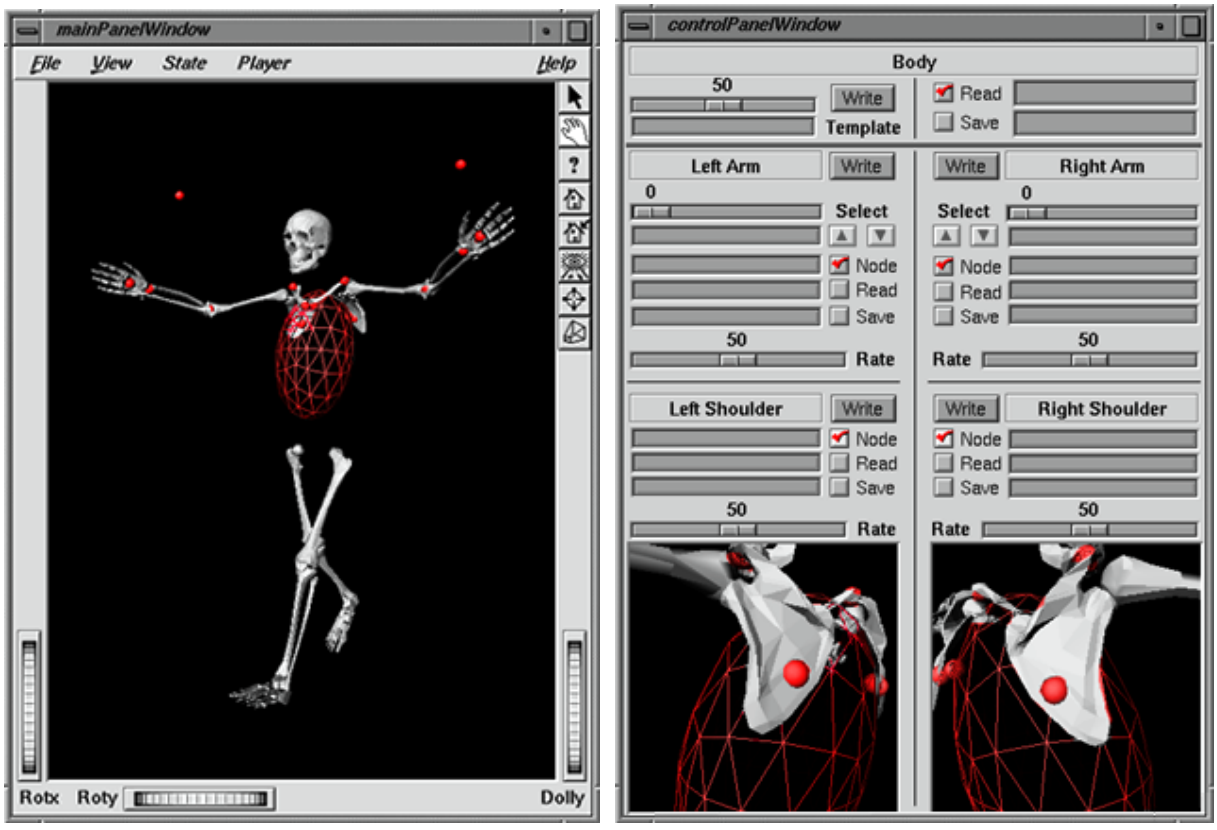

Fig 6.20. An interface devoted to upper limbs and shoulders animation

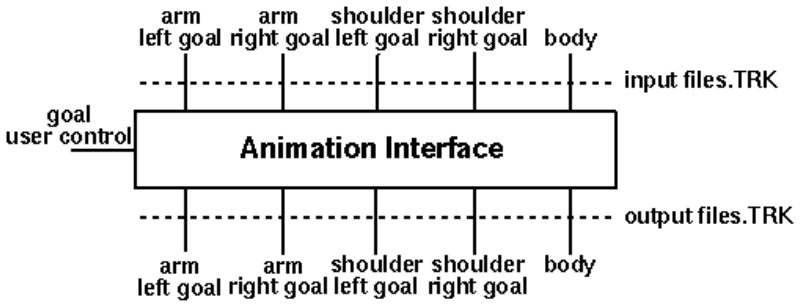

Fig. 6.21. The interface I/Os

For example, the user can play a body walk sequence on the skeleton, and, one after the other, interactively impose specific movements to the upper limbs. Meanwhile, the designed hand center end-effector goal trajectories may be saved as keyframe files for allowing their play back in the next stage. Then, shoulder movements may be interactively superimposed, one after the other, on the body and upper limb animation sequences. Meanwhile, the new body motion, hand trajectories and shoulder trajectories may again be saved as keyframe files for future play-back. The resulting body animation file may finally be applied to anatomic body animation in order to improve the realism of the deformation with respect to the shoulders (Fig. 6.22).

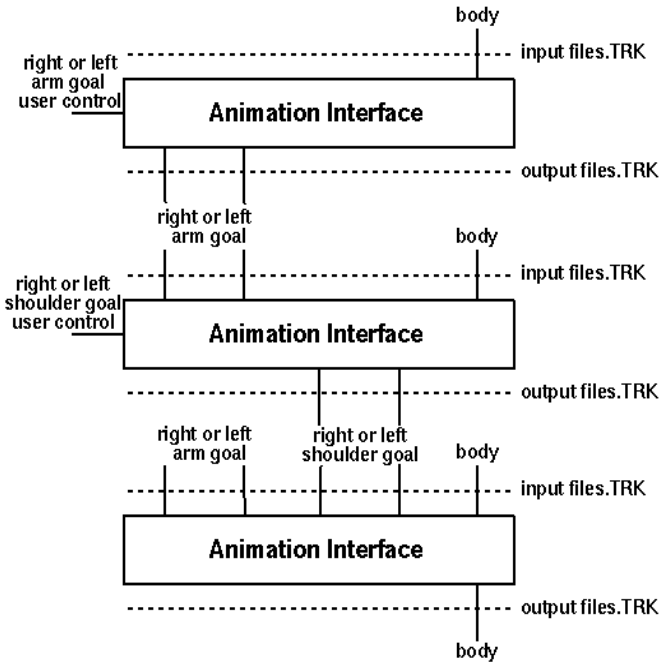

Fig. 6.22. A keyframe combination pipeline example

6.3.3 Results

To conclude this experiment, the resulting motions of the upper limb and shoulder are analyzed. Regarding the shoulder, the interactively generated shoulder movements remain consistent in any case with that of an open chain with the end constrained onto an ellipsoid. However, the realism of the movements generated obviously relies on the animator's ability to attain the natural motion of a real shoulder. The consistency of the generated movements with the motion of the rest of the body is the responsibility of the one who controls the movement. In practice, quite realistic animations may be obtained for simple slow movements, whereas complex fast movements may lead to anarchical animation with respect to the rest of the arm.

The same remarks may be made concerning the control of the arm motion. The approach fails, in particular, when the arm reaches a local minimum configuration. This happens for example when a joint crosses the path between the end-effector and its goal. In such a case, in order to avoid the local minimum configuration, it is necessary to distort the goal trajectory initially

planned, which is likely to compromise the natural look of the animation. An improvement to this approach, that may help solve this problem, would be to use a secondary task, which would avoid the local minimum configuration. Finally, some instability inherent to the multi-end-effectors approach may arise in the animation in the case of conflictual targets between both end-effectors. This may be solved using priority rules (Baerlocher 98).

Besides this, in § 6.2.2, the problem was left to decide whether the *_clavicle_* and *_scapula_* *_twisting* DOFs are necessary or not, to achieve a realistic animation of the human shoulder. The animation interface was compiled with the two library versions separately so as to evaluate the difference between the models. The visual comparison of the animation does not lead to significant differences. Only for extreme superior positions of the shoulder on the thorax, the scapula was observed to move away from it, when the BODY model *without* *_twisting joints_* was used. This was not observed with the other model as this movement was compensated by the *_twisting joints_* rotations. I therefore conclude that, fortunately, the current body model does not necessitate major structural modifications to be used for realistic upper limb animation. The only requirements are to properly adjust the positions of the *_elbow_* and *_wrist_ joints_* respectively to the HR and UR joints on the skeleton, and to add scapulo-thoracic segments from within the application which require a specific control of the shoulder. Therefore, the current BODY *skeleton_* structure may be considered sufficient with respect to the purpose of realistic animation. For purpose of biomechanical simulation, however, the completion of the model would be imperative.

Conclusion

The realistic animation of a virtual skeleton requires the underlying animation hierarchy to be properly fitted onto the skeletal anatomy. This was not the case with the topology of the BODY *skeleton_* structure currently used in LIG. For this reason, I have proposed and processed the anatomic adjustment of the BODY upper limb *joints_* topology to that of a virtual skeleton. However, given the standard status of the BODY *skeleton_* structure in the lab, modification of its structure was not possible. Two areas then required particular attention: the elbow and the shoulder. The problem for the first one was that the *_elbow_twisting* axis was not oriented along the radius pronation/supination axis. For its solution, I have proposed placing the *_elbow_ joints_* on the anatomic HR joint location. The drawback then left to evaluate is that the *_shoulder_–_elbow_* segment can no longer be taken as the humeral axis. Regarding the shoulder, the problem was that the scapulo-thoracic (ST) constraint was not taken into account. Furthermore, the *_clavicle_* (SC) and *_scapula_* (AC) *joints_* revealed to be deprived of *_twisting* DOFs, whose incidence on the motion control of the shoulder was left to evaluate. To solve this, I have proposed the addition of a *_scapulo-thoracic* (ST) node in the upper limb hierarchy, so as to allow the constraining of the scapular motion on a thoracic ellipsoid. I have then developed an animation interface for allowing the control of the upper limb and shoulder motions using inverse kinematics. The comparative analysis of the animations generated with and without the *_clavicle_* (SC) and *_scapula_* (AC) *_twistings* revealed that these DOFs are not indispensable. Finally, the adjunction of *_scapulo-thoracic* (ST) nodes to the upper limb hierarchy appeared to be feasible in the form of plugs on at the interface level, so that no effective modification of the standard BODY *skeleton_* structure is necessary. The possibility of improving the model with joint sinus cones is now investigated in the following chapter.

7 Joints Boundary Modeling

In the BODY *skeleton_* structure currently used in LIG, the *joints_* angles are *independently* bound to range between maximum and minimum values. The shape in Cartesian space of the corresponding bound mobility domain is hard to describe. In § 2.2.1, an analysis by Engin and Tumer was presented (Engin 89a,b), in which qualitative and quantitative descriptions of the shoulder joints boundaries were provided. In this study, the joint boundaries appeared to have conic shapes with elliptic bases. Taking into account this property in the modeling and animation of the human upper limb appears to be an interesting potential improvement to bring to the model. This chapter presents the developments I have led in this direction. This compounds the optional adjunction of a cone data structure to appropriate *joints_* sequences as well as the development of specific functions for bounding the skeletal segments within their respective conic mobility domains. Besides, given the particular shapes of the elliptic bases of the cones, the development of an interface allowing the interactive design and orientation of the cones on the BODY *skeleton_* structure is necessary. The inverse kinematic algorithm used for skeleton animation must also be adjusted so as to take into account the dependency relationships induced by the conic boundaries between the individual *joint_* limits. The effectiveness of the improvement is finally discussed.

7.1 Composite Joint Analysis

7.1.1 Composite Joint Modeling

As briefly explained in Chapter 6, the BODY *skeleton_* structure is built as a SceneLib hierarchy of *joints_* and *n3d_* nodes. The *joints_* components are indeed themselves basic *n3d_* nodes complemented with rotation and limit data around the ***z axis*** of the node coordinate system. This elementary structural entity was then proposed as a basic constituent for the development of more complex articulations (Boulic 91). Given the fact that each node may be freely orientated with respect to its parent node, the modeling of full 3-DOFs Ball_&_Socket joints was thus achieved by inserting circular permutations between three successive 1-DOF rotational *joints_*. This composite approach was applied, in particular, to model the *_clavicle_* (SC), *_scapula_* (AC) and *_shoulder_* (GH) Ball_&_Socket joints of the human shoulder, with the exception that the *_clavicle_* and *_scapula_* *_twisting* DOFs were ignored. Fig. 7.1 illustrates the succession of circular permutations and degrees of freedom as they occur in the SceneLib 3-DOF composite Ball_&_Socket joint structures. Outlined in particular are the *ini* transfer matrices $\mathbf{I}_j$ defining each node $\mathbf{J}_j$ with respect to its parent node, as well as the transfer matrices $\mathbf{M}_j$ induced by each *joint_* rotation.

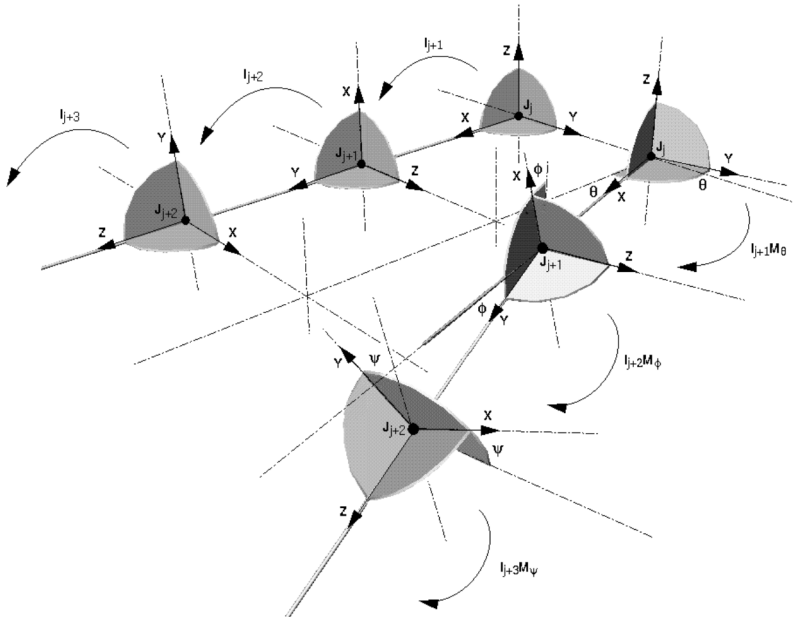

$$\mathbf{I}_{j+1} = \mathbf{I}_{j+2} = \begin{bmatrix} 0 & 1 & 0 \\ 0 & 0 & 1 \\ 1 & 0 & 0 \end{bmatrix}$$

$$\mathbf{M}_{j}(\theta) = \begin{bmatrix} \cos\theta & -\sin\theta & 0 \\ \sin\theta & \cos\theta & 0 \\ 0 & 0 & 1 \end{bmatrix}$$

$$\mathbf{M}_{j+1}(\varphi) = \begin{bmatrix} \cos\varphi & -\sin\varphi & 0 \\ \sin\varphi & \cos\varphi & 0 \\ 0 & 0 & 1 \end{bmatrix}$$

$$\mathbf{M}_{j+2}(\psi) = \begin{bmatrix} \cos\psi & -\sin\psi & 0 \\ \sin\psi & \cos\psi & 0 \\ 0 & 0 & 1 \end{bmatrix}$$

Transfer matrix (column) from $\mathbf{J}_j$ to $\mathbf{J}_{j+3}$: $\mathbf{M}_{j\to j+3} = \mathbf{M}_j(\theta)\mathbf{I}_{j+1}\mathbf{M}_{j+1}(\varphi)\mathbf{I}_{j+2}\mathbf{M}_{j+2}(\psi)\mathbf{I}_{j+3}$

Fig. 7.1. Successive rotations and permutations of a 3-DOF composite Ball_&_Socket joint

Such a composite approach is validated on the basis that any 3-D rotation between two coordinate systems may be decomposed into three successive independent Euler rotations as:

$$\mathbf{R}_{3\times3} = \begin{bmatrix} r_{11} & r_{12} & r_{13} \\ r_{21} & r_{22} & r_{23} \\ r_{31} & r_{32} & r_{33} \end{bmatrix} = \mathbf{R}(\theta,\varphi,\psi) = \mathbf{R}_{\theta}(\theta)\mathbf{R}_{\varphi}(\varphi)\mathbf{R}_{\psi}(\psi) \qquad \text{with: (column rotation)} \qquad (7.1)$$

$$\mathbf{R}_{\theta}(\theta) = \begin{bmatrix} \cos\theta & -\sin\theta & 0 \\ \sin\theta & \cos\theta & 0 \\ 0 & 0 & 1 \end{bmatrix} \qquad \mathbf{R}_{\varphi}(\varphi) = \begin{bmatrix} \cos\varphi & 0 & \sin\varphi \\ 0 & 1 & 0 \\ -\sin\varphi & 0 & \cos\varphi \end{bmatrix} \qquad \mathbf{R}_{\psi}(\psi) = \begin{bmatrix} 1 & 0 & 0 \\ 0 & \cos\psi & -\sin\psi \\ 0 & \sin\psi & \cos\psi \end{bmatrix}$$

$$\mathbf{R}(\theta,\varphi,\psi) = \begin{bmatrix} \cos\theta\sin\psi + \sin\theta\sin\varphi\cos\psi & \cos\theta\cos\psi - \sin\psi\sin\theta\sin\varphi & -\sin\theta\cos\varphi \\ \sin\theta\sin\psi - \cos\theta\sin\varphi\cos\psi & \sin\theta\cos\psi + \sin\psi\cos\theta\sin\varphi & \cos\theta\cos\varphi \\ \cos\varphi\cos\psi & -\cos\varphi\sin\psi & \sin\varphi \end{bmatrix} \qquad (7.2)$$

This conversion from a 3x3 rotation matrix into an Euler sequence is however not bijective. For example, considering the unambiguous 3-D rotation of an object on its bottom (Fig. 7.2), the same 3-D orientation may be described using two distinct rotation sequences (a) and (d), and the rotation matrix may be decomposed into two Euler sequences (θ,φ,ψ), (θ',φ',ψ') as:

$$(\theta,\varphi,\psi) \in [-\pi/2,\pi/2]^3 \qquad \varphi = \text{Arc}\sin(r_{33}) \qquad \theta = \text{Arctan}(r_{13}/r_{23}) \qquad \psi = \text{Arc}\tan(r_{32}/r_{31}) \qquad (7.3)$$

$$(\theta',\varphi',\psi') \in [\pi/2,3\pi/2]^3 \qquad \varphi' = \pi - \varphi \qquad \theta' = \pi + \theta \qquad \psi' = \pi + \psi \qquad (7.4)$$

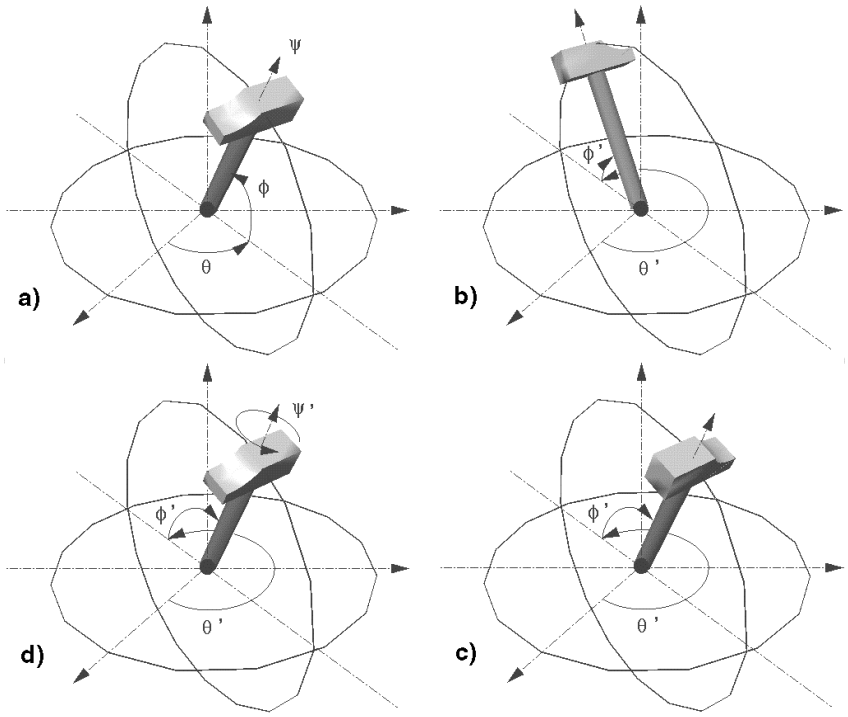

Fig.7.2. The 3-D rotation decomposition in Euler sequence is not bijective: b) → c) → d) ≠ a)

7.1.2 Model Limitations

The modeling of 3-DOF Ball_&_Socket joints using three successive 1-DOF rotational joints may thus be considered consistent with respect to the purpose of 3-D posture description. There are however limitations to the use of such a representation in animation. The equivalence between the 3x3 rotation matrix and three successive individual joints representation pertains as long as the Euler sequence trajectories are generated from the rotation matrix of the desired trajectories, otherwise kinematic singularities may be encountered. A typical example may be given in comparing the ordered mobility of the three elementary *_shoulder_* joints of the BODY *skeleton_* structure – *_flexion, _abduct, _twisting* – with the mobility of real Ball & Socket shoulder joint. Though it is possible for a real gleno-humeral joint to perform an abduction up to 90°, followed by a flexion of 90°, the application of a (0, 90, 0) abduction sequence directly followed by a (90, 0, 0) flexion sequence leaves the BODY arm in an abducted posture. Yet, both abducted and flexed postures are reachable from the rest posture (Fig. 7.3).

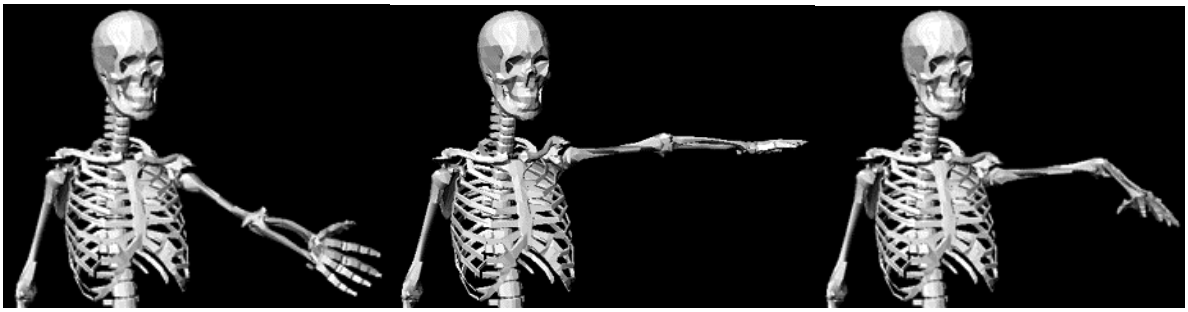

a) b) c)

Fig. 7.3. a) easy flexion b) abduction c) flexion after 90° abduction: a kinematic singularity

As a result, the principle to use when composing 3-D rotation trajectories using Euler sequences, would be to first generate the Euler angle trajectories from the expected rotation matrix. If such a principle is compatible with animation techniques such as keyframing or sensors motion capture, it can not be respected when inverse kinematics are used. This is due to the fact that the inverse kinematics technique is based on the decomposition of the structure mobility into independent degrees of freedom, while consisting of the linearization of the equation of motion around the current posture. Consequently, though a flexed posture may be reached from the rest posture, the flexion of the arm from an abducted posture is impossible using this technique.

Though well known, this problem has not been addressed in LIG. As it is easily skirted round by a slight excursion away from the singularity, it is also not addressed in this study.

Another limitation in the use of individual joint hierarchies to model real structures lays in the handling of joint boundaries. In the BODY *skeleton_* structure currently used in LIG, joint angles are independently bound to range between maximum and minimum values. Thus, for threesomes of successive 1-DOF *joints_*, the mobility of the assembly is restricted to a "cube" in the space of the angular parameters. The resulting bound mobility domain in the 3D Cartesian space may be represented for the first two degrees of freedom as shown in Fig. 7.4. In a), φ is shown bound into $[-\pi/4, \pi/4]$. The corresponding bound mobility domain takes the form of a horizontal groove between the poles of the rotation sphere. In b), the boundaries for φ are extended to $[-\pi/2, \pi/2]$. The bound mobility domain resembles a slice up to the poles between two meridians. In c), the boundaries for φ are extended over the poles, which extends the bound mobility domain over the poles in the form of circular cone sections.

Though such a representation may be considered sufficient for general mechanical simulations, it may not lead to realistic postures concerning the vertebrate bodies, furthermore the human body. As explained in § 2.1.2, real joints are surrounded by articular structures composed of ligaments, capsulae and tendons, whose function is to limit the motion of the bones, and to prevent joint dislocation (Pronk 91). An analysis by Engin and Tumer was mentioned in § 2.2.2, in which the appearance and modeling of the human shoulder joint boundaries were investigated (Engin 89a, b). In this study, the joint boundaries were proved to be of conic shapes with distorted ellipsoid bases (Fig. 7.5, 7.6). Even this description is limited since it does not take into account the fact that the shape of the cone also changes depending on the twisting orientation of the moving bone with respect to the reference bone.

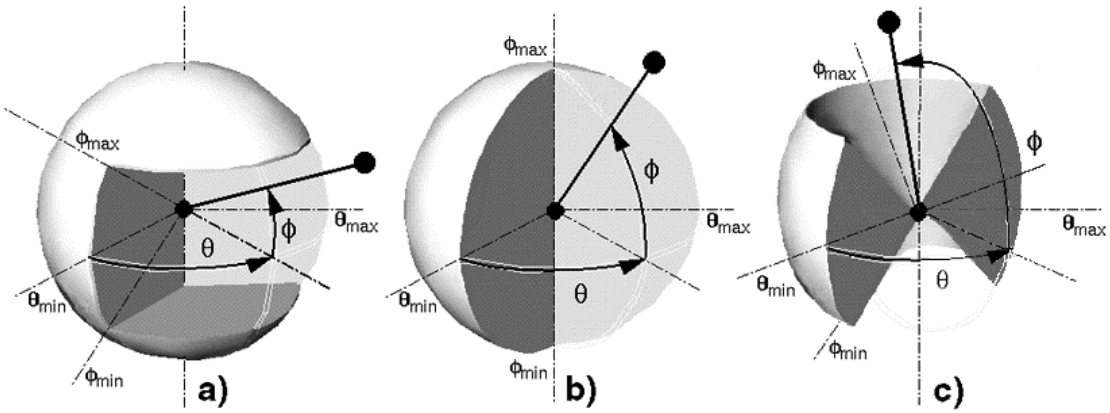

Fig. 7.4. Bound mobility space of an assembly of three independent successive 1-DOF joints

However, these conic bound mobility domains are quite different from those obtained with successions of individual joints (Fig. 7.4). Taking into account the interdependencies between the limits of the elementary joint components with such conic boundary representation may already constitute a notable improvement of the composite joint models. It could lead to a more realistic animation of the vertebrate bodies as well as more accurate simulations with respect to medical and biomechanical purposes. Developments in this direction are thus presented in the next section.

7.2 Joint Sinus Cone Modeling

7.2.1 Cone Structure Conception

The shape of the joint sinus cone is specific to the articulation to which it is associated. In our case, the BODY *skeleton_* data structure may be complemented with specific sinus cone representations for the *_clavicle_* (SC), *_scapula_* (AC) and *_shoulder_* (GH) *joints_*. However, the joint sinus cone property is not specific to the human body but may be applied to any skeletal structure complex joint. The *cone_* structure should therefore be handled at the same level as the *joint_* structure, i.e. not in the BodyLib library but in the SceneLib library (Boulic 91). The idea is to insert, in the composite *joint_* hierarchy, an optional structure that would contain a representation of its conic boundary and which would simultaneously handle all the rotations of its successive elementary *joint_* components, so as to constrain the overall rotation within the cone.

The challenge is to achieve this without disturbing current library procedures, in order to avoid as far as possible any adjustment of the overlaying softs and librairies, such as BodyBuilder or BodyLib. A basic *cone_* structure can then be established as shown in Fig. 7.7. It should contain the description of the cone geometry, as well as its location and orientation with respect to the skeleton, and be connected to the three relevant elementary *joint_* components, so as to simultaneously handle their individual rotations. The joint sinus cone description was provided by Engin and Tumer in the form of 2-D plots of the limit positions of the moving bone extremity, complemented with a localization of the cone axis with respect to the skeleton (Engin 89a, b). This leads therefore to a representation of the joint sinus cone using a 3x3 matrix $\mathbf{D}_C(\alpha)$ defining the cone 3-D orientation and a 2-D polygonal curve defining the basis of the cone at a given height along its axis. This basic structure may then be complemented with Boolean status for optional visualization/activation.

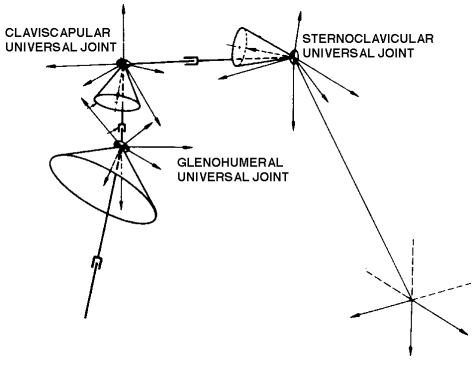

Fig. 7.5. Shoulder joints sinus cones (Engin 89a,b)

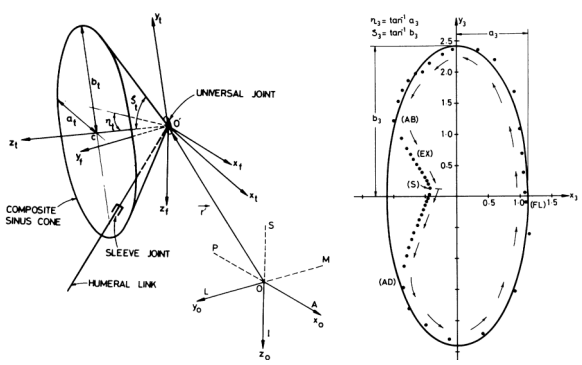

Fig. 7.6. Joint sinus cone description

```
struct cone_
{
  booleen        isactive;   /* activity flag */
  booleen        isvisible;  /* visibility flag */
  joint_         *joint_1;   /* pointer to 1st joint */
  joint_         *joint_2;   /* pointer to 2nd joint */
  joint_         *joint_3;   /* pointer to 3rd joint */
  Matrix 3-D     conerot;    /* cone orientation matrix */
  scalar         height;     /* cone height */
  scalar         longax;     /* cone basis long axis */
  scalar         shortax;    /* cone basis short axis */
  integer        nbnodes;    /* number of basis nodes */
  Vector 3-D     *basis;     /* cone basis node table */
};
```

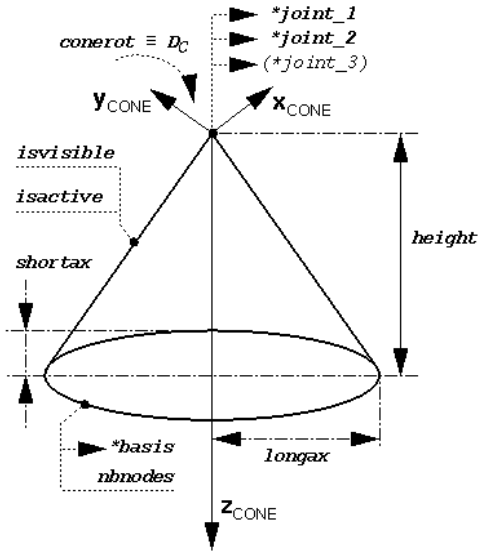

Fig. 7.7. The basic *cone_* structure

In my implementation, I have arbitrarily taken the cone axis along the ***z axis*** of the local coordinate system of the cone. The position of the cone top is necessarily located at the joint center, which, in the case of a Ball_&_Socket like structure, is identical for the three elementary *joints_*. As it delimits the mobility space of the moving limb with respect to the reference bone of the joint, the joint sinus cone should follow the motion of the reference bone and remain unaffected by that of the moving bone. Its orientation should however be defined with respect to the rest posture of the *moving* bone (3x3 orientation matrix $\mathbf{D}_C(\alpha)$).

7.2.2 Joint Rotation Bounding

If defining the basic *cone_* structure is straightforward, bounding the composite Ball_&_Socket joint rotation within the cone is a little more complex. In order to determine whether the moving bone lies inside or outside the cone, it is necessary to describe the orientation of the moving bone with respect to the coordinate system of the cone. Yet, the orientation of the moving bone with respect to the reference bone is defined by the successive product of the elementary joint transfer matrices $\mathbf{M}_j$, the permutation matrices $\mathbf{I}_j$ between consecutive joints, and the *permanent orientation* of the moving bone with respect to the coordinate system of the last elementary *joint_* (Fig. 7.9).

Concerning *joints_*, the transfer matrix accounting for the three elementary rotations and permutations may be easily designated as: (column notation)

$$\mathbf{M}(\theta,\varphi,\psi) = \mathbf{M}_j(\theta)\mathbf{I}_{j+1}\mathbf{M}_{j+1}(\varphi)\mathbf{I}_{j+2}\mathbf{M}_{j+2}(\psi) \quad \text{with:} \tag{7.5}$$

$$\mathbf{I}_{j+1} = \mathbf{I}_{j+2} = \begin{bmatrix} 0 & 1 & 0 \\ 0 & 0 & 1 \\ 1 & 0 & 0 \end{bmatrix} \text{ for the right side} \qquad \mathbf{I}_{j+1} = \mathbf{I}_{j+2} = \begin{bmatrix} 0 & 0 & 1 \\ 1 & 0 & 0 \\ 0 & 1 & 0 \end{bmatrix} \text{ for the left side}$$

The *permanent orientation* of the moving bone is a structural deviation δ instantiated at the skeleton level, corresponding to the deviation of the skeletal segment with respect to the ***z axis*** of the last elementary *joint_* component. In the BODY *template_* file (*.tpl*), this deviation is expressed as the 3-D translation vector defining the position of the child node with respect to the coordinate system of the last elementary joint component (Table 6.2).

As mentioned above, the cone axis is chosen along the ***z axis*** of its local coordinate system. For the boundary test to be consistent, the limb 3-D vector must therefore be considered as the ***z axis*** of a coordinate system deviated from that of the last elementary *joint_*. The limb deviation may then be expressed as a 3x3 rotation matrix which transforms the ***z axis*** of the last *joint_* into the unitary axis of the skeletal limb segment. In order to express this matrix, the *dot* and *cross* products may first be computed, so as to determine the rotation angle and axis (Fig. 7.8). An *axis-angle* vector may then be composed and converted into a 3-D orientation matrix. As a result, the 3-D translation vector may be converted into a 3-D deviation matrix $\mathbf{D}_L(\delta)$ with respect to the coordinate system of the last elementary *joint_* component (Fig. 7.9).

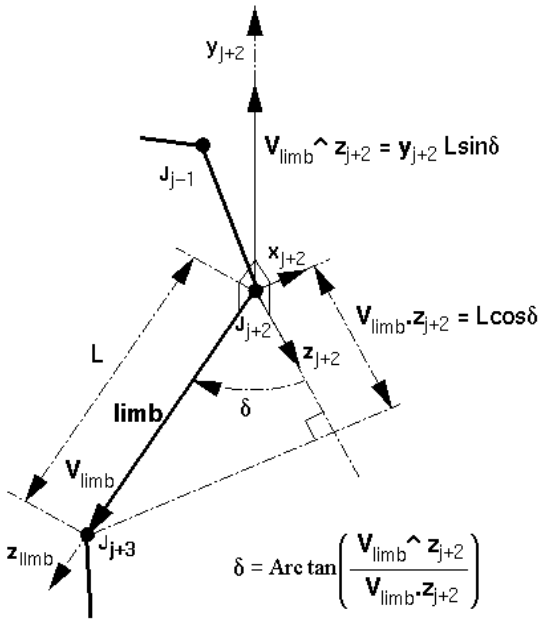

Fig. 7.8. Limb deviation angle determination

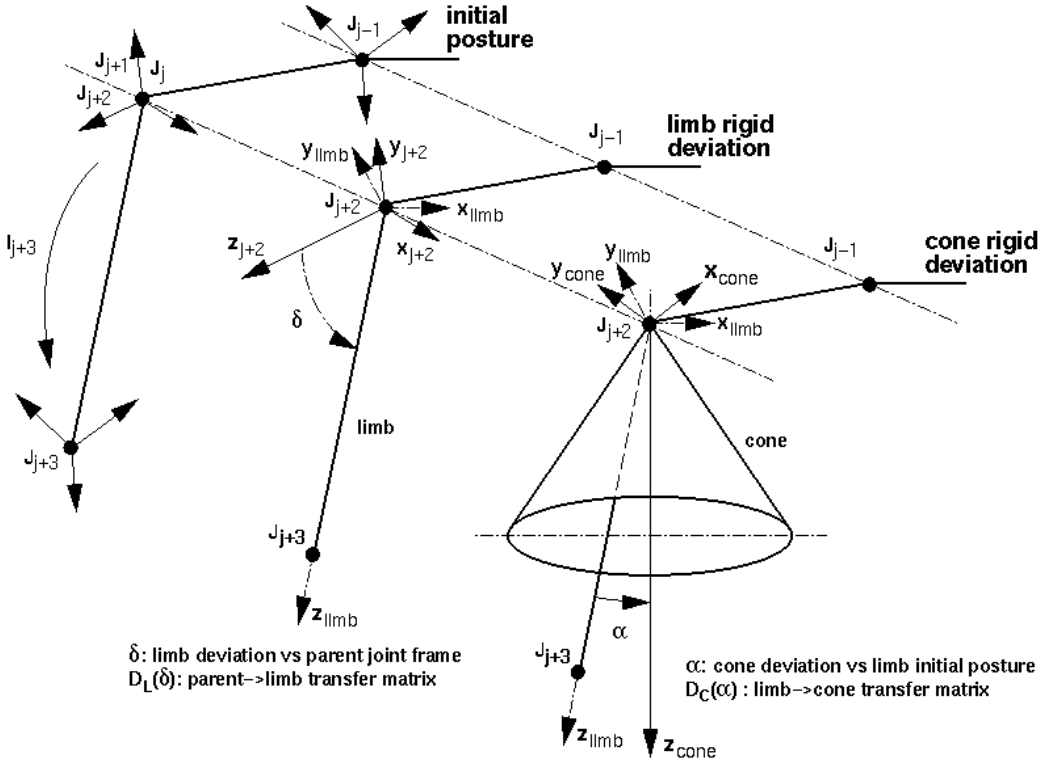

Fig. 7.9. Limb and cone deviations defined with respect to the skeleton rest posture

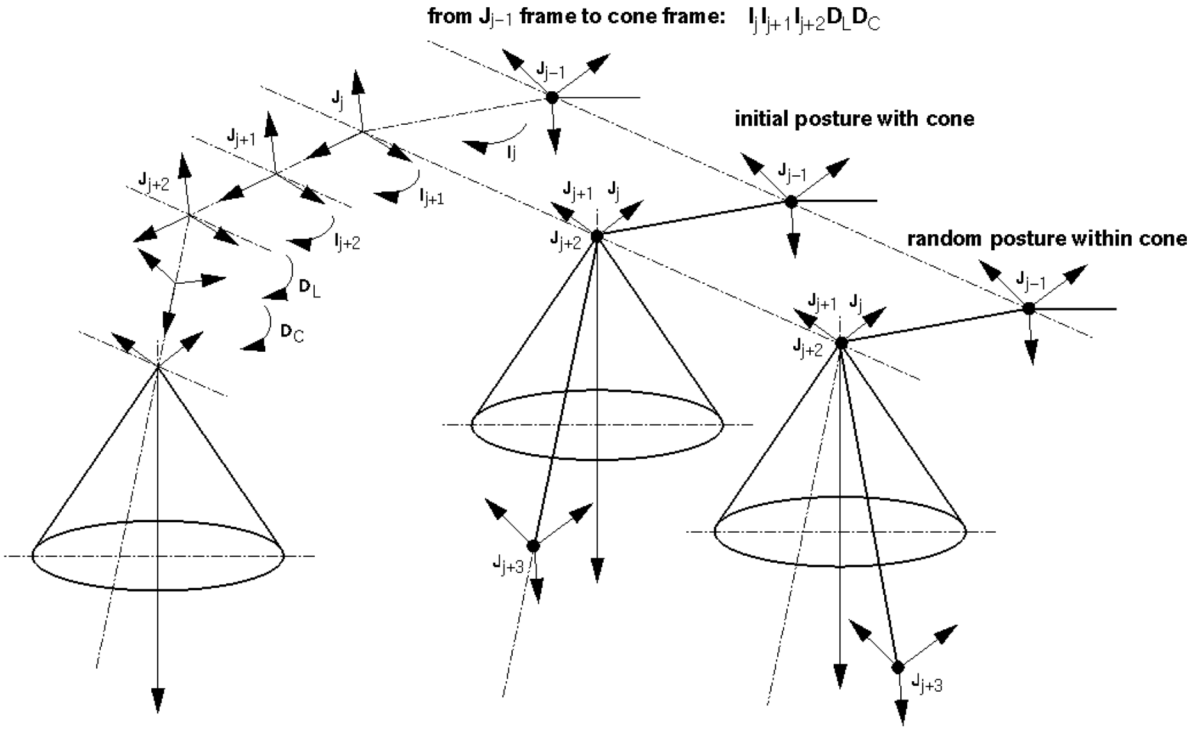

Fig.7.10. Limb segment description relative to the cone coordinate system

As a result, the transfer matrix from the local coordinate system of the cone to the local coordinate system of the skeletal limb segment may be composed as (Fig. 7.10):

$$\mathbf{T} = \mathbf{D}_C^{-1}(\alpha)\cdot\mathbf{D}_L^{-1}(\delta)\cdot\mathbf{I}_{j+2}^{-1}\cdot\mathbf{I}_{j+1}^{-1}\cdot\mathbf{M}(\theta,\varphi,\psi)\cdot\mathbf{D}_L(\delta) \qquad \text{(column matrix)} \qquad (7.6)$$

Once the orientation of the moving limb is expressed in the local coordinate system of the cone, it only remains to determine whether the limb lays inside or outside the cone. Making use of the 2-D polygonal description of the cone basis curve, the 3-D problem may be reduced to a two-dimensional point-in-polygon test. The main difficulty however, does not lay in this test. The objective is not just to identify whether the limb lies in the cone or not, but to determine, first, the position on the cone where the bone should be left instead of crossing the conic boundary, then the *joint_* rotation sequence corresponding to the bound posture.

The first item may be easily obtained by switching from the point-in-polygon test cited above to a line-segments-intersection test applied to the radial limb segment with each segment of the 2-D polygonal cone basis curve (Fig. 7.11). The algorithm used for this purpose does not present any difficulty and may be found in the *Graphics Gems Manuals* (Franklin 92). It is more difficult to determine the second item: how much each elementary *joint_* component involved should be rotated to place the moving limb in the bound posture? To achieve this, the first thing to do is to determine the orientation matrix of the bound posture with respect to the reference coordinate system of the first *joint_*. This may be obtained in assuming that the concerned posture is obtained after rotation β of the moving limb from its previous known posture. The intermediate rotation matrix may then be determined between both postures following the same approach as used for determining the limb deviation (Fig. 7.8), and may be multiplied to the rotation matrix of the known previous posture. The conversion of the matrix into an Euler sequence may finally be performed by assuming the same rotation/permutation sequence order as that of the previous known posture.

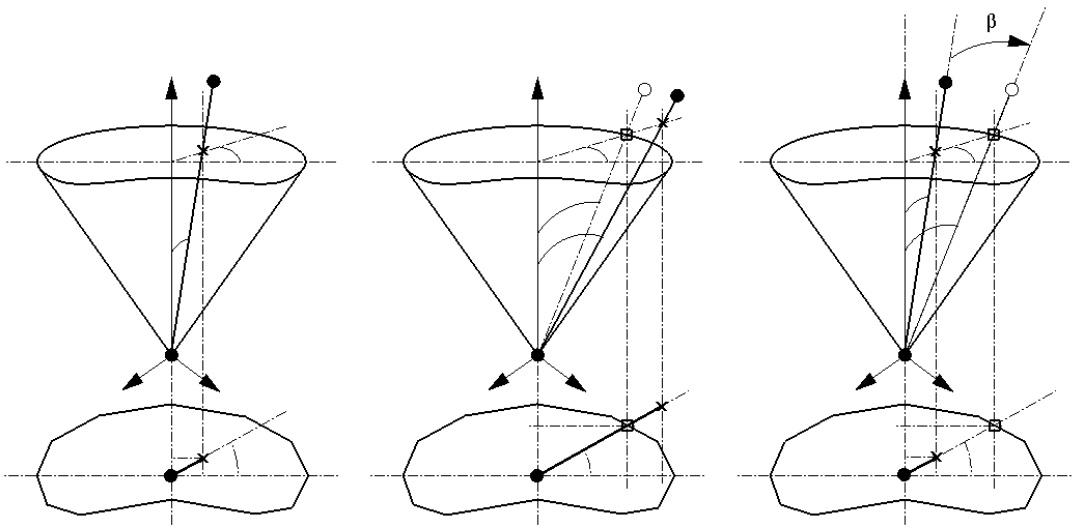

Fig. 7.11. Bound posture identification from the current posture and the outsiding next one

7.2.3 Adjustment for Twistless Joints

As explained in § 6.1.2, some of the joints characterized as Ball_&_Socket joint structures in the real human body have been reduced to 2-DOF structures in the BODY *skeleton_* used in LIG. In particular, this is the case for the *_clavicle_* (SC) and *_scapula_* (AC) joints for which the *_twisting* DOFs were expected to be useless and excluded from the model. These composite joints should however be provided with a joint sinus cone boundary as well as the *_shoulder_* (GH) joint. Besides this, some other joint structures like the *_wrist_* could also benefit from a joint sinus cone boundary, though they actually do not possess *_twisting* DOF. Such composite joints require a specific adaptation of the above procedure. As no twisting DOF is available in these structures, the boundary test procedure should only handle the first two rotation angles of the Euler sequence. More precisely, the determination of the Euler sequence of the bound posture should leave the last angle of the sequence unchanged with respect to the Euler sequence of the previous posture.

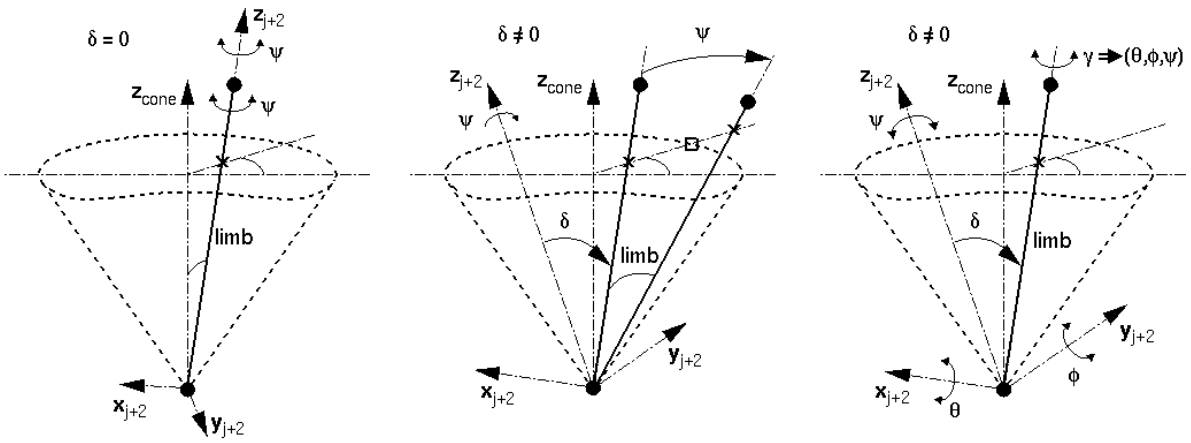

a) no influence b) twisting influence c) rotation decomposition

Fig. 7.12. Twisting DOF influence in the limb motion bounding depending on its deviation

This is however possible only under the condition that the limb axis lays along the virtual *_twisting* ***z axis***, i.e. when the rigid deviation of the limb with respect to the coordinate system of the virtual third joint is null (Fig. 7.12a). In such a case, the limb segment may rotate and be bound on the conic boundary without requiring rotations around its main axis. By contrast, if the limb segment is deviated with respect to the ***z axis*** of the virtual *_twisting joint_*, the Euler decomposition of any of its 3-D rotation movement involves a twisting DOF that can not be instantiated since the *_twisting joint_* does not exist (Fig. 7.12b,c).

Fortunately, unless the joint coordinate systems and rotations are required to fit the biomedical conventions as presented in § 2.3.3, there is nothing that imposes the use of deviated skeletal limb segments with respect to the joint coordinate system axes. Up to now, in LIG, most body templates have been usually designed with default skeletal segments along the ***z axis*** of the (existing or virtual) *_twisting* DOF. This is also fortunately the case for the anatomic template presented in § 6.2.1 since it was developed for animation purposes. It is therefore possible to simplify the boundary test procedure, so that the bound posture orientation may be determined from an Euler conversion, which does not affect the third angle of the sequence, while eventually accounting for it when the *_twisting* DOFs exits. This way, the procedure may be indifferently applied to full 3-DOF as well as to 2-DOF degenerated composite Ball_&_Socket joint structures.

7.3 Cone Design Interface

7.3.1 SKELEDIT Extension

Once the cone structure was implemented, it has been necessary to develop an interface allowing the interactive design of the cone shape and the testing of the associated method for bounding the limb motion within the cone. Such an interface could have been implemented from scratch, ignoring other existing tools working on the body structure. I have preferred to extend an existing program, *Skeledit*, developed at LIG by Eric Chauvineau, which is devoted to the interactive design of BODY *skeleton_* templates.

Skeledit is composed of a *main control panel*, allowing the independent loading of the body *template_* (*.tpl*) and *joint_* files (*.jts*), and a *3-D viewer* for visualizing the resulting hierarchy (Fig. 7.13). With the help of annex control panels for each body section (trunk, lower limbs, upper limbs, etc.), the user may then modify the *skeleton_* topology by interactively specifying the body segment vectors, and correct the limit and rest angle values of the body *joints_*. The resulting *skeleton_* may finally be saved as new *template_* and *joint_* files.

Skeledit originally allows the individual selection of each BODY joint for adjusting its motion range. Consequently, I have chosen to base my extension on the section of the interface which handles these events, so as to provide the user with the option of adjuncting a joint sinus cone when the selected joint is appropriate. For this purpose, a distinction between the independent joints and the composite joint sequences of the BODY *skeleton_* structure was necessary. As my attention was focussed on the human upper limb, I have allowed the adjunction of a joint sinus cone structure to the BODY *_clavicle_* (SC), *_scapula_* (AC) and *_shoulder_* (GH) *joints_* only. Extension to the other Ball_&_Socket joint structures of the body is however possible.

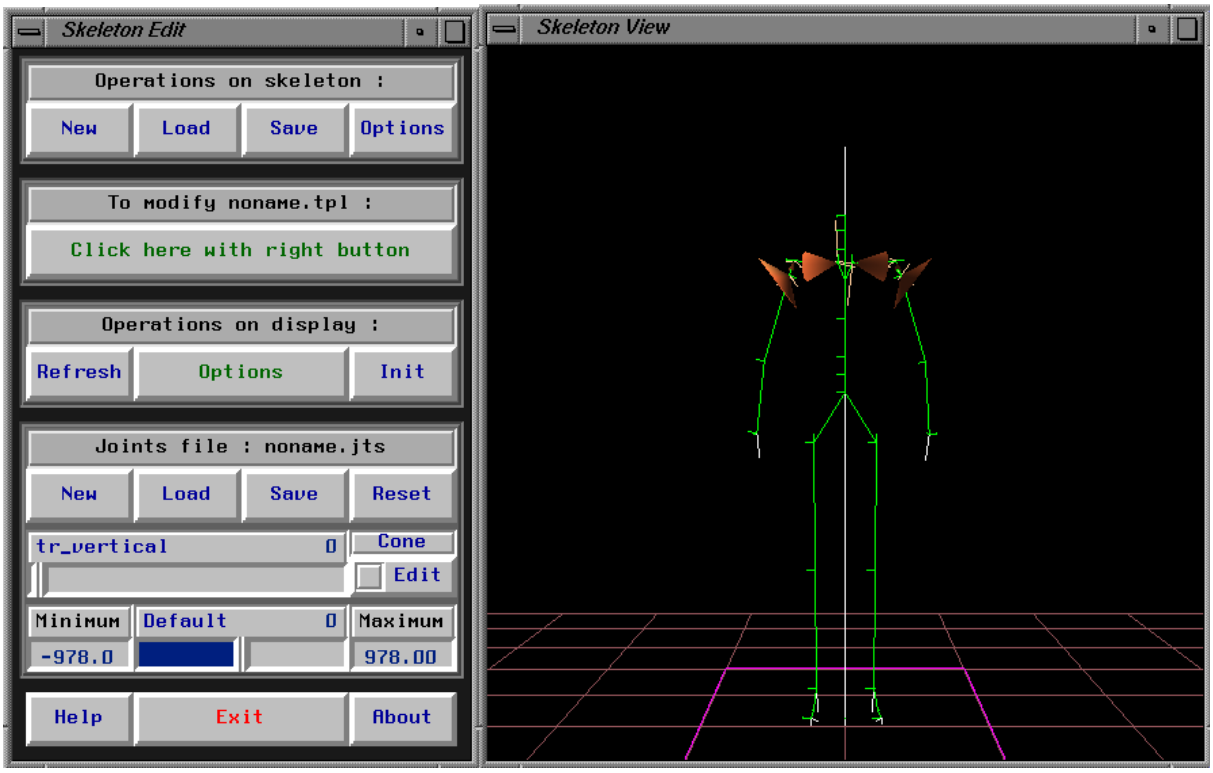

Fig. 7.13. The *skeleton_* editor *Skeledit* (modified from Eric Chauvineau's orginal *Skeledit*)

The interactive design of the joint sinus cones requires allowing:

- the optional adjunction of a sinus cone to appropriate joints.
- the interactive design of the cone basis curve.
- the interactive setting of the cone orientation with respect to the skeleton.
- the motion control of the limb segment for the interactive testing of the cone.

As for the implementation of the shoulder model within BodyLib presented in § 6.2.2, the constraint was to introduce these new functions without spoiling the existing ones. Developments on this basis are presented in the following section.

7.3.2 Cone Interactive Design and Testing

When the joint currently selected is appropriate (*_clavicle_…*, *_scapula_…*, *_shoulder_…*) and the adjunction of a joint sinus cone is required by the user, a default cone structure is created with an elliptic 80x40 mm octagonal basis at an height of 80 mm and properly attached to the concerned Euler joint sequence. Three windows are then displayed (Fig. 7.14):

- the Basis Design window.
- the Cone Orientation window.
- the Control Panel window.

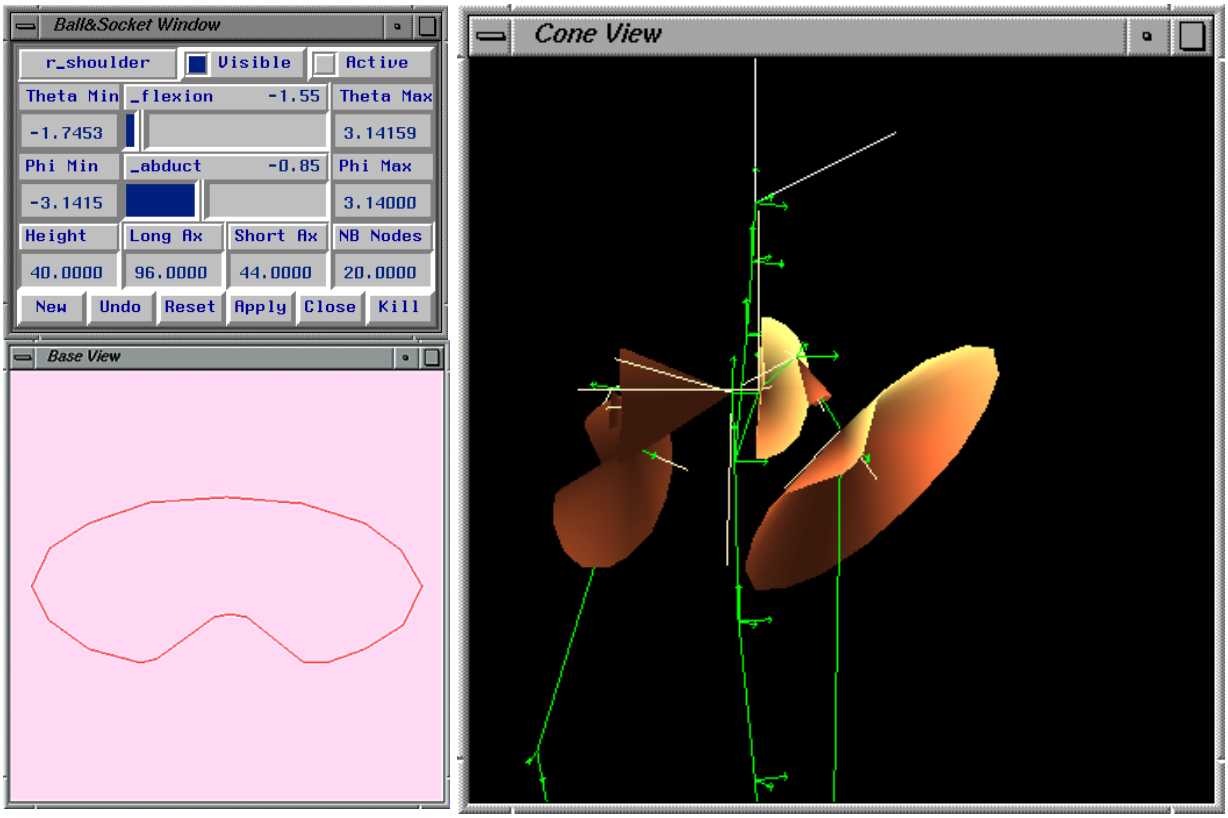

Fig. 7.14. The added *Basis Design*, *Cone Orientation*, and *Control Panel* Windows

The Basis Design Window. The Basis Design window is a 2-D drawing area displaying the polygonal basis of the current cone. In this area, the user can interactively design the shape of the cone basis curve by picking and dragging the existing nodes using the left mouse button. Node addition can be achieved individually by using the middle mouse button, or universally by setting the number in the Control Panel. By contrast, node removal is only allowed individually using the right mouse button. As the changes are directly applied to the current cone attached to the skeleton structure, the resulting design is simultaneously displayed in the Cone Orientation window and the main viewer. The design process is moreover eased by the "Undo", "Reset" and "New" functions made available in the Control Panel.

The Cone Orientation Window. The Cone Orientation window is a local view of the skeleton, centered on the selected joint and displaying the currently edited 3-D cone object. The window offers the usual trackball features for rotating or translating the point of view around the cone. Besides this, pressing simultaneously the *shift*-key from the keyboard and the middle mouse button inhibits the trackball features and allows the user to interactively orientate the 3-D cone object with respect to the skeleton. As the changes are directly applied to the current cone attached to the skeleton structure, the resulting design is simultaneously displayed in the Skeleton Display window. The design process is also eased with the "Undo", "Reset" and "New" functions made available in the Control Panel.

The Control Panel Window. The Control Panel Window allows the specific setting of the general parameters of the cone such as its height, its active and visible states, the long and short axes of the elliptic basis curve and its number of nodes. Common editing features such as "New", "Undo", "Reset", "Apply" and "Kill" are also made available to aid design. Finally

two sliders have been added to allow changes to the first two rotations involved in the Euler sequence. This may be used for positioning the moving limb and controling the bounding effect of the cone. However, the direct individual control of each joint is contradictory to the purpose of testing the combined effect of the whole Euler sequence. This is the reason why another interaction has been developed, which allows the inverse control of the three-joint sequence.

In the original approach, joint limits are handled individually. This approach can no longer be applied as soon as the joint sinus cone actually introduces a relationship between the individual joint boundaries of the Euler sequence. As stated in § 7.2.2, the problem consists in finding for any "outside" posture the Euler sequence, which leaves the limb against the cone. For this purpose, a new interaction mode has been added to the Basis Design window. Pressing the *shift*-key while pressing the left mouse button in that window replaces the design functions attached to the mouse with a function controlling the orientation of the moving limb with respect to the cone. The 2-D position of the mouse cursor is thus interpreted as the intersection of the moving limb with the plane defined by the cone basis. When the cone is active, the coordinates of the corresponding bound limb posture against the cone are obtained using a 2-D line-intersection test as described in § 7.2.2. The conversion of this posture into the corresponding 3-D Euler sequence is then achieved as follows. The deviation of the bound limb posture with respect to the unbound posture is first inquired (Fig. 7.8), and the corresponding 3-D rotation matrix multiplied to the 3-D orientation matrix of the unbound posture. The resulting 3-D orientation matrix corresponding to the bound posture is then converted into an Euler sequence with the assumption of a null deviation between the moving limb segment and the ***z axis*** of the (existing or virtual) *_twisting joint_* (see § 7.2.3). As a result, when the *shift*-key and the left mouse button are pressed together in the Basis Design window, the user can control the 3-D orientation of the moving limb with respect to the cone and verify its effective bounding on the cone border when the cone is active.

7.3.3 Biomechanical Cone Design

As an application, the cone design interface has been used for providing biomechanical joint sinus cones to the upper limb joints of the anatomic BODY *skeleton_* structure. The anatomical and biomechanical data provided by Engin and Tumer were used for this purpose (Engin 89a,b). Joint sinus cones for the *_clavicle_* (SC), *_scapula_* (AC) and *_shoulder_* (GH) *joints_* have thus been approximately interactively designed following the provided 2D distorted elliptic sections and the cone orientation graph (Fig. 7.16) . The comparative designs are shown in Fig. 7.15 whereas the corresponding design parameters are gathered in Table 7.1. The resulting shoulder model may be seen in Figs. 7.13, 7.14, and 7.17.

Table 7.1 Parameters of the instantiated joint sinus cones (basis nodes not detailed)

cone		height	longax	shortax	nbnodes	axis angle	nbjoints
right	**SC**	100	42	25	17	(-0.059, 0.011, 1.399)	2
	AC	30	10.5	8.1	20	(0.019, 0.090, -2.693)	2
	GH	40	96	44	20	(-0.701, -0.660, -2.512)	3
left	**SC**	100	42	25	17	(-0.0477, 0.140, -3.105)	2
	AC	30	10.5	8.1	20	(0.001, -0.057, 0.783)	2
	GH	40	96	44	20	(0.387, 0.536, -0.606)	3

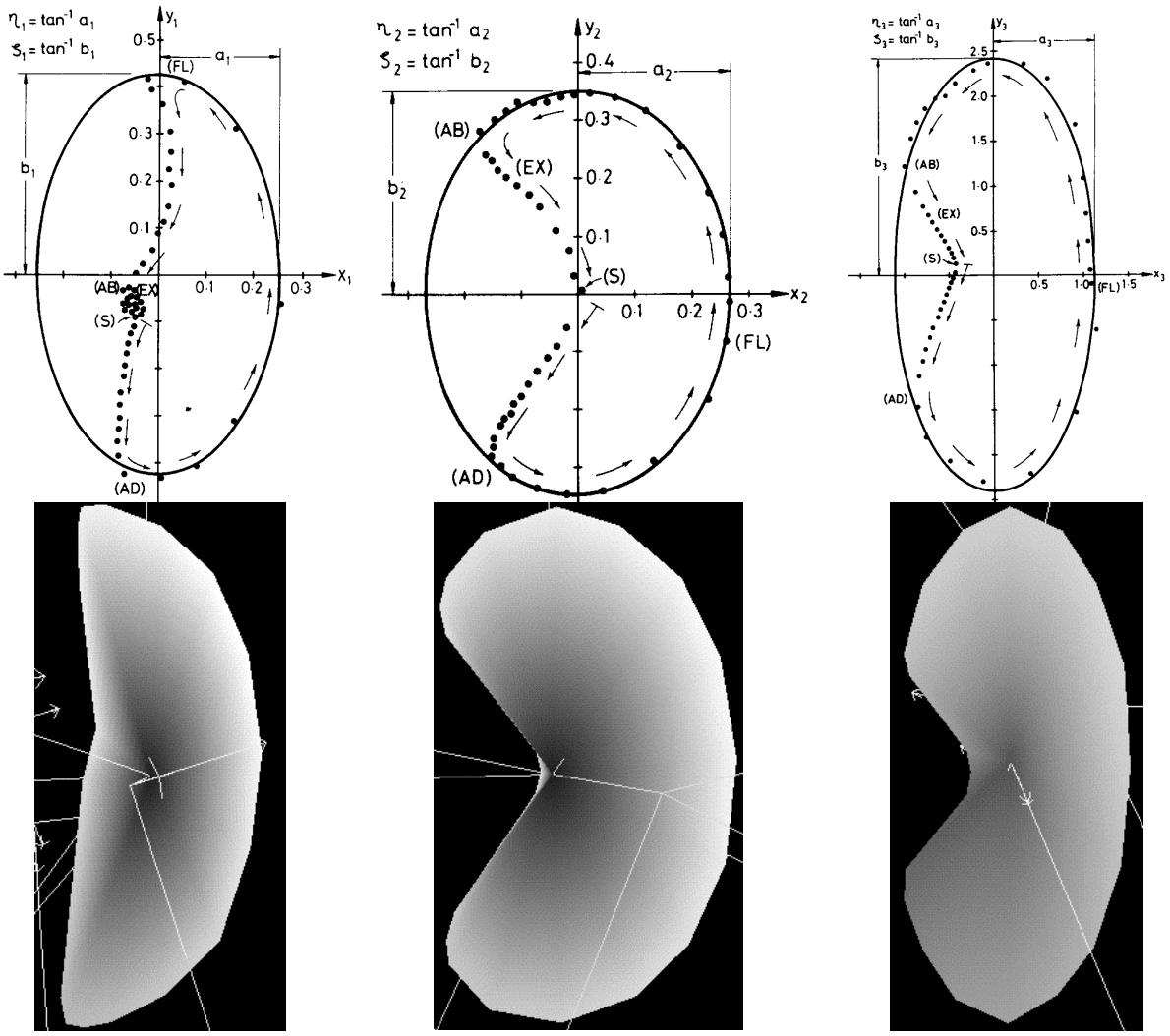

Fig. 7.15. 2-D and 3-D representation of the human shoulder joint sinus cones (Engin 89a,b)

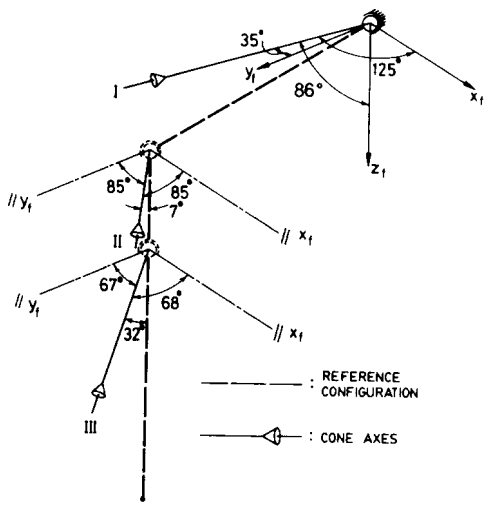

(Engin 89a,b)

Fig. 7.16. Shoulder joint sinus cone orientations

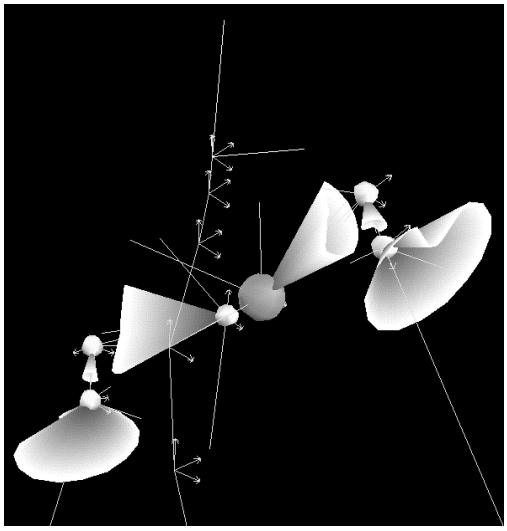

Fig. 7.17. 3-D BODY shoulder model

7.4 Integration

7.4.1 Inverse Kinematics

The inverse kinematics algorithm used for animating the human upper limb model was briefly presented in § 6.3.1. Using this algorithm, new *joint_* angle values are calculated at each inverse kinematics iteration, and are *individually* tested with respect to the limits of the respective *joint_*. However, as detailed in § 7.2.2, the bounding of the skeleton limb segment on the joint sinus cone involves simultaneous rotations in, at least, the first two *joints_* of the composite Ball_&_Socket joint structure. Thus, for adjusting the inverse kinematics algorithm to the use of such conic boundaries, it has been first necessary to extend the *joint_* boundary test function with the simultaneous control of the concerned *joints_* as required. This was easily achieved as each *joint_* structure contains a pointer to the associated *cone_* structure, which contains, itself, pointers to the two or three individual *joints_* to which it is attached. Thus, in the loop which tests each *joint_* with respect to its own limits before updating the skeleton posture, the *joints_* involved in a composite Ball_&_Socket structure could be identified and tested together with respect to the conic boundary.

However, as explained in § 6.3.2, for time saving, when the calculation could make a *joint_* cross over its limits, the usual procedure is to leave the *joint_* on its previous posture, and to fill the related column of the Jacobian with zeros (Boulic 97). Applied with joint sinus cone boundaries, this approach would result in leaving the limb segment away from the conic boundary until the next iteration. This situation has a major disadvantage in the fact that the skeleton limb segment immobilizes inside the bound mobility domain instead of progressing along the cone border towards the goal. Thus, as *joints_* happen to reach the cone boundary, the skeleton is left in an unsatisfying posture, whereas better postures on the cone border could have been reached as well. In order to avoid this situation, it has been necessary to turn back to the more general approach, which consists of leaving the *joints_* against their boundaries and recalculating the Jacobian matrix after updating the posture. Though this approach is time consuming, it has the advantage, in our case, of allowing natural continuous bound movements like circumduction.

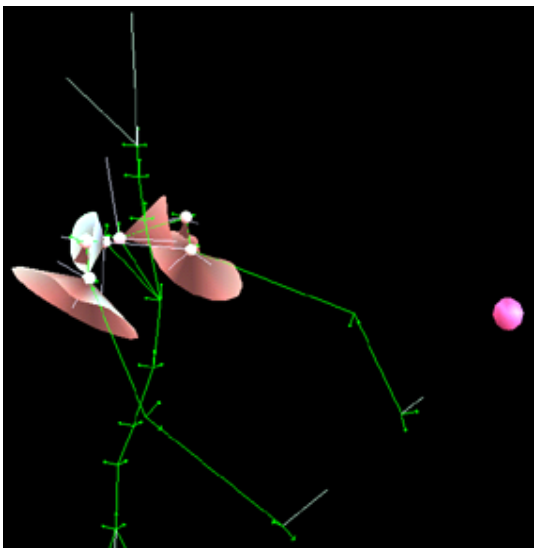

Fig. 7.18. Arm extension conic bounding

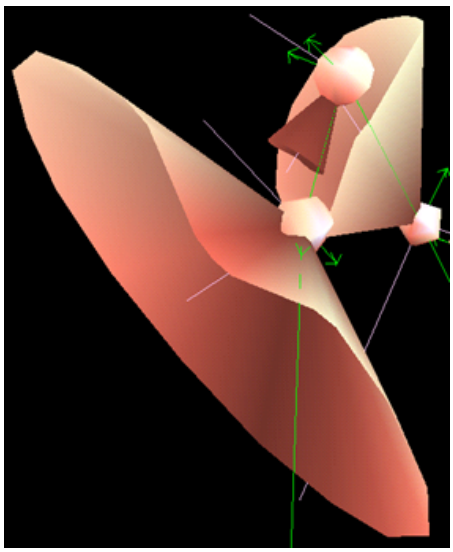

Fig. 7.19. Close view of the joint sinus cones

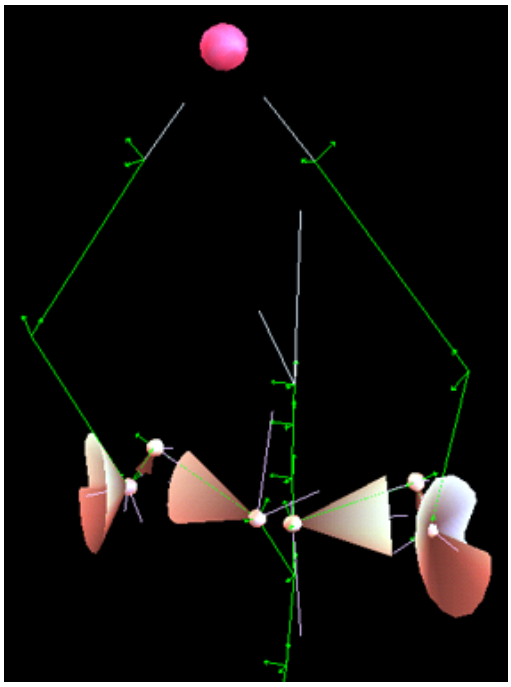

Fig. 7.20. Arm elevation conic bounding

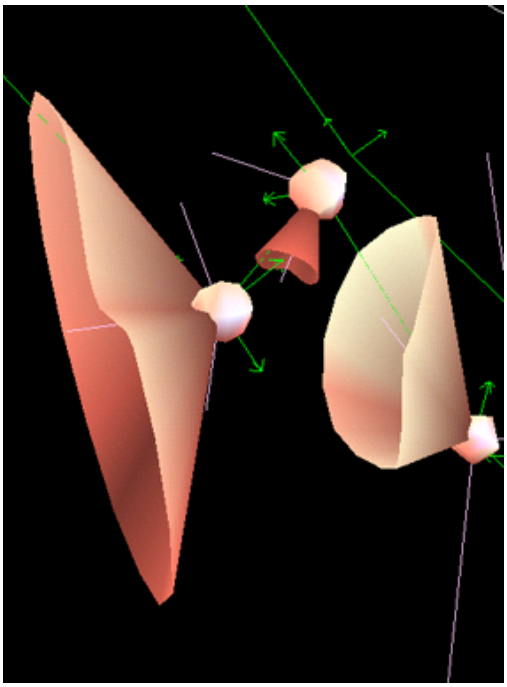

Fig. 7.21. Close view of the joint sinus cones

In order to test the integration of the cone bounded human model within the inverse kinematic algorithm, I have implemented a basic program using the SGI GL library and the 5th-D Toolkit application builder developed at LIG, by Enrico Gobetti and Francis Ballaguer. This program only allows the interactive motion control of the upper limbs using a spaceball device. Contrary to the Inventor Animation Interface presented in § 6.3.2, it does not supply the constraint of the scapular segment on a thorax-like shape. Consequently, the resulting motion is not to be considered as an animation of the upper limb model. The purpose of this development was just to visualize the effective bounding of the skeletal limb segments on the designed joint sinus cones. This development was necessary since, as presented in the next section, using the Animation Interface, only thick 3-D Inventor bones can be visualized instead of the actual limb segments. This program has furthermore the advantage of allowing the interactive design of 3-D goal trajectories. To illustrate this application, global and close views of two bounded postured obtained with this tool are shown in Figs. 7.18 to 7.21.

7.4.2 The Animation Interface

Following the integration with the inverse kinematics algorithm, I have extended the Animation Interface presented in § 6.3.2 so as to allow the visualization and activation of the upper limb joint sinus cones. The resulting 3-D Inventor models may be seen in Figs. 7.22 and 7.23. Given that, in this application, the skeletal limb segments are seen as 3-D Inventor bones, the bounding of the limbs on the joint sinus cones can not be properly evaluated. For a skeletal limb segment laying on the cone, the corresponding 3-D bone would be crossed by the cone surface along its longitudinal section, which may give the impression that the motion of the limb is not bound to the cone. In order to diminish this effect, the coordinates of the basis nodes of the 3-D Inventor joint sinus cones have been slightly scaled up so as to contain at least the extremity of the concerned bone.

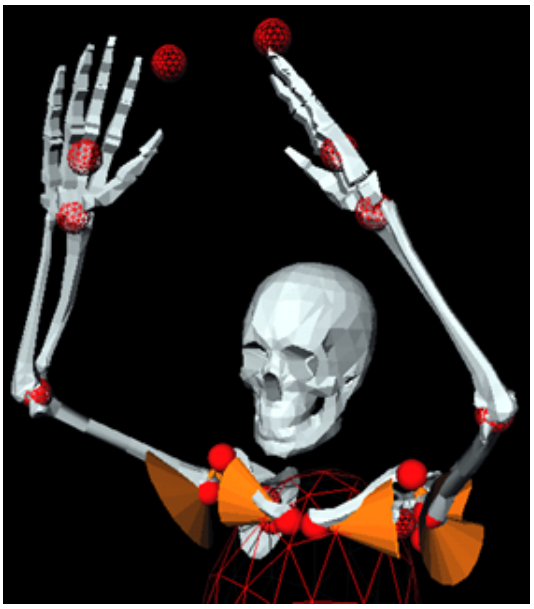

Fig. 7.22. Elevation bounding in Inventor

Fig. 7.23. Extension bounding in Inventor

7.4.3 Results

As a conclusion to this development, the combined effects of the scapulo-thoracic constraint and the conic bounding of the joints on the realism of the resulting upper limb movements have been considered. Though the implementation has proven to be achievable and bound to lead to more realistic animation, several drawbacks have been observed to the simultaneous use of both approaches.

The first drawback may be outlined as being the major down-slowing of the interaction and the animation when all skeletal segments are bound onto the joint sinus cones. In such a situation, two inverse kinematics loops are running for the right and left upper limbs, each accounting for two end-effectors and for the conic bounding of three skeletal limb segments following the approach developed in § 7.2.2. This is to be added to the heavy rendering in the three Inventor viewers of the scene involving the 3-D skeleton model. As a result, it is more difficult to generate a smooth animation of the model as well as to properly coordinate the movements of the scapulas with those of the upper limbs.

The second drawback has been observed to be the competition between the scapulo-thoracic (ST) constraint and the bounding on the *_clavicle_* (SC) and the *_scapula_* (AC) joint sinus cones. This behavior can be explained by the distinct origins of the 3-D skeleton model and the joint sinus cones provided by Engin and Tumer (see § 7.3.3). Measured on a real subject, the shapes of the SC and AC joint sinus cones are necessarily influenced by the effective constraining of the motion of the scapula on the thorax. Applied with a different 3-D skeleton model, they are likely to be incompatible with the substitute ST constraint. In my approach, the joint sinus cone happens to be given the priority since the ST constraint is involved in the inverse kinematics algorithm in the form of an end-effector trajectory. Though the scapula tends to follow its goal on the thoracic ellipsoid, the clavicle and scapula limb segments may be replaced back against their respective cones. Consequently, the motion of the scapula may be notably extended away from the thorax, when it does not oscillate between both states.

Anyway, involving the scapulo-thoracic constraint in the inverse kinematics calculation is indispensable since this constraint provides the motion coordination between the clavicle and the scapula. As stated in § 7.4.1, this is what is actually missing, when only the joint sinus cones are taken into account.

Furthermore, the motion of the shoulder loop bones was already looking quite realistic, though without bounding the corresponding limb segments on specific joint sinus cones. This may again be attributed to the fact that the shapes obtained by Engin and Tumer for the SC and AC joint sinus cones may be influenced in a major way by the scapulo-thoracic constraint (Engin 89a,b). It may eventually even be the case that with only the use of the scapulo-thoracic constraint, the motion in the *_clavicle_* (SC) and *_scapula_* (AC) *joints_* is bound within a conic bound mobility domain. Nevertheless, these observations, to this point, only involve the clavicle and scapula bones, and may call into question the use of joint sinus cones for the *_clavicle_* (SC) and *_scapula_* (AC) joints only. This is not the case for the *_shoulder_* (GH) joint sinus cone which is due to the gleno-humeral cartilagenous surfaces and ligamentous structures and which does not depend neither on the *_clavicle_* (SC) and *_scapula_* (AC) joints nor on the scapulo-thoracic constraint.

As a result, a solution to both the drawbacks invoked above could be to remove the SC and AC joint sinus cones from the model so as to give the priority to the scapulo-thoracic constraint, whereas keeping the GH joint sinus cone for improving the bound rotation of the *_shoulder_* (GH) joint. On the one hand, this would reduce the inverse kinematics computation time and ease the interactive animation of the model, whereas, on the other hand, it would solve the observed instability due to the conflict between the *_clavicle_* (SC) and *_scapula_* (AC) joint sinus cones and the scapulo-thoracic constraint. This compromise was proved to be satisfying and was adopted for the generation of realistic upper limb animations.

7.4.4 Anatomic Body Animation

Using the Animation Interface and the compromised upper limb model invoked previously, I have composed several keyframe animation files following the approach presented in § 6.3.2. These have been generated by direct interaction with the model or by interactive modification of existing body animations obtained from motion capture or computer graphics designers. These include:

- elementary reference movements, such as abduction/adduction, flexion/extension, etc.
- composite reference movement, such as elevation, circumduction, etc.
- shoulder and upper limb movements superimposed on walking, dancing, etc. sequences.

As the realism of a skeleton animation may be difficult to attain, these animation files have been finally played back on the anatomic muscle body model designed at LIG by Thierry Michellod. This model is a refined female body model composed using metaballs following the anatomic muscular topology. Fig 7.24 has been composed based on these animations. The other model composed by Luciana Porcher-Nedel (Nedel 98b) using prismatic physically-based muscle models (Nedel 98a) has not been completed yet to allow testing of my animations. Besides, the automatic generation of the skin layer is also not available yet on both models. The deformations generated on the muscle layer by the underlying skeleton animations may anyway be estimated as promising.

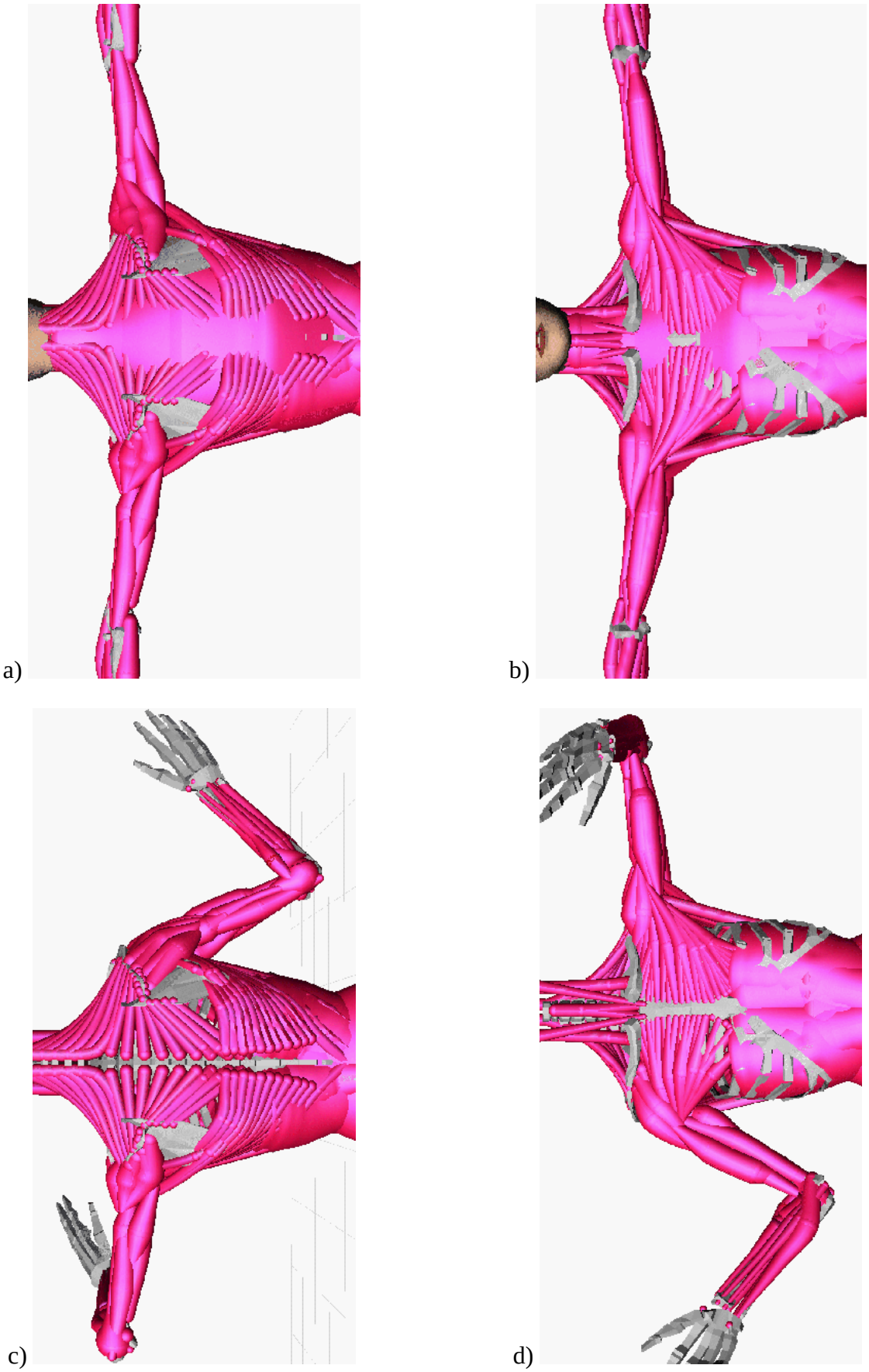

Fig. 7.24. Animation of a virtual anatomic muscled body model (Thierry Michellod, LIG)

Conclusion

In this chapter, I have investigated the possibility of improving the realism of the virtual skeleton animation with the design of realistic joint sinus cone boundaries. Following the biomechanical descriptions provided by Engin and Tumer, I have proposed the adjunction of a *cone_* structure to the *skeleton_ joints_* at the SceneLib level, and developed a respective library for joint sinus cone handling and *skeleton_* limb segment conic bounding. In particular, I have taken into account the twistless state of the BODY *_clavicle_* (SC) and *_scapula_* (AC) *joints_*. Then, I have extended LIG's *Skeledit* skeleton_ editor interface to allow the interactive cone design, and applied it to design biomechanical joint sinus cones on the BODY shoulder model. I have finally adjusted the inverse kinematics algorithm so as to operate the simultaneous bounding of the individual *joints_* commonly involved within a sinus cone boundary. This has allowed the application and testing of the joint sinus cone extension onto the virtual skeleton animation. Results tend to reveal a competition, instead of a redundancy, between the scapulo-thoracic constraint and the conic bounding of the skeleton limb segments. This may be attributed to a possible incompatibility of the joint sinus cone shapes obtained by Engin and Tumer with the scapulo-thoracic constraint implemented in Chapter 6. Besides, the Jacobian re-calculations induced by the bounding of the *skeleton_* limbs on the six cones notably diminish the interest of the approach. I have then proposed a compromise with the removal of the *_clavicle_* and *_scapula_* joint sinus cones while maintaining the *_shoulder_* (GH) joint sinus cone and the scapulo-thoracic constraint. The model was finally applied to the generation of various upper limb animations, which satisfyingly apply to the animation of anatomic muscled body models.

8 Conclusion

In this thesis, the modeling of the human upper limb, and of the human shoulder in particular, has been investigated for both purposes of accurate biomechanical simulation and realistic virtual body animation. This work has been achieved in close collaboration with European partners in the context of the CHARM project and with other collaborators at LIG involved in the realistic animation of anatomic body models. My contribution to both purposes, and more generally to the research on the modeling, simulation and animation of musculoskeletal systems, is summarized in this concluding chapter. In particular, it outlines the investigations I have led, the syntheses I have provided, the suggestions and developments I have made as well as the implementations I have achieved on this basis. Perspectives of potential future investigations and developments are finally proposed as a conclusion to this work.

8.1 Contribution

8.1.1 Investigations

Research in Computer Animation usually leads to the development of original approaches for the realistic modeling of various phenomena, though without much attention to the actual physical processes involved in the real ones. On the contrary, when the objective is fundamentally the modeling of a real phenomenon by taking into account these real processes, free creativity is considerably undermined, to the benefit of accurate references and respect to the available knowledge, theories, models and methods which have so far made the rule for such objective.

This was actually the case for the long term basic research project CHARM, which aimed at the accurate realistic simulation of the human upper limb with the help of the most elaborated models and methods available, including knowledge of the skeletal, muscular and material constitutions and biomechanics. In particular, my responsibility in this project has led me to investigate many highly theoretical fields, in order to point out or develop models and approaches to apply for succeeding in the project goals.

This included investigations in:

- the skeletal and muscular anatomy and biomechanics of the upper limb
- the former skeletal and muscular upper limb models proposed

- the physiology and biomechanics of muscle contraction
- the available models for muscle contraction simulation
- the available methods for muscle force prediction
- the physiology and biomechanics of soft tissues
- the former approaches followed for deformation simulation
- the theoretical nonlinear mechanics and incremental finite element methods
- the biomechanical models for soft tissues and the former finite element applications

8.1.2 Syntheses

In Chapter 1, I have provided an analysis of the overall pipeline of the project with full details of the different stages involved and their respective input/output. However, the general procedure to follow as well as the coordination between its different stages did not appear so clearly at the beginning of the project. Though we all knew that we wanted to achieve the biomechanical modeling and simulation of a musculoskeletal system including the finite element deformation of soft tissues, we didn't know at first how the different stages of this program could be developed and coordinated towards the achievement of the simulation. If the literature partially brought answers to these queries, our ambitious project had no precedent, and no publication was found providing grounds and directions towards its complete achievement with sufficient details on the available models and methods to apply.

It is essentially in this sense that my efforts in CHARM constitute a more general contribution to Research. In the context of the project, my work led to two major publications:

- a book, published by *Springer* (Maurel 98), aiming at delineating the available biomechanical constitutive relationship for soft tissue modeling with respect to the continuum mechanics theory, and at clarifying how such highly nonlinear relationships could be applied using finite element methods

- an extensive paper in *Computer Methods in Biomechanics and Biomedical Engineering* published by *Gordon and Breach* (Maurel 99), aiming at describing the development of the biomechanical musculoskeletal upper limb model as well as at providing directions towards its implementation and simulation following approaches proposed in the literature

The book replies to a lack of synthesis concerning the various forms that constitutive relationships may take, to a lack of grounds for these forms with respect to the theoretical mechanics, and to a lack of guidance towards their application to simulation using numerical methods. In biomechanics, any representation is called a "model", most models ignore the others, and numerical methods are almost always illustrated on simple linear examples. The literature also offers some elaborate manuals investigating deeply, but separately, physiology, theoretical mechanics, soft tissue biomechanics and numerical methods. Very few of them, however, allow a global understanding of these disciplines and their interrelationships in the scope of a biomechanical simulation.

The paper replies to a lack of grounds concerning the modeling of musculoskeletal systems, as well as to a lack of guidance concerning the approach to follow towards such a simulation. If many models of musculoskeletal systems may be found in the literature, they are usually imposed with assumptions after anatomical and biomechanical considerations, and left to *a posteriori* validation. The *a priori* considerations, which led to these assumptions, are rarely detailed. In my case, I have aimed at forming a basis for the choices and assumptions involved in the development of the upper limb model. The originality of my contribution in this direction may thus consist less in the proposed upper limb model itself than in the presentation of its development and of the general approach followed in CHARM, which is provided in § 1.3, and which was received for publication with very good reviews.

8.1.3 Suggestions

The purpose of my investigations and syntheses was not reduced to the extensive reviewing of the literature for itself, but essentially to the outlining of the most appropriate models and approaches towards the achievement of the objectives of CHARM. On this basis, I had:

- an intensive collaboration with UG for the implementation of the data structure as well as for the development of the interface of the topological modeler. In particular, I have defined the structures and parameters that should be contained in the classes, and specified the editing procedure and interactions that should be offered by the topological modeler.

- an intensive collaboration with IST for the selection of biomechanical models for muscle, tendon and skin as well as for their application to muscle force prediction and simulation using the finite element method. In particular, I have suggested the use of Otten-Kaufmann's or Zajac's models for muscle force prediction following Karlsson's approach, and the application of Fung's QLV theory with, among others, Woo's or Trevisan's 1-D models for tendons, Horowitz's or Humphrey's 3-D models for muscle, and Shoemaker's or Tong's 2-D models for layered skin.

The reality of suggestions is that they are not bound to be followed. This happened to be the case for some of mine:

- because I had missed more appropriate models or approaches:
  this concerns essentially the use of dynamic optimization techniques with Zajac's model as well as its combination with the finite element simulation of muscle contraction, as this has been successfully achieved by IST partners

- because I was not in the appropriate situation to take the decisions:
  this concerns essentially the selection of the constitutive models of muscle and skin for implementation in the ABAQUS finite element software. My preference was for Horowitz and Shoemaker's models but their implementation appeared to be inappropriate to IST partners

Also, the model I have developed and proposed for the simulation of muscle contraction was not considered, given a more appropriate approach combining Zajac's and Humphrey's model which was developed by partners.

8.1.4 Developments

Nevertheless, the development of the biomechanical model of human upper limb was actually my own responsibility and, in this context, I have been able to make choices. This essentially concerns:

- the development of the kinematic model: in particular, the definition of the joint rotations, the coordinate systems and the modeling of the ST joint

- the development of the rigid-body model: in particular, the definition of cylindrical inertias, and the splitting of the forearm inertias into ulna and radius inertias

- the modeling of the muscle action topology: in particular, the anatomically-based subdivision in action-lines of broad muscles and the collection of PCSA data

- the design of the 3-D topological model of the human upper limb: in particular, the specification of joint extremum values, and the design of guides so as to insure valid action-lines, as far as possible, for any configuration of the upper limb skeleton

The model I have developed was achieved with full respect to the reported anatomy and biomechanics of the upper limb, and every one of my choices was grounded in my analysis. Its originality may be stated by the fact that my model was the first one to be fully implemented and applied to simulation without referring to any commercial software. This was part of the originality in CHARM. A compromise between accuracy and simplicity was necessary in this scope, and has been achieved in the development of my model.

8.1.5 Implementations

The theoretical investigations I have led were closely related to CHARM. However, the knowledge I have gained in anatomy and biomechanics could be also used for realistic modeling of the human upper limb. In particular, it has been used to extend the *BodyBuilder* interface for allowing the design of anatomically correct models of the human body. If the unrealistic deformations around the shoulder could be diminished with the former body models, the realistic animation of the shoulder bones became a necessity when the deformation was expected to arise from realistic anatomic muscle components. Hence my investigation towards the extension of the BODY *skeleton_* structure for allowing the realistic animation of the upper limb skeleton.

In this direction, I have proposed:

- the adjustment of the *_elbow_* and *_wrist_* joints to definite anatomic locations, in order to allow realistic pronation/supination movements of the radius

- the adjustment of the *_clavicle_* (SC), *_scapula_* (AC) and *_shoulder_* (GH) joints to definite anatomic locations, in order to prevent from dislocation of the 3-D *skeleton_* in motion

- the adjunction of *_twisting joints_* to the *_clavicle_* and *_scapula_* joints, in order to take into account the real mobility of the shoulder joints

- the adjunction of a *scapulo-thoracic* segment as child of the scapula joint, in order to allow the constraining of the motion of the scapula against the thorax

- the modeling of the joint sinus cones for composite joint structures, in order to allow the realistic bounding of the skeleton mobility

and on these bases, I have:

- extended the *SceneLib* library for handling of the conic boundaries between joints

- extended the *BodyLib* library for handling of the adjuncted joints and segments

- extended the *InkLib* library so as to take into account the conic boundaries between joints in the inverse kinematics algorithm

- extended the interface of the skeleton editor *Skeledit* to allow the interactive design of the joint sinus cones on the body

- designed an anatomically correct template for the BODY human upper limb

- designed biomechanically correct sinus cones for the upper limb joints

- implemented an interface to allow the realistic animation of the scapula on the thorax

I have also tested and established that, in its current state, the BODY *skeleton_* structure is acceptable for generating sufficiently realistic scapular movements. The *_twisting* DOFs of the *_clavicle_* (SC) and *_scapula_* (AC) joints are clearly indispensable for a biomechanically valid representation of the shoulder motion, but for the purpose of generally realistic animation, they can be omitted without major degradation of the natural appearance of the generated motion.

In what concerns the modeling of the ST constraint, the adjunction of a *scapulo-thoracic* segment is necessary so as to materialize the point of the scapula, which is supposed to remain in contact with the ellipsoidal thorax. However, this adjunction does not affect the format of the keyframe animation files so that it may be operated when the template is being loaded by the animation interface without requiring permanent modifications of the hierarchy. Realistic animation may thus be generated using the interface and played on common bodies without requiring major updating of the animation environment developed at LIG.

8.2 Perspectives

8.2.1 Developments in CHARM

The originality of CHARM has been the combination of several disciplines and techniques for the common objective of improving the representation and understanding of the human body.

The high resolution images of the Visible Human have been used for reconstituting the anatomical musculoskeletal components using the most elaborate techniques (snakes) for 3-D reconstruction. High-level motion control techniques derived from robotics, automatics and artificial intelligence have been applied with an improved simulation algorithm for the dynamic simulation of the upper limb model. Complex constitutive relationships for modeling the highly nonlinear viscoelastic behaviors of soft tissues have been implemented and applied to their simulation using performant finite element routines. The best currently available model for muscle contraction was also applied with improved optimization techniques to the prediction of forces in the musculature and the simulation of muscle contraction. Improved techniques have finally been developed for achieving the photo-realistic animated texturing of the anatomic musculoskeletal components.

The development of an underlying biomechanical model including properties for joints, muscles and soft tissues was a necessary basis for all these developments. These constitute an initial step for further advances in research. Anatomists have found the VHD model to be a gold standard for structure identification and labelling. The models developed could be of use for medical education as well as for clinical applications like surgical simulation. Orthopedicians and sports scientists consider our developments as offering unprecedented insights into the complex kinematics of the articulations and into the unknown neuro-muscular control strategies. In what concerns the computer graphics research community, CHARM constitutes an outstanding contribution towards the realistic physically-based modeling and animation of the human body.

A first improvement could be brought with respect to the time consuming performances of the system. The high resolution of the 3-D model has been a major breakdown for the comfort of interaction using the topological modeler as well as for interactive motion control. Besides, the meshing capability of the finite element software was so overloaded that the computations on muscles had to be performed separately from the skeletal rigid motion. The use of an optimized 3-D model would thus generally be a benefit to all developments. Following this note, another improvement would be to provide the optional use of simple linear models for soft tissues so as to allow a real time deformation of soft tissues. This would allow fast sufficient preliminary evaluations of the motions and deformations before engaging into longer finite element computations.

Other potential extension to CHARM may be established on the current limitations of the model. A major one has been clearly stated by Dr. Pierre Hoffmeyer of the Clinique Orthopédique of Geneva, who expressed a specific interest in the simulation of pathological behaviors. Indeed, the human upper limb model has been based on the body of a normal man. The resulting implementations only allow the analysis and simulation of normal movements. From the medical point of view, it would have been more interesting if our application allowed the modeling and analysis of abnormal or injured articulations. For example, a common injury such as a simple shoulder dislocation can not be simulated with our system.

A major extension to the CHARM developments could thus be to replace the current ideal kinematic joint models by improved dynamic models taking into account the articular cartilagenous surfaces, the contact pressions and the gliding movements involved in real articulations.

Another interest for the medical community has been expressed as the possibility of trial of virtual surgical interventions and evaluating their consequences on the musculoskeletal dynamics. For example, in some cases of severe musculotendinal or articular injuries, the possibility of modifying the attachment topology of one or several actuators is investigated. Given a slight modification of the point of application of a force around a joint may have noticeable effects on the torque generated, it is often difficult to predict the success of a surgical intervention. There would thus be a great interest in such an application allowing the preliminary simulation of the resulting musculoskeletal mechanics. This is actually possible with the developments achieved. The only limitation is that the user has to switch from one interface to the other and to handle different files at each stage of the simulation. The different programs would gain by being integrated into a single interactive application.

8.2.2 Developments in LIG

Where my developments in LIG are concerned, their originality goes along with their necessity. As long as rough body models have been used, the unrealistic deforming of the shoulder has been very limited and did not consist of a major inconvenience with respect to the applications. For this reason, there have not been many investigations in Computer Graphics towards the improvement of the shoulder model. One effort to account for the shoulder rhythm may be outlined, made by Badler et al. (Badler 93) who applied empirical results expressing the clavicular and scapular elevation as a function of the humeral abduction. However, such relationships apply only for given movements and it may be predicted that this is not sufficient to constrain the motion of a scapula bone against the thorax. As soon as the use of a refined body model based on anatomical constituents is planned, the development of an improved shoulder model is a necessity. In this direction, my investigation for the realistic modeling and animation of the human shoulder is unprecedented.

Concerning the objective of generating realistic, nice looking animation, the design of realistic anatomical body models may constitute a major advance in Computer Graphics. Virtual Humans are bound to become more and more integrated into our every day lives, and the major reason for this may actually be the realism of their appearance. Current applications are limited to specific anthropologic simulations and major entertainment programs such as advertisements, computer games or the cinema. We may think, however, of a not too distant future, where the interface of every domestic information service like the bank, post, airport, etc., will be provided with highly intelligent and realistic virtual human figures. Widespread realism thus constitutes more of a challenge for progress than a luxury.

However, the need of a realistic shoulder model may be questioned as a virtual human is likely expected to be dressed. A first simple reply may be given that, as soon as the use of a highly realistic body model will not engage noticeable constraints with respect to the use of a basic one, there will be no consistency to prefer a basic one. Besides, at the time when such realism is achieved, standard bodies and tools are bound to emerge, and the same virtual body would be expected to be suitable for most applications, in particular for medical applications.

The existing gap between developments such as those achieved in CHARM and the usual techniques applied for computer animation are bound to be reduced, and the distinction between the animation techniques used in one field and the other, bound to disappear. My investigations towards the realistic modeling of the human shoulder using the animation environment at LIG constitute a first advance in this direction.

Following these considerations, the first natural extension to my developments may be the extension of the motion control techniques applied to the realistic animation of the human shoulder. An immediate improvement of my current approach, that is already engaged, is the integration of the scapulo-thoracic constraint in the Jacobian matrix of the inverse kinematics algorithm, so as to allow the automatic adjustment of the scapula on the thorax while the upper limb extremity is the only end-effector controlled. Another approach in this direction could also be the adaptation of a dynamic simulation algorithm to the simultaneous control of the upper limb and shoulder motions. The natural extension to this is then to proceed with optimization techniques in order to relate the predicted forces in the actuators to the deformations of physically-based muscle models, such as the one proposed by Luciana Porcher-Nedel in LIG (Nedel 98a,b).

A last extension, that could be more generally brought to my implementations in LIG and to the developments initiated in CHARM, would be to incorporate the current knowledge in artificial intelligence with the objective of modeling the neurological coordination of human motion. As presented in § 2.1, § 3.1 and § 4.4, natural motion always involves the simultaneous contraction of several dynamic actuators, themselves subjected to chemico-mechanic excitation-activation processes. If the inverse approach followed in CHARM allows the prediction of this coordination and the determination of the neural excitation histories of each actuator of the model, the direct generation of motion from simultaneous neuro-muscular control strategies is far from being achieved. Such an investigation may be seen as the ultimate challenge towards the realistic animation of the human body, before joining the more ambitious project of developing the autonomous behavior of Virtual Humans. Research on the human character still has wide fields of investigation in these directions.

References

Arczewski 93	K. Arczewski, J. Pietrucha (1993), *Mathematical Modelling of Complex Mechanical Systems - Vol. 1: Discrete Models* (Ellis Horwood)
Audu 85	M.L. Audu, D.T. Davy (1985), "The influence of muscle model complexity in musculoskeletal modeling", *J. Biomech. Engng*. – Vol. 107, pp. 147-157
Allaire 77	P.E. Allaire, J.G. Thacker, R.F. Edlich, G.J. Rodenheaver, M.T. Edgerton (1977), "Finite deformation theory for in-vivo human skin", *J. Bioeng.*, 1, 239–249
Argyris 80	J.H Argyris, J.St. Doltsinis, W.C. Knudson, J. Szimmat, K.J. Willam, H. Wüstenberg (1980), "Eulerian and Lagrangian techniques for elastic and inelastic large deformation processes", in *Computational Methods in Non-linear Mechanics*, ed. by J.T. Oden, E.B.Becker. Amsterdam: North-Holland Publishing Co.
Badler 79	N. Badler, J. O'Rourke, H. Toltzis (1979), "A Spherical Representation of a Human Body for Visualizing Movement", Proc. IEEE, Vol. 67, No. 10, pp. 1397-1403
Badler 93	N. I. Badler, C. B. Phillips, B. L. Webber (1993), *Simulating Humans*, Oxford University Press
Baerlocher 98	P. Baerlocher, R. Boulic (1998), "Task-priority formulations for the kinematic control of highly redundant articulated structures", to appear in Proc. of IROS '98, Victoria, Canada
Baker 90	H.H. Baker (1990), "Surface modeling with medical imagery", *3D Imaging in Medicine* (Eds. K.H. Höhne et al.), pp. 227-288, NATO ASI Series, Vol. F60, Springer Verlag
Bapu 80	P. Bapu, S. Evans, P. Kitka, M. Korna, J. McDaniel (1980), "User's Guide for Combiman Programs", version 4, University of Dayton Research Institute, Dayton, Ohio
Baratta 93	R.V. Baratta, M. Solomonow (1993), "Isotonic length/force models of nine different skeletal muscles", *Medical & Biological Engineering & Computing*, 31, 449–458
Becheiraz 98	P. Becheiraz, D.Thalmann (1998), "A Behavioral Animation System for Autonomous Actors personified by Emotions", *Proc. First Workshop on Embodied Conversational Characters* (WECC '98), Lake Tahoe, California
Beskos 75	D.E Beskos, J.T. Jenkins (1975), "A mechanical model for mammalian tendon", *J. Appl. Mech.*, 42, 755–758
Best 94	T.M. Best, J. McElhaney, W.E. Garrett Jr, B.S. Myers (1994), "Characterization of the passive responses of live skeletal muscle using the quasilinear theory of viscoelasticity", *J. Biomechanics*, 27, 413–419

Beylot 96 P. Beylot, P. Gingins, P. Kalra, N. Magnenat-Thalmann, W. Maurel, D. Thalman, J. Fasel (1996), "3D interactive topological modeling using visible human dataset", *Proc. Eurographics '96, Computer Graphics Forum*, 15, 3, C-33–C-44

Birk 91 D.E. Birk, F.H. Silver, R.L. Trelstad (1991), "Matrix assembly", in *Cell Biology of Extracellular Matrix*, 2nd Edn. By E.D. Hay. New York: Plenum Press

Blackeley 80 F.M. Blakeley (1980), "CYBERMAN", Chrysler Corp. Detroit, Mich.

Blatz 69 P.J. Blatz, B.M. Chu, H. Wayland (1969), "On the mechanical behavior of elastic animal tissue", *Trans. Soc. Rheol.*, 13, 82–102

Boulic 91 R. Boulic, O. Renault (1991), "3Dhierarchies for animation", in N.Magnenat Thalmann, D.Thalmann (eds): *New Trends in Animation and Vizualization*, Wiley Professional Computing, pp 59-77, John Wiley &son, Chichester

Boulic 92 R. Boulic, D. Thalmann (1992), "Combined direct and inverse kinematic control for articulated figure motion editing", *Computer Graphics Forum*, 2(4), pp. 189-202

Boulic 94 Boulic R., Huang Z., Thalmann, D. (1994), "Goal Oriented Design and Correction of Articulated Figure Motion with the TRACK System", Journal of Computer and Graphics, Vol. 18, No. 4, pp. 443-452, Pergamon Press

Boulic 95 R. Boulic, Z. Huang, J. Shen, T. Molet, T. Capin, B. Lintermann, K. Saar, D. Thalmann, N. Magnenat-Thalmann, A. Schmitt, L. Moccozet, P. Kalra, I. Pandzic (1995), "A system for the Parallel Integrated Motion of Multiple Deformable Human Characters with Collision Detection", Conference EUROGRAPHICS'95 Maastricht, *Computer Graphics Forum*, 14(3), pp. 337-348

Boulic 96 R. Boulic, R. Mas (1996), "Hierarchical Kinematic Behaviors for Complex Articulated Figures", in Thalmann & Magnenat Thalmann (Eds.): *Interactive Computer Animation*, ISBN 0-13-518309-X, Prentice Hall Europe

Boulic 97 R. Boulic, R. Mas, D. Thalmann (1997), "Interactive Identification of the Center of Mass Reachable Space for an Articulated Manipulator", *Proc. of International Conference of Advanced Robotics ICAR'97*, pp. 589–594, ISBN 0-7803-4160-0, Monterey

Bro-Nielsen 96 M. Bro-Nielsen, S. Cotin (1996), "Real-time volumetric deformable models for surgery simulation using finite elements and condensation", *Proc. Eurographics '96, Computer Graphics Forum*, 15, 3, C-57–C-66

Bruwer 87 M. Bruwer, H. Cruse (1987), "The human arm as a redundant manipulator: the control of path and joint angles", *Biol. Cybern.*, (54):125-132

Buchthal 51 F. Buchthal, E. Kaiser (1951), "The rheology of the cross-striated muscle fibre with particular reference to isotonic conditions", *Dan. Biol. Med.*, 21, 7, 233–291

Buford 76 W.L. Buford Jr., L.M. Myers, D.E. Thompson (1976), "A computer graphics system for musculoskeletal modeling", *Mathematical Biosciences*, Vol. 28, No. 1/2, pp. 607-610

Buford 90 W.L. Buford, L.M. Meyers, A.M. Hollister (1990), "Modeling and Simulation System for the Human Hand", *J. Clinical Engineering*, 15, 1990, 445-451

Bullock 88 D. Bullock, S. Grossberg (1988), "Neural dynamics of planned-arm movements: emergent invariants and speed accuracy properties", In MIT Press, *Neural Networks and Natural Intelligence*

Capelo 81 A. Capelo, V. Comincioli, R. Minelli, C. Poggesi, C. Reggiani, L. Ricciardi (1981), "Study and parameters identification of a rheological model for excised quiescent cardiac muscle", *J. Biomechanics*, 14, 1–11

Carton 62 Carton (1962), "Elastic properties of single elastic fibers", *J. Applied Physiol.*, 17, 547–551

Celniker 91 G. Celniker, D. Gossard (1991), "Deformable curve and surface finite-elements for free-form shape design", *Proc. Siggraph '91, Computer Graphics*, 25, 257–266

Chadwick 89 J.E. Chadwick, D.R. Haumann, R.E. Parent (1989), "Layered Construction for Deformable Animated Character", SIGGRAPH'89, Computer Graphics, Vol. 23, No. 3, pp. 243-252

Chao 78 E. Y. Chao and B. F. Morrey (1978) "Three-Dimensional Rotation of the Elbow", *Journal of Biomechanics*, **11**, 57–73.

Chao 93 E.Y.S. Chao, J.D. Lynch, M.J. Vanderploeg (1993), "Simulation and Animation of Musculoskeletal Joint Systems", *Journal of Biomechanical Engineering*, Vol. 115, pp. 562-568, November 1993

CHARM TR Esprit Project 9036 CHARM, Part I: Technical Annex (EC Report) (1993),

CHARM D5 J.A.C. Martins, E.B. Pires, C. Mateus, J.A.Carvalho, L.R. Salvado, S. Barata (1995), "Algorithmic proposals for the solution of the equations of motion resulting from the finite element discretization", Esprit Project 9036 CHARM, IST Lisbon

CHARM D10 E.B. Pires, J.A.C. Martins, J.A.Carvalho, L.R. Salvado, G. Engel (1996), "3-D Finite Element Prototype", Esprit Project 9036 CHARM, IST Lisbon.

CHARM D6 G. Hegron, A. Razavi, B. Arnaldi, J.-L.- Nougaret, J.P. Galivel, D. Villard, (1995), "Models for High-level Motion Control", Esprit Project 9036 CHARM, EMN Nantes/IRISA Rennes.

CHARM D8 R. Mas, J. Blat (1995), "Interface for validation tasks and set of testing sequences", Esprit Project 9036 CHARM, Universitat de les Illes Balears.

CHARM D14 S. Dorr, A. Schmitt, K. Saar, A. Stosser (1995), "High end rendering module producing photorealistic pictures", Esprit Project 9036 CHARM, Universitat Karlsurhe

Chen 92 D.T. Chen, D. Zeltzer (1992), "Pump it up: computer animation of a biomechanically based model of muscle using the finite element method", *Proc. Siggraph '92, Computer Graphics*, 26, 89–98

Christie 80 G.W. Christie, I.C. Medland (1980), "A static finite strain, finite element stress analysis of bioprosthetic heart valves", *Proc. Int. Conf. on Finite Elements in Biomechanics*, Feb. 18–20, University of Arizona

Christie 82 G.W. Christie, I.C. Medland (1982), "A non-linear finite element stress analysis of bioprosthetic heart valves", in *Finite Elements in Biomechanics*, ed. by R.H. Gallagher, B.R. Simon, P.C. Johnson, J.F. Gross. Chichester, UK: John Wiley & Sons

Chuong 83 C.J. Chuong, Y.C. Fung (1983), "Three-dimensional stress distribution in arteries", *J. Biomech. Engng.*, 105, 268–274

Costa 94a K.D. Costa, P.J. Hunter, J.M. Rogers, J.M. Guccione, L.K. Waldman, A.D. McCulloch (1994a), "A three-dimensional finite element method for large elastic deformations of ventricular myocardium: Part I - cylindrical and spherical polar coordinates", *ASME J. Biomech. Eng.*, Submitted 1994.

Costa 94b K.D. Costa, P.J. Hunter, J.S. Wayne, L.K. Waldman, J.M. Guccione, A.D. McCulloch (1994), "A three-dimensional finite element method for large elastic deformations of ventricular myocardium: Part II - prolate spherical coordinates.", *ASME J. Biomech. Eng.*, Submitted 1994.

Cozot 96 R. Cozot, D. Villard (1996), "Formal computation of non-rigid multibody systems dynamics", In SCS (ed.) *10th European Simulation Multiconference*, Budapest Hungary

Crisp 72 J.D.C. Crisp (1972), "Properties of tendon and skin", in *Biomechanics: Its Foundations and Objectives*, Y.C. Fung. New York: Prentice-Hall

Crowninshield 81 R. D. Crowninshield, R. A. Brand (1981), "A physiologically based criterion of muscle force prediction in locomotion", *J. Biomechanics*, Vol. 14, No. 11, pp. 793-801

Cutts 93 A. Cutts (1993), "Muscle physiology and electromyography", in *Mechanics of Human Joints: Physiology, Pathophysiology, and Treatment*, ed. by V. Wright, E.L. Radin. New York: Marcel Dekker

Danielson 73 D.A. Danielson (1973), "Human skin as an elastic membrane", *J. Biomechanics*, 6, 539–546

Davy 87 D.T. Davy, M.L. Audu (1987), "A dynamic optimization technique for predicting muscle forces in the wing phase of gait", J. Biomechanics, Vol. 20, No. 2, pp. 187-201

Delp 90 S.L. Delp, J.P. Loan, M.G. Hoy, F.E. Zajac, E.L. Topp, J.M. Rosen (1990), "An interactive graphics-based model of the lower extremity to study orthopaedic surgical procedures", IEEE Transactions on Biomedical Engineering, vol. 37, pp. 757-767

Delp 95 S.L. Delp, J.P. Loan (1995), "A software system to develop and analyze models of musculoskeletal structures", Computers in Biology and Medicine, vol. 25, pp. 21-34

Demiray 72 H. Demiray (1972), "A note on the elasticity of soft biological tissues", *J. Biomechanics*, 5, 309–311

Deng 88 X.Q. Deng (1988), "A finite element analysis of surgery of the human facial tissue", Ph.D. thesis, Columbia University, New York

Diamant 72 J. Diamant, A. Keller, E. Baer, M. Lii, R.G.C. Arridge (1972), "Collagen, ultrastructure and its relations to mechanical properties as a function of ageing", *Proc. R. Soc. London*, B. 180, 293–315

Dooley 82 M. Dooley (1982), "Anthropometric Modeling Programs - A Survey", *IEEE Computer Graphics and Applications*, 2(9):17-25

Dvir 78 Z. Dvir and N. Berme (1978), "The Shoulder Complex in Elevation of the Arm: A Mechanism Approach", *Journal of Biomechanics*, **11**, 219–225

Elliott 65 D.H. Elliott (1965), "Structure and function of mammalian tendon", *Biol. Rev.* , 40, 392–421

Elsen 93 Elsen PA, Pol EJD, Viergener MA (1993), "Medical Image Matching - A Review with Classification", *IEEE Engineering in Medicine and Biology*, 12:26-39

Emering 97 L. Emering, R. Boulic, S. Balcisoy, D. Thalmann (1997), "Real-Time Interactions with Virtual Agents Driven by Human Action Identification", First ACM Conf. on Autonomous Agents'97, pp. 476-477, Los Angeles - Marina Del Rey

Engel 97 G. Engel, J.A.C Martins, C:M. Mateus, E.B. Pires (1997), "Optimisation Techniques for the analysis of the upper limb mouvements and muscle forces", *V Encontro Nacional de Mecânica Computacional*, Universidade do Minho, Guimarães, Portugal, Outubro de 1997, published in Actas, Vol.2, pp. 1181-1192.

Engin 80 A.E. Engin (1980), "On the Biomechanics of the Shoulder Complex", *Journal of Biomechanics*, **13**, 575–590.

Engin 84 A.E. Engin (1984), "On the Theoretical Modelling of Human Joints", in *Mathematical Modelling in Science and Technology* (ed. J. R. Avula), Pergamon Press, New York, pp. 560–565

Engin 87 A.E. Engin and R.D. Peindl (1987), "On the Biomechanics of Human Shoulder Complex – I. Kinematics for Determination of the Shoulder Complex Sinus", *Journal of Biomechanics*, **20**, 2, 103–117.

Engin 89a A.E. Engin and S.T. Tumer (1989), "Three-Dimensional Kinematic Modelling of the Human Shoulder Complex – I. Physical Model and Determination of Joint Sinus Cones", *Journal of Biomechanical Engineering*, **111**, 107–112.

Engin 89b A.E. Engin and ST. Tumer (1989), "Three-Dimensional Kinematic Modelling of the Human Shoulder Complex – II. Mathematical Modelling and Solution via Optimization", *Journal of Biomechanical Engineering*, **111**, 113–121.

Essa 93 I. Essa, S. Sclaroff, A. Pentland (1993), "Physically based modeling for graphics and vision", in *Directions in Geometric Computing*, ed. by Ralph Martin. Winchester, UK: Information Geometers

Feit 79 T.S. Feit (1979), "Diastolic pressure-volume relations and distribution of pressure and fiber extension accross the wall of a model left ventricle", *Biophys. J.*, 28, 143–166

Fetter 82 W.A. Fetter (1982), "A progression of human figures simulated by computer graphics", IEEE Computer Graphics and Applications 2(9):9-13

Flash 85 T. Flash, N. Hogan, "The coordination of human movements: an experimentally confirmed mathematical model", J. Neuroscience, Vol. 5, pp. 1688-1703

Franklin 92 Antonion Franklin (1992), "Faster Line Segment Intersection", David Kirk (eds.): *Graphics Gems III*, Academic Press, pp. 199-202

Frisen 69a M. Frisen, M. Magi, L. Sonnerup, A. Viidik (1969), "Rheological analysis of soft collagenous tissues – Part I: Theoretical considerations", *J. Biomechanics*, 2, 13–20

Frisen 69b M. Frisen, M. Magi, L. Sonnerup, A. Viidik (1969), Rheological analysis of soft collagenous tissues – Part II: Experimental evaluations and verifications, *J. Biomechanics*, 2, 21–28

Fuchs 96 H. Fuchs, A. State, E.D. Pisano, W.F. Garrett, G. Hirota, M.A. Livingston, Mary C. Whitton, and Stephen M. Pizer (1996), "(Towards) Performing Ultrasound-Guided Needle Biopsies from within a Head-Mounted Display", Proceedings of Visualization in Biomedical Computing 1996, (Hamburg, Germany, September 22-25, pp. 591-600

Fuchs 98 H. Fuchs, M.A. Livingston, R. Raskar, D. Colucci, K. Keller, A. State, J.R. Crawford, P. Rademacher, S.H. Drake, A.A. Meyer, MD. (1998), "Augmented Reality Visualization for Laparoscopic Surgery", Proc. 1st Int. Conf. on Med. Image Comput. and Computer-Assisted Intervention (MICCAI '98), 11-13, MIT, Cambridge, MA, USA

Fung 67 Y.C. Fung (1967), "Elasticity of soft tissues in simple elongation", *Am. J. Physiol.*, 213, 1532–1544

Fung 72 Y.C. Fung (1972), "Stress-strain history relations of soft tissues in simple elongation", in *Biomechanics: Its Foundations and Objectives*, Y.C. Fung, N. Perrone, M. Anliker. Englewood Cliffs, NJ: Prentice-Hall

Fung 87 Y.C. Fung (1987), "Mechanics of soft tissues", in *Handbook of Bioengineering*, co-ed. by R. Skalak, S. Chien. New York: McGraw-Hill

Fung 93a Y.C. Fung (1993), "Bioviscoelastic solids", in *Biomechanics: Mechanical Properties of Living Tissues.* Berlin: Springer-Verlag

Fung 93b Y.C. Fung (1993), "Skeletal muscle", in *Biomechanics: Mechanical Properties of Living Tissues.* Berlin: Springer-Verlag

Galford 70 J.E. Galford, J.H. McElhaney (1970), "A viscoelastic study of scalp, brain and dura", *J. Biomechanics*, 3, 211–221

Gascuel 91 M. P. Gascuel, A. Verroust, C. Puech (1991), "A modeling system for complex deformable bodies suited to animation and collision processing", *J. Visual. Comp. Anim*., 2

Geiger 93 Geiger B (1993), *Three Dimensional Modeling of Human Organs and Its Application to Diagnosis and Surgical Planning*, These, INRIA, France.

Gingins 96a P. Gingins, P. Beylot, P. Kalra, N. Magnenat-Thalmann, W. Maurel, D. Thalmann, J. Fasel (1996), "Modeling using the Visible Human Dataset", *Proc. Medical Informatics Europe*, IOS Press, 739–743

Gingins 96b P. Gingins, P. Kalra, P. Beylot, N. Magnenat-Thalmann, J. Fasel (1996), "Using VHD to build a comprehensive human model", *The Visible Human Project Conference*, Oct.7-8, Bethesda, MD, 1996

Girard 85 M. Girard, A.A. Maciejewski (1985), "Computational Modeling for the computer animation of legged figures", *Computer Graphics*, 19(3), pp. 263-270

Glancy 72 J.J. Glancy, S.E. Larsen (1972), "Users Guide for Program SIMULA", Dynamic Science, Inc., Phoenix, Ariz.

Glantz 74 S.A. Glantz (1974), "A constitutive equation for the passive properties of muscle", *J. Biomechanics* , 7, 137–145

Glantz 77 S.A. Glantz (1977), "A three-element description for muscle with viscoelastic passive elements", *J. Biomechanics* , 10, 5–20

Gonzalez 93 R. Gonzalez, R. Woods (1993), "Digital Image Processing", Addison-Weslwy: Reading, MA.

Gonzalez 96 R.V. Gonzalez, E.L. Hutchins, R.E. Barr, L.D. Abraham (1996), "Development and evaluation of a musculoskeletal model of the elbow joint complex", *J. biomech. Engng.*, Vol. 118, pp. 32-40

Gou 70 P.F. Gou (1970), "Strain energy functions for biological tissues", *J. Biomechanics*, 3, 547–550

Gourret 89 J.P. Gourret, N. Magnenat Thalmann, D. Thalmann (1989), "Simulation of object and human skin deformations in a grasping task", *Proc. Siggraph '89, Computer Graphics*, 23, 21–30

Grant 91 *Grant's Atlas of Anatomy*, (Williams & Wilkins, Baltimore, 1991), 9th ed.

Guccione 91 J.M. Guccione, A.D. McCulloch (1991), "Passive material properties of intact ventricular myocardium determined from a cylindrical model", *J. Biomech. Engng.*, 113, 42–55

Hainaut 76 K. Hainaut (1976), *Introduction à la Biomécanique* (Maloine, Paris, 1976)

Hardt 78 D. Hardt (1978), "Determining muscle forces in the leg during normal human walking. An application and evaluation of optimization methods", *J. Biomech. Engng*., Vol. 100, pp. 72

Harris 80 R. Harris, J. Bennett, L. Dow (1980), "CAR-II - A Revised Model for Crew Assessment of Reach", technical report 1400.06B, Analytics, Willow Grove, Pa.

Haut 69 R.C Haut, R.W. Little (1969), "The rheological properties of canine anterior cruciate ligaments", *J. Biomechanics*, 2, 289–298

Hawkins 92 D. Hawkins, M. Hull (1992), "An activation-recruitment scheme for use in muscle modeling", *J. Biomechanics*, Vol. 25, No. 12, pp. 1467

Helm 91 F.C.T. van der Helm, R. Veenbaas (1991), "Modelling the Mechanical Effect of Muscles with Large Attachment Sites: Application to the Shoulder Mechanism", *Journal of Biomechanics*, **27**, 1151–1163

Helm 92 F.C.T. van der Helm, H.E.J. Veeger, G.M. Pronk, L.V.H. van der Woude, R.H. Rozendal (1992), "Geometry Parameters for Musculoskeletal Modelling of the Shoulder System", *J. Biomechanics*, **25**, 2, 129–144.

Helm 94a F.C.T. van der Helm (1994), "Analysis of the Kinematic and Dynamic Behavior of the Shoulder Mechanism", *J. Biomechanics*, **27**, 527–550.

Helm 94b F.C.T. van der Helm (1994), "A Finite Element Musculoskeletal Model of the Shoulder Mechanism", *Journal of Biomechanics*, **27**, 551–569.

Helm 95 F.C.T. van der Helm, G. M. Pronk (1995), "Three-Dimensional Recording and Description of Motions of the Shoulder Mechanism", *Journal of Biomechanical Engineering*, **117**, 27–40.

Hill 38 A.V. Hill (1938), The heat of shortening and the dynamic constants of muscle, *Proc. R. Soc*., B. 126, 136–195

Högfors 87 C. Högfors, G. Sigholm, P. Herberts (1987), "Biomechanical Model of the Human Shoulder – I. Elements", *Journal of Biomechanics*, **20**, 157–166.

Högfors 91 C. Högfors, B. Peterson, G. Sigholm, P. Herberts (1991), "Biomechanical Model of the Human Shoulder Joint", *J. Biomechanics*, **24**, 699–709.

Högfors 95 C. Högfors, D. Karlsson, B. Peterson (1995), "Structure and internal consistency of a shoulder model", *J. Biomechanics*, 28, 7, 767–777

Horowitz 88a A. Horowitz, I. Sheinman, Y. Lanir, M. Perl, S. Sideman (1988), Non-linear incompressible finite element for simulating loading and unloading of cardiac tissue – Part I: Two-dimensional formulation for thin myocardial strips, *J. Biomech. Engng.*, 110, 57–62

Horowitz 88b A. Horowitz, I. Sheinman, Y. Lanir (1988), Non-linear incompressible finite element for simulating loading and unloading of cardiac tissue – Part II: Three-dimensional formulation for thick ventricular wall segments, *J. Biomech. Engng*., 110, 62–68

Horowitz 88c A. Horowitz, I. Sheinman, Y. Lanir, M. Perl, R.K. Strumpf (1988), Structural three-dimensional constitutive law for the passive myocardium, *J. Biomech. Engng*., 110, 200–207

Huang 90 X. Huang, M.M. Black, I.C. Howard, E.A. Patterson (1990), "A two-dimensional finite element analysis of a bioprosthetic heart valve", *J. Biomechanics*, 23, 753–762

Huang 94 Z. Huang, N. Magnenat Thalmann, D. Thalmann (1994), "Interactive human motion control using a closed-form of direct and inverse dynamics", Proc. Pacific Graphics '94, Beijing

Humphrey 87 J.D. Humphrey, F.C.P. Yin (1987), "On constitutive relations and finite deformations of passive cardiac tissue – Part I: A pseudo-strain energy function", *J. Biomech. Engng.*, 109, 298–304

Humphrey 90 J.D. Humphrey, RK Strumpf, F.C.P. Yin (1990), "Determination of a constitutive relation for passive myocardium – Parts I and II", *J. Biomech. Engng.*, 112, 333-346

Hunter 88 P.J. Hunter, A.D. McCulloch, P.M.F. Nielsen, B.H. Smaill (1988), Computational Methods in Bioengineering, chapter, "A finite element model of passive ventricular mechanics", ASME, BED

Hunter 94 I.W. Hunter, L. Jones, M.A. Sagar, T. Doukoglou, S. LaFontaine, P.J. Hunter (1994), "A teleoperated microsurgical robot and associated virtual environment for eye surgery", *Presence*

Huxley 57 H.E. Huxley (1957), "The mechanism of muscular contraction", *Science,* 164, 1356–1366

Huxley 71 H.E. Huxley (1971), "The structural basis of muscular contraction", *Proc. R. Soc., B.* 178, 131–149

Huxley 74 H.E. Huxley (1974), "Review lecture on muscular contraction", *J. Physiol*., 243, 1–43

Huygue 91a J.M. Huygue, D.H. Van Campen, T. Arts, R.M. Heerthaars (1991), "The constitutive behaviour of passive heart muscle tissue: a quasilinear viscoelastic formulation", *J. Biomechanics*, 24, 841–849

Huygue 91b J.M. Huygue, D.H van Campen, T. Arts, R.M. Heethaars (1991), "A two-phase finite element model of the diastolic left ventricle", *J. Biomechanics*, 24, 527–538

INRIA TR F. Multon, J.-L. Nougaret, G. Hegron, L. Millet, B. Arnaldi (1997), *A Software Toolbox to Carry-out Virtual Experiments on Human Motion*, Rapport de Recherche INRIA No. 3303

Inman 44 V.T. Inman, J.B. Saunders, L.C. Abbott (1944), "Observations on the function of the shoulder joint", J. Bone Joint Surgery, 26-A: 1-30

Inman 46 V.T. Inman, J.B. Saunders, L.C. Abbott (1946), "Observations on the function of the clavicle", California Med, 65-A: 158-166

Janz 73 R.F. Janz, A.F. Grimm (1973), Deformation of the diastolic left ventricle – Part I: Non-linear elastic effects, *Biophys. J.*, 13, 689–704

Janz 74 R.F. Janz, R.K. Bruce, T.F. Moriarty (1974), "Deformation of the diastolic left ventricle – Part II: Non-linear geometric effects", *J. Biomechanics*, 7, 509–516

Jensen 75 R.H. Jensen, D.T. Davy (1975), "An investigation of muscle lines of action about the hip: a centroid line approach vs the straight line approach", *J. Biomechanics*, Vol. 8, pp. 103-110

Johnson 92 G.A. Johnson, K.R. Rajagopal, S.L-Y Woo (1992), "A single integral finite strain (SIFS) model of ligaments and tendons", *Advances in Bioengineering*, 22, 245–248

Johnson 96 G.R. Johnson, D. Spalding, A. Nowitzke, N. Bogduk (1996), "Modelling the muscles of the scapula morphometric and coordinate data and functional implications", *J. Biomechanics*, Vol. 29, No. 8, pp. 1039-1051

Kalra 95 P. Kalra, P. Beylot, P. Gingins, N. Magnenat-Thalmann, P. Volino, P. Hoffmeyer, J. Fasel, F. Terrier (1995), "Topological modeling of human anatomy using medical data", *Computer Animation* '95, 172–180

Kapandji 80 I.A. Kapandji (1980), *Physiologie Articulaire – Tome 1, Membre Superieur* – (Maloine, Paris)

Karakaplan 80 A.D. Karakaplan, M.P. Bienek, R. Skalak (1980), "A mathematical model of lung parenchyma", *J. Biomech. Engng.*, 102, 124–136

Karlsson 92 D. Karlsson, B. Peterson (1992), "Towards a Model for Force Predictions in the Human Shoulder", *Journal of Biomechanics*, **25**, 189–199

Kass 87 M. Kass, A. Witkin, D. Terzopoulos (1987), "Snakes: Active Contour Models, International Journal of Computer Vision", 1(4):321-331

Kastelic 78 J. Kastelic, A. Galeski, E. Baer (1978), "The multicomposite ultrastructure of tendon", *Connective Tissue Research*, 6, 11–23

Kastelic 80 J. Kastelic, I. Palley, E. Baer (1980), "A structural mechanical model for tendon crimping", *J. Biomechanics*, 13, 887–893

Katona 80 M.G. Katona (1980), "Combo-viscoplasticity: an introduction with incremental formulation", *Computers & Structures*, 11, 217–224

Kaufman 89 K.R. Kaufman, K.N. An, E.Y-S. Chao (1989), "Incorporation of the muscle architecture into the muscle length tension relationship", *J. Biomechanics*, 22, 943–948

Kawato 90 M. Kawato, Y. Maeda, Y. Uno, R. Suzuki (1990), "Trajectory formation of arm movement by cascade neural networks model based on minimum torque-change criterion", *Biol. Cybern.*, (54):275-288

Kenedi 64 R.M. Kenedi, T. Gibson, C.H. Daly (1964), "Bioengineering studies of the human skin", in *Biomechanics and Related Bioengineering Topics*, ed. by R.M. Kenedi. Oxford: Pergamon Press

Kingsley 81 E.C. Kingsley, N.A. Schofield, K. Case (1981), "SAMMIE - A Computer Aid for Man-Machine Modeling", *Computer Graphics*, (Proc. Siggraph'81), Vol. 15, No. 3, pp. 163-169

Kinzel 83 G. L. Kinzel, L. J. Gutkowski (1983), "Joint Models, Degrees of Freedom, and Anatomical Motion Measurement", *Journal of Biomechanical Engineering*, **105**, 55–61.

Kleiber 89 M. Kleiber (1989), *Incremental Finite Element Modeling in Non-linear Solid Mechanics*, transl. ed.: C.T.F. Ross. Chichester: Ellis Horwood

Koch 96 R.M. Koch, M.H. Gross (1996), "Simulating facial surgery using finite element models", *Proc. Siggraph '96*, *Computer Graphics*, 30, 421–428

Kuhn 96 Ch. Kuhn, U. Kühnapfel, H.-G. Krumm (1996), "A 'Virtual Reality' based Training System for Minimally Invasive Surgery", *Proc. Computer Assisted Radiology (CAR '96)*, Paris

Kwan 89 M.K. Kwan, S L-Y. Woo (1989), "A structural model to describe the non-linear stress-strain behavior for parallel-fibered collagenous tissues", *J. Biomech. Engng.*, 111, 361–363

Kwan 93 M.K. Kwan, T.H-C. Lin, S.L-Y. Woo (1993), "On the viscoelastic properties of the anteromedial bundle of the anterior cruciate ligament", *J. Biomechanics*, 26, 4–5, 447–452

Lanir 79 Y. Lanir (1979), "The rheological behavior of the skin: experimental results and a structural model", *Biorheology*, 16, 191–202

Lanir 83a Y. Lanir (1983), "Constitutive equations for fibrous connective tissues", *J. Biomechanics*, 16, 1–12

Lanir 83b Y. Lanir (1983), "Constitutive equations for the lung tissue", *J. Biomech. Engng.*, 105, 374–380

Lanir 87 Y. Lanir (1987), "Skin mechanics", in *Handbook of Bioengineering*, ed. by R. Skalak, S. Chien. New York: McGraw-Hill

Larrabee 86 W.F. Larrabee Jr, J.A. Galt (1986), "A finite element model of skin deformation – Part III: The finite element model", *Laryngoscope '96*, 413–419

Lee 82 G.C. Lee, N.T. Tseng (1982), "Finite element analysis in soft tissue mechanics", in *Finite Elements in Biomechanics*, ed. by R.H. Gallagher, B.R. Simon, P.C. Johnson, J.F. Gross. Chichester, UK: John Wiley & Sons

Lee 83 G.C. Lee, N.T. Tseng, Y.M. Yuan (1983), "Finite element modeling of lungs including interlobar fissures and the heart cavity", *J. Biomechanics*, 16, 9, 679–690

Leipholz 74 H. Leipholz (1974), *Theory of Elasticity*. Leyden: Nordhoff

Lemaitre 90 J. Lemaitre, J.-L. Chaboche (1990), *Mechanics of solid materials* (originally published in French as Mécanique des matériaux solides by Dunod, Paris, 1985 and cop. Bordas, Paris, 1985) transl. by B. Shrivastava. Cambridge: Cambridge University Press

Liu 78 J.T. Liu, G.C. Lee (1978), "Static finite deformation analysis of the lung", *J. Engng. Mech. Div.*, ASCE, 104, (EMI) 225–238

Lockett 72 F.J. Lockett (1972), *Non-linear Viscoelastic Solids*, London: Academic Press

Lorensen 87 W.E. Lorensen, H.E. Cline (1987), "Marching cubes: a high resolution 3D Surface Construction Algorithm", *Proc. Siggraph'87*, *Computer Graphics*, Vol. 21, No. 4, pp. 163-169

Lorensen 95 W.E. Lorensen (1995), "Marching through the Visible Man", Proc. IEEE Visualization '95, pp. 368-373,

Maciejewski 90 A.A. Maciejewski (1990), "Dealing with ill-conditioned equations of motion for articulated figures", *IEEE Computer Graphics and Applications*, 10(3), pp. 63-71

Mal 91 A.K. Mal, S.J. Singh (1991), *Deformation of elastic solids*, Englewood Cliffs, NJ: Prentice-Hall

Martins 98 J.A.C. Martins, E.B. Pires, L.R. Salvado, P.B. Dinis (1998), "A numerical model of the passive and active behavior of skeletal muscles", *Computer Methods in Applied Mechanics and Engineering*, 151, 419–433.

Massaquoi 93 S.G. Massaquoi (1993), "Evaluation of linear multiinput-multi-output feedback control of a human arm model, Msc Thesis, MIT, Boston, Massachussets

Mateus 96 C.M. Mateus (1996), "Use of Optimization Techniques in Redundant Biomechanical Systems", M.Sc.Thesis, Instituto Superior Tecnico, Lisboa.

Maurel 96 W. Maurel, D. Thalmann, P. Hoffmeyer, P. Beylot, P. Gingins, P. Kalra, N. Magnenat-Thalmann (1996), "A biomechanical musculoskeletal model of human upper limb for dynamic simulation", *EGCAS '96, 7th Eurographics Workshop on Computer Animation and Simulation '96* (Springer, Poitiers 1996), 121–136.

Maurel 98 W. Maurel, Y. Wu, N. Magnenat Thalmann, D. Thalmann (1998), *Biomechanical Models for Soft Tissue Simulation* (Springer-Verlag Berlin/Heidelberg), 173 pp.

Maurel 99 W. Maurel, D. Thalmann (1999), "A case study on human upper limb modelling for dynamic simulation", *Computer Methods in Biomechanics and Biomedical Engineering*, Vol ??, pp. 1-17 (to appear soon)

McMahon 87 T.A. McMahon (1987), "Muscle Mechanics", in *Handbook of Bioengineering*, ed. by R. Skalak, S. Chien. New York: McGraw-Hill

Meek 90 S.G. Meek, J.E. Wood, S.C. Jacobsen (1990), "Modeling musculoskeletal movement systems: joint and body segmental-dynamics, musculoskeletal actuation, and neuromuscular control"; in *Multiple Muscle Systems*, J.M. Winters, S.L-Y. Woo (eds.) Springer Verlag, New York

Mooney 40 M. Mooney (1940), "A theory of large elastic deformation", *J. Appl. Phys.*, 11, 582–92

Multon 98 F. Multon (1998), "Biomedical Simulation of Human Arm Motion", *Proceedings of ESM'98*, Manchester, UK, pp. 305-309

NAG 91 NAG Fortran Library, Concise Reference, Mark 15, Numerical Algorithms Group Limited, 1991

Nedel 98a L. Nedel, D.Thalmann (1998), "Real Time Muscle Deformations Using Mass-Spring Systems", *Proc. CGI '98*, IEEE Computer Society Press

Nedel 98b L. Porcher-Nedel, D. Thalmann (1998), "Modeling and Deformation of Human Body using an Anatomy-Based Approach", *Proc. Computer Animation '98*, Philadelphia, IEEE Computer Society Press, pp. 34-40.

Needleman 83 A. Needleman, S.A. Rabinowitz, D.K. Bogen, T.A. McMahon (1983), "A finite element model of the infarcted left ventricle", *J. Biomechanics*, 16, 45–58

Nishimura 85 H. Nishimura, M. Hirai, T. Kawai, T. Kawata, I. Shirakawa, K. Omura (1985), "Object Modeling by Distribution Function and a Method of Image Generation", *Trans. IECE Japan*, Vol. J68-D, No.4, pp. 718-725

Noser 94 H. Noser, D. Thalmann (1994), "Towards Autonomous Synthetic Actors", in: Synthetic Worlds, Springer, Tokyo, (T.L.Kunii, A.Luciani, eds) pp. 143-158

Noser 95 H. Noser, D. Thalmann (1995), "Synthetic Vision and Audition for Digital Actors", Proc. Eurographics `95, Maastricht, pp.325-336

Noser 96 H. Noser, D. Thalmann (1996), "The Animation of Autonomous Actors Based on Production Rules", *Proc. Computer Animation '96*, IEEE Computer Society Press, pp.47-57.

Noser 97 H. Noser (1997), "A Behavioral Animation System Based on L-systems and Synthetic Sensors for Actors", PhD Thesis, Computer Graphics Lab, LIG-DI-EPFL, CH 1015 Lausanne

Oden 89 J.T. Oden, J.M. Steele (1989), *Finite Elements of Non-linear Continua*. New York: Dekker

Ogden 84 R.W. Ogden (1984), *Non-linear Elastic Deformations*. Chichester: Ellis Horwood/New York: John Wiley & Sons

Orlandea 77 N. Orlandea, M.A. Chase, D.A. Calahan (1977), "A sparsity-oriented approach to dynamic analysis and design of mechanical systems, Part I and II", *ASME Journal of Engineering Industry*, 99, 773-784

Otten 87 E. Otten (1987), "A myocybernetic model of the jaw system of the rat", *Orofacial Research Group*, Bloemsingel 10, 9712 KZ Groningen, The Netherlands

Pandy 90 M.G. Pandy, F.E. Zajac, E. Sim, W.S. Levine (1990), "An Optimal control model for maximum-height human jumping", *J. Biomechanics*, Vol. 23, No. 12, pp. 1185-1198

Pandy 92 M.G. Pandy, F.C. Anderson, D.G. Hull (1992), "A parameter optimisation approach for the optimal control of large-scale musculoskeletal systems", *J. biomech. Engng.*, Vol. 114, No. 12, pp. 450-459

Pao 78 Y.C. Pao, P.A. Chevalier, J.R. Rodarte, L.D. Harris (1978), "Finite element analysis of the strain variations in excised lobe of canine lung", *J. Biomechanics*, 11, 91–100

Peindl 87 R.D. Peindl, A.E. Engin (1987), "On the Biomechanics of Human Shoulder Complex – II. Passive Resistive Properties Beyond the Shoulder Complex Sinus", *Journal of Biomechanics*, **20**, 2, 119–134.

Peng 78 S.T.J. Peng, R.F. Landel, G.S. Brody (1978), "In vitro study of human skin rheology", *Proc. 6Th N.E. Bioeng. Conf.*, 350–354

Pieper 92 S.D. Pieper (1992), *CAPS: Computer-Aided Plastic Surgery*, Ph. D. Dissertation, MIT

Pioletti 97 D.P. Pioletti (1997), *Viscoelastic properties of soft tissues: application to knee ligaments and tendons*, Ph.D. Thesis, EPFL –Lausanne

Pipkin 86 A.C. Pipkin (1986), "Large Deformations with Small Strains", in *Lectures on Viscoelasticity Theory*, *App. Math. Sci.*, 7, 115–128

Pires 97 E.B. Pires, J.A.C. Martins, L.R. Salvado, P.B. Dinis (1997), "A finite a element model for the behavior of skeletal muscles", invited lecture, *International Conference on Applied Analysis*, Lisbon

Platt 81 S. Platt, N.I. Badler (1981), "Animating facial expressions", *Proc. Siggraph '81*, *Computer Graphics*, 15, 3, 245–252

Pommet 94 A. Pommet, B. Pflesser, M. Riemer, T. Schiemann, R. Schubert, U. Tiede, K.L. Höhne (1994), "Advances in Medical Visualization", *in State of the Art Reports, Eurographics '94*, Oslo, Norway, Sept. 12-16, pp. 111-139

Pronk 91 G. Pronk (1991), "The Shoulder Girdle, Analyzed and Modelled Kinematically", Diss. Technische Universiteit Delft.

Raikova 92 R. Raikova (1992), "A General Approach for Modelling and Mathematical Investigation of the Human Upper Limb", *Journal of Biomechanics*, **25**, 857–867.

Ringelberg 85 J. Ringelberg, "EMG and force prediction of some human shoulder muscles during isometric abduction", *J. Biomechanics*, Vol. 18, No. 12, pp. 939-947

Sagar 94 M.A. Sagar, D. Bullivant, G.D. Mallinson, P.J. Hunter, I.W. Hunter (1994), "A virtual environment and model of the eye for surgical simulation", in *Computer Graphics Proceedings*, pages 205-212

Scheepers 97 F. Scheepers, R. Parent, W. Carlson, S. May (1997), "Anatomy-Based Modeling of the Human Musculature", *Proceedings of SIGGRAPH '97*, Los Angeles, pp. 163-172

Schiemann 96 T. Schiemann, J. Nuthmann, U. Tiede, K.H. Höhne (1996), "Segmentation of the Visible Human for High Quality Volume based Visualization", in Höhne, K.H., Kikinis, R. (Eds.): *Visualization in Biomedical Computing*, Lecture Notes in Computer Science 1131, Springer-Verlag, 13-22

Sederberg 86 T.W. Sederberg, S. Parry (1986), "Free-form deformations of solid geometric models", *Proc. Siggraph '86*, *Computer Graphics*, 20, 151–160

Seireg 73 A. Seireg, R. Arvikar (1973), "A mathematical model for evaluation of forces in lower extremities of the musculoskeletal system", *J. Biomechanics*, Vol .6, 313-326

Seireg 89 A. Seireg, R. Arvikar (1989), *Biomechanical Analysis of the Musculoskeletal Structure for Medicine and Sports* (Himisphere Publishing Corporation, 1989)

Shen 93 J. Shen, N.Magnenat Thalmann, D.Thalmann (1993), "Muscle-Based Human Body Deformation", *Proc 3rd Conf. on CAD/CG*, Beijing, pp.95-100, 1993

Shen 95 J. Shen, D. Thalmann (1995), "Interactive Shape Design using Metaballs and Splines", *Implicit Surfaces' 95*, Grenoble, France, April, 1995

Shoemaker 86 P.A. Shoemaker, D. Scheider, M.C. Lee, Y.C. Fung (1986), "A constitutive model for two-dimensional soft tissues and its application to experimental data", *J. Biomechanics*, 19, 6, 695–702

Sims 96 D. Sims (1996), "Putting the Visible Human to Work", *IEEE Computer Graphics and Applications*, Janvier 1996, pp. 14-15

Snyder 72 R.W. Snyder (1972), "Large deformation of isotropic biological tissue", *J. Biomechanics*, 5, 601–606

Snyder 75 R.W. Snyder, L.H.N. Lee (1975), "Experimental study of biological tissue subjected to pure shear", *J. Biomechanics*, 8, 415–419

State 96 A. State, M.A. Livingston, G. Hirota, W.F. Garrett, M.C. Whitton, H. Fuchs, E.D. Pisano (MD), "Technologies for Augmented-Reality Systems: Realizing Ultrasound-Guided Needle Biopsies", *Proceedings of SIGGRAPH '96* (New Orleans, LA, August 4-9, 1996), pp. 439-446

Steketee 85 S.N. Steketee, N.I. Badler, (1985) "Parametric keyframe interpolation incorporating kinetic adjustment and phrasing control", *SIGGRAPH'85*, Vol. 19, No. 3, pp. 255-262

Taber 91a L.A. Taber (1991), "On a non-linear theory for muscle shells – Part I: Theoretical development", *J. Biomech. Engng*., 113, 56–62

Taber 91b L.A. Taber (1991), "On a non-linear theory for muscle shells – Part II: Application to the beating of the left ventricle", *J. Biomech. Engng*., 113, 63–71

Terzopoulos 87 D. Terzopoulos, J. Platt, A. Barr, K. Fleischer (1987), "Elastically deformable models", *Proc. Siggraph '87, Computer Graphics*, 21, 205–214

Terzopoulos 88 D. Terzopoulos, K. Fleischer (1988), "Modeling inelastic deformation: viscoelasticity, plasticity, fracture", *Proc. Siggraph '88, Computer Graphics*, 22, 269–278

Terzopoulos 90 D. Terzopoulos, K. Waters (1990), "Physically-based facial modeling, analysis and animation", *J. Visual. Comp. Anim*., 1, 73–80

Terzopoulos 91 D. Terzopoulos, K. Waters (1991), "Techniques for realistic facial modeling and animation", *Proc. Computer Animation'91*, ed. by N. Magnenat-Thalmann, D. Thalmann. Tokyo: Springer-Verlag, pp. 59-74.

Thalmann 90 D. Thalmann (1990), "Robotics methods for Task-level and Behavioral Animation", in: *Scientific Visualization and Graphics Simulation*, John Wiley, pp.129-147.

Thalmann 95 D. Thalmann, R. Boulic, Z. Huang, H. Noser (1995), "Virtual and Real Humans Interacting in the Virtual World", *Proc. International Conference on Virtual Systems and Multimedia '95*, Gifu, Japan, pp.48-57

Thalmann 96 D. Thalmann, J. Shen, E. Chauvineau (1996), "Fast Realistic Human Body Deformations for Animation and VR Applications", *Computer Graphics International '96*, Pohang,Korea

Thalmanns 87 N. Magnenat Thalmann, D. Thalmann (1987), "The direction of synthetic actors in the film Rendez-vous a Montreal", *IEEE Computer Graphics and Applications,* 7(12):9-19

Thalmanns 88 N. Magnenat Thalmann, R. Laperrière, D. Thalmann (1988), "Joint-Dependent Local Deformations for Hand Animation and Object Grasping", *Proc.Graphics Interface '88*, Edmonton.

Thalmanns 90 N. Magnenat Thalmann, D. Thalmann (1990), *Computer Animation: Theory and Practice,* Springer-Verlag, Heidelberg, New York, Tokyo, (2nd edition) 240 pages

Thalmanns 93 N. Magnenat Thalmann, D. Thalmann (eds) (1993), *Virtual Worlds and Multimedia*, John Wiley, Chichester

Thalmanns 96 N. Magnenat Thalmann, D. Thalmann (eds) (1996), *Interactive Computer Animation*, Prentice Hall

Thomson 64 Arthur Thompson (1896) – *A Handbook of Anatomy for Art Students* – Dover Publications Inc. 1964 – Oxford University Press

Tiede 96 U. Tiede, T. Schiemann, K.H. Höhne (1996), "Visualizing the Visible Human", *IEEE Computer Graphics and Applications*, pp. 7-9

Tong 76 P. Tong, Y.C. Fung (1976), "The stress-strain relationship for the skin", *J. Biomechanics*, 9, 649–657

Trevisan 83 Trevisan (1983), *Etude des propriétés rhéologiques des tissus biologiques – Application au comportement mécanique des ligaments naturels et artificiels*, Ph.D. Thesis, Paris XII

Twigg 74 D.W. Twigg, R.N. Karnes (1974), *PROMETHEUS A User-Oriented Program for Human Crash Dynamics*, Report No. BCS 40038, Boeing Computer Services, Inc., Seattle, Washington

Udupa 91 J.K. Udupa, H.M. Hung, K.S. Chuang (1991), "Surface and Volume Rendering in 3D Imaging: a comparison", *Journal of Digital Imaging*, 4, 3: 159-168

Vawter 80 D.L. Vawter (1980), "A finite element model for macroscopic deformation of the lung", in *Finite Elements in Biomechanics*, ed. by R.H. Gallagher, B.R. Simon, P.C. Johnson, J.F. Gross. Chichester, UK: John Wiley & Sons

Veeger 91 H.E.J. Veeger, F.C.T. van der Helm, L.H.V. van der Woude, G.M. Pronk and R.H. Rozendal (1991), "Inertia and Muscle Contraction Parameters for Musculoskeletal Modelling of the Shoulder Mechanism", *Journal of Biomechanics*, **24**, 7, 615–629.

Veronda 70 D.R. Veronda, R.A. Westmann (1970), "Mechanical characterization of skin-finite deformations", *J. Biomechanics*, 3, 111–124

Viidik 68 A. Viidik (1968), "A rheological model for uncalcified parallel-fibered collagenous tissue", *J. Biomechanics*, 1, 3–11

Viidik 73 A. Viidik (1973), "Functional properties of collagenous tissues", *International Review of Connective Tissue Research*, 6, 127–216, ed. by D.A. Hall, D.S. Jackson. New York: Academic Press

Viidik 80 A. Viidik, J. Vuust (1980), *Biology of collagen: proceedings of a symposium*, Aarhus, July/August 1978. London: Academic Press

Viidik 87 A. Viidik (1987), "Properties of tendons and ligaments", in *Handbook of Bioengineering*, ed. by R. Skalak, S. Chien. New York: McGraw-Hill

Voges 97 U. Voges, E. Holler, B.Neisius, M. Schurr, T. Vollmer (1997), "Evaluation of ARTEMIS, the Advanced Robotics and Telemanipulator System for Minimally Invasive Surgery", *Proceedings IARP 2nd Workshop on Medical Robotics*, Forschungszentrum Karlsruhe, pp. 137-148

Warwick 73 *Gray's Anatomy*, 35th British edn. by R. Warwick, P. L. Williams (1973). Philadelphia: W.B. Saunders

Waters 87 K. Waters (1987), "A muscle model for animating three-dimensional facial expressions", *Proc. Siggraph '87, Computer Graphics*, 21, 17–24

Wehage 82 R.A. Wehage, E.J. Hang (1982), "Generalized coordinate partitioning of dimension reduction in analysis of constrained dynamic systems", *ASME, J. Mech. Design.*, 104, 247-255

Wertheim 47 M.G. Wertheim (1847), "Mémoire sur l'élasticité et la cohésion des principaux tissus du corps humain", *Annls. Chim. Phys.*, 21, 385–414

Wilhelms 97 J. Wilhelms, A. Van Gelder (1997), "Anatomically Based Modeling", *Proceedings of SIGGRAPH '97*, Los Angeles, pp. 173-180

Willmert 82 K.D. Willmert (1982), "Visualizing Human Body Motion Simulations", *IEEE Computer Graphics and Applications*, 2(9):35-38

Winter 90 D.A. Winter (1990), "Muscle mechanics", in *Biomechanics and Motor Control of the Human Movements*, 2nd edn. New York: Wiley

Woo 82 SL-Y. Woo (1982), "Mechanical properties of tendons and ligaments – Parts I & II", *4th Int. Cong. Biorh. Symp. Mech. Prop. Liv. Tiss.*, 385–408

Woo 93 S.L.-Y. Woo, G.A. Johnson, B.A. Smith (1993), "Mathematical modeling of ligaments and tendons", *J. Biomech. Engng.*, 115, 468–473

Wood 89 J.E. Wood, S.G. Meek, S.C. Jacobsen (1989), "Quantitation of Human Shoulder Anatomy for Prosthetic Arm Control - I. Surface Modelling", *Journal of Biomechanics*, **22**, 3, 273–292.

Wu 95 Y. Wu, N. Magnenat-Thalmann, D. Thalmann (1995), "A dynamic wrinkle model in facial animation and skin ageing", *J. Visual. Comp. Anim.*, 6, 195–205

Yamaguchi 95 G.T. Yamaguchi, D.W. Moran, J. Si (1995), "A computationally efficient method for solving the redundant problem in biomechanics", *J. Biomechanics*, Vol. 28, No. 8, pp. 999-1005

Yoshimoto 92 S. Yoshimoto (1992), "Ballerinas Generated by a Personal Computer", *The Journal of Visualization and Computer Animation*, Vol. 3, pp.85-90

Youm 79 Y. Youm, R.F. Cryer, K. Thambyrajah, A.E. Flatt and B.L. Sprague (1979), "Biomechanical Analysis of Forearm Pronation-Supination and Elbow Flexion-Extension", *Journal of Biomechanics*, **12**, 245–255.

Young 91 D.E. Young, R.A. Schmidt (1991), "Motor programs as units of movement control", in *Making them move: mechanics, control and animation of articulated figures*, Ed. by N. Badler, B. Barsky, D. Zeltzer, pp. 129-155

Zajac 86 F.E. Zajac, E.L. Topp, P.J. Stevenson (1986), "A dimensionless musculotendon model", *Proc. 8th A. Conf. IEEE Engng. Med. Biol. Soc.*, 601–604, Dallas-Ft Worth, TX, 7–10 Nov.

Zajac 89 F.E. Zajac (1989), "Muscle and tendon: properties, models scaling and application to biomechanics and motor control", *CRC Critic. Rev. in Biomed. Engng.*, 17, 359–411

Zeltzer 88 D. Zeltzer, K. Sims (1988), "A figure editor and gait controller to task level animation", *SIGGRAPH'88*, Tutorial Notes on Synthetic Actors: The impact of A.I. and Robotics on Animation, pp. 164-182

Zeng 87 Y.J. Zeng, D. Yager, Y.C. Fung (1987), "Measurement of the mechanical properties of the human lung tissue", *J. Biomech. Engng.*, 109, 160–174

Zienkiewicz 89 O.C. Zienkiewicz, R.L. Taylor (1989), *The finite element method*, 4th edn. London: McGraw-Hill

Zuylen 88 E.J. van Zuylen, A. van Velzen, J.J. Denier van der Gon (1988), "A Biomechanical Model for Flexion Torques of Human Arm Muscles as a Function of Elbow Angle", *Journal of Biomechanics*, **21**, 183–190

Appendix A

A.1 Coordinate Systems and Matrices for Hierarchical Modeling

	Absolute Reference		SC reference frame		GH reference frame
O_0	1st right higher voxel	O_{SC}	center, on sternum	O_{GH}	center, on scapula
X_0	⊥ to FP, forward	X_{SC}	⊥ to FP, forward	Z_{GH}	⊥ to scap. plane, forw.
Y_0	⊥ to SP, forward	Y_{SC}	⊥ to SP, to the left	X_{GH}	from Trigonum Spinae
	ST reference frame		SC local frame		GH local frame
O_T	center of ellipsoid	O_{SC}	center, on clavicle	O_{GH}	center, on humerus
Y_T	⊥ to SP, to the left	Y_C	/ / to ($O_{SC}O_{AC}$), to O_{AC}	Z_H	⊥ to hfp, forward
Z_T	long axis, upwards	X_C	⊥ to Y_C, in clp, forward	Y_H	long humeral axis, upw.
	AC reference frame		UH reference frame		UR reference frame
O_{AC}	center, on clavicle	O_{UH}	center, on humerus	O_{UR}	center, on ulna
X_{AC}	/ / to ($O_{SC}O_{AC}$), to O_{AC}	Z_{UH}	/ / to ($O_{UH}O_{HR}$), outward	Z_{UR}	/ / to ($O_{HR}O_{UR}$), to hand
Y_{AC}	⊥ to X_{AC}, in clp, backw.	X_{UH}	⊥ to ($O_{GH}O_{UH}O_{HR}$), forw.	Y_{UR}	rest, ⊥ ($O_{HR}O_{UR}O_R$), inw.
	AC local frame		UH local frame		UR local frame
O_{AC}	center, on scapula	O_{UH}	center, on ulna	O_{UR}	center, on radius
Y_S	⊥ to scap. plane backw.	Z_U	/ / to ($O_{UH}O_{HR}$), outward	Z_R	/ / to ($O_{HR}O_{UR}$), to hand
X_S	from Trigonum Spinae	X_U	⊥ to ($O_{UH}O_{HR}O_{UR}$), forw.	Y_R	⊥ to ($O_{HR}O_{UR}O_R$), inw.
	Humerus inertial frame		Ulna inertial frame		Radius inertial frame
O_{HI}	center of humerus	O_{UI}	center of ulna	O_{RI}	center of radius
Z_{HI}	⊥ to hfp, forward	Z_{UI}	/ / to ($O_{UH}O_{HR}$), outward	Z_{RI}	/ / to ($O_{HR}O_{UR}$), to hand
Y_{HI}	long humeral axis, upw.	X_{UI}	⊥ to ($O_{UH}O_{HR}O_{UR}$), forw.	Y_{RI}	⊥ to ($O_{HR}O_{UR}O_R$), inw.

($O_TX_TY_TZ_T$) in ($O_0X_0Y_0Z_0$)				($O_{SC}X_{SC}Y_{SC}Z_{SC}$) in ($O_0X_0Y_0Z_0$)				($O_{AC}X_{AC}Y_{AC}Z_{AC}$) in ($O_{SC}X_CY_CZ_C$)				($O_{GH}X_{GH}Y_{GH}Z_{GH}$) in ($O_{AC}X_SY_SZ_S$)				($O_{ST}X_SY_SZ_S$) in ($O_{AC}X_SY_SZ_S$)			
0	1	0	337.2	0	1	0	356.1	0	-1	0	0	1	0	0	2.71	1	0	0	-122.26
-0.996	0	0.089	233.3	-1	0	0	180.2	1	0	0	165.4	0	0	-1	-3.41	0	1	0	-17.02
0.089	0	0.996	-483.9	0	0	1	-335.2	0	0	1	0	0	1	0	-42.3	0	0	1	-90.43
0	0	0	1	0	0	0	1	0	0	0	1	0	0	0	1	0	0	0	1

($O_{UH}X_{UH}Y_{UH}Z_{UH}$) in ($O_{GH}X_HY_HZ_H$)				($O_{UR}X_{UR}Y_{UR}Z_{UR}$) in ($O_{UH}X_UY_UZ_U$)				($O_{UI}X_{UI}Y_{UI}Z_{UI}$) in ($O_{UH}X_UY_UZ_U$)			
0	0	1	-4.95	0	1	0	0.195	-0.978	-0.187	-0.0872	-12.26
0	-1	0	-293.6	-0.115	0	0.993	241.8	0.0519	0.185	-0.981	120.3
1	0	0	7.99	0.993	0	0.105	46.13	0.2001	-0.965	-0.172	23.59
0	0	0	1	0	0	0	1	0	0	0	1

($O_{RI}X_{RI}Y_{RI}Z_{RI}$) in ($O_{UR}X_RY_RZ_R$)				($O_{HI}X_{HI}Y_{HI}Z_{HI}$) in ($O_{GH}X_HY_HZ_H$)			
-.83	-.55	-0.1	13.5	0	1	0	-0.92
-.56	0.83	0.03	0.89	0	0	1	-140.6
-.08	0.08	-.99	-109	1	0	0	0
0	0	0	1	0	0	0	1

⊥ : normal to ... / / : parallel to ...
ST: Scapulo-Thoracic SC: Sterno-Clavicular
FP: Frontal Plane SP: Sagital Plane
UH: Ulno-Humeral UR: Ulno-Radial
O_{HR}: HR center (Tab 5.4) HR: Humero-Radial
O_R: radius end (Tab 5.5) GH: Gleno-Humeral
clp:clavicular plane scp: scapular plane hfp: humeral front plane AC: Acromio-Clavicular

Table 4. Coordinates systems and matrices for hierarchical modeling.

A.2 Joint Coordinate Systems and Limits

5.1 Sterno-Clavicular joint

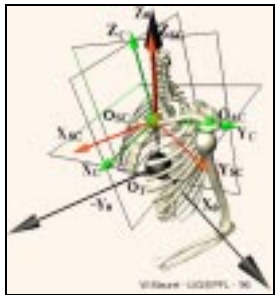

angle	θ_C	φ_C	ψ_C
axis	Z_C	X_C	Y_C
min	- 5°	+0°	-30°
max	+30°	+40°	+10°
rest	+22°	+24°	+ 0°

5.2 Acromio-Clavicular joint

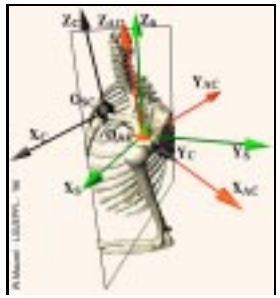

angle	θ_S	φ_S	ψ_S
axis	Z_S	X_S	Y_S
min	-68°	-10°	-10°
max	-60°	+0°	+0°
rest	-65°	-7°	-6°

5.3 Gleno-Humeral joint

angle	θ_H	φ_H	ψ_H
axis	Z_H	X_H	Y_H
min	-40°	-100°	-90°
max	+100°	+50°	+90°
rest	-13°	+3°	+0°

5.4 Ulno-Humeral joint

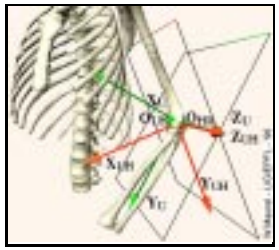

angle	θ_U	min	max	rest
axis	Z_U	-140°	+0°	-57°

5.5 Ulno-radial joint

angle	θ_R	min	max	rest
axis	Z_R	+0°	+180°	+100°

5.6 Scapulo-thoracic joint

(a,b,c) ellipsoid parameters

$\left(\theta_{O_{ST}}, \varphi_{O_{ST}}\right)$ spherical coordinates

$$\begin{cases} x_{O_{ST}} = a.\cos\varphi_{O_{ST}}\cos\theta_{\varphi_{ST}} \\ y_{O_{ST}} = b.\cos\varphi_{O_{ST}}\sin\theta_{\varphi_{ST}} \\ z_{O_{ST}} = c.\sin\varphi_{O_{ST}} \end{cases}$$

parameter	a	b	c
axis	X_T	Y_T	Z_T
value	+120	+150	+210

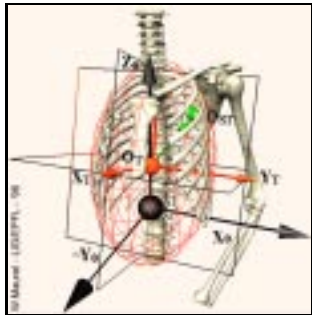

angle	θ_{Ost}	φ_{Ost}
min	+120°	+20°
max	+140°	+40°
rest	+130°	+29°

Table 5. Joints Rotations.

A.3 Forearm-Hand Equivalent Rigid Body Determination

The equation dynamics for the 3-body articulated chain may be detailed as:

$$\sum_{i=1}^{3}\begin{Bmatrix} m_i\boldsymbol{\Gamma}^{G_i}_{i/0} = m_i\mathbf{g} + \mathbf{F}_{ext/i} \\ \mathbf{I}_{i/O_1}\,\mathbf{J}_{i/0} = \mathbf{M}^{O_1}_{ext/i} \end{Bmatrix} \quad \Leftrightarrow \quad \begin{cases} \sum_{i=1}^{3} m_i\boldsymbol{\Gamma}^{G_i}_{i/0} = m_1\boldsymbol{\Gamma}^{G_1}_{1/0} + m_2\boldsymbol{\Gamma}^{G_2}_{2/0} + m_3\boldsymbol{\Gamma}^{G_3}_{3/0} \\ \sum_{i=1}^{3} \mathbf{I}_{i/O_1}\,\mathbf{J}_{i/0} = \mathbf{I}_{1/O_1}\,\mathbf{J}_{1/0} + \mathbf{I}_{2/O_1}\,\mathbf{J}_{2/0} + \mathbf{I}_{3/O_1}\,\mathbf{J}_{3/0} \end{cases} \tag{A.3.1}$$

body: $i = 1,2,3$ properties: $l_i,\ m_i,\ \mathbf{I}_{i/G_i}$

$\boldsymbol{\Gamma}^{P}_{i/j},\ \mathbf{J}_{i/j}$: linear and angular acceleration vectors of $P \in i$ with respect to j

Then, using the decomposition relationships: $\boldsymbol{\Gamma}^{O_i}_{i/0} = \boldsymbol{\Gamma}^{O_i}_{i-1/0}$ $\boldsymbol{\Omega}_{i/0} = \boldsymbol{\Omega}_{i-1/0} + \boldsymbol{\Omega}_{i/i-1}$

$$\begin{cases} \boldsymbol{\Gamma}^{P}_{i/0} = \left[\dfrac{d^2\mathbf{AP}}{dt^2}\right]_{i/0} = \boldsymbol{\Gamma}^{A}_{i/0} + \left[\dfrac{d\mathbf{V}_{i/0}}{dt}\right]_{i/0} \wedge \mathbf{AP} + \mathbf{V}_{i/0} \wedge \left[\mathbf{V}_{i/0} \wedge \mathbf{AP}\right] \\ \mathbf{J}_{i/0} = \left[\dfrac{d\mathbf{V}_{i/0}}{dt}\right]_{i/0} = \mathbf{J}_{i-1/0} + \left[\dfrac{d\mathbf{V}_{i/i-1}}{dt}\right]_{i/i-1} \end{cases} \tag{A.3.2}$$

and considering for simplicity the case of plane motion, (A.3.2) becomes:

$$\boldsymbol{\Omega}_i = \alpha_i\mathbf{y}_i \qquad \mathbf{y}_0 = \mathbf{y}_1 = \mathbf{y}_2 = \mathbf{y}_3 = \mathbf{y}_4$$

$$\begin{cases} \boldsymbol{\Gamma}^{G_3}_{3/0} = \boldsymbol{\Gamma}^{O_2}_{2/0} + l_2\left(\ddot{\alpha}_1 + \ddot{\alpha}_2\right)\mathbf{z}_2 - l_2\left(\dot{\alpha}_1 + \dot{\alpha}_2\right)^2\mathbf{x}_2 + \frac{l_3}{2}\left(\ddot{\alpha}_1 + \ddot{\alpha}_2 + \ddot{\alpha}_3\right)\mathbf{z}_3 - \frac{l_3}{2}\left(\dot{\alpha}_1 + \dot{\alpha}_2 + \dot{\alpha}_3\right)^2\mathbf{x}_3 \\ \mathbf{J}_{\substack{Y \\ 3/0}} = \left(\ddot{\alpha}_1 + \ddot{\alpha}_2 + \ddot{\alpha}_3\right)\mathbf{y}_0 \end{cases} \tag{A.3.3}$$

Considering now an equivalent rigid body $(II) = (2) + (3)$ with properties $l_{II},\ m_{II},\ \mathbf{I}^{Y}_{II/O_2}$:

$$\begin{cases} m_2\boldsymbol{\Gamma}^{G_2}_{2/0} + m_3\boldsymbol{\Gamma}^{G_3}_{3/0} = \left(m_2 + m_3\right)\boldsymbol{\Gamma}^{O_2}_{2/0} + l_2\left(m_3 + \dfrac{m_2}{2}\right)\left[\left(\ddot{\alpha}_1 + \ddot{\alpha}_2\right)\mathbf{z}_2 - \left(\dot{\alpha}_1 + \dot{\alpha}_2\right)^2\mathbf{x}_2\right] \\ \qquad\qquad + m_3\dfrac{l_3}{2}\left[\left(\ddot{\alpha}_1 + \ddot{\alpha}_2 + \ddot{\alpha}_3\right)\mathbf{z}_3 - \left(\dot{\alpha}_1 + \dot{\alpha}_2 + \dot{\alpha}_3\right)^2\mathbf{x}_3\right] \\ m_{II}\boldsymbol{\Gamma}^{G_{II}}_{II/0} = m_{II}\boldsymbol{\Gamma}^{O_2}_{II/0} + m_{II}\dfrac{l_{II}}{2}\left[\left(\ddot{\alpha}_1 + \ddot{\alpha}_2\right)\mathbf{z}_2 - \left(\dot{\alpha}_1 + \dot{\alpha}_2\right)^2\mathbf{x}_2\right] \end{cases} \tag{A.3.4}$$

$$\begin{cases} \mathbf{I}^{y}_{2/O_2}\,\mathbf{J}^{y}_{2/0} + \mathbf{I}^{y}_{3/O_2}\,\mathbf{J}^{y}_{3/0} = \left[\left(\mathbf{I}^{y}_{2/O_2} + \mathbf{I}^{y}_{3/O_2}\right)\left(\ddot{\alpha}_1 + \ddot{\alpha}_2\right) + \mathbf{I}^{y}_{3/O_2}\ddot{\alpha}_3\right]\mathbf{y}_0 \\ \mathbf{I}^{y}_{II/O_2}\,\mathbf{J}^{y}_{II/0} = \mathbf{I}^{y}_{II/O_2}\left(\ddot{\alpha}_1 + \ddot{\alpha}_2\right)\mathbf{y}_0 \end{cases} \tag{A.3.5}$$

Confronting both sides, the conditions for equivalence with the hand assumed as a rigid prolongation of the arm may be expressed as:

$$\begin{cases} m_{II}\boldsymbol{\Gamma}^{G_{II}}_{II/0} = (m_2+m_3)\boldsymbol{\Gamma}^{O_2}_{2/0} + \left[l_2\left(m_3+\frac{m_2}{2}\right) + m_3\frac{l_3}{2}\right]\left[(\ddot{\alpha}_1+\ddot{\alpha}_2)\mathbf{z}_2 - (\dot{\alpha}_1+\dot{\alpha}_2)^2\mathbf{x}_2\right] \\ \mathbf{I}^{y}_{II/O_2}\boldsymbol{J}^{y}_{II/0} = \left(\mathbf{I}^{y}_{2/O_2} + \mathbf{I}^{y}_{3/O_2}\right)(\ddot{\alpha}_1+\ddot{\alpha}_2)\mathbf{y}_0 \end{cases} \tag{A.3.6}$$

Considering now the cylinder assumption, the center of mass and inertia matrix for a homogeneous cylinder along the $\mathbf{z}$ axis, with radius r and height h, are given by:

center of mass: $$\mathbf{OG} = \frac{h}{2}\mathbf{z} \tag{A.3.7}$$

inertia matrix: $$\mathbf{I}_{i/G_i} = \begin{bmatrix} I^{Y}_{i/G_i} & 0 & 0 \\ 0 & I^{Y}_{i/G_i} & 0 \\ 0 & 0 & I^{Z}_{i/G_i} \end{bmatrix} \quad \text{with:} \quad \begin{cases} I^{Y}_{i/G_i} = m_i\left(\frac{r_i^2}{4}+\frac{l_i^2}{12}\right) \\ I^{Z}_{i/G_i} = m_i\frac{r_i^2}{2} \end{cases} \tag{A.3.8}$$

Applied to bodies $(II)=(2)+(3)$, it gives:

$$I^{y}_{3/O_2} = m_3\left(\frac{r_3^2}{4}+\frac{l_3^2}{12}+\frac{(2l_2+l_3)^2}{4}\right) \qquad I^{y}_{II/O_2} = m_{II}\left(\frac{r_{II}^2}{4}+\frac{l_{II}^2}{3}\right) \tag{A.3.9}$$

As a result, the mechanical properties of the equivalent hand-forearm cylinder may be obtained from those of the forearm and the hand using:

$$r_{II} = \left[\begin{array}{l} \frac{m_2}{m_{II}}\left(r_2^2+\frac{4}{3}l_2^2\right)-\frac{4}{3}l_{II}^2+ \\ \frac{m_3}{m_{II}}\left(r_3^2+\frac{1}{3}l_3^2+(2l_2+l_3)^2\right) \end{array}\right]^{1/2} \qquad \begin{array}{l} m_{II} = m_2+m_3 \\ l_{II} = l_2\left(1+\frac{m_3}{m_2+m_3}\right) \end{array} \tag{A.3.10}$$

where m_{II}, l_{II}, r_{II} are the mass, length and radius of the hand-forearm equivalent cylinder.

Table 1 Parameters evaluation for cylindrical rigid body modeling (Maurel 99).

$$\mathbf{I}_{i/G_i} = \begin{bmatrix} I^{Y}_{i/G_i} & 0 & 0 \\ 0 & I^{Y}_{i/G_i} & 0 \\ 0 & 0 & I^{Z}_{i/G_i} \end{bmatrix}$$

$$I^{Y}_{i/G_i} = m_i\left(\frac{r_i^2}{4}+\frac{l_i^2}{12}\right) \quad I^{Z}_{i/G_i} = m_i\frac{r_i^2}{2}$$

Segment	humeral	forearm	hand	forearm + hand	ulnar	radial
m (kg)	1.81	1.12	0.46	1.58	0.79	0.79
h (cm)	27.4	27.13	11.073	38.253	38.253	38.253
r (cm)	4.165	2.535	2.467	2.365	2.365	2.365
I^{Y}_{i/G_i} (kg.cm^2)	121.1	70.5	5.4	194.877	97.438	97.438
I^{Z}_{i/G_i} (kg.cm^2)	15.7	3.6	1.4	4.418	2.209	2.209

Appendix B

B.1 Upper Limb Action Line Topology

Lines / PCSA	Coordinates (X, Y, Z)	Bone
Anconeus	O(601, 285, -588)	Hum.
2.50	I(596, 289, -611)	Ulna
Biceps	O(487, 246, -291)	Scap.
long	G1(499, 215, -297)	Hum.
	G2(506, 213, -317)	Hum.
3.21	G3(518, 227, -355)	Hum.
Biceps short	O(472, 210, -302)	Scap.
3.08		
Biceps	I(565, 254, -622)	Radius
Brachialis	O(552, 257, -467)	Hum.
8.40	I(572, 278, -620)	Ulna
Brachiorad.	O(585, 279, -532)	Hum.
4.70	I(490, 117, -752)	Radius
Coracobrach.	O(476, 211, -301)	Scap.
2.51	I(535, 249, -423)	Hum.
Deltoideus	O(468, 231, -272)	Clav.
anterior	G1(493, 217, -319)	Hum.
8.63	G2(526, 229, -376)	Hum.
Deltoideus	O(511, 222, -273)	Scap.
lateral	G1(524, 207, -303)	Hum.
8.63	G2(526, 210, -318)	Hum.
Delt. post.	O(484, 288, -274)	Scap.
8.63	G(540, 250, -376)	Hum.
Deltoideus	I(547, 241, -405)	Hum.
Infraspinatus	O(449, 315, -355)	Scap.
	G(532, 243, -300)	Hum.
9.51	I(528, 216, -297)	Hum.
Latis. upper	O(341, 321, -431)	VT07
2.83	G(440, 336, -419)	Scap.
Latis. medial	O(342, 325, -558)	VT11
2.83	G(420, 326, -484)	R09
Latissimus	O(344, 299, -692)	V3
dorsi	G1(440, 310, -590)	R11
lower	G2(461, 299, -551)	R10
2.83	I(512, 231, -348)	Hum.
Levator	O(354, 228, -203)	VC3
2.82	I(402, 283, -278)	Scap.
Pect. maj. up.	O(407, 190, -310)	Clav.
6.80		
Pect. maj. low	O(356, 133, -437)	Stern.
6.80	G(416, 145, -413)	R03
Pectoralis	I(524, 220, -344)	Hum.
major		
Pect. min.	O(432, 139, -448)	R04
3.74	I(462, 217, -301)	Scap.

Lines / PCSA	Coordinates (X, Y, Z)	Bone
Pronator teres	O(559, 303, -573)	Hum.
2.00	I(531, 182, -686)	Radius
Rhomb. upper	O(334, 265, -256)	VC6
3.14	I(402, 311, -288)	Scap.
Rhomb. lower	O(332, 302, -332)	VT03
3.14	I(419, 335, -363)	Scap.
Serratus ant.	O(458, 159, -457)	R05
upper	G(461, 239, -384)	R04
7.00	I(407, 317, -302)	Scap.
Serratus ant.	O(478, 173, -561)	R08
lower	G(466, 260, -453)	R07
7.00	I(421, 330, -362)	Scap.
Subclavius	O(399, 207, -326)	R01
2.00	I(458, 234, -278)	Clav.
Subscapularis	O(445, 312, -341)	Scap.
13.51	I(491, 223, -319)	Hum.
	O(600, 288, -569)	Hum.
Supinator	G1(598, 299, -611)	Ulna
	G2(584, 251, -623)	Radius
3.00	G3(565, 230, -635)	Radius
	I(547, 219, -654)	Radius
Supraspinatus	O(461, 270, -301)	Scap.
	G(504, 233, -284)	Hum.
5.21	I(511, 207, -297)	Hum.
Teres major	O(469, 310, -391)	Scap.
10.20	I(506, 237, -339)	Hum.
Teres minor	O(475, 305, -373)	Scap.
2.92	I(535, 235, -311)	Hum.
Trap. upper	O(330, 248, -185)	VC2
5.30	I(498, 236, -259)	Clav.
Trap. medial	O(331, 312, -333)	VT03
5.30	I(408, 324, -303)	Scap.
Trapezius	O(340, 330, -507)	VT09
lower	G(427, 334, -363)	Scap.
5.30	I(472, 294, -276)	Scap.
Triceps long	O(498, 261, -331)	Scap.
2.30		
Triceps lateral	O(532, 233, -333)	Hum.
2.30		
Triceps short	O(530, 259, -385)	Hum.
2.30		
Triceps	I(593, 316, -594)	Ulna

(O: origin; I: insertion; G: guide)

Table 3. Muscle PCSA(cm^2) [Veeger 91] and topology (cm) in (O_0,(X_0,Y_0,Z_0)).

Appendix C

C.1 The Virtual Work Principle

$$\delta\hat{W}^{acc} = \delta\hat{W}^{int} + \delta\hat{W}^{ext}$$

Eulerian:

$\delta\hat{W}^{acc} = \int_v \delta\hat{\mathbf{u}}^T \rho \boldsymbol{\Gamma}^v \, dv$	inertial Eulerian virtual work
$\delta\hat{W}^{int} = -\int_v \mathrm{Tr}\left(\delta\hat{\mathbf{e}}^T \boldsymbol{\sigma}\right) dv = -\int_v \delta\hat{\boldsymbol{e}}^T \boldsymbol{\sigma} \, dv$	internal Eulerian virtual work
$\delta\hat{W}^{ext} = \int_v \delta\hat{\mathbf{u}}^{f^T} \mathbf{f}^v \, dv + \int_s \delta\hat{\mathbf{u}}^{t^T} \mathbf{t}^s \mathbf{n} \, ds$	external Eulerian virtual work

with:

ρ,	current local mass density
dv, ds	current volume and surface element
$\mathbf{n}$	unitary vector normal to the current surface elements ds
$\boldsymbol{\Gamma}^v$	current Eulerian acceleration vector
$\mathbf{f}^v$, $\mathbf{t}^s$	current external Eulerian body/surface force vectors
$\boldsymbol{\sigma}$ (vectorial form $\boldsymbol{\sigma}$)	current internal *Cauchy stress* tensor
$\delta\hat{\mathbf{e}}$ (vectorial form $\delta\hat{\boldsymbol{e}}$)	current elementary virtual *Eulerian strain tensor*
$\delta\hat{\mathbf{u}}$	elementary virtual *Eulerian* displacement vector

Lagrangian:

$\delta\hat{W}^{acc} = \int_V \delta\hat{\mathbf{u}}^T \rho_0 \boldsymbol{\Gamma}^v \, dV$	inertial Lagrangian virtual work
$\delta\hat{W}^{int} = -\int_V \mathrm{Tr}\left(\delta\hat{\mathbf{E}}^T \mathbf{S}\right) dV = -\int_V \delta\hat{\boldsymbol{E}}^T \boldsymbol{S} \, dV$	internal Lagrangian virtual work
$\delta\hat{W}^{ext} = \int_V \delta\hat{\mathbf{u}}^{f^T} \mathbf{f}^v \, dV + \int_S \delta\hat{\mathbf{u}}^{t^T} \mathbf{t}^s \mathbf{N} \, dS$	external Lagrangian virtual work

with:

ρ_0	initial local mass density
dV, dS	initial volume and surface element
$\mathbf{N}$	unitary vector normal to the initial surface elements dS
$\boldsymbol{\Gamma}^v$	current Lagrangian acceleration vector
$\mathbf{f}^v$, $\mathbf{t}^s$	current external Lagrangian body/surface force vectors
$\mathbf{S}$ (vectorial form $\boldsymbol{S}$)	current internal *Piola-Kirchhoff* second stress tensor
$\delta\hat{\mathbf{E}}$ (vectorial form $\delta\hat{\boldsymbol{E}}$)	current elementary virtual *Lagrangian strain* tensor
$\delta\hat{\mathbf{u}}$	elementary virtual *Lagrangian* displacement vector

Infinitesimal:

$\delta\hat{W}^{acc} = \int_V \delta\hat{\mathbf{u}}^T \rho_0 \boldsymbol{\Gamma}^v \, dV$	inertial infinitesimal virtual work
$\delta\hat{W}^{int} = -\int_V \mathrm{Tr}\left(\delta\hat{\boldsymbol{\epsilon}}^T \boldsymbol{\sigma}\right) dV = -\int_V \delta\hat{\boldsymbol{\epsilon}}^T \boldsymbol{\sigma} \, dV$	internal infinitesimal virtual work
$\delta\hat{W}^{ext} = \int_V \delta\hat{\mathbf{u}}^{f^T} \mathbf{f}^v \, dV + \int_S \delta\hat{\mathbf{u}}^{t^T} \mathbf{t}^s \mathbf{N} \, dS$	external infinitesimal virtual work

C.2 The Constitutive Relationship

Elasticity. The theory of elasticity states that the stress at any time depends only on the local deformation at that time. The constitutive equation for isotropic elastic materials is (Oden 89):

$$\mathbf{S} = \alpha_0\mathbf{I} + \alpha_1\mathbf{E} + \alpha_2\mathbf{E}^2 \text{ with: } \alpha_0,\ \alpha_1,\ \alpha_2 \text{ polynomials in terms of strain invariants } I_1,\ I_2,\ I_3 \quad \text{(C.2.1)}$$

A particular case of elasticity is considered when there exists a strain energy function W such that the strain may be derived from it. In this case, the material is said *hyperelastic*. The isotropic strain energy function W is usually assumed composed of *distortional* and *dilational* components, and expressed in terms of the strain invariants $I_1,\ I_2,\ I_3$ as:

$$\mathbf{S} = \frac{\partial W(\mathbf{E})}{\partial \mathbf{E}} \quad \text{with:} \quad \begin{matrix} W(I_1, I_2, I_3) = W_I(I_1, I_2) + W_{II}(I_3) \\ W_I(I_1, I_2) = \sum_{p,q=0}^{\infty} C_{pq0}(I_1 - 3)^p (I_2 - 3)^q \end{matrix} \quad \text{with:} \quad \begin{matrix} C_{000} = 0 \\ (p, q, r) \text{ integers} \end{matrix} \quad \begin{matrix} \\ W_{II}(I_3) = \sum_{r=1}^{\infty} C_{00r}(I_3 - 1)^r \end{matrix} \quad \text{(C.2.2)}$$

In particular, if the isotropic hyperelastic material is incompressible, the stress tensors may be decomposed into elastic and pressure stress components as:

$$\mathbf{S} = \frac{\partial W_I(I_1, I_2)}{\partial \mathbf{E}} + L\frac{\partial I_3}{\partial \mathbf{E}} \quad \text{with:} \quad L = -\frac{p}{2J} \quad p\text{: } \textit{hydrostatic pressure} \quad \text{(C.2.3)}$$

Finally, in the case of small deformation, the constitutive relation above, which still contains *geometrical* and *physical* non-linearities within $\mathbf{E}$, its exponent and coefficients, may be linearized into the common *Hooke* law (Leipholz 74):

$$\boldsymbol{\sigma} = \mathbf{K}^M\boldsymbol{\epsilon} = \lambda \mathrm{Tr}(\boldsymbol{\epsilon})\mathbf{I} + 2\mu\boldsymbol{\epsilon} \quad \text{with:} \quad \lambda = \frac{\nu E}{(1+\nu)(1-2\nu)} \quad \mu = \frac{E}{2(1+\nu)} \quad \text{(C.2.4)}$$

$\lambda,\ \mu$: *Lamé* constants $\quad E$: *Young* modulus $\quad \nu$: *Poisson* coefficient

Linear Viscoelasticity. The viscoelastic behaviors suggest a general linear relationship between the stress, the strain and their derivatives with respect to time in the form:

$$\left[\mathbf{P}_0 + \mathbf{P}_1\frac{\partial}{\partial t} + \mathbf{P}_2\frac{\partial^2}{\partial t^2} + \ldots\right]\mathbf{S}(t) = \left[\mathbf{Q}_0 + \mathbf{Q}_1\frac{\partial}{\partial t} + \mathbf{Q}_2\frac{\partial^2}{\partial t^2} + \ldots\right]\mathbf{E}(t) \quad \text{(Lockett 72)} \quad \text{(C.2.5)}$$

Solution of (C.2.5) may be carried out as *stress relaxation* behavior or as *creep* behavior as:

$$\mathbf{S}(t) = \int_0^t \boldsymbol{\Phi}(t-\tau)\frac{\partial \mathbf{E}(\tau)}{\partial \tau}d\tau \quad \text{with: } \boldsymbol{\Phi} \text{ tensorial } \textit{relaxation} \text{ function of the material} \quad \text{(C.2.6)}$$

$$\mathbf{E}(t) = \int_0^t \boldsymbol{\Psi}(t-\tau)\frac{\partial \mathbf{S}}{\partial \tau}d\tau \quad \text{with: } \boldsymbol{\Psi} \text{ tensorial } \textit{creep} \text{ function of the material} \quad \text{(C.2.7)}$$

In particular, for isotropic materials, they may be developed into:

$$\mathbf{S}(t) = \left[\int_0^t \lambda(t-\tau)\mathrm{Tr}\left(\dot{\mathbf{E}}(\tau)\right)d\tau\right]\mathbf{I} + 2\int_0^t \mu(t-\tau)\dot{\mathbf{E}}(\tau)d\tau \qquad \mathbf{E}(t) = \left[\int_0^t \chi(t-\tau)\mathrm{Tr}\left(\dot{\mathbf{S}}(\tau)\right)d\tau\right]\mathbf{I} + 2\int_0^t \zeta(t-\tau)\dot{\mathbf{S}}(\tau)d\tau \quad \text{(C.2.8)}$$

which may lead to common models such as *Kelvin-Voigt's* or *Maxwell's* (Lemaitre 90):

$$\mathbf{S} = \mathbf{K}^{M}\mathbf{E} + \mathbf{D}^{M}\dot{\mathbf{E}} \qquad \text{with:} \qquad \begin{cases} \mathbf{K}^{M}\mathbf{E} = \lambda \mathrm{Tr}(\mathbf{E})\mathrm{I} + 2\mu\mathbf{E} & \lambda, \mu \text{ are } \textit{Lamé} \text{ coefficients} \\ \mathbf{D}^{M}\dot{\mathbf{E}} = \lambda\theta_{\lambda}\mathrm{Tr}(\dot{\mathbf{E}})\mathrm{I} + 2\mu\theta_{\mu}\dot{\mathbf{E}} & \theta_{\lambda}, \theta_{\mu} \text{ are constants for viscosity} \end{cases} \tag{C.2.9}$$

$$\dot{\mathbf{E}} = \mathbf{H}^{M}\mathbf{S} + \mathbf{N}^{M}\dot{\mathbf{S}} \qquad \text{with:} \qquad \begin{cases} \mathbf{H}^{M}\mathbf{S} = \dfrac{1+\nu}{E\eta_1}\mathbf{S} - \dfrac{\nu}{E\eta_2}\mathrm{Tr}(\mathbf{S})\mathbf{I} & \text{E, } \nu \textit{ Young} \text{ modulus and } \textit{Poisson} \text{ coefficient} \\ \mathbf{N}^{M}\dot{\mathbf{S}} = \dfrac{1+\nu}{E\eta_1}\dot{\mathbf{S}} - \dfrac{\nu}{E\eta_2}\mathrm{Tr}(\dot{\mathbf{S}})\mathbf{I} & \eta_1, \eta_2 \text{ constants for viscosity} \end{cases} \tag{C.2.10}$$

However, the general isotropic relations defined above are not suitable in practice for the numerical solution of viscoelastic problems. Solutions are then rather looked for in the form of series decompositions such as that detailed here for stress relaxation for an isotropic material (Katona 80, Pipkin 86):

$$\mathbf{S}(t) = \mathbf{K}^{E}\mathbf{E}(t) - \mathbf{D}^{P}\sum_{i=1}^{n_P} P_i\,\mathbf{P}_i - \mathbf{D}^{Q}\sum_{i=1}^{n_Q} Q_i\,\mathbf{Q}_i \qquad \text{with:} \qquad \mathbf{P}_i = \int_0^t \frac{\mathbf{E}(\tau)}{\beta_i} e^{-\frac{t-\tau}{\beta_i}}\,d\tau \qquad \mathbf{Q}_i = \int_0^t \frac{\mathbf{E}(\tau)}{\gamma_i} e^{-\frac{t-\tau}{\gamma_i}}\,d\tau$$

$$\mathbf{K}^{E} = \boldsymbol{\Phi}(0) = \mathbf{D}^{P}P(0) + \mathbf{D}^{Q}Q(0) \tag{C.2.11}$$

where P_i, Q_i, β_i, γ_i and $\mathbf{D}^{P}$, $\mathbf{D}^{Q}$ are the *relaxation moduli*, *relaxation times* and constant matrix for bulk and shear respectively. Similar expressions may be written for small deformations, using the Cauchy stress tensor $\boldsymbol{\sigma}$ and the linearized strain tensor $\boldsymbol{\epsilon}$.

C.3 Temporal Integration Methods

$$\mathbf{M}_n\ddot{\mathbf{U}}_{n+1} + \mathbf{D}_n\dot{\mathbf{U}}_{n+1} + \mathbf{K}_n\Delta\mathbf{U} = \mathbf{L}_{n+1} - \mathbf{R}_n \qquad \text{with:} \qquad \mathbf{R}_n = \mathbf{L}_n - \mathbf{M}_n\ddot{\mathbf{U}}_n + \mathbf{D}_n\dot{\mathbf{U}}_n \qquad \text{(C.3.1)}$$

The Finite Difference Methods. Similar to the geometric finite difference method, the finite difference discretization is here applied to the time basis and is based on finite difference approximations of the acceleration and velocity in terms of the unknown incremental displacement vector $\mathbf{U}_n$. There are mainly two groups (Kleiber 89):

Explicit Integration: This method is usually known as the *central difference* method.

$$\mathbf{A}_n\Delta\mathbf{U} = \mathbf{L}_n - \mathbf{P}_n \qquad \text{where:} \qquad \mathbf{A}_n = \left(\frac{1}{\Delta t^2}\mathbf{M}_n + \frac{1}{2\Delta t}\mathbf{D}_n\right) \qquad \mathbf{P}_n = \mathbf{R}_n - \left(\frac{1}{\Delta t^2}\mathbf{M}_n - \frac{1}{2\Delta t}\mathbf{D}_n\right)\left(\mathbf{U}_n - \mathbf{U}_{n-1}\right)$$

$$\ddot{\mathbf{U}}_n = \frac{1}{\Delta t^2}\left[\Delta\mathbf{U} - \left(\mathbf{U}_n - \mathbf{U}_{n-1}\right)\right] \qquad \dot{\mathbf{U}}_n = \frac{1}{2\Delta t}\left[\Delta\mathbf{U} + \left(\mathbf{U}_n - \mathbf{U}_{n-1}\right)\right] \qquad \text{(C.3.2)}$$

with: $\mathbf{A}_n$: effective stiffness matrix at step n
$\mathbf{L}_n$: nodal external force vector at step n
$\mathbf{P}_n$: effective internal force vector at step n

After solving for the nodal increment vector $\Delta\mathbf{U}$, all the tangent matrices can be updated before considering the next step. This method is said to be conditionally stable, i.e. the time step must be smaller than the critical value, which may be calculated from the mass, damping and stiffness properties of the complete element assemblage.

Implicit Integration: This method is known as the *Newmark method*. (C.3.3)

$$\mathbf{A}_n\Delta\mathbf{U} = \mathbf{L}_{n+1} - \mathbf{P}_n \qquad \text{with:} \qquad \mathbf{U}_{n+1} = \mathbf{U}_n + \dot{\mathbf{U}}_n\Delta t + \left[\left(\frac{1}{2} - \alpha\right)\ddot{\mathbf{U}}_n + \alpha\ddot{\mathbf{U}}_{n+1}\right]\Delta t^2 \qquad \dot{\mathbf{U}}_{n+1} = \dot{\mathbf{U}}_n + \Delta t\left[(1-\beta)\ddot{\mathbf{U}}_n + \beta\ddot{\mathbf{U}}_{n+1}\right]$$

$$\mathbf{A}_n = \left(\frac{1}{(\alpha\Delta t)^2}\mathbf{M}_n + \frac{\beta}{\alpha\Delta t}\mathbf{D}_n + \mathbf{K}_n\right) \qquad \mathbf{P}_n = \mathbf{R}_n - \mathbf{M}_n\left[\frac{1}{\alpha\Delta t}\dot{\mathbf{U}}_n + \left(\frac{1}{2\alpha} - 1\right)\ddot{\mathbf{U}}_n\right] + \mathbf{D}_n\left[\left(\frac{\beta}{\alpha} - 1\right)\dot{\mathbf{U}}_n + \frac{\Delta t}{2}\left(\frac{\beta}{\alpha} - 2\right)\ddot{\mathbf{U}}_n\right]$$

$\mathbf{A}_n$: effective stiffness matrix at n
$\mathbf{P}_n$: effective internal force vector at n
α, β: parameters for tuning stability and accuracy
$\mathbf{L}_{n+1}$: nodal external force vector at n+1

A basic difference with respect to the explicit approach is that, since the equilibrium is considered at time $t+\Delta t$, the tangent stiffness matrix $\mathbf{K}_n$ appears as factor to the required incremental displacement $\Delta\mathbf{U}$. Furthermore, for some values of parameters α and β, there is no critical time-step limit, and a much larger time-step Δt can be used.

The Linear Iteration Methods. In the explicit approaches, the solution of the incremental finite element equations may be considered entirely consistent with the dynamic equilibrium conditions at time t, since the configuration is known at this time. By contrast, in the implicit approaches, the configuration at time $t+\Delta t$, for which the equilibrium conditions are established, is unknown. It is usually necessary therefore, to perform additional iterations, in order to find a more accurate solution *within each time interval*.

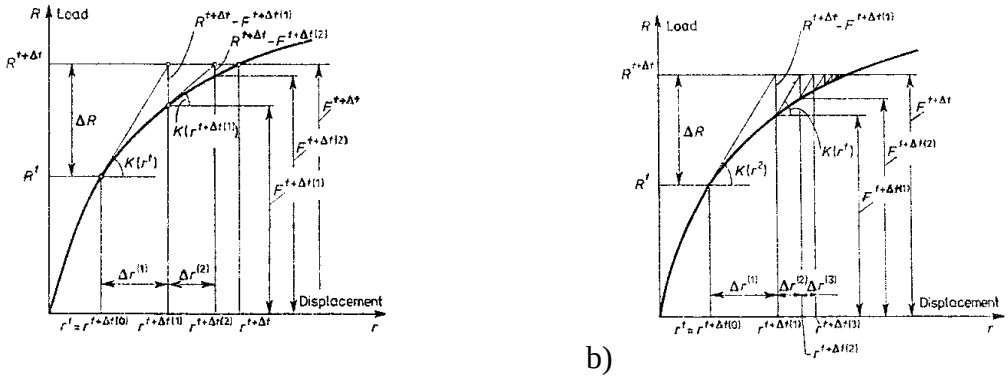

a) b)

Fig. C.1 Full (a) and modified (b) Newton-Raphson scheme (Kleiber 89)

This may be achieved using *Newton-Raphson* schemes (Fig. C.1) (Kleiber 89):

$$\mathbf{M}_n\ddot{\mathbf{U}}_{n+1\_i} + \mathbf{D}_n\dot{\mathbf{U}}_{n+1\_i} + \mathbf{K}_{n+1\_i}\Delta\mathbf{U}_i = \mathbf{L}_{n+1} - \mathbf{R}_{n+1\_i-1} \quad \text{with:} \quad \mathbf{K}_{n+1\_0} = \mathbf{K}_n \quad \mathbf{R}_{n+1\_0} = \mathbf{R}_n \quad \mathbf{U}_{n+1\_0} = \mathbf{U}_n \qquad \text{(C.3.4)}$$

where the internal nodal force vector $\mathbf{R}_{n+1\_i-1}$ corresponds to the stress state with displacement:

$$\mathbf{U}_{n+1\_i-1} = \mathbf{U}_{n+1\_i-2} + \Delta\mathbf{U}_{i-1} \quad \text{with:} \quad \Delta\mathbf{U}_{i-1}\text{: i-th correction to the incremental displacement vector}$$

This scheme is called *full Newton-Raphson scheme* since the updating and factorizing of the effective stiffness matrix takes place in each iteration. It is usually not very efficient in general geometric and material nonlinear response calculations. Thus, a *modified Newton-Raphson* scheme has been developed in which the tangent stiffness matrix $\mathbf{K}_n$ is updated at the beginning of each increment only. All nonlinearities are then taken into account in $\mathbf{R}_{n+1\_i}$.

The Mode Superposition Method. As integration must be carried out for many time steps, it may be more effective to first transform the equilibrium equation into a form in which the step-by-step solution is less costly. The basic way is a change of basis from p generalized *nodal* displacements to q generalized *modal* displacements $(q \ll p)$, prior to incremental solution. $\mathbf{U}_n$ may be expressed in terms of the generalized modal displacement vector $\mathbf{V}_n$ as:

$$\mathbf{U}_n = \boldsymbol{\Psi}\mathbf{V}_n \quad \text{with:} \quad \boldsymbol{\Psi}_{p\times q} = \begin{bmatrix}\boldsymbol{\psi}_1 & \cdots & \boldsymbol{\psi}_q\end{bmatrix} \quad \text{so that:} \quad \mathbf{K}_0\boldsymbol{\Psi} = \mathbf{M}_0\boldsymbol{\Psi}\boldsymbol{\Omega}^2 \qquad \text{(C.3.5)}$$

$$\omega_k = 2\pi f_k \quad f_k\text{: natural frequencies } \left(k \equiv (1,\cdots,q)\right) \quad \boldsymbol{\Omega}^2 = \begin{bmatrix}\omega_1^2 & 0 & 0\\ 0 & \ddots & 0\\ 0 & 0 & \omega_q^2\end{bmatrix}$$

with:
- $\mathbf{V}_n$ generalized modal displacement vector at step n
- $\boldsymbol{\psi}_k$ eigenvectors of the linearized eigenproblem at time 0
- $\boldsymbol{\Psi}$ modal transfer matrix composed of the column eigenvectors

The resulting modal equation of motion takes then the general form:

$$\ddot{\mathbf{V}}_{n+1\_i} + \boldsymbol{\Lambda}\dot{\mathbf{V}}_{n+1\_i} + \boldsymbol{\Omega}^2\Delta\mathbf{V}_i = \tilde{\mathbf{L}}_{n+1} - \tilde{\mathbf{R}}_{n+1\_i-1} \quad \text{with:} \quad \tilde{\mathbf{R}}_{n+1\_i-1} = \boldsymbol{\Psi}^T\mathbf{R}_{n+1\_i-1} \quad \tilde{\mathbf{L}}_{n+1} = \boldsymbol{\Psi}^T\mathbf{L}_{n+1} \qquad \text{(C.3.6)}$$

$$\tilde{\mathbf{M}}_n = \boldsymbol{\Psi}^T\mathbf{M}_n\boldsymbol{\Psi} \equiv \mathbf{I} \qquad \tilde{\mathbf{D}}_n = \boldsymbol{\Psi}^T\mathbf{D}_n\boldsymbol{\Psi} = \boldsymbol{\Lambda} \qquad \tilde{\mathbf{K}}_n = \boldsymbol{\Psi}^T\mathbf{K}_n\boldsymbol{\Psi} = \boldsymbol{\Omega}^2$$

Solution may thus be more easily obtained converted from the modal solution (Kleiber 89).

C.4 Physically-Based Modeling

Lagrange Formalism. Using generalized coordinates q_i ($\mathbf{x} = \mathbf{x}(q_i, t)$), and assuming a constant mass density ($\rho \equiv \rho_0$), the equation of motion of the continuous medium may be expressed using the *Lagrange* equation as: (C.4.1)

$$\frac{d}{dt}\left(\frac{\partial U}{\partial \dot{q}_i}\right) - \frac{\partial U}{\partial q_i} = f_{q_i}^{int} + f_{q_i}^{ext} \quad \text{with:}$$

$U = \frac{1}{2}\rho\left(\frac{d\mathbf{x}}{dt}\right)^2$ kinetic energy of an elementary volume

$f_{q_i}^{int}$ projections on q_i of the internal force vector

$f_{q_i}^{ext}$ projections on q_i of the external force vector

In their approach (Terzopoulos 87), Terzopoulos et al. considered the deformable body as an isotropic hyper-viscoelastic material such that the internal force vector derives from internal viscous and elastic potential energies as: (C.4.2)

$$f_{q_i}^{int} = -\frac{\partial W_{visco}^{int}}{\partial \dot{q}_i} - \frac{\partial W_{elast}^{int}}{\partial q_i} \quad \text{with:}$$

$W_{visco}^{int} = \frac{1}{2}\eta \dot{q}_i^{\,2}$ viscous energy function assumed linear

$W_{elast}^{int} = \int_V \left\| \mathbf{C} - \mathbf{C}^0 \right\|_\alpha^2 dV$ elastic strain energy function

with:

η	uniform constant damping density
$\mathbf{C}$	Cauchy-Green right dilation tensor of the deformation
$\mathbf{C}^0$	dilation tensor associated to the natural shape of the body
$\| \|_\alpha$	α-weighted matrix norm

The Lagrange equation of motion may thus be obtained in the form:

$$\frac{d}{dt}\left(\rho \frac{dq_i}{dt}\right) + \eta \frac{dq_i}{dt} + \frac{\partial W_{elast}^{int}}{\partial q_i} = f_{q_i}^{ext} \qquad \text{(C.4.3)}$$

With this approach, any kind of material behavior may be modeled as soon as the proper strain energy function is provided.

The Finite Difference Method. The *finite difference method* is a particular case of finite element discretization. Instead of a geometric element of arbitrary shape, the discretization is based on grid subdivisions of the continuous domain along its main axes. For example, the first and second derivative of a 2-D function $u_{m,n} = u[m,n]$ with subdivision steps $h_1 \times h_2$ are: (C.4.4)

forward:

$$D_1^+(u)[m,n] = \frac{u_{m+1,n} - u_{m,n}}{h_1}$$

$$D_2^+(u)[m,n] = \frac{u_{m,n+1} - u_{m,n}}{h_2}$$

central:

$$D_{11}(u)[m,n] = D_1^-\left[D_1^+(u)\right][m,n]$$

$$D_{22}(u)[m,n] = D_2^-\left[D_2^+(u)\right][m,n]$$

backward:

$$D_1^-(u)[m,n] = \frac{u_{m,n} - u_{m-1,n}}{h_1}$$

$$D_2^-(u)[m,n] = \frac{u_{m,n} - u_{m,n-1}}{h_2}$$

$$D_{12}^+(u)[m,n] = D_{21}^+(u)[m,n] = D_1^+\left[D_2^+(u)\right][m,n] \qquad D_{12}^-(u)[m,n] = D_{21}^-(u)[m,n] = D_1^-\left[D_2^-(u)\right][m,n]$$

Applied to a continuous problem, such as the Virtual Work equation, the discretization method leads indifferently to a same tensorial equation as defined in § 4.1.1 (Terzopoulos 87).

Appendix D

D.1 Finite Element Implementation for Skin (CHARM D10)

$$W = \frac{1}{2}\left(\alpha_1 E_{11}^2 + \alpha_2 E_{22}^2 + \alpha_3 E_{33}^2 + \alpha_3 E_{21}^2 + 2\alpha_4 E_{11}E_{22}\right) + \frac{1}{2}ce^{a_1E_{11}^2+a_2E_{22}^2+a_3E_{12}^2+a_3E_{21}^2+2a_4E_{11}E_{22}+\gamma_1E_{11}^3+\gamma_2E_{22}^3+\gamma_4E_{11}^2E_{22}+\gamma_5E_{11}E_{22}^2} \text{ (Tong 76)} \quad \text{(D.1.1)}$$

Considering plane state of stress, the components of the 2nd Piola-Kirchhoff stress tensor were derived as (CHARM D10):

$$S_{11} = \frac{\partial W}{\partial E_{11}} = \alpha_1 E_{11} + \alpha_4 E_{22} + cA_1 X \qquad A_1 = a_1 E_{11} + a_4 E_{22} + \frac{3}{2}\gamma_1 E_{11}^2 + \gamma_4 E_{11}E_{22} + \frac{1}{2}\gamma_5 E_{22}^2$$

$$S_{22} = \frac{\partial W}{\partial E_{22}} = \alpha_4 E_{11} + \alpha_2 E_{22} + cA_2 X \qquad A_2 = a_4 E_{11} + a_2 E_{22} + \frac{3}{2}\gamma_2 E_{22}^2 + \frac{1}{2}\gamma_4 E_{11}^2 + \gamma_5 E_{11}E_{22} \quad \text{(D.1.2)}$$

$$S_{12} = \frac{\partial W}{\partial E_{12}} = \alpha_3 E_{12} + ca_3 E_{12} X \qquad X = e^{a_1E_{11}^2+a_2E_{22}^2+a_3E_{12}^2+a_3E_{21}^2+2a_4E_{11}E_{22}+\gamma_1E_{11}^3+\gamma_2E_{22}^3+\gamma_4E_{11}^2E_{22}+\gamma_5E_{11}E_{22}^2}$$

For implementation in ABAQUS, the constitutive Jacobian was developed in the form:

$$\frac{\partial \Delta\sigma_{ij}}{\partial \Delta\varepsilon_{rs}} = -\delta_{rs}\sigma_{ij} + \delta_{ir}\sigma_{sj} + \sigma_{ir}\delta_{js} + \frac{1}{J}F_{ik}\left(\frac{\partial \mathbf{S}}{\partial \mathbf{E}}\right)_{klmn} F_{rm}F_{sn}F_{jl} \qquad \text{with:} \quad \text{(D.1.3)}$$

$$\frac{\partial S_{11}}{\partial E_{11}} = \alpha_1 + c\left(\frac{\partial A_1}{\partial E_{11}}X + A_1\frac{\partial X}{\partial E_{11}}\right) \qquad \frac{\partial S_{22}}{\partial E_{22}} = \alpha_2 + c\left(\frac{\partial A_2}{\partial E_{22}}X + A_2\frac{\partial X}{\partial E_{22}}\right)$$

$$\frac{\partial S_{11}}{\partial E_{22}} = \alpha_2 + c\left(\frac{\partial A_1}{\partial E_{22}}X + A_1\frac{\partial X}{\partial E_{22}}\right) \qquad \frac{\partial S_{22}}{\partial E_{12}} = \frac{\partial S_{22}}{\partial E_{21}} = cA_2\frac{\partial X}{\partial E_{12}}$$

$$\frac{\partial S_{11}}{\partial E_{12}} = \frac{\partial S_{11}}{\partial E_{21}} = cA_1\frac{\partial X}{\partial E_{12}} \qquad \frac{\partial S_{22}}{\partial E_{11}} = \alpha_4 + c\left(\frac{\partial A_2}{\partial E_{11}}X + A_2\frac{\partial X}{\partial E_{11}}\right)$$

$$\frac{\partial S_{12}}{\partial E_{11}} = \frac{\partial S_{21}}{\partial E_{11}} = ca_3E_{12}\frac{\partial X}{\partial E_{11}}$$

$$\frac{\partial S_{12}}{\partial E_{12}} = \frac{\partial S_{21}}{\partial E_{21}} = \frac{\partial S_{12}}{\partial E_{21}} = \frac{\partial S_{21}}{\partial E_{12}} = \alpha_3 + ca_3\left(X + \frac{\partial X}{\partial E_{12}}\right)$$

$$\frac{\partial S_{12}}{\partial E_{22}} = \frac{\partial S_{21}}{\partial E_{22}} = ca_3E_{12}\frac{\partial X}{\partial E_{22}}$$

$$\frac{\partial A_1}{\partial E_{11}} = a_1 + 3\gamma_1E_{11} + \gamma_4E_{22} \qquad \frac{\partial X}{\partial E_{11}} = X\left(2a_1E_{11} + 2a_4E_{22} + 3\gamma_1E_{11}^2 + 2\gamma_4E_{11}E_{22} + \gamma_5E_{22}^2\right)$$

$$\frac{\partial A_1}{\partial E_{22}} = \frac{\partial A_2}{\partial E_{11}} = a_4 + \gamma_4E_{11} + \gamma_5E_{22} \qquad \frac{\partial X}{\partial E_{22}} = X\left(2a_2E_{22} + 2a_4E_{11} + 3\gamma_2E_{22}^2 + \gamma_4E_{11}^2 + 2\gamma_5E_{11}E_{22}\right)$$

$$\frac{\partial A_2}{\partial E_{22}} = a_2 + 3\gamma_2E_{22} + \gamma_5E_{11} \qquad \frac{\partial X}{\partial E_{12}} = 2a_3E_{12}X$$

D.2 Finite Element Implementation for Active/Passive Muscle

$$W_f = W_f\left(\lambda_f, \zeta^{CE}\right) = W_{PE}\left(\lambda_f\right) + W_{SE}\left(\lambda_f, \zeta^{CE}\right) \quad \text{with:} \quad \text{(CHARM D10, Pires 97, Martins 98)} \quad \text{(D.2.1)}$$

$W_{PE}\left(\lambda_f\right) = T_0^M \int^{\lambda_f} f_{PE}(\lambda) d\lambda$ strain energy of the parallel element PE

$W_{SE}\left(\lambda_f, \zeta^{CE}\right) = T_0^M \int^{\lambda_f} f_{SE}\left(\lambda, \zeta^{CE}\right) d\lambda$ strain energy of the series element SE

The force in the parallel element was chosen in the form of a parabola as proposed by Chen and Zeltzer (Chen 92):

$$F^{PE} = F_0^M f_{PE}\left(\lambda^M\right) \qquad f_{PE}\left(\lambda^M\right) = \begin{cases} 4\left(\lambda^M - 1\right)^2 & \text{for } \lambda^M > 1 \\ 0 & \text{otherwise} \end{cases} \quad \text{(D.2.2)}$$

whereas the force in the series element was integrated from its stiffness as (Martins 98):

$$K^{SE} = \frac{dF^{SE}}{dL^{SE}} = \frac{100F^{SE} + 10F_0^M}{L_0^M} \qquad \zeta^{CE} = \frac{L^{CE} - L_0^{CE}}{L_0^{CE}} = \frac{L_0^{CE}}{L_0^M}\left(\frac{L^{CE} - L_0^{CE}}{L_0^{CE}}\right) \quad \text{(Pandy 90)} \quad \text{(D.2.3)}$$

$$F^{SE} = F_0^M f_{SE}\left(\lambda^M, \zeta^{CE}\right) \qquad f_{SE}\left(\lambda^M, \zeta^{CE}\right) = \begin{cases} 0.1\left(e^{100\left(\lambda - 1 - \zeta^{CE}\right)} - 1\right) & \text{for } \lambda^M > 1 + \zeta^{CE} \\ 0 & \text{otherwise} \end{cases} \quad \text{(D.2.4)}$$

The 2nd Piola-Kirchhoff stress was then derived in the form: (**N** undeformed fiber direction)

$$\mathbf{S} = W_1'\left(2J^{-2/3}\mathbf{I} - \frac{2}{3}I_1^C\mathbf{C}^{-1}\right) + W_f'\left[J^{-2/3}\lambda_f^{-1}(\mathbf{N}\otimes\mathbf{N}) - \frac{1}{3}\lambda_f\mathbf{C}^{-1}\right] + JW_J'\mathbf{C}^{-1} \quad \text{with:} \quad \text{(D.2.5)}$$

$$W_1' = \frac{\partial W_1}{\partial I_1^C} = bce^{b\left(I_1^C\right)-3} \qquad W_f' = W_{PE}' + W_{SE}' = T_0^M\left(f_{PE} + f_{SE}\right) \qquad W_J' = \frac{\partial W_J}{\partial J} = \frac{2}{D}(J-1)$$

The complex material tangent operator was finally derived as: $\mathbf{H} = \frac{\partial^2 W}{\partial \mathbf{E}^2} = \frac{\partial \mathbf{S}}{\partial \mathbf{E}}$ (D.2.6)

Curriculum Vitae

Walter Maurel was born in 1969 in Nice, France. He has acquired a general engineering education in ENSAM (Ecole Nationale Supérieure d'Arts et Métiers) and graduated in 1992. He then spent one year studying image processing and synthesis at the Ecole des Mines and the Université Jean Monnet in Saint-Etienne, where he received his DEA (*Diplome d'Etude Approfondie*) in digital image science.

Besides this, he has also gained experience from several internships in industry, in particular in mechanical conception and C.A.O. After this, he has joined the Computer Graphics Lab of EPFL (LIG) and worked in several European projects, essentially oriented towards the application of virtual reality in medicine. He is currently Ph. D. research assistant at LIG.

His main interests in computer animation are the physically-based modeling and simulation techniques. More generally, he is fond of clay modeling and artistic hand-drawn animation.

Publications

P. Beylot, P. Gingins, P. Kalra, N. Magnenat-Thalmann, W. Maurel, D. Thalman, J. Fasel (1996), "3D interactive topological modeling using visible human dataset", *Proc. Eurographics '96, Computer Graphics Forum*, 15, 3, C-33–C-44

P. Gingins, P. Beylot, P. Kalra, N. Magnenat-Thalmann, W. Maurel, D. Thalmann, J. Fasel (1996), "Modeling using the Visible Human Dataset", *Proc. Medical Informatics Europe*, IOS Press, 739–743

W. Maurel, D. Thalmann, P. Hoffmeyer, P. Beylot, P. Gingins, P. Kalra, N. Magnenat-Thalmann (1996), "A biomechanical musculoskeletal model of human upper limb for dynamic simulation", *EGCAS '96, 7th Eurographics Workshop on Computer Animation and Simulation '96* (Springer, Poitiers 1996), 121–136.

W. Maurel and Y. Wu, N. Magnenat Thalmann, D. Thalmann, *Biomechanical Models for Soft Tissue Simulation* (Springer-Verlag Berlin/Heidelberg 1998), 173 pp.

W. Maurel, D. Thalmann (1999), "A case study on human upper limb modelling for dynamic simulation", *Computer Methods in Biomechanics and Biomedical Engineering*, Vol ??, pp. 1-17 (to appear soon).

W. Maurel, D. Thalmann (????), "Human shoulder modeling including scapulo-thoracic constraint and joint sinus cones" (dedicated to a computer graphics audience – in preparation).